REPORT DOCUMENTATION PAGE	*Form Approved* *OMB No. 0704-0188*

1. REPORT DATE *(DD-MM-YYYY)* 7 September 2004	**2. REPORT TYPE** Final Report	**3. DATES COVERED** *(From - To)* 18 Oct 2001 to 30 Sep 2004

4. TITLE AND SUBTITLE
Final Report on N00014-02-1-0115 Non-Rayleigh Reverberation Studies

5a. CONTRACT NUMBER

5b. GRANT NUMBER
N00014-02-1-0115

5c. PROGRAM ELEMENT NUMBER

5d. PROJECT NUMBER
ARL #09119

6. AUTHOR(S)
Douglas A. Abraham

5e. TASK NUMBER
ARL #.01

5f. WORK UNIT NUMBER

7. PERFORMING ORGANIZATION NAME(S) AND ADDRESS(ES)
The Pennsylvania State University
Applied Research Laboratory
P. O. Box 30
State College, PA 16804-0030

8. PERFORMING ORGANIZATION REPORT NUMBER

9. SPONSORING/MONITORING AGENCY NAME(S) AND ADDRESS(ES)
Dr. John A. Tague, Code 321
Office of Naval Research
800 North Quincy Street
Arlington, VA 22217

10. SPONSOR/MONITOR'S ACRONYM(S)

11. SPONSOR/MONITOR'S REPORT NUMBER(S)

12. DISTRIBUTION/AVAILABILITY STATEMENT
Unlimited distribution

13. SUPPLEMENTARY NOTES

14. ABSTRACT

The primary focus of the research was on developing a statistical model for non-Rayleigh reverberation that allowed for analysis of the reverberation statistics, and therefore the sonar system probability of false alarm, as a function of sonar system and environmental parameters. Non-Rayleigh reverberation is a statistical representation of clutter in active sonar systems. False alarms arising from clutter are recognized as the primary hindrance to automating the detection-classification-localization (DCL) sonar signal processing chain for low- and mid-frequency systems operating in shallow water environments.
The most significant accomplishment was a novel derivation of the well known K distribution using a finite number of scatterers as opposed to the traditionally assumed infinite (negative binomial distributed) number. This derivation allowed linking the shape parameter of the K distribution to sonar parameters such as transmit waveform bandwidth and array beamwidth as well as environmental parameters such as scatterer density and multipath propagation.

15. SUBJECT TERMS
non-Rayleigh reverberation, multipath propagation, array processing, modeling sonar detection performance

16. SECURITY CLASSIFICATION OF:			**17. LIMITATION OF ABSTRACT**	**18. NUMBER OF PAGES**	**19a. NAME OF RESPONSIBLE PERSON**
a. REPORT	**b. ABSTRACT**	**c. THIS PAGE**			Douglas A. Abraham
Unclassified	Unclassified	Unclassified	Unlimited	103	**19b. TELEPHONE NUMBER** *(Include area code)* (703) 243-1160 ext 229

Standard Form 298 (Rev. 8/98)
Prescribed by ANSI Std. Z39.18

DISTRIBUTION STATEMENT A
Approved for Public Release
Distribution Unlimited

Final Report on N00014-02-1-0115 *Non-Rayleigh Reverberation Studies*

Douglas A. Abraham
The Pennsylvania State University
Applied Research Laboratory
P.O. Box 30
State College, PA 16804
email: abrahad@psu.edu
phone: 814-863-7089

September 7, 2004

1 Executive summary

This report documents the research performed under ONR Grant Number N00014-02-1-0115 entitled *Non-Rayleigh Reverberation Studies.* The primary focus of the research was on developing a statistical model for non-Rayleigh reverberation that allowed for analysis of the reverberation statistics, and therefore the sonar system probability of false alarm, as a function of sonar system and environmental parameters. Non-Rayleigh reverberation is a statistical representation of clutter in active sonar systems. False alarms arising from clutter are recognized as the primary hindrance to automating the detection-classification-localization (DCL) sonar signal processing chain for low- and mid-frequency systems operating in shallow water environments.

The most significant accomplishment was a novel derivation of the well known K distribution using a finite number of scatterers as opposed to the traditionally assumed infinite (negative binomial distributed) number. This derivation allowed linking the shape parameter of the K distribution to sonar parameters such as transmit waveform bandwidth and array beamwidth as well as environmental parameters such as scatterer density and multipath propagation. Other accomplishments include modeling broadband active sonar detection performance in K-distributed reverberation, developing an efficient simulation method for K-distributed reverberation accounting for

the effects of propagation and spectral shaping, extending the finite-number-of-scatterers K-distribution model to account for multipath propagation and conventional (fixed weight) array processing.

This research resulted in five published conference papers and four published journal articles, all of which are included in the final section of this report.

2 Long term goals

The long-term goals of this project begin with understanding the relationship between the statistical distribution of the reverberation induced matched filter envelope and the sonar system parameters and propagation and scattering properties of the ocean environment. With this understanding it will be possible to develop and analyze signal processing algorithms that appropriately account for non-Rayleigh reverberation. Such algorithms and analysis are imperative for the successful incorporation of broadband sonar into fleet systems and can provide more accurate modeling for sonar system performance prediction, simulation, and design optimization.

3 Novel derivation of K-distributed reverberation

This derivation of the K distribution starts with a finite number of exponentially distributed scatterers within an active sonar resolution cell. Under simple propagation conditions, the shape parameter of the K distribution is shown to be proportional to the number of these scatterers within the resolution cell, a number proportional to the sonar beamwidth, the range, the cosine of the grazing angle, and inversely proportional to the transmit waveform bandwidth.

The theoretical model is compared with real data to validate the beamwidth and bandwidth assumptions. The latter turns out to hold only for low bandwidths, with the inverse proportionality leveling and changing to an increase owing to an over-resolution of fundamental scattering elements (e.g., rocks, exposed ridges, mud volcanoes, or ship wrecks).

These results are documented in [1, 2, 3, 4].

4 Analysis of detection performance in K-distributed reverberation

Using the model described in the previous section, the probability of detection was determined for a broadband transmit waveform in the presence of K-distributed reverberation. It was observed that increasing bandwidth always improved probability of detection; however, it was most effective when the reverberation was nearly Rayleigh (i.e., a large K-distribution shape parameter). This echoes the previous results of the author (performed under a previous ONR contract) published in [5] which did not take into account the effects of the spreading of the target echo as bandwidth increases.

These results are documented in [6].

5 Simulation of non-Rayeleigh reverberation

Reverberation simulators began by generating individual scatterers and propagating acoustic rays from the source to each scatterer and then on to the receiver. Although this method provided detailed control over the scattering statistics and the ability to simulate reverberation from high bandwidth transmit waveforms, it is obviously extremely computationally intensive. Thus, reverberation simulation nearly entirely moved into methods that assume that the reverberation envelope statistics are Rayleigh, requiring only the computation of the reverberation power and any potential correlations between beams. An alternative method was developed that essentially bridges the gap between these two extremes. In this method, reverberation is simulated after matched filtering and beamforming using the K distribution. Multipath propagation was included by applying a finite-impulse-response filter to direct-path-only reverberation and the spectrum was shaped to account for Doppler scales and the transmit waveform spectrum. Approximate random number generation techniques were developed for the K distribution that are computationally less intensive than direct generation, allowing for a quicker implementation.

These results are documented in [7].

6 Modeling the effects of propagation and array processing

The finite-number-of-scatterers K distribution model was developed under the assumption of direct-path-only propagation and ideal spatial filtering.

The model was then extended to account for multipath propagation where it was seen that, compared with direct-path-only propagation, multipath propagation has the effect of making reverberation more Rayleigh-like. It was also observed that increasing the vertical aperture of the sonar source or receiver has the effect of making the reverberation more non-Rayleigh by decreasing the number of contributing paths at higher angles compared with an omni-directional source or receiver.

The model was similarly extended to account for conventional (fixed weight) array processing (i.e., conventional beamforming - CBF) where it was seen that the shape parameter was better approximated as proportional to the 6-dB array beamwidth than the 3-dB array beamwidth. Narrowband simplifications were also derived along with a rule of thumb for their region of validity—these will be invaluable in statistical data analysis dictating the maximum bandwidth that should be analyzed under the narrowband model assumptions. Broadband and narrowband signal simulation methods for array data were also derived.

These results are documented in [8, 9, 10].

References

[1] D. A. Abraham and A. P. Lyons, "Reverberation envelope statistics and their dependence on sonar beamwidth and bandwidth," in *Impact of Littoral Environmental Variability on Acoustic Predictions and Sonar Performance*, N. G. Pace and F. B. Jensen, Eds. 2002, pp. 539–546, Kluwer Academic Publishers.

[2] A. P. Lyons, D. A. Abraham, and E. Pouliquen, "Predicting scattered envelope statistics of patchy seafloors," in *Impact of Littoral Environmental Variability on Acoustic Predictions and Sonar Performance*, N. G. Pace and F. B. Jensen, Eds. 2002, pp. 211–218, Kluwer Academic Publishers.

[3] D. A. Abraham and A. P. Lyons, "Novel physical interpretations of K-distributed reverberation," *IEEE Journal of Oceanic Engineering*, vol. 27, no. 4, pp. 800–813, October 2002.

[4] D. A. Abraham and A. P. Lyons, "Reverberation envelope statistics and their dependence on sonar bandwidth and scatterer size," *IEEE Journal of Oceanic Engineering*, vol. 29, no. 1, pp. 126–137, January 2004.

[5] D. A. Abraham, "Signal excess in K-distributed reverberation," *IEEE Journal of Oceanic Engineering*, vol. 28, no. 3, pp. 526–536, July 2003.

[6] D. A. Abraham, "Broadband detection in K-distributed reverberation," in *Proceedings of IEEE Sensor Array and Multichannel Signal Processing Workshop*, August 2002, pp. 53–57.

[7] D. A. Abraham and A. P. Lyons, "Simulating non-Rayleigh reverberation and clutter," *IEEE Journal of Oceanic Engineering*, vol. 29, no. 2, April 2004, in press.

[8] J. R. Preston and D. A. Abraham, "Non-Rayleigh reverberation characteristics near 400 Hz observed on the New Jersey Shelf," *IEEE Journal of Oceanic Engineering*, vol. 29, no. 2, April 2004, in press.

[9] D. A. Abraham, A. P. Lyons, and K. M. Becker, "The effect of multipath on reverberation envelope statistics," in *Proceedings of 7th European Conference on Underwater Acoustics*, Delft, The Netherlands, July 2004.

[10] D. A. Abraham and A. P. Lyons, "Array modeling of non-rayleigh reverberation," in *Proceedings of Institute of Acoustics Conference on Sonar Signal Processing*, Loughborough, England, September 2004.

7 Publications

The following publications are attributable to grant N00014-02-1-0115 *Non-Rayleigh Reverberation Studies.* They are in sequence on the following pages.

1. A. P. Lyons, D. A. Abraham and E. Pouliquen, *Predicting the scattered amplitude statistics of patchy seafloors*, proceedings of SACLANTCEN Conference on *Impact of Environmental Littoral Variability on Acoustic Predictions and Sonar Performance*, Kluwer Academic Publishers, pp. 211–218, September 2002.
2. D. A. Abraham and A. P. Lyons, *Reverberation envelope statistics and their dependence on sonar beamwidth and bandwidth*, proceedings of SACLANTCEN Conference on *Impact of Environmental Littoral Variability on Acoustic Predictions and Sonar Performance*, Kluwer Academic Publishers, pp. 539–546, September 2002.

3. D. A. Abraham, *Broadband detection in K-distributed reverberation*, Proceedings of IEEE Sensor Array Multichannel (SAM) Signal Processing Workshop, Arlington, Virginia, pp. 53–57, August 2002.
4. D. A. Abraham and A. P. Lyons, *Novel physical interpretations of K-distributed reverberation*, IEEE Journal of Oceanic Engineering, vol. 27, no. 4, pp. 800–813, October 2002.
5. D. A. Abraham and A. P. Lyons, *Reverberation envelope statistics and their dependence on sonar bandwidth and scatterer size*, IEEE Journal of Oceanic Engineering, Vol. 29, No. 1, pp. 126–137.
6. D. A. Abraham and A. P. Lyons, *Simulation of non-Rayleigh reverberation and clutter*, IEEE Journal of Oceanic Engineering, Vol. 29, No. 2, pp. 347–362, April, 2004.
7. J. R. Preston and D. A. Abraham, *Non-Rayleigh reverberation characteristics near 400 Hz observed on the New Jersey Shelf*, IEEE Journal of Oceanic Engineering, Vol. 29, No. 2, pp. 215–235, April, 2004.
8. D. A. Abraham, A. P. Lyons, and K. M. Becker *The effect of multipath on reverberation envelope statistics*, Proceedings of the Seventh European Conference on Underwater Acoustics, ECUA 2004, Delft, The Netherlands, July, 2004.
9. D. A. Abraham and A. P. Lyons *Array modeling of non-Rayleigh reverberation*, Proceedings of Institute of Acoustics Conference on Sonar Signal Processing, Loughborough, England, September, 2004.

PREDICTING SCATTERED ENVELOPE STATISTICS OF PATCHY SEAFLOORS

ANTHONY P. LYONS AND DOUGLAS A. ABRAHAM

The Pennsylvania State Univ., Applied Research Lab., P.O. Box 30, State College, PA 16804
E-mail: apl2@psu.edu

ERIC POULIQUEN

SACLANT Undersea Research Centre, Viale San Bartolomeo 400, 19138 La Spezia, Italy
E-mail: pouliq@saclantc.nato.int

Local hydrodynamic or biological influences often produce seafloors in shallow water that consist of differing types of material. The scattering properties from the components of these kinds of seafloors may have a complicated relationship in terms of their frequency dependence and/or angular response. Consequently, this relationship directly influences the angular and frequency response of the scattered envelope distributions. The probability distribution function (PDF) for a scattering scenario such as this is not easy to obtain analytically. However, a recently developed model for a patchy seafloor with a single dominating component [1] allows for numerical analysis of the envelope PDF for more complicated seafloors through the use of Hankel transforms of the joint characteristic function (JCF) of the complex envelope. The JCF is straightforward to construct for complicated patchy seafloors. In this study, a direct link between environmental parameters and the envelope distributions of backscatter is developed. The influence of the relative scattering properties of the seafloor patches on the scattered envelope statistics will be examined in detail.

1 Introduction

The envelope distribution resulting from roughness scattering from a seafloor with uniform properties is expected to be Rayleigh as the central limit theorem holds resulting in Gaussian reverberation. Local hydrodynamic or biological influences, however, often produce seafloors in shallow water that consist of several different types of material. Seagrass and shellfish are examples of scatterers that often do not exist uniformly on the seabed but are distributed in patches of varying density. Examples of heterogeneous seafloors are shown in the photographs displayed in Fig. 1. Patchiness in the scattering properties commonly found in shallow water suggests that the Rayleigh distribution model might not always be appropriate, especially when the area ensonified by the transmit and receive beams is not large enough to encompass enough of the patches of differing scattering strength. The acoustic expression of non-uniform seafloors manifests itself in the form of non-Rayleigh or heavy tailed envelope distribution functions and is termed clutter. Clutter affects the detection of targets in acoustic imagery by increasing the probability of false alarm. In this respect clutter is at least as important, if not more important, a problem to object detection than mean scattered levels in shallow water. To ameliorate the effect of clutter through adaptive systems or signal processing algorithms

N.G. Pace and F.B. Jensen (eds.), Impact of Littoral Environmental Variability on Acoustic Predictions and Sonar Performance, 211-218.

it will first be necessary to understand the properties and causes of non-Rayleigh scattered envelope statistics at high frequency.

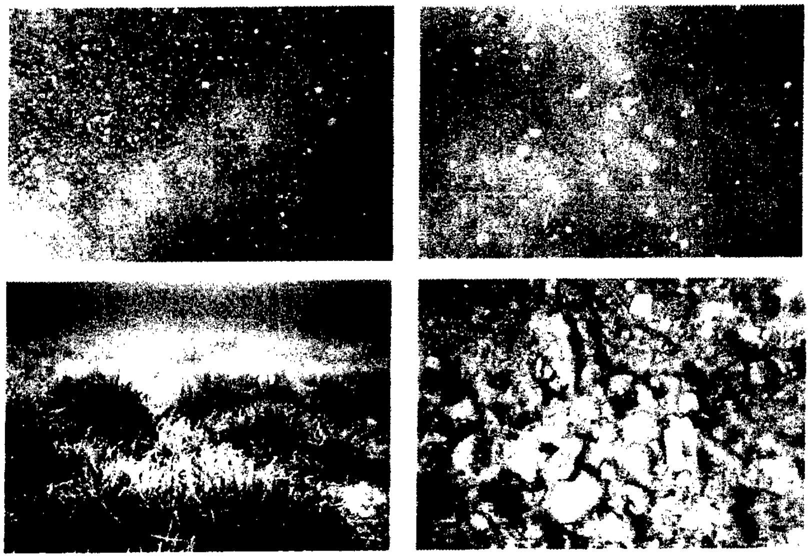

Figure 1. Examples of heterogeneous seafloors: clockwise from top left gravel, shell, rocks, *Posidonia oceanica* seagrass.

The statistical character of reverberation is a function of the sonar system parameters of beamwidth, bandwidth and frequency and environmental properties such as the number, size distribution, and scattering strength of patches. The relationship between the scattering strength of the patches and that of the surrounding seafloor can be a function of frequency and grazing angle and so directly influences the angular and frequency response of the scattered envelope distributions. In order to improve predictive capabilities for high-frequency acoustic systems operating in shallow water areas that have spatially heterogeneous seafloors it is imperative to link the scattered envelope distributions to seafloor scattering models. Unfortunately, there are very few physics-based models that link a description of the environment and sonar system to the probability density function of the clutter induced matched filter envelope output. Additionally, these models, which assume an infinite number of scatterers [2], do not retain the pertinent description of the environment that would allow prediction of how the envelope PDF changes as a function of sonar system parameters or is affected by varying environmental scattering mechanisms. A recently developed model for a seafloor consisting of a finite number of scattering patches [1] allows for numerical analysis of the envelope PDF for more complicated seafloors through the use of Hankel transforms of the joint characteristic function (JCF) of the complex envelope. The JCF is straightforward to construct for complicated patchy seafloors allowing a direct link between environmental parameters and the envelope distributions of backscatter to be developed. Using these concepts, the influence of the relative scattering properties of the seafloor patches on the angular and frequency response of the scattered envelope statistics will be examined in detail for several example scenarios in this paper.

2 Statistical model for scattering patches on a Gaussian background

Abraham and Lyons have recently developed a theoretical model for scattered envelope distributions resulting from interface scattering from a seafloor comprised of patches [1]. Diffuse scattering from the interface produces a Gaussian distributed return from each patch by virtue of the central limit theorem, with power proportional to the patch area and backscattering coefficient. Now assume that there are n such patches within a resolution cell of the sonar system. The clutter component of the complex envelope of the received signal in this resolution cell (i.e., after beamforming and matched filtering) may then be represented as

$$R=\sum_{i=1}^{n}\sqrt{A_i}Z_i \tag{1}$$

where A_i is the area of the i^{th} patch and Z_i is a zero-mean, complex, Gaussian random variable with variance σ^2. In the model of Abraham and Lyons it was assumed that the patches dominated the background scattering and were characterized as having an exponentially distributed area

$$A_i \sim f(a)=\frac{1}{\mu}e^{-\frac{a}{\mu}} \tag{2}$$

where μ is the average patch area. Assuming that A_i and Z_i are independent of each other and the responses of the other patches, the JCF of R is shown to be [1]

$$\Phi_K(\omega,\gamma)=\frac{1}{\left[1+\frac{1}{4}\mu\sigma^2\left(\omega^2+\gamma^2\right)\right]^n} \tag{3}$$

This turns out to be of the same form as that for the JCF of the K-distribution [1] with shape parameter $\alpha = n$, the number of patches in a resolution cell, and scale parameter $\lambda = \mu\sigma^2$, the average area of each patch times the backscattered power per unit area of each patch. The resultant sum is non-Gaussian owing to the random power of each component even though each patch produces a Gaussian response.

Using the equivalence of the matched filter envelope for scattering from patches (with no contribution from background scattering) to a K-distribution, the complex envelope in the case including background scattering can be described in a manner analogous to adding a Gaussian target to K-distributed reverberation [3]. The complex envelope of the reverberation is now written as the sum of the contribution of the scattering patches and of the Gaussian background

$$R = Z_0 + \sum_{i=1}^{n} \sqrt{A_i} Z_i \ . \tag{4}$$

The background seafloor scattering (Z_0) can be thought of being composed of a multitude of scatterers and is therefore complex Gaussian distributed with zero mean owing to the central limit theorem. The CDF for the combined patch and background-scattered envelope can be found by using the JCF of the complex envelope [3]. The advantage of using JCFs is that the JCF of the combined patch plus background scattering is the product of the individual JCFs. The JCF for the patch scattering is given by Eq. (3) and the JCF for the Gaussian background with power λ_0 would be

$$\Phi_B(a) = e^{-\frac{\lambda_0}{4}a} \tag{5}$$

and the JCF, Φ_A, for the combined background reverberation plus patch scattering, would be the product of Φ_K given by Eq. (3) and Φ_B given by Eq. (5). The cumulative distribution function (CDF) can be obtained from the JCF via a Hankel transform of order one,

$$F_Y(y) = \sqrt{y} H_1 \left\{ \sqrt{y}, \frac{1}{x} \Phi_A\left(x^2\right) \right\} \tag{6}$$

A useful indicator of the non-Rayleigh behavior of scattering is the scintillation index given by

$$\sigma_I^2 = \frac{\mu_2 - \mu_1^2}{\mu_1^2} \tag{7}$$

where μ_1 and μ_2 are the first and second moments of $Y = |R|^2$. Assuming that the form of the complex matched filter is described by Eq. (4), the first and second moments can easily be derived (b.d.) as $\mu_1 = \lambda_0 + \alpha\lambda$ and $\mu_2 = 2\mu_1^2 + 2\alpha\lambda^2$ yielding the scintillation index

$$\sigma_I^2 = 1 + \frac{2\alpha\lambda^2}{\left(\lambda_0 + \alpha\lambda\right)^2} \tag{8}$$

Experimentally determined values of high frequency reverberation scintillation index from Lyons and Abraham [4] will be compared later to predicted values.

3 Seafloor patch scattering models

The backscattered signal from a sonar resolution cell may consist of contributions from a number of surface features or patches. These include surface scattering from a variety of bare sediment types, such as sands or gravels, and volume scattering from various types of vegetation or shell distributions of varying density. In this section, backscattering coefficient models will be described for the individual components of scattering: rough sand or gravel with homogeneous roughness and impedance properties and dense, homogeneous shell distributions or *Posidonia oceanica* seagrass patches. We are interested in effects of the relative scattering from the different patches over the whole angular range for backscatter for frequencies from 10–100 kHz.

The model used in this study for scattering from a rough sand interface is a combination of a perturbation approximation surface scattering model for low grazing angle regimes and a Kirchhoff approximation for steep angles (i.e., near $\theta = 90^{\circ}$). As the models and the assumptions used in their derivation are discussed in Lyons, et al. [5], we will give only a brief description of the required model inputs here. The surface scattering model requires the statistical properties of the seafloor roughness, which is assumed to exhibit power-law spectra with isotropic statistics:

$$W(\mathbf{K}) = \Gamma K^{-\xi} \tag{9}$$

where **K** is a 2-D wavenumber vector with magnitude equal to the wavenumber K, Γ is the spectral strength, and ξ is the spectral exponent. The acoustic properties of density ratio, compressional velocity ration are also required for the interface scattering model as is the compressional loss parameter, which is related to the attenuation coefficient. This model will also be used for scattering from a gravel interface.

The model used to estimate scattering from a shell-covered seafloor is essentially that described in Stanton [6]. The scattering coefficient as a function of grazing angle for this model is given by

$$s_A(\theta) = F\left(\frac{\Re_{12}^2}{4\pi}\right)\sin^2\theta \tag{10}$$

where $\Re_{12}^2$ is the reflection coefficient and $\Re_{12}^2 = (\rho c - 1)/\,\rho c + 1)$, where ρ and c are the mass density and sound speed of the shell material, respectively, normalized by the corresponding quantities for the surrounding water. F is the packing factor and is equal to the fraction of the seafloor covered by shells. The angular dependence of seafloor scattering for shell-covered areas is included via Lambert's law in the model. High-frequency scattering data from a shell-covered seafloor presented in Lyons and Abraham [4] support the typical $\sin^2\theta$ dependence predicted by the model. The scattering coefficient for the shell-covered seafloor scattering model is frequency independent as long as the packing factor remains constant.

Due to a lack of understanding of the exact mechanisms causing scatter, backscatter from *Posidonia oceanica* seagrass will be estimated using a simple empirical model instead of a physical model, which is given by the expression:

$$s_B(\theta) = \psi \sin\theta \tag{11}$$

where ψ is the strength of the return at normal incidence. Implicit in this model is the assumption of uniform scatter in all directions. While this model is unrealistic for surfaces, it is often used for volume scattering from fish or bubbles (a probable mechanism for scattering from seagrasses). We also assume that the scattered level is independent of frequency. Evidence for the frequency independence of backscattering from *Posidonia oceanica* over the range of 20–100 kHz as well as the $\sin\theta$ dependence can be found in Lyons and Pouliquen [7].

4 Results and discussion

Scattering strength calculations based on the individual scattering models presented above are presented in Fig. 2. Parameters from Stanic *et al.* [8] are used as inputs to model sand interface scattering and from Stanic, et al. [9] for gravel interface scattering with the values of spectral strength and spectral exponent changed to 0.015 and 3.0 respectively (a statistically rougher seafloor than in reference [9]). The parameter ψ was set to 0.01 in the seagrass scattering model to match data presented in Lyons and Pouliquen [7] while the parameter combination $F\Re_{12}^2/4\pi$ was set to 0.03 in the shell-covered seafloor model to match data presented in Lyons and Abraham [4].

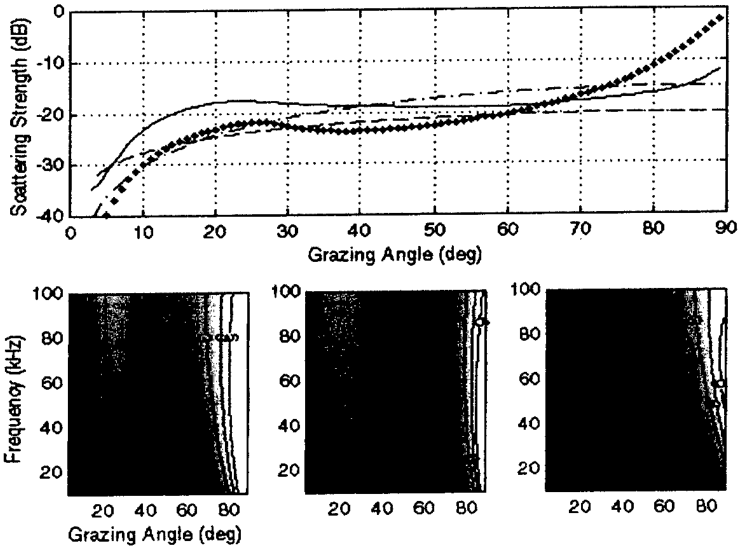

Figure 2. Top: Predictions of 80 kHz scattering strength for sand (diamonds), shell-covered (dash-dot line), gravel (solid line), and seagrass-covered (dashed line) seafloors. Bottom: Differences in scattering strength versus grazing angle and frequency between sand and: seagrass-covered (left), shell-covered (middle), and gravel (right) seafloors. Larger values are lighter on these plots and contour lines of 3, 6 and 9 dB are also shown.

For the examples used in the present study, the resolution cell consists of a combination of only two of the four possible surface types. In the following examples a sand bottom was chosen to be the scattering patch type. The bottom panels of Fig. 2 show the difference between predictions for sand scattering and each of the three other seafloor types. It is apparent that the seafloor appears acoustically patchy, i.e., has scattering from the patches that is significantly above the background, near normal incidence. Experimentally determined scintillation index values from 80 kHz scattering data for several non-homogeneous seafloors were presented in Lyons and Abraham [4] as a function of area. Figure 3 shows these values replotted as a function of grazing angle. The data show non-Rayleigh behavior near normal incidence (values greater than one are indicative of a non-Rayleigh envelope distribution). Scintillation index estimated using the predicted scattering strengths, the number of patches (a function of the ensonified area) at normal incidence equal to 2, and a patch to background area ratio of 1:4 are shown in Fig. 4. The angular dependence of scintillation index predicted using realistic parameter values is seen to agree well with experimental values.

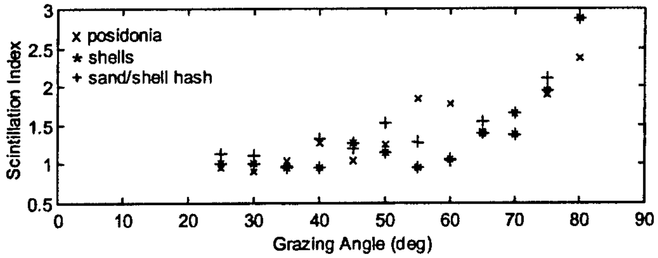

Figure 3. Experimental values of scintillation index versus grazing angle from [4].

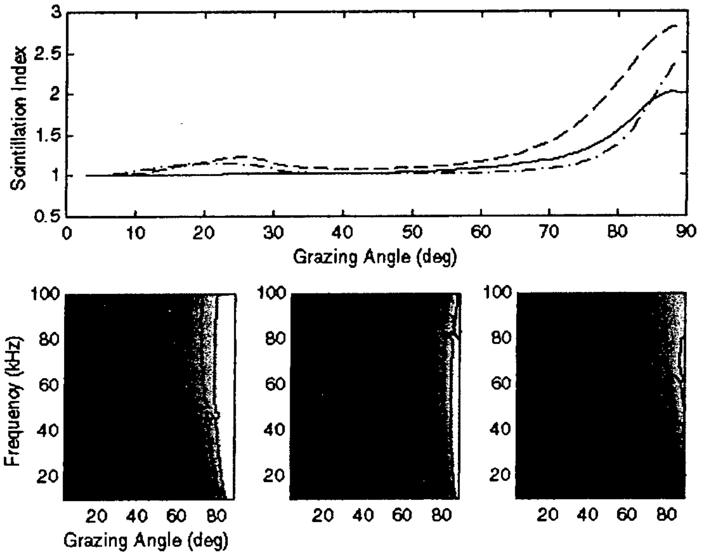

Figure 4. Top: Predictions of 80 kHz scintillation index versus grazing angle for sand patches on: shell-covered (dash-dot line), gravel (solid line), and seagrass-covered (dashed line) seafloors. Bottom: Scintillation index versus grazing angle and frequency for sand patches on: seagrass-covered (left), shell-covered (middle), and gravel (right) seafloors. Larger values are lighter on these plots and contour lines of 1.1, 1.5 and 2 are also shown.

5 Conclusions

In this paper a predictive model for the statistical distribution of clutter resulting from scattering from two different contributing seafloor types within the same resolution cell has been developed. The seafloors were modeled as being comprised of a finite number of homogeneous exponentially sized scattering patches (in contrast to the more traditional asymptotic derivation of the K-distribution) on a background (the area around the scattering patches) that was assumed to produce a Gaussian scattered return. Comparisons of scintillation index predictions made using the developed model and realistic input parameters for several example seafloor descriptions were compared with scintillation index estimated from high-frequency acoustic scattering data. The predicted scintillation index compared quite favorably with the level and angular dependence of experimental data. The strong peak seen in both the experimental and predicted scintillation index near normal incidence resulted solely from the angular dependence of the relative scattering strengths of the two contributing seafloor types within a resolution cell. The importance of the present work lies in the ability to link the clutter envelope distribution to measurable geo-acoustic properties in conjunction with sonar system parameters, providing the foundation necessary for solving several important problems related to the detection of targets in non-Rayleigh clutter. The direct link between system and environmental parameters and the statistical distribution of reverberation will allow: performance prediction for different systems based on seafloor properties, extrapolation of performance to other system/bandwidths, and optimization of system parameters such as bandwidth to local environment.

Acknowledgements

The Office of Naval Research sponsored this work (grant numbers N00014-01-1-0352 and N00014-02-1-0115).

References

1. Abraham, D.A. and Lyons, A.P., Novel physical interpretations of K-distributed reverberation, *IEEE J. Oceanic Eng.* (submitted 2001).
2. Jakeman, E. and Pusey, P.N., A model for non-Rayleigh sea echo, *IEEE Trans. Ant. and Prop.* **24**, 806–814 (1976).
3. Abraham, D.A., Signal Excess in K-distributed reverberation, *IEEE J. Oceanic Eng.* (submitted 2001).
4. Lyons, A.P. and Abraham, D.A., Statistical characterization of high-frequency shallow-water seafloor backscatter, *J. Acoust. Soc. Am.* **106**, 1307–1315 (1999).
5. Lyons, A.P., Anderson, A.L. and Dwan, F.S., Acoustic scattering from the seafloor: Modeling and data comparison, *J. Acoust. Soc. Am.* **95**, 2441–2451 (1994).
6. Stanton, T.K., On acoustic scattering by a shell-covered seafloor, *J. Acoust. Soc. Am.* **108**, 551–555 (2000).
7. Lyons, A.P. and Pouliquen E., Measurements of high-frequency acoustic scattering from seabed vegetation. In *Proc. 16th Int. Congress of Acoustics and the 135th Meeting of the Acoustical Society of America* (AIP, Woodbury, NY, 1998) pp. 1627–1628.
8. Stanic, S., Briggs, K.B., Fleischer, P., Ray, R.I. and Sawyer, W.B., Shallow-water high-frequency bottom scattering off Panama City, Florida, *J. Acoust. Soc. Am.* **83**, 2134–2144 (1988).
9. Stanic, S., Briggs, K.B., Fleischer, P., Sawyer, W.B. and Ray, R.I., High-frequency acoustic backscattering from a coarse shell ocean bottom, *J. Acoust. Soc. Am.* **85**, 125–136 (1988).

REVERBERATION ENVELOPE STATISTICS AND THEIR DEPENDENCE ON SONAR BEAMWIDTH AND BANDWIDTH

D. A. ABRAHAM AND A. P. LYONS
The Pennsylvania State University, Applied Research Laboratory
P.O. Box 30, State College, PA 16870, USA
E-mail: d.a.abraham@ieee.org, apl2@psu.edu

In order to combat high reverberation power levels in shallow water operational areas, active sonar systems have employed increased bandwidth transmissions and larger arrays. Both of these techniques have the effect of limiting the contribution of reverberation in each range-bearing resolution cell of the sonar by decreasing the cell size, which can also have an adverse effect on the probability density function (PDF) of the reverberation induced matched filter envelope. This effect is examined using real data in conjunction with a recently developed model [1, 2] predicting that the shape parameter of K-distributed reverberation is proportional to the range-bearing resolution cell size. Estimation of the shape parameter of the K-distribution from real data as a function of the beamwidth of the towed-array receiver confirms this relationship. Although a similar effect may be expected for changes in the bandwidth of the transmit waveform, real data analysis indicates that, as bandwidth increases, the shape parameter estimate first decreases as expected but then increases, implying the data become more Rayleigh-like at higher bandwidths. An explanation for this counterintuitive effect is proffered wherein it is hypothesized that increasing bandwidth over-resolves scatterers in range but not in angle. After accounting for the size of the scatterers with respect to the size of the range resolution cell in the model of [1, 2], the shape parameter of an equivalent K-distribution for circular scatterers is seen to closely resemble the observed data.

1 Introduction

Heavy-tailed, non-Rayleigh reverberation has been observed in active sonar systems with varying array sizes and transmit waveform bandwidths. A descriptive analysis of the effects of changing bandwidth and center frequency (and thus array beamwidth) was presented in [3]. In this paper, real data from SACLANT Undersea Research Centre's SCARAB 1997 sea-trial (C. Holland, Scientist in Charge) are analyzed in conjunction with the model developed in [1, 2]. This model assumes that reverberation in a given range-bearing resolution cell arises from a finite number of scatterers that have an exponentially distributed size. The resulting reverberation envelope is then K-distributed with the shape parameter equal to half the number of scatterers in the range-bearing resolution cell and the scale parameter proportional to the average power of a single scatterer. Assuming that the scatterers are uniformly distributed on or in the seafloor, this implies that the shape parameter of K-distributed reverberation is proportional to the size of the range-bearing resolution cell. The size of the range-bearing resolution cell is approximately the range times the beamwidth divided by the bandwidth, the latter two of which are considered in this paper.

In Section 3, it is seen that estimates of the K-distribution shape parameter change linearly with beamwidth. However, as seen in Section 4, the shape parameter estimates first decrease as bandwidth increases, but then begin to increase, indicating a trend toward more Rayleigh reverberation. It is hypothesized that this results from over-resolving scatterers. Appropriate modification of the model of [1, 2] reveals a trend in the K-distribution shape parameter similar to that observed in the real data as bandwidth increases.

2 Sea-trial description

The data to be analyzed were taken during the SCARAB '97 sea-trial sponsored by the SACLANT Undersea Research Centre in La Spezia, Italy. The trial occurred off the coast of Italy in June, 1997 in the Capraia Basin which is north of the Island of Elba. The data analyzed in this paper were taken June 2–3 using the Centre's low-frequency towed hydrophone-array and the Towed Vertically Directive Source (TVDS), which was configured to send a linear frequency modulated (LFM) pulse with a two second duration spanning 450–700 Hz. The subsequent reverberation was recorded from the towed-array for 40 seconds following each of 49 transmissions throughout the basin. Owing to the shallow water environment and downward refracting sound speed profiles that were measured during the sonar data acquisition, the reverberation data are dominated by bottom scattering.

The towed-array receiver was comprised of 128 hydrophones with a 0.5 meter spacing, resulting in a design frequency of 1500 Hz. The array data were beamformed with a hanning window such that the beampatterns of adjacent beams overlapped at their 3 dB down points at 900 Hz, resulting in 54 beams equally spaced in wavenumber, spanning from forward to aft along the array. The signal processing applied to the beamformed data prior to analysis of the reverberation statistics included basebanding, match filtering and normalization.

2.1 Fit of the Rayleigh and K-distributions

Before evaluating the shape parameter of the K-distribution and how it changes with array beamwidth and transmit waveform bandwidth, it is necessary to determine how well fit the data are by the K-distribution. The Kolmogorov-Smirnov (KS) test [4] is applied to the normalized matched filter data to test the ability of the Rayleigh and K-distribution models to represent the observed data. The KS test evaluates the maximum difference between the sample cumulative distribution function (CDF) generated by the data and a test CDF which is, in this case, either the Rayleigh or K-distribution with their parameters estimated from the data being tested. The Rayleigh distribution only depends on its power, which is estimated by the sample intensity (i.e., the average of the matched filter intensity over the window being tested). As the data have already been normalized to have unit power, this should be near one. Estimation of the K-distribution parameters is more involved; the method of moments estimator (MME), as described in [5], has been employed.

For the data under consideration, windows 1000 samples long (4 seconds of data at a 250 Hz sampling rate) with fifty percent overlap are used to estimate the model parameters and then form the KS test statistic. Using the asymptotic p-value of the KS test statistic [4], the data are either accepted as being well fit by the Rayleigh or K-distribution or rejected. At the $p = 0.05$ level, 68% of the data are well fit by the Rayleigh distribution and 97.4%

are well fit by the K-distribution. Thus, the K-distribution is accepted as a good model for these data and it is noted that a significant portion of the data are Rayleigh-like. Note that only data between 2 and 40 seconds following the end of signal transmission on each ping are utilized in this and subsequent data analysis. Over these times the data are reverberation limited except on the few beams where nearby shipping dominated the reverberation or where geological features precluded acoustic propagation (e.g., the Island of Capraia causing shadow zones).

3 Beamwidth effect

Based on the model developed in [1, 2], it may be hypothesized that the effective number of scatterers parameter (α) of the K-distribution is proportional to the area of the range-bearing resolution cell. As such, if the beamwidth of the sonar is doubled, then α should also double, regardless of the density of scatterers as long as they are uniformly placed within the range-bearing resolution cell.

The beamwidth of a sonar approximately doubles when the array size is halved. The same effect may be accomplished by coherently summing adjacent beams. The towed-array data have been spatially filtered into 54 beams that overlap at the 3 dB down points of their beampatterns at 900 Hz. The transmit waveform being analyzed ranged from 450 to 700 Hz, at which frequencies the beampatterns of adjacent beams overlap, respectively, at the 0.75 and 1.8 dB down points. A beampattern having width equal to the combined width of the individual beams may be formed without significant destruction of the mainlobe by coherently summing every other beam at this spacing. This does result in a ripple in the mainlobe with less than a one decibel height at 450 Hz and less than a two decibel height at 700 Hz.

The shape parameter of the K-distribution is estimated from either the original beam data or the summed beam data after matched filtering and normalization. For each beam, the data are separated into windows that are 500 samples long (at a sampling rate of 250 Hz this is 2 seconds of data) with an 80% overlap. For the i^{th} window on the j^{th} beam of the p^{th} ping, call this estimate $\hat{\alpha}_k(p,i,j)$ where the index k indicates the span of how many original beams the beam-sum is formed over (beam-spans of $k = 1$, 3, 5, 7, and 9 are analyzed). The estimates of the shape parameter from a single ping of data are displayed in Fig. 1 in the form of histograms for each of the beam-spans. As expected, the data exhibit a trend toward higher values as the beamwidth increases. On the figure this is evident from the median, mean (which was trimmed by removing the largest and smallest 0.5 percent of the values), and the quantity of estimates that exceed 50. It is also clear that there is a wide range of values observed on this single ping, indicating that the density of scatterers (i.e., frequency of occurrence) varies within the geographic region represented by this ping. To remove this variability, the ratio of the estimated shape parameters on the summed beams to that estimated on the individual beams is formed for each individual data window,

$$\Delta_k\left(p,i,j,j'\right) = \frac{\hat{\alpha}_k(p,i,j)}{\hat{\alpha}_1\left(p,i,j'\right)} \tag{1}$$

where $j' = j, \ldots, j+k-1$ represent the original beams that span the beamwidth of summed beam j. An average value is formed for each ping and beam-sum,

$$\bar{\Delta}_k(p) = \frac{1}{m} \sum_{i,j,j'} \Delta_k(p,i,j,j') \tag{2}$$

where the summation is over the m cases of the indices (i,j,j') such that the method of moments estimators provide shape parameter estimates for both the individual and summed beams and the estimates satisfy $\hat{\alpha}_k(p,i,j) < 10^4$ and $\hat{\alpha}_1(p,i,j') < 10^4$. Extremely large estimates of α are discarded because of their high variability.

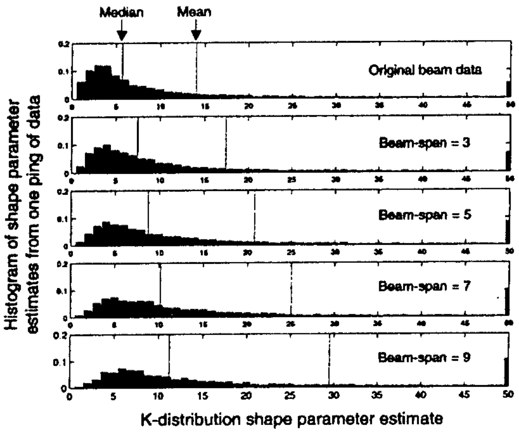

Figure 1. Histograms of the estimates of the K-distribution shape parameter from a single ping for various beamwidths. The expected trend toward higher values of α as beamwidth increases is evident in the mean, median and number of estimates exceeding 50.

The change in the shape parameter predicted by the model of [1, 2] is exactly the change in beamwidth. This is formed in a similar manner to how the change in the shape parameter is estimated from the data, by taking the average of the change in beamwidth between the summed beams and each of the individual beams for all of the summed beams. Despite the fact that beamwidth varies with arrival angle, the ratios of the beamwidths of the summed to individual beams do not vary significantly. These average ratios are computed for the edges of the frequency band of the transmit waveform (450 and 700 Hz) and also for the peak power frequency of the source (600 Hz) and shown with the average change in the estimated shape parameter of the K-distribution in Fig. 2. In the figure, it is seen that the estimated changes $\bar{\Delta}_k(p)$ fall very close to the predictions and that the average value over all pings has a slope similar to that predicted for the 450 Hz case, but is biased high. This may be explained by first noting that the expected change (1) is formed from the ratio of two random variables, say $\Delta = \frac{X}{Y}$. Assuming that both X and Y are positive random variables, it can be shown (through the use of Jensen's inequality) that $E[\Delta] > \frac{E[X]}{E[Y]}$. This result also requires that the two random variables in the ratio be independent, which is not the case with the real data analyzed. However, for the minimal dependence that is expected, the result should be approximate and does proffer an explanation for the bias seen in the data.

The data shown in Fig. 2 are also seen to increase in variability as the beam-span increases. This may be the result of variability induced by non-stationarity in the frequency of occurrence of scatterers on the bottom over wider angles or may arise from the increased variability of shape parameter estimates when α is large. The latter of which is expected to occur more often for larger beamwidths (i.e., larger range-bearing resolution cell sizes) and when the data are nearly Rayleigh distributed (which is known to occur frequently in this data set).

The close similarity between the estimated and predicted change in the K-distribution shape parameter indicates that, within our ability to estimate it, the shape parameter is proportional to the beamwidth of the towed-array receiver. This also implies that a K-distribution model assuming a finite number of scatterers with the shape parameter tied to the number of scatterers in a sonar range-bearing resolution cell can provide more realistic simulations or predictions of sonar system performance as a function of system parameters such as beamwidth and possibly bandwidth, which will be examined in the next section.

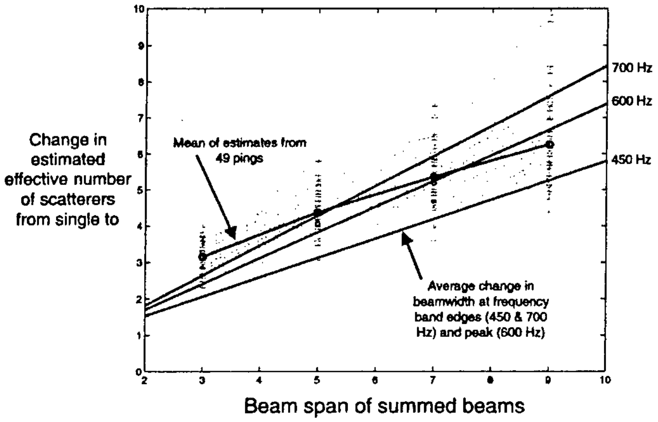

Figure 2. Change in the shape parameter of the K-distribution between summed and individual beams as a function of the span of the beams summed (i.e., beamwidth). The + marks are the average values from each ping. The change as estimated from the data is very similar to that predicted by the change in beamwidth with the exception of an explainable upward bias.

4 Bandwidth effect

The model developed in [1, 2] assumed that the scatterers were fully within the sonar resolution cell. Owing to the asymmetry between the down-range and cross-range extents of the sonar range-bearing resolution cell, this may not always be the case for higher bandwidth transmit waveforms where the scatterers may be over-resolved in range and not in bearing. For example, a sonar system with an array receiver with a 2 degree beamwidth (similar to the array used in the SCARAB sea-trial at broadside) and a 250 Hz bandwidth transmit waveform will have a 3 m down-range extent and a 350 m cross range at 10 km. In this section, the model of [1, 2] is extended to consider the case of over-resolved scatterers. Counterintuitively, the model, and subsequent data analysis, illustrate that when the bandwidth increases to the point of over-resolving scatterers, the reverberation becomes more Rayleigh-like rather than more non-Rayleigh.

The finite-number-of-scatterers model of [1, 2] assumed that the complex envelope of the matched filter output was the sum of n scatterers with random phases,

$$Z = \sum_{i=1}^{n} A_i e^{j\theta_i}, \tag{3}$$

where A_i is the contribution from the i^{th} scatterer and θ_i is its phase. If the scatterer amplitudes are not exponentially distributed, the matched filter envelope is not necessarily K-distributed. However, the shape parameter of the K-distribution, as obtained by moment matching, may still be used to represent how similar the PDF is to the Rayleigh distribution (large values yield Rayleigh-like data and small values yield data heavier tailed than Rayleigh). Without significant effort, it can be shown that the shape and scale parameters of the K-distribution, in terms of the moments of the individual scatterer contribution, are

$$\tilde{\alpha} = \frac{n}{2}\left(\frac{4E\left[A_i^2\right]^2}{E\left[A_i^4\right] - 2E\left[A_i^2\right]^2}\right) \quad \text{and} \quad \tilde{\lambda} = E\left[A_i^2\right]\left(\frac{E\left[A_i^4\right]}{2E\left[A_i^2\right]^2} - 1\right).$$

Evaluation of the moments of A_i for various scatterer shapes and orientations may be computed either analytically or numerically and used to examine how $\tilde{\alpha}$ changes as a function of the down-range extent of the sonar resolution cell (Δ) and the average size of the scatterer (μ). For various scatterer shapes having exponentially distributed area, it was found that $\tilde{\alpha}/\frac{n}{2}$ was unity for large values of $\gamma = \frac{\Delta}{\sqrt{\mu}}$ and increased as γ decreased. This implies that as Δ is decreased (i.e., bandwidth is increased), the effective number of scatterers can increase and the reverberation can become more Rayleigh-like, an unexpected result.

The number of scatterers within a sonar resolution cell (n) depends on the size of the resolution cell and the density and size of the scatterers. Assuming randomly placed scatterers, it can be shown that the average number of scatterers is proportional to γ when γ is large and tapers down to a constant greater than zero when γ is small. Combining this effect with the aforementioned one wherein $\tilde{\alpha}$ increases as γ decreases, we expect that as bandwidth is increased, one might observe $\tilde{\alpha}$ to first decrease when the scatterers are all within the resolution cell and then increase as the scatterers become over-resolved. This trend is observed in the histograms of the K-distribution shape parameter from one ping of data as shown in Fig. 3 where the shape parameter decreases when bandwidth is raised from 0.5 Hz to about 8 Hz, at which point it begins to increase again and the data become more Rayleigh-like.

For each analysis window, the K-distribution shape parameter estimates (if they exist) are normalized by the minimum estimated value over all bandwidths processed and then averaged over all beams for ranges less than 10 km. These are displayed for each of the 49 pings of data in Fig. 4 along with the average value over all pings and that predicted by the over-resolved scatterer model for a circular scatterer. This latter is normalized so that its lowest value is one, which is what was done to the real data, and scaled on its abscissa so that the minimum aligns with the minimum of a least squared error fitting of a quadratic function to the average of the estimated changes in the shape parameter. From this figure it is clear that the data are initially in a stage where increasing bandwidth results in a proportionate decrease in the K-distribution shape parameter. However, the shape parameter estimates begin to increase when the bandwidths reach about 8 Hz. The effective number of scatterers ($\tilde{\alpha}$) predicted from a model assuming that circular scatterers are over-resolved well approximates the observed data, despite the obvious oversimplifications of its development. It should be noted that the results presented here are circumstantial and not evidentiary proof that the phenomenon observed in the data arises from over-resolution of scatterers. It is possible that this bandwidth effect is caused by other conditions such as propagation through a shallow water environment, although preliminary investigation does not lend much support to this alternative hypothesis.

Increased bandwidth is expected to result in heavier-tailed reverberation than Rayleigh, not more Rayleigh-like reverberation. Thus, the phenomenon of a return to Rayleigh-like reverberation at high bandwidth that is observed in both the data analysis and model is in some sense counterintuitive. Mathematically, this may arise from an increased rate of convergence of the central limit theorem that results from a reduction in the variability of the individual components. This result might initially lead one to suspect that the Rayleigh-like reverberation at higher bandwidth will result in improved detection performance. However, if over-resolution of the scatterers is the underlying mechanism producing the phenomenon, then it may be expected to induce dependence of the data samples (not necessarily correlation) which will reduce the effectiveness of a detector that incoherently combines (e.g., integrates) the matched filter intensity over multiple ranges to account for spreading of the target echo. Thus, a net gain in detection performance is not guaranteed.

5 Conclusion

In this paper, the statistics of the reverberation induced matched filter envelope were evaluated as a function of the sonar's receive array beamwidth and transmit waveform bandwidth. The statistics were quantified by the shape parameter of the K-distribution, which, when the scatterers are small compared with the sonar's resolution, is proportional to array beamwidth and inversely proportional to the transmit waveform bandwidth. Real data analysis supported both of these results except that at higher bandwidths, the shape parameter was seen to increase indicating a return toward Rayleigh-like reverberation. Accounting for the size of the scatterers in the model produced a similar trend which was seen to well represent the observed data. These results may be used to improve the accuracy of performance prediction and simulation of sonar systems in cluttered environments and possibly to help set optimal sonar bandwidths.

Acknowledgements

This work was sponsored by the Office of Naval Research under grant numbers N00014-02-1-0115 and N00014-01-1-0352.

References

1. Abraham, D.A. and Lyons, A.P., Exponential scattering and K-distributed reverberation. In *Proc. of MTS/IEEE Oceans 2001 Conference*, 1622–1628, (2001).
2. Abraham, D.A. and Lyons, A.P., Novel physical interpretations of K-distributed reverberation. *IEEE Journal of Oceanic Engineering*, in review (2002).

3. Abraham, D.A. and Holland, C.W., Statistical analysis of low-frequency active sonar reverberation in shallow water. *Proc. of 4th European Conf. on Underwater Acoustics*, (1998).
4. Fisz, M., *Probability Theory and Mathematical Statistics*, 3th ed. (John Wiley & Sons, 1963).
5. Abraham, D.A., Modeling non-Rayleigh reverberation. SR-266, SACLANT Undersea Research Centre, La Spezia, Italy (1997).

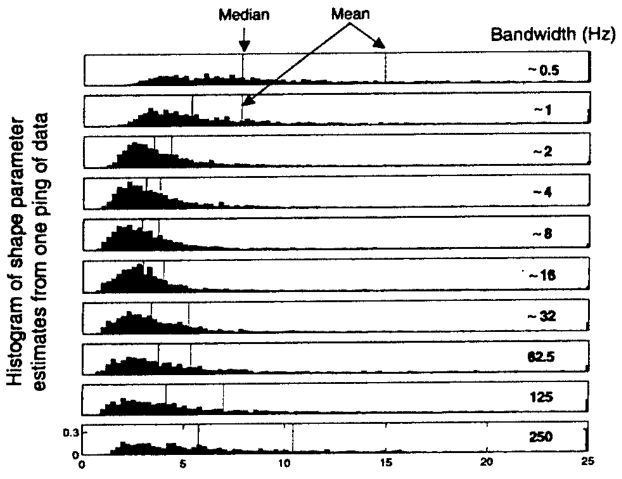

Figure 3. Histograms of the estimates of the K-distribution shape parameter from a single ping for various bandwidths. The expected trend toward lower values of α as bandwidth increases is evident at the lower bandwidths, but does not continue at the higher bandwidths.

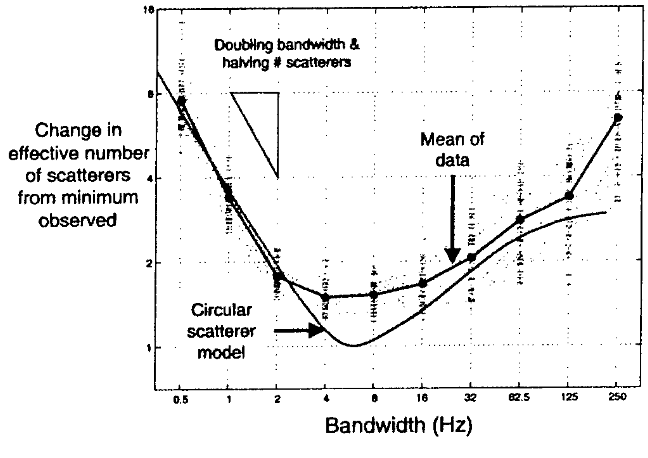

Figure 4. Change in the shape parameter of the K-distribution from the minimum observed over various bandwidths. The + marks are the average values from each ping, the 'o' marks are the averages over all pings for the given bandwidth.

BROADBAND DETECTION IN K-DISTRIBUTED REVERBERATION

Douglas A. Abraham

The Pennsylvania State University
Applied Research Laboratory, P.O. Box 30
State College, PA 16804
email: d.a.abraham@ieee.org
phone: (814) 863-9828

ABSTRACT

In active sonar, broadband waveforms can improve the signal-to-reverberation power ratio (SRR) by decreasing the size of the resolution cell. Unfortunately, this can adversely affect detection performance by spreading the target across several cells and adversely affect false alarm performance by making the reverberation more severely non-Rayleigh. In this paper, the performance of a detector that integrates the matched filter intensity is examined as a function of bandwidth. It is observed that performance depends only on the total target energy (E_t), not how it is distributed throughout the processing window. Thus, for this detector, the shape of the target echo is less important than E_t. Given a constant E_t, it was observed that probability of detection (P_d) increased with bandwidth, but was bounded above by a number less than one. The performance is coarsely quantified by the deflection, which was seen to increase with either bandwidth or E_t and decrease with the size of the target, the density of reverberation scatterers (e.g., number per meter down-range) and their average power. The deflection is most sensitive to bandwidth when the density of scatterers is high (i.e., the reverberation is nearly Rayleigh). Thus, increasing bandwidth provides the most added value when the reverberation is nearly Rayleigh distributed.

As an example, P_d for a fixed probability of false alarm (P_{fa}) is examined for a cylindrical target shape and compared to that of a detector that takes the maximum value over the processing window. The detection performance comparison showed that the maximum value detector outperforms the summation detector when the target echo is essentially a single highlight, but can perform significantly worse when the target echo energy is spread.

1. INTRODUCTION

Active sonar systems that operate in shallow water suffer from increased reverberation power levels compared with deep water operational environments. To counter this decrease in detection capability, higher bandwidth transmit waveforms have been employed in order to increase the signal to reverberation power ratio (SRR) by reducing the reverberation power. Unfortunately, this can have the adverse effect of increasing the tails of the probability density function (PDF) of the reverberation induced matched filter envelope. The result is a trade-off between increasing the SRR at the expense of an increase in the P_{fa}. As shown in [1], there is still a net gain in performance if the target echo remains isolated in a single range bearing resolution cell and the reverberation arises from a finite number of exponentially sized scatterers, which leads to a K-distributed matched filter envelope. This paper examines the case of when a target is over-resolved by the transmit waveform (after pulse compression) and the resulting target echo is spread across multiple range cells.

2. BROADBAND DETECTION

The bandwidth of the transmit waveform affects both the target response and the statistical description of the reverberation. As shown in [2], when reverberation is assumed to arise from a finite number of scatterers having exponential amplitude, the matched filter envelope is K-distributed with the shape parameter inversely proportional to the transmit waveform bandwidth. Depending on the bandwidth of the transmit waveform, the target echo may reside solely in one range cell, or be spread across several independent range cells (with extent equal to one over the bandwidth). This spreading, which occurs even in environments with no multipath, may be countered by using an incoherent summation of the matched filter intensity as a detection statistic. Alternatively, the maximum value of the matched filter envelope over the extent of target spreading may be used as a detec-

---

This work was sponsored by the Office of Naval Research under grant number N00014-02-1-0115.

tion statistic, which is essentially a generalized likelihood ratio test (GLRT) assuming all the target energy is in one range bin and it is unknown which one.

Neither of these detectors is optimal in the Neyman Pearson sense; however, both are practical in that they may be implemented without knowledge of the signal structure and exploit some information about the target (spreading and point-like target highlights). Choosing a threshold based on a false alarm performance specification requires knowledge of the PDF of the reverberation. In practice this may be accomplished using a statistical normalizer [3]. In this paper, it is assumed that the threshold may be set exactly.

Let $X_1, \ldots ,X_m$ be the matched filter intensity output that span the target echo and are spaced every one-over-the-bandwidth so they may be assumed to be independent. Assuming an additive target model, the matched filter intensity is

$$X_i = \left| A_i e^{j\theta_i} + \sqrt{V_i} Z_i \right|^2 \tag{1}$$

for $i = 1, \ldots ,m$ where $m = T_t W$ where T_t is the time extent of the target and W is the transmit waveform bandwidth and the sampling rate of the complex matched filter output. The target echo is described by its amplitude and phase for the i^{th} range bin, A_i and θ_i. In this paper, only a non-fluctuating target model is considered where A_i and θ_i are constants. The reverberation is described according to the product formulation of the K-distribution where V_i is a unit-scale gamma random variable with shape α and Z_i is a zero-mean complex Gaussian random variable with power λ. In [4, 2] it is shown that α is proportional to the number of scatterers within a resolution cell and therefore proportional to beamwidth and scatterer density and inversely proportional to bandwidth. The scale parameter λ is twice the average power in a single scatterer.

2.1. Incoherent summation

The spreading of the target into multiple range bins may be countered by summing the intensities to form the test statistic (referred to as INC)

$$T_a = \sum_{i=1}^{m} X_i. \tag{2}$$

The distribution function of T_a is difficult to obtain analytically, even under the reverberation-only hypothesis. Amindavar and Ritcey [5] obtained the cumulative distribution function (CDF) of an incoherent combination of K-distributed clutter for a multiple pulse radar application through the use of Padé approximations to the moment generating function. As this requires significant effort for different parameter values (α, λ, A_i), the shifted gamma approximation is considered owing to its ease of evaluation. This approximation involves approximating the test statistic by a scaled and shifted gamma random variable. The three parameters of the shifted-gamma distribution are obtained by matching moments with the test statistic (the moment equations from [4] are shown in the appendix). Defining

$$E_t = \sum_{i=1}^{m} A_i^2 \tag{3}$$

as the total target energy, the first three moments of T_a, $\mu_k = E\left[T_a^k\right]$ for $k = 1, 2, 3$, for a non-fluctuating target are

$$\mu_1 = E\left[T_a\right] = m\lambda\alpha + E_t, \tag{4}$$

$$\mu_2 \;=\; \mu_1^2 + m\lambda^2\alpha\left(\alpha+2\right) + 2\lambda\alpha E_t \tag{5}$$

and

$$\begin{aligned} \mu_3 \;=\;& 3\mu_1\mu_2 - 2\mu_1^3 + 2m\lambda^3\alpha\left(\alpha^2+6\alpha+6\right) \\ &+6\lambda^2\alpha\left(\alpha+2\right)E_t. \end{aligned} \tag{6}$$

It is significant that these moments only depend on the target echo structure through the total target energy E_t. This result is similar to the relationship found in non-central chi-squared random variables where the PDF of their sum depends on the sum of the individual non-centrality parameters. The result also implies that the total target energy drives the performance *of this detector* and not how the energy is spread across range bins. This is not the case for the detector considered in the following section. As a final caveat, the above result does not necessarily imply that the PDF of the test statistic (and therefore P_d) depends on the A_i only through E_t, which remains to be proven. However, as the first four moments (fourth not shown here) only depend on E_t, any possible dependence will only result in differences in the extreme tails of the distribution and therefore not largely affect P_d.

As bandwidth increases, the test statistic becomes the summation of *iid* random variables (without loss of generality, we can assume that A_i is a constant equal to $\sqrt{\frac{E_t}{m}}$) and therefore approaches a Gaussian random variable. As such, it is worthwhile to consider the deflection,

$$\begin{aligned} d \;=\;& \frac{\left(\mu_1^1-\mu_1^0\right)^2}{\mu_2^0-\left(\mu_1^0\right)^2} = \frac{E_t^2}{m\lambda^2\alpha\left(\alpha+2\right)} \\ =\;& \frac{E_t^2}{\beta T_t\lambda^2\left(1+\frac{\beta}{4W}\right)} \end{aligned} \tag{7}$$

where the superscripts on μ_k indicate the target present (μ_k^1) and reverberation only (μ_k^0) hypotheses and β is the density of scatterers encountered within a beam in units of number of scatterers per second (so $\alpha = \frac{n}{2} = \frac{\beta}{2W}$ where n is the number of scatterers in a range-bearing resolution cell [4]). Clearly increasing β, T_t, or λ decreases performance while increasing E_t or bandwidth W improves performance. However, from this analysis, increasing bandwidth provides less and less improvement. For example, consider the change in deflection achieved by doubling bandwidth

$$\Delta d = \frac{d(2W)}{d(W)} = 1 + \frac{1}{1+8\frac{W}{\beta}}. \tag{8}$$

When either β is large (i.e., the reverberation is near Rayleigh) or W is small, the deflection nearly doubles (i.e., the expected 3 dB increase achieved by doubling bandwidth). However, when bandwidth continues to increase, the improvement becomes minimal, dropping below one decibel when $\frac{W}{\beta} \approx 0.36$.

2.2. Maximum detector

Under the assumption that the target echo is best approximated by a single dominant point reflector, choosing the maximum of the matched filter intensity over the same processing window as the incoherent integration represents a GLRT over an unknown location. The test statistic has the form

$$T_b = \max_{i=1,\dots,m} X_i. \tag{9}$$

The CDF of T_b is easily seen to be

$$F_b(t) = \prod_{i=1}^{m} F_K(t;\alpha,\lambda,A_i) \tag{10}$$

where $F_K(h;\alpha,\lambda,A)$ is the CDF of the matched filter intensity when the reverberation is K-distributed and an additive, non-fluctuating target with power A^2 is present. As seen in [4, 1], the CDF of a shifted gamma variate with matching moments provides a good approximation to K-distributed reverberation with a target. The moments may be obtained from eqs. (4)–(6) by setting $m = 1$ with $E_t = A_i^2$. When no signal is present ($A_i = 0$), the actual CDF of the K-distribution may be used to yield

$$F_b(t) = \left[1 - \frac{2}{\Gamma(\alpha)}\left(\frac{t}{\lambda}\right)^{\frac{\alpha}{2}} K_\alpha\left(2\sqrt{\frac{t}{\lambda}}\right)\right]^m. \tag{11}$$

3. DETECTION EXAMPLES

P_{fa} and P_d are obtained from the CDF of the test statistic under the null and alternative hypotheses. As previously mentioned, the CDF of T_a is approximated by that of a shifted gamma random variable. Though not evaluated here, the approximation is quite good when either α or m are reasonably large and the CDF is not too close to one (e.g., $P_{fa} < 10^{-3}$). The worst fit is for small values of P_{fa} when $m = 2$ and α is small. When $m = 1$, the exact K-distribution CDF is used for P_{fa} (for both detectors) and the shifted gamma approximation is used for P_d. Note that a better approximation in the tails may be obtained by matching the first, second, and fourth moments of the shifted gamma, although this does not always result in a valid solution.

3.1. Simply spread targets

Suppose that the target echo energy is spread equally into l of m cells. Thus, $A_i = \sqrt{\frac{E_t}{l}}$ for $i = 1,\dots,l$ and equals zero for $i > l$. The exact ordering is irrelevant owing to the form of eq. (10). P_d for $P_{fa} = 10^{-3}$ for the INC detector and the MAX detector as a function of bandwidth are shown in Figs. 1–4 for a short duration target ($T_t = 10$ ms) and a long duration target ($T_t = 50$ ms) when the reverberation arises from many small scatterers ($\beta = 20$ per ms) and from a few large scatterers ($\beta = 1$ per ms). The short and long target durations correspond to physical sizes of 7.5 and 37.5 m respectively. The average power of a scatter is chosen according to $\mu = \frac{1}{2\sqrt{\beta}}$ so that the reverberation power is $\alpha\lambda = \frac{1}{W}$. In all cases, $E_T = 15$ dB so the SRR is the same for each figure and proportional to bandwidth.

Several points may be made from these P_d curves. Three basic results that are essentially common knowledge are that P_d improves with bandwidth and suffers for situations with either targets with greater spreading or reverberation that is more severely non-Rayleigh. In the shorter target, it is clearly seen that both detectors perform identically when the target is not over-resolved as there is only one range cell under consideration and therefore the detectors are identical in structure. For the near-Rayleigh reverberation cases, the MAX detector performs well even when the energy is displaced into a small number of highlights. However, when the reverberation is moderately non-Rayleigh, the performance of the MAX detector degrades significantly when the target energy is spread. The INC detector does not suffer this drawback and provides nearly the same performance as the MAX detector with a single highlight (even if the target energy is fully spread) for short target durations and adequate performance for longer target durations. From these results, it may be concluded that the INC detector is best to use when the target duration is short or the reverberation is non-Rayleigh. The MAX detector is best only when there are a small number of highlights that are well separated (i.e., a long target echo duration) and the INC detector must integrate many terms that do not contribute to the total target echo energy (i.e., high bandwidth). This result has been observed in Rayleigh reverberation [6] where a GLRT that summed several of the largest peaks showed improved performance over incoherent integration. These results may imply that the GLRT structure does not provide the gain expected over incoherent integration when the reverberation is non-Rayleigh. However, the detector structure alluded to in [6] that first integrated to account for target spreading may provide a good compromise between recouping target spreading losses and accounting for significantly separated target echo energy (e.g., as occur with multipath propagation).

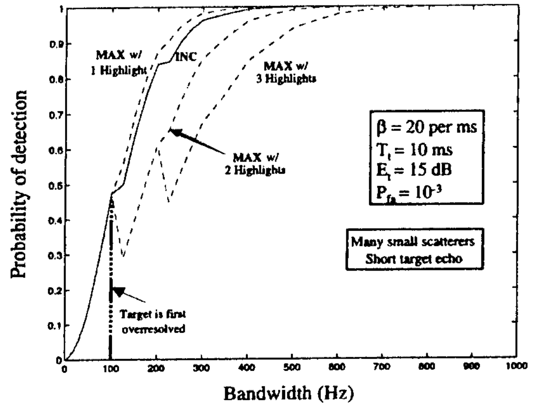

Fig. 1. P_d vs. bandwidth for a short target echo in nearly Rayleigh reverberation

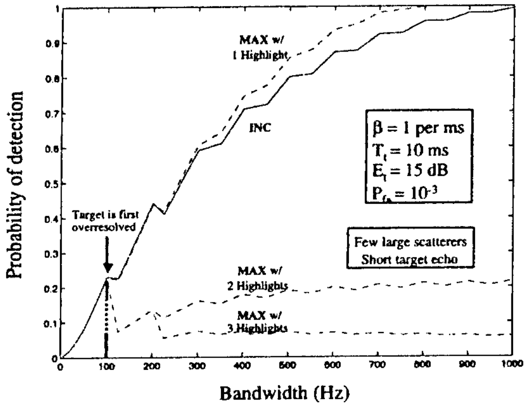

Fig. 2. P_d vs. bandwidth for a short target echo in non-Rayleigh reverberation

3.2. Cylindrical target

Consider a cylindrically shaped target with length 37.5 m and diameter 7.5 m (similar to the size of the simply spread targets in the previous section). Suppose that an active sonar system transmits a 0.5 s long LFM waveform with center frequency 2000 Hz. At broadside, the target echo is essentially a point reflector while at an aspect angle of 45 degrees, it resembles a two point reflector. P_d for these two cases is shown in Figs. 5 and 6 for the near-Rayleigh ($\beta = 20$ scatterers per ms) and non-Rayleigh ($\beta = 1$ scatterer per ms) cases with $P_{fa} = 10^{-3}$ and an average (over all bandwidths evaluated) target echo energy of 15 dB. As in the previous section, the average scatterer power is chosen so that $\alpha\lambda = \frac{1}{W}$ and the target echo time extent is assumed to be 50 ms.

The detection results seen in these figures follow the results of the previous section. The single-highlight character of the target echo at broadside results in the MAX detector outperforming the INC detector in both Rayleigh-like and non-Rayleigh reverberation. However, when the echo energy is spread, as occurs when the aspect moves off broadside to the target, the INC detector performs equivalently to the MAX detector in Rayleigh-like reverberation and out-

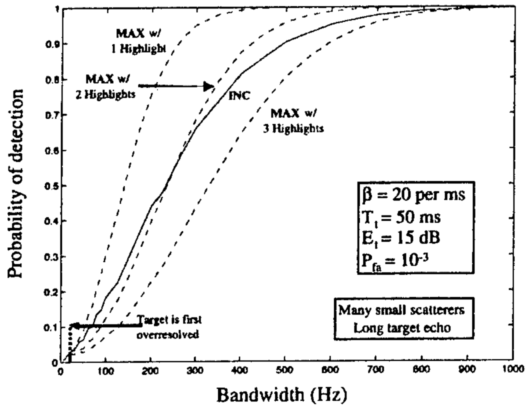

Fig. 3. P_d vs. bandwidth for a long target echo in nearly Rayleigh reverberation

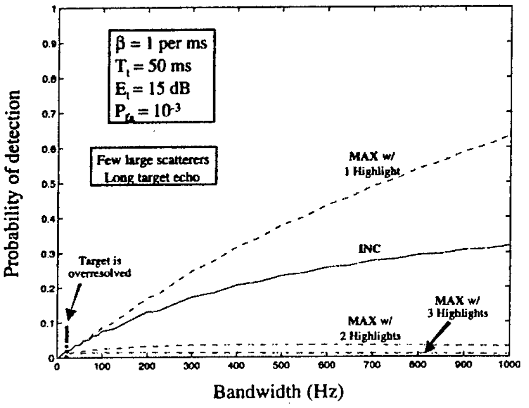

Fig. 4. P_d vs. bandwidth for a long target echo in non-Rayleigh reverberation

performs the MAX detector in non-Rayleigh reverberation.

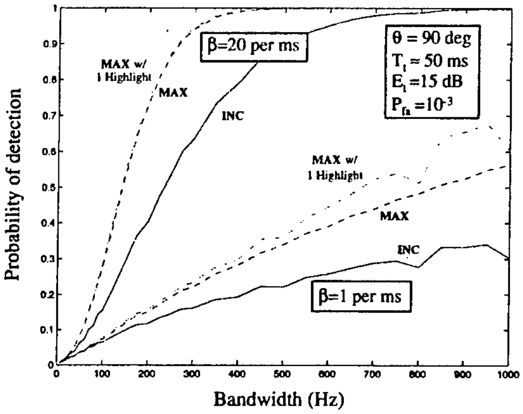

Fig. 5. P_d vs. bandwidth for a cylindrical target at broadside.

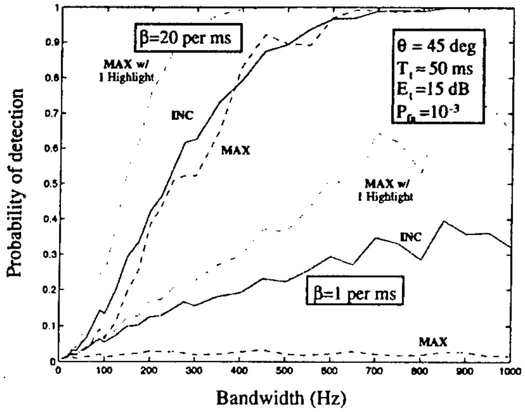

Fig. 6. P_d vs. bandwidth for a cylindrical target at an aspect of 45 degrees

4. CONCLUSIONS

This paper has considered the active sonar detection of targets in K-distributed reverberation using broadband waveforms. Two detectors were evaluated, an incoherent summation and a maximum detector. For both detectors, increasing bandwidth improved detection performance with the improvement being most significant when the reverberation is near-Rayleigh. When the target echo is predominantly a single highlight, the maximum detector performs better than the incoherent summation, though only minimally when the echo is not overly long in duration. When the target energy is spread, even into just two highlights, the incoherent summation is better than the maximum detector, significantly so in severely non-Rayleigh reverberation. Additionally, the performance of the incoherent summation detector was seen to be dependent on the total echo energy and not how it is distributed throughout the extent of the echo. Evaluation of detection performance for a cylindrical target illustrated that the maximum detector performs best at broadside aspect in both near-Rayleigh and non-Rayleigh reverberation. Off broadside, the detectors perform similarly in near-Rayleigh reverberation, but the performance of the maximum detector degrades significantly in severely non-Rayleigh reverberation.

5. REFERENCES

[1] D. A. Abraham, "Signal excess in K-distributed reverberation," *IEEE Jnl. of Oceanic Eng.*, 2001, Submitted in Sep. 2001.

[2] D. A. Abraham and A. P. Lyons, "Novel physical interpretations of K-distributed reverberation," *IEEE Jnl. of Oceanic Eng.*, 2001, Submitted in Sep. 2001.

[3] D. A. Abraham, "Statistical normalization of non-Rayleigh reverberation," in *Proc. of Oceans 1997 Conf.*, Halifax, Nova Scotia, Oct. 1997, pp. 500–505.

[4] D. A. Abraham and A. P. Lyons, "Exponential scattering and K-distributed reverb.," in *Proc. of Oceans 2001 Conf.*, Honolulu, Hawaii, Nov. 2001, pp. 1622–1628.

[5] H. Amindavar and J. A. Ritcey, "Padé approx. for detectability in K-clutter and noise," *IEEE Trans. on Aero. and Elect. Sys.*, vol. 30, no. 2, pp. 425–434, April 1994.

[6] D. A. Abraham, K. L. Hillsley, and J. Norrmann, "A robust model-based detector for active sonar," in *Proc. of Oceans 2001 Conf.*, Nov. 2001, pp. 2139–2146.

A. APPENDIX

The test statistic (2) may be approximated by a shifted gamma random variable, $T_a \approx aG + b$ where G is a unit-scale gamma random variable with shape parameter c. The CDF of T_a is then approximated by

$$F_a(t) \approx F_c\left(\frac{t-b}{a}\right) \tag{12}$$

where $F_c(x) = \frac{\gamma(c,x)}{\Gamma(c)}$ is the incomplete gamma function. The parameters (a, b, c) are obtained from the first three moments of T_a ($\mu_k = E\left[T_a^k\right]$ for $k = 1, 2, 3$) according to [4]

$$a = 0.5\left[\frac{\mu_3 - 3\mu_1\mu_2 + 2\mu_1^3}{\mu_2 - \mu_1^2}\right], \tag{13}$$

$$c = \frac{\mu_2 - \mu_1^2}{a^2} \text{ and } b = \mu_1 - ac. \tag{14}$$

Novel Physical Interpretations of *K*-Distributed Reverberation

Douglas A. Abraham and Anthony P. Lyons

***Abstract*—Interest in describing and modeling envelope distributions of sea-floor backscatter has increased recently, particularly with regard to high-resolution active sonar systems. Sea-floor scattering that results in heavy-tailed-matched-filter-envelope probability distribution functions (i.e., non-Rayleigh distributions exemplified by the *K*, Weibull, Rayleigh mixture, or log-normal distributions) is often the limiting factor in the performance of these types of sonar systems and in this context is referred to as reverberation or acoustic clutter analogous to radar clutter. Modeling of reverberation has traditionally entailed fitting various candidate distributions to time samples of the envelope of the scattered sonar (or radar) returns. This type of descriptive analysis and the asymptotic (infinite number of scatterers) analysis defining the *K*-distribution yield little insight into the environmental mechanisms responsible for heavy-tailed distributions (e.g., distributions and clustering of discrete scatterers, patchiness in geo-acoustic properties, scattering strength of scatterers, etc.) and do not allow evaluation of the effect of changing sonar system parameters such as bandwidth and beamwidth. In contrast, we derive the envelope distribution for the scattered returns starting from simple physical descriptions of the environment with a finite number of scatterers. It is shown that plausible descriptions of the environment can lead to *K*-distributed reverberation. This result explains, at least partially, the success of the *K*-distribution in the modeling of radar clutter and sonar reverberation at a variety of frequencies and scales. The finite-number-of-scatterers model is then used to predict how the shape parameter of the *K*-distribution will change as the beamwidth of a towed-array receiver is varied. Analysis of reverberation data from a low-frequency (450–700 Hz) active sonar system illustrates that, within our ability to estimate it, the shape parameter of the *K*-distribution is proportional to the beamwidth of the towed-array receiver, a result important for sonar simulation and performance prediction models. These results should prove useful in developing methods for modeling, predicting and mitigating reverberation on high-resolution sonar systems.**

***Index Terms*—Clutter, *K*-distribution, non-Rayleigh, reverberation, scattering.**

I. INTRODUCTION

HIGH-resolution active sonar systems have been developed to improve detection performance by lowering the power of the interfering reverberation in a given resolution cell. Unfortunately, this can have the adverse effect of producing reverberation with a statistical distribution that is significantly more heavy-tailed than the traditionally assumed Rayleigh distribution at the matched filter envelope, leading to an increase in the probability of false alarm (P_{fa}). The Rayleigh distribution is obtained by assuming that there are enough scatterers contributing to the reverberation in any given resolution cell (after beamforming and matched filtering) so that the central limit theorem (CLT) holds and the received signal is Gaussian, resulting in a Rayleigh distributed envelope. Non-Rayleigh reverberation, in particular reverberation with tails heavier than Rayleigh, can occur when the conditions of the CLT are violated. For example, there may be too few scatterers in the resolution cell or the scatterers may not be identically distributed.

Statistical analysis of the reverberation envelope usually entails fitting the observed data to a set of models to determine which provides the best representation [1]–[5]. Researchers are usually forced into such descriptive analyses because there are very few physics-based models that link a tenable description of the environment and sonar system to the probability density function (PDF) of the reverberation induced matched filter envelope output. Among them are Crowther's model [6] for sea-bed backscatter when the sea-bed is comprised of patches of differing types and Middleton's *KA*-distribution [7] which was developed using counting functionals in what he terms a "physical-statistical" approach. The *KA*-distribution is a generalization of the well-known *K*-distribution [8], [9], which is itself derived in the limit by assuming that the number of scatterers in a resolution cell follows a negative binomial distribution with a mean that tends to infinity. The *K*-distribution has also been described as a compound process arising from the modulation of Rayleigh backscatter by an intensity that varies slowly in time and is well modeled by the gamma distribution [10]. Owing to their complicated nature or limited applicability, the models of Crowther and Middleton are rarely employed. The *K*-distribution, however, is a standard model for radar clutter [11] and has been shown to represent sonar reverberation well [5], [12]–[14]. Unfortunately, neither the asymptotic derivation nor the compound representation (which is phenomenological) of the *K*-distribution retain the pertinent description of the environment that would allow prediction of the PDF of the matched filter envelope and how it changes as a function of sonar system parameters or is affected by varying environmental scattering mechanisms.

In this paper, we start with a plausible physical description of the sea-floor scattering environment and derive the PDF for the reverberation envelope while retaining the environmental characterization necessary for predictive analysis such as changes in PDF as a function of system or environmental parameters. In Section III-A, it will be shown that reverberation arising from a finite number of discrete scattering objects having an exponential size distribution results in a *K*-distributed matched filter envelope. The shape parameter of the *K*-distribution is related to the number of

Manuscript received October 5, 2002; revised July 3, 2002. This work was supported by the Office of Naval Research under Grants N00014-02-1-0115 and N00014-01-1-0352.

The authors are with the Applied Research Laboratory, Pennsylvania State University, State College, PA 16804-0030 USA (e-mail: d.a.abraham@ieee.org).

Digital Object Identifier 10.1109/JOE.2002.804324

scatterers within each resolution cell of the sonar system and the scale parameter is related to the average size of the scatterers. Scattering from a sea floor comprised of a finite number of patches of differing sizes is considered in Section III-B. Interface scattering from each individual patch produces a Gaussian reverberation response; however, when the patches are assumed to have an exponentially distributed size, the reverberation envelope is seen to be *K*-distributed. These models that are based on a finite number of scatterers allow the prediction of the PDF of the reverberation induced matched filter envelope and how it changes as a function of sonar system parameters such as transmit waveform bandwidth and receiving array beamwidth. In Section IV, experimental data from a low-frequency active sonar system are used to show that the *K*-distribution shape parameter is, as predicted by the model of Section III-A, proportional to the beamwidth of the towed-array receiver.

II. BACKGROUND

Active sonar systems transmit signals and process the resulting echoes for the purposes of detecting, classifying and localizing targets. The transmitted pulse, say $s(t)$, reflects off of a potential target and a multitude of inhomogeneities and irregularities (i.e., scatterers) in the ocean medium and is then received by an array of hydrophones. The response of each scatterer is modeled as a time-delayed and amplitude-scaled version of the transmitted pulse. The hydrophone array is designed to allow spatial filtering (i.e., beamforming) of the array data which improves the signal-to-noise power ratio (SNR) by rejecting energy coming from directions away from the main response axis (MRA) while accepting energy from a limited region in angle about the MRA. The received signal after beamforming may be described as

$$X_\theta(t) = A_0\, s(t-\tau_0) + \sum_{i=1}^{m} A_i\, s(t-\tau_i) + V_\theta(t) \qquad (1)$$

where θ represents the angle of the MRA, $s(t)$ is the transmitted pulse, A_0 and τ_0 are the target echo amplitude and arrival time, A_i and τ_i represent the amplitude and arrival time of the reverberation component from the ith scatterer, $V_\theta(t)$ is the ambient noise, and m is the total number of scatterers contributing to reverberation on this particular beam. Note that, in this paper, random variables are generally denoted by upper-case letters and constants by lower-case ones. It will be initially assumed that there is no acoustic wave propagation with multiple boundary interaction (e.g., multipath propagation). This case will be discussed in Section III-C.

If the interfering signals (the reverberation or clutter and ambient noise) are assumed to be a white Gaussian random process, then, the optimal detection processing [15] requires matched filtering the beam data by correlating them with the transmitted waveform. If the autocorrelation function of the transmitted waveform is

$$R_{ss}(t) = \int_{u=-\infty}^{\infty} s(u)s(u+t)\,du \qquad (2)$$

then, the matched filter output has the form

$$X(t) = A_0\, R_{ss}(t-\tau_0) + \sum_{i=1}^{m} A_i\, R_{ss}(t-\tau_i) + V(t) \qquad (3)$$

where t now represents time delay and $V(t)$ is the ambient noise after matched filtering. The effect of matched filtering is to reduce the number of scatterers that contribute to $X(t)$ at time t. If T_r is the width of the autocorrelation function of $s(t)$, then, only scatterers with delays τ_i such that $|t-\tau_i| < T_r/2$ will contribute to $X(t)$ at time t. Scatterers that are farther away in time are attenuated by the $R_{ss}(t-\tau_i)$ term in (3). T_r is also taken as the size of the resolution cell in range (delay) and is usually well approximated by one over the bandwidth of the transmit waveform. It should be noted that matched filtering is not necessarily optimal when the interfering signals are non-Gaussian or correlated in time; however, it is often employed as it can in many cases significantly increase SNR. Additionally, the optimal processor at this stage is not known when the interferences are non-Gaussian.

After matched filtering, and assuming little or no target Doppler, the beam output $X(t)$ may be modeled as a bandpass random process with energy predominantly in the transmission band. As such, the envelope of the process is a sufficient statistic for the detection of fluctuating targets and nonfluctuating targets with random phase when the interfering components are Gaussian [15]. The importance of sufficiency in this application is that the optimal likelihood ratio detector then only requires access to the sufficient statistic and not the complete data. Thus, the design and performance analysis of a detection algorithm may be determined solely from the statistical description of the envelope. Owing to the one-to-one correspondence between the matched filter envelope and intensity, the latter may be equivalently used as a sufficient statistic. The envelope is also of interest when the interfering components are not Gaussian. As seen in Appendix A, the envelope is a sufficient statistic for the more general case where the complex envelope of the interfering components has a circularly symmetric PDF. Reverberation that can be described as arising from the product between a Gaussian component and some positive modulating random variable has a circularly symmetric complex envelope PDF. The *K*-distribution, Rayleigh mixture, and Crowther's model satisfy these requirements.

A convenient intermediate step in forming the envelope of $X(t)$ is to first form the complex envelope by basebanding the data (i.e., frequency shifting with a complex exponential at the center frequency of the band, f_c) followed by low-pass filtering to remove out-of-band components

$$\begin{aligned}\tilde{X}(t) &= \mathrm{LPF}\left\{2\,X(t)e^{-j2\pi f_c t}\right\} \\ &= A_0\, e^{-j2\pi f_c \tau_0}\tilde{R}_{ss}(t-\tau_0) \\ &\quad + \sum_{i=1}^{m} A_i\, e^{-j2\pi f_c \tau_i}\tilde{R}_{ss}(t-\tau_i) + \tilde{V}(t) \qquad (4)\end{aligned}$$

where $\tilde{R}_{ss}(t)$ is the basebanded autocorrelation function of the transmit waveform and $\tilde{V}(t)$ is the complex envelope of the ambient noise after matched filtering. In this paper, variables with a tilde are complex. The envelope is then simply the modulus of the complex envelope, $Y(t) = |\tilde{X}(t)|$. When the reverberation dominates the ambient noise and no target is present, the complex envelope simplifies to the middle term of (4) and may be approximated by assuming that the autocorrelation function is binary and either fully passes the individual scatterer echoes when they are within the resolution cell, or fully rejects them when they are not

$$\tilde{X}(t) \approx \tilde{R}(t) = \sum_{i=1}^{m} A_i\, e^{-j2\pi f_c \tau_i} \tilde{R}_{ss}\,(t-\tau_i) \approx \sum_{i=1}^{n(t)} A_i\, e^{-j\theta_i} \tag{5}$$

where $n(t)$ is the number of scatterers that contribute to the complex envelope at time delay t and $\theta_i = 2\pi f_c \tau_i$. For notational simplicity, it is assumed that these $n(t)$ scatterers are indexed by $i = 1, \ldots, n(t)$. The time delays τ_i are assumed to be uniformly random over an integer number of periods of the center frequency f_c so θ_i may be equivalently assumed to be uniformly distributed from 0 to 2π. It should be noted that if the transmit waveform is a short rectangular continuous wave pulse and matched filtering is not employed [i.e., $s(t) = \cos(2\pi f_c t)$ for $t \in (0, T)$ with T an integer multiple of $1/f_c$] then the result of (5) is exact rather than approximate.

Traditionally, it has been assumed that $n(t)$ is nonrandom and large enough that the CLT [16] applies and $\tilde{R}(t)$ is a zero mean complex Gaussian random process, leading to a Rayleigh distributed envelope

$$Y(t) \sim f_Y(y) = \frac{2y}{\lambda_0}\, e^{-(y^2/\lambda_0)} \tag{6}$$

where λ_0 is the power. The *K*-distribution has been shown to arise by first assuming that $n(t)$ is a random integer following a negative binomial distribution and then letting the average value of $n(t)$ tend to infinity [9]. The PDF for a *K*-distributed reverberation envelope is

$$Y(t) \sim f_Y(y) = \frac{4}{\sqrt{\lambda}\,\Gamma(\alpha)} \left(\frac{y}{\sqrt{\lambda}}\right)^{\alpha} K_{\alpha-1}\left(\frac{2y}{\sqrt{\lambda}}\right) \tag{7}$$

where $K_\nu(z)$ is the Basset function (i.e., a modified Bessel function of the third kind) [17], λ is a scale parameter, α is the shape parameter, and the power is $E[Y^2] = \alpha\lambda$. The Rayleigh distribution is a submember of the K-distribution that is obtained when $\alpha \to \infty$, while $\lambda = \lambda_0/\alpha$.

The significance of these two results lies in their validity irrespective of the PDF of the amplitudes A_i, as long as the distributions satisfy some minimal regularity conditions such as independence and finite variance. However, owing to their asymptotic nature, these results do not allow the analysis of a sonar system as a function of the beamwidth or bandwidth; that is, when the number of scatterers within a resolution cell is finite and is allowed to change with system parameters (e.g., increasing bandwidth) or environmental conditions. In particular, a sonar system with a large receiving array or a wide bandwidth transmitter may reduce the resolution cell size so that not enough scatterers are present for the CLT to hold or for the *K*-distribution to be accurate as an asymptotic approximation. In this situation, the distribution of the summation in (5) will depend highly on the PDFs of the scatterer echo amplitudes and delays. The following section considers two plausible physical characterizations of sea-floor scattering with a finite number of scatterers or a finite number of patches, both leading to the *K*-distribution for the matched filter envelope PDF. The derivations may not be rigorous with regard to the physics as they require some simplifying assumptions, yet they provide the desired link between the number of scatterers and the statistical distribution of the detection statistic.

III. Sea-Floor Scattering Models

Central to the novel physical interpretation of *K*-distributed reverberation arising from a finite number of scatterers is an assumption of a specific functional form for describing the size frequency distribution of discrete scatterers or scattering patches. In nature, distributions of size often exhibit the property that there are far fewer large objects or features than small. This is true for the size distributions of large geologic sea-floor features such as seamounts or bathymetry [18] as well as for smaller features such as rock outcrops and fragments or even gas bubbles in sediment [19]. Various probability distribution functions have been used to fit data that display this characteristic including the exponential and the power law functions. The exponential function, in particular, has often been found to be useful for describing the size distribution of large-scale geologic sea-floor features including fault displacements and lengths [20] and sea-floor slopes [21]. Additionally, for many sites, both terrestrial and extraterrestrial, the exponential distribution has often provided the best fit to rock size data [22], [23]. In the case of discrete objects such as boulders and rocks, exponential size distributions are justified based on the theory of fracture and fragmentation [23].

Given the validity of an exponential function for describing the size distribution of many types of natural features, in the following analysis, we assume that the size of a randomly occurring scatterer is described by an exponential distribution function. Although numerical methods could be used to obtain the PDF of the matched filter envelope for a number of other distribution functions, the exponential form has the advantage of resulting in an analytical solution. In the following sections, both reverberation arising from discrete scatterers and from sea-floor patches of different scattering strength are considered.

A. *Exponentially Sized Discrete Scatterers*

Assuming that reverberation arises from a finite number of scattering objects that have an exponentially distributed size and that the amplitude of the scattering return is proportional to its size (e.g., as in geometrical scattering [24]), then A_i in (5) would be exponentially distributed with PDF

$$f_A(a) = \frac{1}{\mu}\, e^{-(a/\mu)} \tag{8}$$

where μ is the average size of the scatterers. Assuming that the amplitude and delay of each scatterer are independent of each other and of those of other scatterers, the distribution of $\tilde{R}(t)$ may be found by forming the joint characteristic function (CF) of its in-phase (real) and quadrature (imaginary) components

$$\tilde{R}(t) = U(t) + jV(t). \tag{9}$$

The joint CF of the sum in (5) is the product of the joint CFs of the components of the sum or, as the summands are statistically identical, the joint CF of $A_i e^{-j\theta_i}$ raised to the power $n(t)$. Let

$\tilde{R} = \tilde{R}(t)$, $U = U(t)$, $V = V(t)$, $n = n(t)$, $A = A_i$ and $\theta = \theta_i$. The joint CF of $\tilde{R}(t)$ is then

$$\begin{aligned}\Phi_{\tilde{R}}(\omega, \gamma) &= E\left[e^{j\omega U + j\gamma V}\right]\\ &= \left\{E\left[e^{j\omega A\cos\theta + j\gamma A\sin\theta}\right]\right\}^n\\ &= \left\{\int_{a=0}^{\infty}\left[\frac{1}{2\pi}\int_{\theta=0}^{2\pi} e^{ja(\omega\cos\theta+\gamma\sin\theta)}\,d\theta\right]\frac{e^{-(a/\mu)}}{\mu}\,da\right\}^n\\ &= \left\{\int_{a=0}^{\infty}\left[\frac{1}{2\pi}\int_{\theta=0}^{2\pi} e^{ja\sqrt{\omega^2+\gamma^2}\cos(\theta-\beta)}\,d\theta\right]\frac{e^{-(a/\mu)}}{\mu}\,da\right\}^n\\ &= \left\{\int_{a=0}^{\infty} J_0\left(a\sqrt{\omega^2+\gamma^2}\right)\frac{e^{-(a/\mu)}}{\mu}\,da\right\}^n\\ &= \frac{1}{[1+\mu^2(\omega^2+\gamma^2)]^{n/2}}\end{aligned} \tag{10}$$

where $\beta = \arctan(\gamma/\omega)$and

$$J_0(x) = \frac{1}{\pi}\int_{\theta=0}^{\pi} e^{jx\cos\theta}\,d\theta \tag{11}$$

is a Bessel function of the first kind and order zero [17], and simplification of the last line comes from Gradshteyn and Ryzhik [25, p. 729, 6.611-1].

Inversion of $\Phi_{\tilde{R}}(\omega, \gamma)$ would show that the exponential scattering model in fact results in *K*-distributed reverberation. It is, however, easier to derive the joint CF for *K*-distributed reverberation and exploit the uniqueness property of CFs than to invert (10). In order to accomplish this it is convenient to use the product description of *K*-distributed reverberation. Ward [10] noted that it was possible to describe *K*-distributed reverberation as the product between a Rayleigh speckle component and a slowly fluctuating variable following a square-root gamma distribution. The complex envelope of such reverberation would have the form

$$\tilde{R}(t) = \sqrt{P(t)}\,\tilde{Z}(t) \tag{12}$$

where $\tilde{Z}(t)$ is a zero-mean, low-pass, complex, Gaussian random process with variance λ and $P(t)$ is a gamma distributed random process with unit scale, shape parameter $\alpha(t)$ and a low-pass spectrum. A more realistic model would allow $\tilde{Z}(t)$ to be nonstationary with a time-varying variance. However, for the purposes of this paper, such a generality is not necessary, so the variance is assumed constant in order to simplify notation. If $\tilde{Z}(t) = U(t) + jV(t)$, then $U(t)$ and $V(t)$ are independent, zero-mean, real, Gaussian random processes with variance $\lambda/2$. The joint CF of $\tilde{R}(t)$ in (12) is found to be [with $\alpha = \alpha(t)$, $P = P(t)$, $U = U(t)$, and $V = V(t)$]

$$\begin{aligned}\Phi_K(\omega, \gamma) &= E\left[e^{j\omega\sqrt{P}U + j\gamma\sqrt{P}V}\right]\\ &= E_P\left[E_{U|P}\left[e^{j\omega\sqrt{P}U}\right]E_{V|P}\left[e^{j\gamma\sqrt{P}V}\right]\right]\\ &= \int_{p=0}^{\infty} e^{-(\lambda/4)(\omega^2+\gamma^2)p} f_P(p)\,dp\\ &= \int_{p=0}^{\infty}\frac{p^{\alpha-1}}{\Gamma(\alpha)}\,e^{-[1+(\lambda/4)(\omega^2+\gamma^2)]p}\,dp\\ &= \frac{1}{\left[1+\frac{\lambda}{4}\left(\omega^2+\gamma^2\right)\right]^{\alpha}}\end{aligned} \tag{13}$$

where the CF of a zero-mean Gaussian random variable with variance $\lambda/2$ is [26]

$$E\left[e^{j\omega U}\right] = e^{-(\lambda/4)\omega^2}. \tag{14}$$

Clearly, (10) and (13) have the same form, illustrating that exponentially sized scatterers produce *K*-distributed reverberation with the shape parameter of the *K*-distribution equal to half the number of scatterers

$$\alpha = \frac{n}{2} \tag{15}$$

and the scale parameter related to the average scatterer size through

$$\lambda = 4\mu^2. \tag{16}$$

The importance of the last two equations lies in the fact that they link the parameters of the *K*-distribution to a physical model of the environment, making prediction of the reverberation PDF possible for different sonar system configurations.

It is worthwhile to note that the previous derivation does not imply the following converse statement: if the matched filter envelope is *K*-distributed, then, the scatterer amplitude in (5) must be exponentially distributed. In fact, there are other statistical distributions that may be used to describe the scatterer amplitude that will result in a *K*-distributed matched filter envelope. An example of this may be found in the work of Lord [27] where the joint PDF of an s-dimensional spherically invariant random vector is described as having an exponential form in terms of the vector length. For the two-dimensional case that represents the complex data model of (5), this results in a gamma distributed vector length (i.e., scatterer amplitude) with a shape parameter equal to 2 and is seen to result in a *K*-distributed vector length (i.e., the matched filter envelope) when n such vectors are summed.

B. Exponentially Sized Sea-Floor Patches

A theoretical model for reverberation resulting from interface scattering off of a sea floor comprised of patches was developed by Crowther [6] where it was assumed that the patches were characterized by a two-dimensional Markov model. Suppose instead that the patches dominate the background and are characterized as having random size; for example, an exponentially distributed area

$$B_i \sim f_B(b) = \frac{1}{\mu}\,e^{-(b/\mu)} \tag{17}$$

where B_i is the area for the ith patch and μ is the average patch area. Diffuse scattering from the interface produces a Gaussian distributed return from each patch by virtue of the CLT, with power proportional to the patch area and backscattering coefficient. Now assume that there are n such patches within a resolution cell of the sonar system. The reverberation component of the complex envelope of the received signal in this resolution cell (i.e., after beamforming and matched filtering) may then be represented as

$$\tilde{R} = \sum_{i=1}^{n}\sqrt{B_i}\,\tilde{Z}_i \tag{18}$$

where $\tilde{Z}_i$ is a zero-mean, complex, Gaussian random variable with variance σ^2. Such a characterization of the sea floor can not be described by the model (5) of the previous section because the time delay of the individual scatterers is not uniformly distributed.

Noting that an exponential random variable is a gamma random variable with unit shape parameter, the joint CF of one term in the summation of (18) is found from (13) by setting $\alpha = 1$ and $\lambda = \mu\sigma^2$. Assuming that the responses from each patch are statistically independent then leads to the joint CF of the summation

$$\Phi_{\tilde{R}}(\omega, \gamma) = \frac{1}{\left[1 + \frac{1}{4}\,\mu\sigma^2(\omega^2 + \gamma^2)\right]^n}. \tag{19}$$

Clearly, this is the same form as that of (13) for the joint CF of the K-distribution with $\alpha = n$, the number of patches in a resolution cell, and $\lambda = \mu\sigma^2$, the average area of each patch times the backscattering power per unit area. It is interesting to note that even though each patch produces Gaussian reverberation, the resultant sum is non-Gaussian owing to the random power of each component. This result also illuminates the fact that the K-distribution, at the bandpass or complex envelope stage, is closed under addition when the summands have the same-scale parameter ($\lambda = \mu\sigma^2$). Thus, if the sea-bed is comprised of patches of differing types the result will still be K-distributed if the scale parameters are equal; i.e., $\mu_i\sigma_i^2 = \mu_j\sigma_j^2$. When the scale parameters are not equal, the envelope will not be K-distributed; however, if one patch type dominates the other in the sense of $\mu_0\sigma_0^2 \gg \mu_1\sigma_1^2$ then, the K-distribution may be a good approximation.

C. Multipath Propagation

As previously admitted, the models and methods used in the previous sections to link a description of the environment in terms of the number of scatterers within a resolution cell of a sonar system to the statistical distribution of the matched filter envelope are at times coarse approximations. Perhaps, the most egregious of the omissions has revolved around the implicit assumptions about acoustic propagation between the source array, the scatterers, and the receiving array. No mention has been made of any particular model; however, it has been unrealistically assumed that no multipath propagation occurs. Were it to occur, the effect would be to make the reverberation at any given time more Rayleigh-like, owing to scatterers arriving from different parts of the sea-floor through alternative acoustic propagation paths. That the K-distribution is closed under addition indicates that the envelope may still be K-distributed in the presence of multipath if the path amplitudes do not vary significantly. If the path amplitudes do differ significantly, the joint CF of the complex envelope would be a product of terms similar to (13) and the envelope distribution would have to be found computationally through either Padé approximations [28] or a numerical Hankel transform.

Under multipath propagation conditions the reverberation would also become more correlated in time, which exposes a second weakness of the current derivation. The link between exponential scattering and the K-distribution has been established for first-order PDFs. The second–order PDFs (i.e., joint PDFs between samples from two different times) have not yet been established and thus limit the physical interpretation of the random processes of the product formulation of K-distributed reverberation, $P(t)$ and $\tilde{Z}(t)$.

IV. BEAMWIDTH ANALYSIS OF EXPERIMENTAL DATA

A potential use for the models described in the previous section lies in improving the fidelity of models that simulate sonar systems or predict their performance. In the sonar community, the Rayleigh distribution and the associated receiver operating characteristic curves of probability of detection versus probability of false alarm, as may be found in Urick [29] or Burdic [30], are typically used regardless of the goodness of fit of the Rayleigh distribution to observed reverberation data. The radar community has accepted statistical models that are more representative of their heavy-tailed data including the Weibull and K-distributions [11], though these models tend to be used with measured parameters rather than ones derived from physics based models [11], [31].

As a motivating example, consider a sonar system operating in an environment where the scatterer density and propagation are such that there are $n = 20$ scatterers in a particular range-bearing resolution cell with each scatterer having average power so that (using the results of Section III-A) $\lambda = 4\mu^2 = 0.1$. The reverberation power at the matched filter output is then $P_1 = \alpha\lambda = 1$ where $\alpha = n/2 = 10$. The probability of false alarm for K-distributed reverberation and the Rayleigh distribution of the same power are shown in Fig. 1, as Case 1. At $P_{fa} = 10^{-6}$, the K-distribution predicts a threshold level 1.7-dB higher than that predicted by the Rayleigh distribution, illustrating how it accounts for the heavier tails of the non-Rayleigh reverberation and will, in turn, result in more accurate predictions of the probability of detection when the reverberation is not Rayleigh distributed. In the future, it may be possible to obtain values for n and μ from geophysical measurements of scatterer size and density (i.e., frequency of occurrence). For now, however, these must be estimated from observed reverberation data, as is done in the analysis of the following sections.

Now, suppose that a sonar system were employed with a towed-array receiver twice the size of the previous example. The larger array provides beamwidths half the size of the smaller array and would therefore yield half as many scatterers in the range-bearing resolution cell under consideration, resulting in $\alpha = 5$ and the expected 3-dB reduction in the reverberation power level. The P_{fa} curves for this situation are shown in Fig. 1, as Case 2, and illustrate a 2.7-dB difference in the predicted threshold levels for the Rayleigh and K-distributional models when $P_{fa} = 10^{-6}$. The disparity in prediction is worse when n, and, therefore, α, is smaller and better when n is larger and the K-distribution more closely resembles the Rayleigh distribution.

Under both distributional models of this example (Rayleigh and K), the reverberation power level decreases by a factor of two when the array size is doubled. However, under the K-distribution model, the shape parameter also decreases by a factor of two. It is this aspect of the finite-number-of-scatterers model developed in Section III-A that we wish to examine using real data,

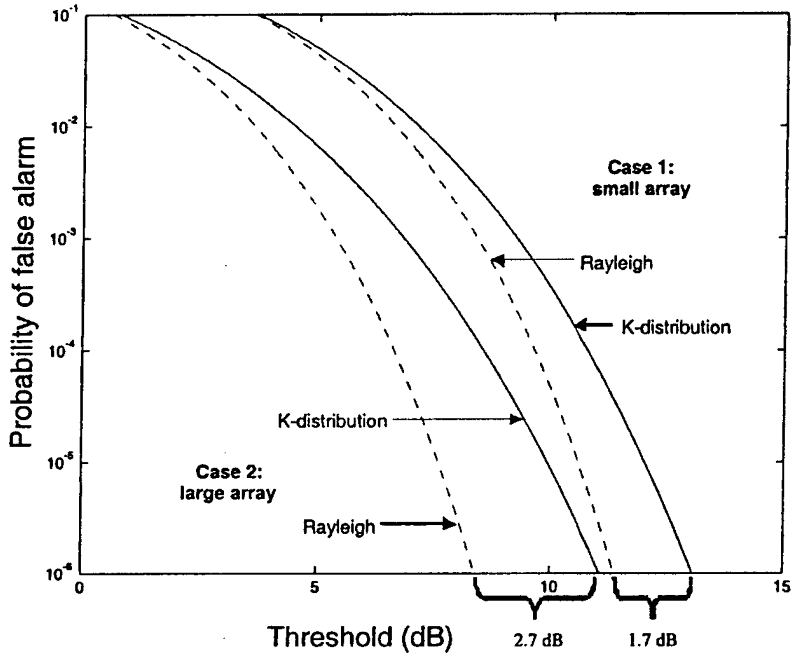

Fig. 1. Probability of false alarm under the Rayleigh and *K*-distributional models. When $P_{fa} = 10^{-6}$, the Rayleigh model predicts a 1.7 dB smaller threshold than the *K*-distribution for Case 1 and a 2.7-dB smaller threshold for Case 2. Case 2 differs from Case 1 in that the receiving towed-array is twice as large yielding a beamwidth that is twice as small.

specifically to see if the estimated shape parameter changes linearly with the beamwidth of a sonar receiving array as is predicted by the model. The following sections describe the sea-trial from which data are analyzed, illustrate that they are well described by the *K*-distribution, and finally examine the dependence of the shape parameter on the beamwidth of the towed-array receiver.

A. Sea-Trial Description

The data to be analyzed were taken during the SCARAB '97 sea-trial (Chief Scientist, Charles Holland) sponsored by the SACLANT Undersea Research Centre, La Spezia, Italy. The trial occurred off the coast of Italy in June, 1997 in the Capraia Basin which is north of the Island of Elba and contained several components related to scattering and reverberation [32]. The data analyzed in this paper were taken on June 2–3 using the Centre's low-frequency towed hydrophone-array and the towed vertically directive source (TVDS), which was configured to send a linear frequency modulated pulse with a 2-s duration spanning 450–700 Hz. The subsequent reverberation was recorded from the towed-array for 50 s following each transmission. Forty-nine such pings of data were collected at the points shown in Fig. 2. Owing to the shallow water environment and downward refracting sound-speed profiles that were measured during the sonar data acquisition, the reverberation data are dominated by bottom scattering. As described in [33], bottom scattering from the western portion of the Capraia Basin seems to be dominated by magmatic rock outcrops while the central and eastern parts of the basin are dominated by scattering from sub-bottom sediment volume inhomogeneities. The analysis presented in [33] illustrated how the latter produced Rayleigh distributed reverberation and the former produced heavier-tailed non-Rayleigh reverberation.

The towed-array receiver was comprised of 128 hydrophones with a 0.5-m spacing, resulting in a design frequency of 1500 Hz. The array data were beamformed with a hanning window such that the beampatterns of adjacent beams overlapped at their 3-dB down points at 900 Hz, resulting in 54 beams equally spaced in wavenumber, spanning from forward to aft along the array. The signal processing applied to the beamformed data prior to analysis of the reverberation statistics included basebanding, match filtering and normalization. The normalizer is of the cell-averaging type [11] with a split-window and gap, as described in [34]. The leading and lagging windows each contained 100 samples at a sampling rate of 250 Hz,[1] so the reverberation power estimate is formed by averaging 0.8 s of reverberation data. The gap on each side of the sample being normalized was 5-samples long.

B. Fit of the Rayleigh and K-Distributions

The shape parameter of the *K*-distribution is estimated from the beamformed, matched filtered, and normalized data. Before evaluating the shape parameter and how it changes with array beamwidth, it is necessary to determine how well fit the data are by the *K*-distribution. Fig. 3 contains the probability of false alarm estimated from a window of normalized matched filter data 2000 samples long (8 s). The ping from which these data are obtained is noted in Fig. 2. The P_{fa} obtained from the Rayleigh and *K*-distributions whose parameters are estimated from this data are also shown where the *K*-distribution clearly provides a

---

[1] As the sampling rate is equal to the transmit waveform bandwidth, consecutive samples are approximately uncorrelated.

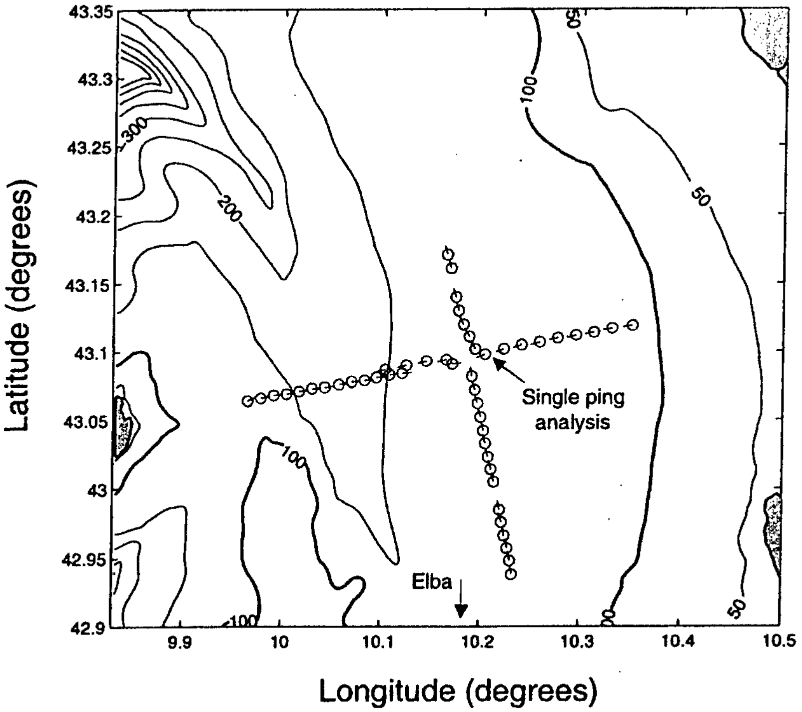

Fig. 2. Locations of each ping of data analyzed on a bathymetric map of the Capraia Basin. Each circle indicates the location of the ship. The trailing line from each circle illustrates where the towed-array was located relative to the ship (i.e., ship heading minus 180°). Bathymetry is in meters.

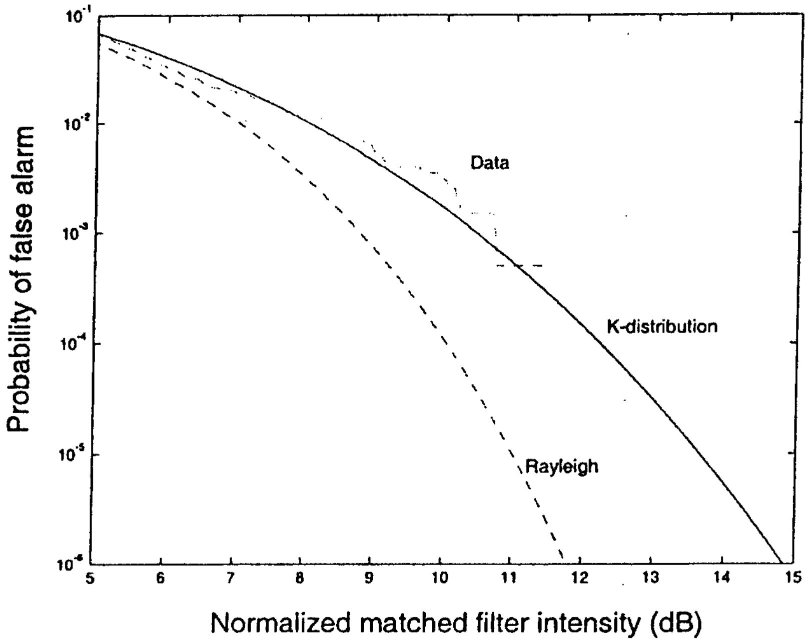

Fig. 3. Probability of false alarm estimated from normalized matched filter data along with Rayleigh and K-distribution models with parameters estimated from the data.

better fit to the data. This particular segment of data was chosen to illustrate that the Rayleigh distribution is not always a good fit to observed reverberation data. A significant portion of the data collected and analyzed, however, were well fit by the Rayleigh distribution. As the K-distribution has the Rayleigh distribution as a submember, the K-distribution fit these data well too.

In order to quantify how much of the data are well fit by the Rayleigh and K-distributions, the Kolmogorov–Smirnov (KS) test [35] is applied to the normalized matched filter data to test the ability of the models to represent the observed data. The KS test evaluates the maximum difference between the sample cumulative distribution function (CDF) generated by the data and

TABLE I
PERCENT OF DATA ACCEPTED AS BEING WELL FIT BY THE RAYLEIGH OR K-DISTRIBUTIONS BASED ON THE K–S TEST AT VARIOUS LEVELS OF FALSE REJECTION

	All data		Only data with K MME solution	
p-value	Rayleigh	K-distribution	Rayleigh	K-distribution
0.001	86.2	98.8	84.7	98.9
0.01	78.5	98.3	76.0	98.4
0.05	68.0	97.4	64.4	97.6
0.1	60.6	96.6	56.2	96.8

a test CDF which is, in this case, either the Rayleigh or K-distribution with their parameters estimated from the data being tested. The Rayleigh distribution only depends on its power, which is estimated by the sample intensity (i.e., the average of the matched filter intensity over the window being tested). As the data have already been normalized to have unit power, this should be near one. Estimation of the K-distribution parameters is more involved. The method of moments estimator (MME) has been employed and is described in detail in Appendix B.

For the data under consideration, windows 1000-samples long (4 s of data) with 50% overlap are used to estimate the model parameters and then form the KS test statistic. Using the asymptotic p-value[2] of the KS test statistic [35], the data are either accepted as being well fit by the Rayleigh or K-distribution or rejected. Table I contains the results for various p-values. For example, at the $p = 0.05$ level, 68% of the data are well fit by the Rayleigh distribution and 97.4% are well fit by the K-distribution. Note that only data between 2 and 40 s following the end of signal transmission on each ping are utilized in this and subsequent data analysis. Over these times, the data are reverberation limited except on the few beams where nearby shipping dominated the reverberation or where geological features precluded acoustic propagation (e.g., the Island of Capraia causing shadow zones).

As described in Appendix B, the method of moments does not always yield a solution for the K-distribution parameters. When a solution is not available, the shape parameter of the K-distribution is arbitrarily set to $\hat{\alpha} = 100$ and the scale parameter is obtained using the moment equation described in (39). That these cases tend to be when the data are nearly Rayleigh is evident from the change in acceptance percentages seen in Table I when only those data yielding an MME solution are considered. In this case, a slightly higher percentage of the data are well fit by the K-distribution and slightly smaller percentage are well fit by the Rayleigh distribution. Based on the acceptance percentages shown in Table I, the K-distribution is accepted as a good model for these data and it is noted that a significant portion of the data are Rayleigh-like.

C. Real Data Analysis

Based on the model developed in Section III-A, it may be hypothesized that the effective number of scatterers parameter (α) of the K-distribution is proportional to the area of the range-bearing resolution cell. As such, if the beamwidth of the sonar is doubled, then α should also double, regardless of the density of scatterers as long as they are uniformly placed within the range-bearing resolution cell. This latter point implies that the effect should occur for all the data observed, regardless of whether they are non-Rayleigh or Rayleigh-like.

The beamwidth of a sonar approximately doubles when the array size is halved. The same effect may be accomplished by coherently summing adjacent beams. As previously mentioned, the towed-array data have been spatially filtered into 54 beams that overlap at the 3-dB down points of their beampatterns at 900 Hz. The transmit waveform being analyzed ranged from 450 to 700 Hz, at which frequencies the beampatterns of adjacent beams overlap, respectively, at the 0.75- and 1.8-dB down points. A beampattern having width equal to the combined width of the individual beams may be formed without significant destruction of the mainlobe by coherently summing every other beam at the spacing described above. This does result in a ripple in the mainlobe with less than a one decibel height at 450 Hz and less than a two decibel height at 700 Hz. To illustrate this beam-summing, the beampatterns of three of the original beams near broadside to the array and the summed beam they form are shown in Fig. 4. From this figure, it may be seen that the width of the broadside beam at 700 Hz is 2.6°. At 450 Hz, the broadside beam is 4.1° wide.

The shape parameter of the K-distribution is estimated from either the original beam data or the summed beam data after matched filtering and normalization. For each beam, the data are separated into windows that are 500-samples long (at a sampling rate of 250 Hz this is 2 s of data) with an 80% overlap. For the ith window on the jth beam of the pth ping, call this estimate $\hat{\alpha}_k(p, i, j)$ where the index k indicates the span of how many original beams the beam-sum is formed over (beam-spans of $k = 1, 3, 5, 7$, and 9 are analyzed). The MME, as described in Appendix B, is used to estimate the K-distribution shape parameter. The estimates of the shape parameter from the single ping of data mentioned in the previous section are displayed in Fig. 5 in the form of histograms for each of the beam-spans. As expected, the data exhibit a trend toward higher values as the beamwidth increases. On the figure, this is evident from the median, mean (which was trimmed by removing the largest and smallest 0.5 percent of the values), and the quantity of estimates that exceed 50. It is also clear that there is wide range of values observed on this single ping, indicating that the density of scatterers (i.e., frequency of occurrence) varies within the geographic region represented by this ping. To remove this variability, the ratio of the estimated shape parameters on the summed beams to that estimated on the individual beams is formed for each individual data window

$$\Delta_k(p, i, j, j') = \frac{\hat{\alpha}_k(p, i, j)}{\hat{\alpha}_1(p, i, j')} \tag{20}$$

where $j' = j, \ldots, j + k - 1$ represent the original beams that span the beamwidth of summed beam j. An average value is formed for each ping and beam sum

$$\overline{\Delta}_k(p) = \frac{1}{m} \sum_{i,j,j'} \Delta_k(p, i, j, j') \tag{21}$$

---

[2] The p-value is the probability that a data sample would be rejected when it should be accepted as being well fit by the model under consideration.

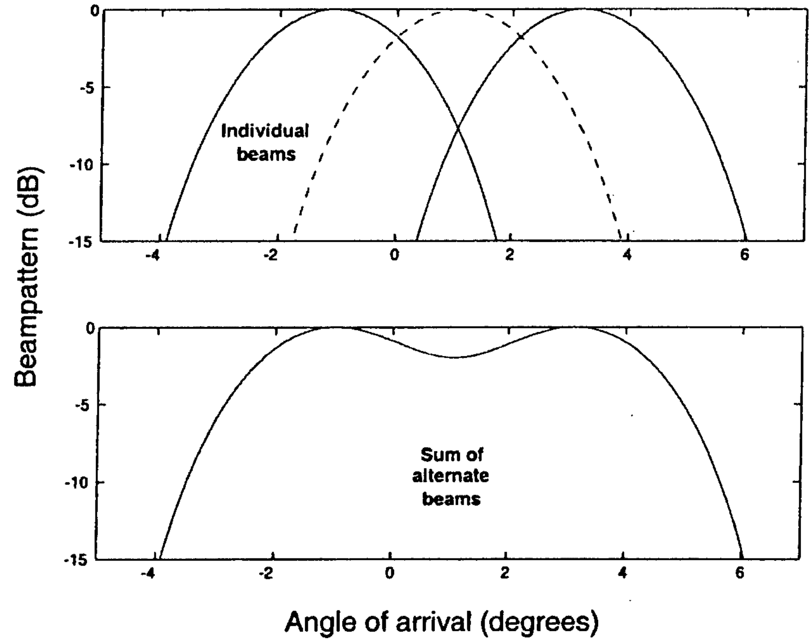

Fig. 4. Beampatterns of three original beams near broadside to the array and the summed beam that spans them at 700 Hz. The ripple in the main-lobe of the summed beam, approximately 2 dB, is at its worst at this frequency.

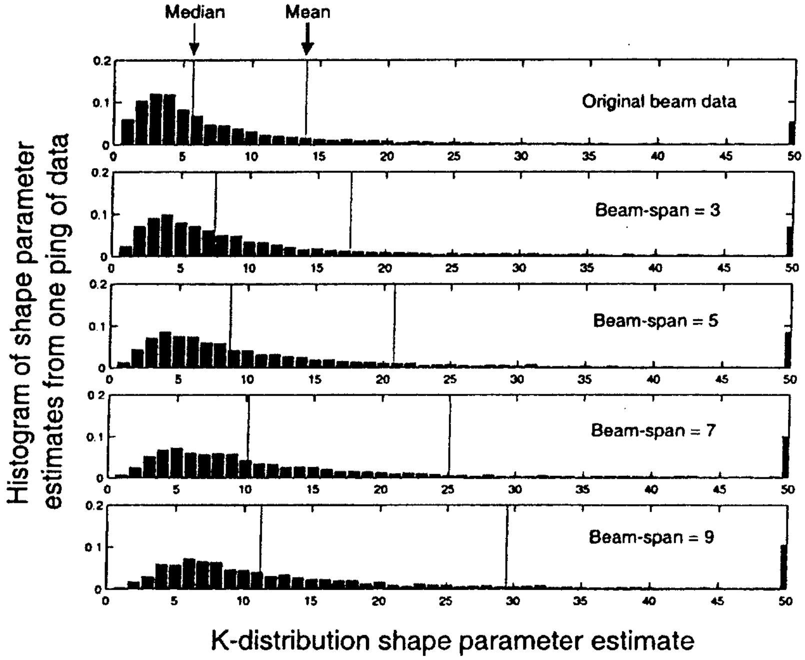

Fig. 5. Histograms of the estimates of the K-distribution shape parameter from a single ping for various beamwidths. The expected trend toward higher values of α as beamwidth increases is evident in the mean, median and number of estimates exceeding 50.

where the summation is over the m cases of the indices (i, j, j') such that the method moments estimators provide shape parameter estimates for both the individual and summed beams and the estimates satisfy $\hat{\alpha}_k(p, i, j) < 10^4$ and $\hat{\alpha}_1(p, i, j') < 10^4$. Extremely large estimates of α are discarded because of their high variability. As shown in Appendix B, the Cramér–Rao lower bound (CRLB) for the variance of any unbiased estimator of α is well approximated by α^2, especially for large α. Thus, when α is large, it is difficult to accurately estimate its value even when an efficient estimator is used and the MME is not likely to be efficient.

The change in the shape parameter predicted by the model is exactly the change in beamwidth. This is formed in a similar manner to how the change in the shape parameter is estimated from the data, by taking the average of the change in beamwidth between the summed beams and each of the individual beams

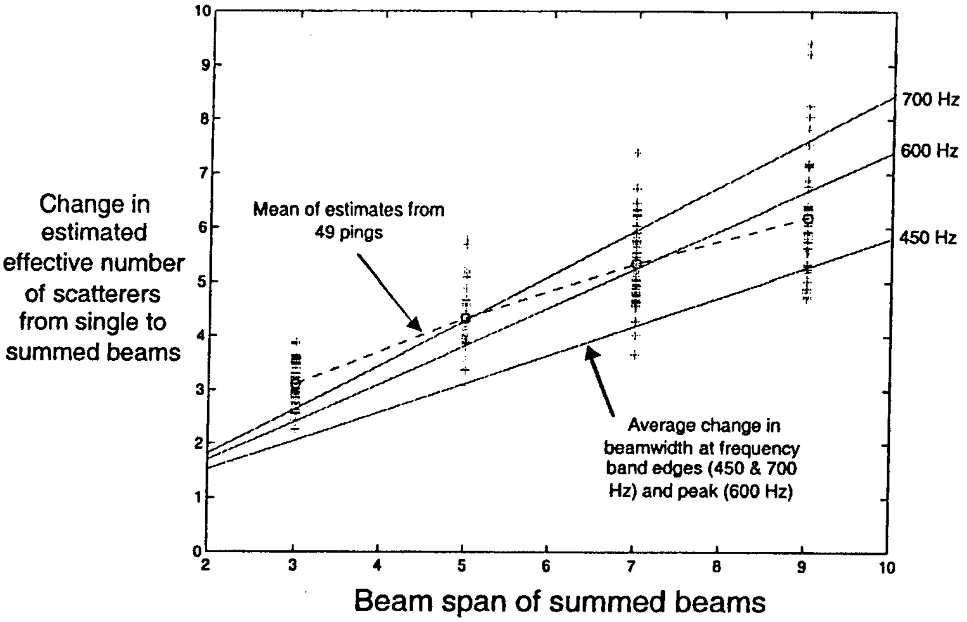

Fig. 6. Change in the shape parameter of the K-distribution between summed and individual beams as a function of the span of the beams summed (i.e., beamwidth). The + marks are the average values from each ping. The change as estimated from the data is very similar to that predicted by the change in beamwidth with the exception of an explainable upward bias.

for all of the summed beams. Despite the fact that beamwidth varies with arrival angle, the ratios of the beamwidths of the summed and individual beams do not vary significantly. These average ratios are computed for the edges of the frequency band of the transmit waveform (450 and 700 Hz) and also for the peak power frequency of the source (600 Hz) and shown with the average change in the estimated shape parameter of the K-distribution in Fig. 6. In the figure, it is seen that the estimated changes $\overline{\Delta}_k(p)$ fall very close to the predictions and that the average value over all pings has a slope similar to that predicted for the 450 Hz case, but is biased high. This may be explained by first noting that the expected change (20) is formed from the ratio of two random variables, say $\Delta = X/Y$. Assuming that both X and Y are positive random variables, it can be shown through the use of Jensen's inequality [36] that $E[\Delta] > E[X]/E[Y]$. This result also requires that the two random variables in the ratio be independent, which is not the case with the real data analyzed. However, for the minimal dependence that is expected, the result should be approximate and does proffer an explanation for the bias seen in the data.

The data shown in Fig. 6 are also seen to increase in variability as the beam-span increases. This may be the result of variability induced by nonstationarity in the frequency of occurrence of scatterers on the bottom over wider angles or may arise from the increased variability of shape parameter estimates when α is large. The latter of which is expected to occur more often for larger beamwidths (i.e., larger range-bearing resolution cell sizes) and when the data are nearly Rayleigh distributed (which is known to occur frequently in this data set).

The close similarity between the estimated and predicted change in the K-distribution shape parameter indicates that, within our ability to estimate it, the shape parameter is proportional to the beamwidth of the towed-array receiver. This also implies that a K-distribution model assuming a finite number of scatterers with the shape parameter tied to the number of scatterers in a sonar range-bearing resolution cell can provide more realistic simulations or predictions of sonar system performance as a function of system parameters such as beamwidth (shown here) and possibly bandwidth when the reverberation data are known to be non-Rayleigh.

V. CONCLUSION

In this paper, the statistical distribution of reverberation resulting from two plausible scenarios for sea-floor scattering has been examined. Sea floors composed of exponentially sized individual scatterers were considered as well as those comprised of homogeneous patches that have exponential size and are dominated by interface scattering. In both cases, the matched filter envelope was found to be K-distributed with the shape parameter related to either the number of scatterers or the number of patches and the scale parameter related to the average size of the scatterer or patch and backscattering coefficient. The models were developed using a finite number of scatterers or patches, in contrast to the more traditional asymptotic derivation of the K-distribution that requires an infinite number of scatterers. The importance of this lies in the ability to link the reverberation envelope distribution to measurable geo-acoustic properties in conjunction with the lens with which they are viewed (i.e., the sonar system). To illustrate this, low-frequency active sonar reverberation data were analyzed in terms of the shape parameter of the K-distribution and the beamwidth of the towed-array receiver. The analysis confirmed that, as predicted by the finite-number-of-scatterers model, the shape parameter of the K-distribution is proportional to the array beamwidth, even when the data were well described by the Rayleigh distribution (i.e., a large number of scatterers in each range-bearing resolution cell).

The relationships presented in this paper provide the foundation necessary for solving several important problems related to the detection of targets in non-Rayleigh reverberation including both environmentally driven concerns and signal processing issues. Some of the former include prediction of the reverberation induced envelope probability distribution functions from measured geo-acoustic data as well as consideration of more complicated sea-floor scattering and multipath propagation scenarios. Signal processing issues that may now be addressed include the development of optimal and suboptimal detectors and system performance evaluations that account for non-Rayleigh reverberation such as evaluating the trade-offs between improved SNR derived from an increase in the transmit signal bandwidth and the concomitant increase in false alarms resulting from heavier reverberation distribution tails.

APPENDIX A
SUFFICIENCY OF THE ENVELOPE FOR CIRCULARLY SYMMETRIC REVERBERATION

Let the complex envelope of an active sonar return be composed of a target component and interference (reverberation or clutter, and ambient noise)

$$\tilde{X} = Ae^{-j\theta} + \tilde{Z} \tag{22}$$

where A and θ are the amplitude and phase of the target echo and $\tilde{Z}$ is the complex envelope of the interference. Equation (22) may be obtained from (4) by setting $t = \tau_0$ and grouping the latter terms into $\tilde{Z}$, which is assumed to have a circularly symmetric PDF; that is, if $\tilde{Z} = U + jV$ then

$$f_{U,V}(u, v) = f_{U,V}(u^2 + v^2). \tag{23}$$

Sufficiency is typically shown using the Neyman factorization theorem [37] where the PDF is factored into two terms, the first one depending on the statistic to be proven sufficient and the parameters for which it is sufficient and the second term only depending on the data. The random variables in (22) are A, θ, $U = \Re e\{\tilde{Z}\}$, and $V = \Im m\{\tilde{Z}\}$. Conditioning on A and θ, the joint PDF of $\tilde{X} = X_r + jX_i$ is

$$\begin{aligned} f_{\tilde{X}}(x_r, x_i \,|\, A, \theta) &= f_{U,V}(x_r - A\cos\theta,\, x_i - A\sin\theta) \\ &= f_{U,V}\left((x_r - A\cos\theta)^2 + (x_i - A\sin\theta)^2\right) \\ &= f_{U,V}\left(A^2 + x_r^2 + x_i^2 - 2Ax_r\cos\theta - 2Ax_i\sin\theta\right) \\ &= f_{U,V}\left(A^2 + x_r^2 + x_i^2 - 2A\sqrt{x_r^2 + x_i^2}\cos(\theta - \beta)\right) \end{aligned} \tag{24}$$

where $\beta = \arctan(x_i/x_r)$. Now, if θ is assumed to be independent of A and uniformly random over $(0, 2\pi)$ then

$$\begin{aligned} f_{\tilde{X}}(x_r, x_i) &= E_{A,\theta}\left[f_{\tilde{X}}(x_r, x_i|A, \theta)\right] \\ &= \frac{1}{2\pi} E_A\left[\int_0^{2\pi} f_{U,V}\left(A^2 + y^2 - 2Ay\cos(\theta - \beta)\right) d\theta\right] \\ &= \frac{1}{2\pi} E_A\left[\int_0^{2\pi} f_{U,V}\left(A^2 + y^2 - 2Ay\cos(\theta)\right) d\theta\right] \\ &= \frac{1}{2\pi}\int_0^{\infty} f_A(a)\int_0^{2\pi} f_{U,V}\left(a^2 + y^2 - 2ay\cos(\theta)\right) d\theta\, da \end{aligned} \tag{25}$$

where $y = \sqrt{x_r^2 + x_i^2}$. Clearly the joint PDF of $\tilde{X} = X_r + jX_i$ can be described as only depending on (x_r, x_i) through the envelope $y = \sqrt{x_r^2 + x_i^2}$. Thus, $f_{\tilde{X}}(x_r, x_i)$ can be factored so that the envelope $Y = |\tilde{X}|$ is seen to be a sufficient statistic for target parameters required to define $f_A(a)$ and interference parameters required to define $f_{U,V}(u, v)$.

By making varying assumptions about the distribution on the target amplitude, the common Swerling target models [38] may be obtained. When $f_A(a) = \delta(a - a_0)$, then the target has a constant amplitude $A = a_0$ and the nonfluctuating or Swerling 0 target model arises. When A is Rayleigh distributed the target component $Ae^{j\theta}$ is a zero-mean complex Gaussian random variable, which produces the fluctuating or Swerling 1 target model. Sufficiency of the envelope may also be shown for the one-dominant-plus-Rayleigh Swerling 3 target through a similar procedure.

APPENDIX B
ESTIMATION OF THE *K*-DISTRIBUTION SHAPE PARAMETER

Considering the PDF of (7), estimation of α and λ for the *K*-distribution certainly seems to be a formidable problem. Ward [31] provided an empirical formula for α based on the grazing angle and cross-range resolution of a vertically polarized radar. Raghavan [39] proposed an estimator based on approximating the *K*-distribution by a gamma distribution. The estimators resulted in a form depending on the arithmetic and geometric sample means that perform well when the *K*-distribution is distinctly non-Rayleigh. Joughin *et al.* [40] presented an analysis of maximum likelihood estimators (MLE) for the parameters obtained through a numerical maximization of the likelihood function. They compared the MLE to Raghavan's method [39] and method of moment estimators based on either the first and second or second and fourth moments. Simulation analysis showed that the MLE performed best when α was small with Raghavan's method being nearly equivalent and that when α is large the MME using the first two moments performs best with the MLE being nearly equivalent.

Because the maximum likelihood techniques require numerical optimization routines and evaluation of Bessel functions, they are computationally intensive and therefore inappropriate for evaluation of large data sets. The MMEs are relatively quick but suffer from a nonzero probability of not returning a solution. Despite this failing they are used in the data analysis presented in Section IV because they require significantly less computational power than the maximum likelihood based techniques. In this section, the MME that is employed is described and an approximation to the CRLB is derived for the shape parameter and seen to be well approximated by α^2.

A. MME

Based on the results of Joughin *et al.* [40] MME using the first two moments is recommended. This estimator provides an acceptable trade-off between performance and cost of implementation. Let the matched filter envelope data used to estimate the *K*-distribution shape parameter be $Y_1, \ldots, Y_n$. Define the sample moments of the envelope as

$$m_1 = \frac{1}{n}\sum_{i=1}^{n} Y_i \tag{26}$$

and

$$m_2 = \frac{1}{n} \sum_{i=1}^{n} Y_i^2. \tag{27}$$

The moments of the matched filter envelope following a *K*-distribution are easily obtained from the product form of the *K*-distribution [10]

$$E\left[Y^i\right] = \lambda^{i/2} \Gamma\left(1 + \frac{i}{2}\right) \frac{\Gamma\left(\alpha + \frac{i}{2}\right)}{\Gamma(\alpha)}. \tag{28}$$

Matching the second moment results in choosing

$$m_2 = \lambda \alpha \tag{29}$$

which, when solved for λ and substituted into the relationship for the first moment results in

$$m_1 = \frac{1}{2} \sqrt{\frac{\pi m_2}{\alpha}} \frac{\Gamma\left(\alpha + \frac{1}{2}\right)}{\Gamma(\alpha)} \tag{30}$$

or, equivalently

$$\frac{m_2}{m_1^2} = \frac{4\alpha \Gamma^2(\alpha)}{\pi \Gamma^2\left(\alpha + \frac{1}{2}\right)}. \tag{31}$$

Owing to the gamma functions, no closed form solution for α is obtainable. Defining the function

$$h(\alpha) = \frac{4\alpha \Gamma^2(\alpha)}{\pi \Gamma^2\left(\alpha + \frac{1}{2}\right)} \tag{32}$$

it can be seen that (31) will be satisfied when $g(\alpha) = 0$ in the function

$$g(\alpha) = \left[h(\alpha) - 1\right]^{-1} - \left[\frac{m_2}{m_1^2} - 1\right]^{-1}. \tag{33}$$

The function $g(\alpha)$ is chosen because it is numerically stable for a wide range of α. The method of moments estimate of α may then be obtained through use of a Newton–Raphson iteration [41] to find the root of $g(\alpha)$. The iteration is

$$\hat{\alpha} := \hat{\alpha} - \frac{g(\hat{\alpha})}{g'(\hat{\alpha})} \tag{34}$$

which requires the derivative

$$g'(\alpha) = \frac{-\alpha^{-1} h(\alpha)}{\left[h(\alpha) - 1\right]^2} \left\{1 + 2\alpha \left[\psi(\alpha) - \psi\left(\alpha + \tfrac{1}{2}\right)\right]\right\} \tag{35}$$

where

$$\psi(\alpha) = \frac{\Gamma'(\alpha)}{\Gamma(\alpha)} \tag{36}$$

is the digamma function [17]. Note that for large α most algorithms evaluating the gamma function will have problems. Application of Stirling's approximation [41] to the gamma function results in

$$\frac{\Gamma(\alpha)}{\Gamma\left(\alpha + \frac{1}{2}\right)} \approx \frac{1}{\sqrt{\alpha}} \left[\frac{e^{1/2}}{\left(1 + \frac{1}{2\alpha}\right)^{\alpha}}\right] \left[1 + \frac{1}{2\alpha(12\alpha + 7)}\right] \tag{37}$$

which should be used for $\alpha > 20$.

A reasonable initial estimate of α is obtained by using the approximation of (37), without the third multiplicative term, in the natural logarithm of (31). Applying a second order approximation to $\log(1 + (1/2\alpha)) \approx (1/2\alpha) - (1/8\alpha^2)$ then results in the starting point

$$\hat{\alpha} = \frac{1}{4} \left[\log\left(\frac{\pi m_2}{4 m_1^2}\right)\right]^{-1}. \tag{38}$$

After the Newton–Raphson iteration has converged, λ is estimated according to (29)

$$\hat{\lambda} = \frac{m_2}{\hat{\alpha}}. \tag{39}$$

Examination of the function $h(\alpha)$ reveals that it approaches infinity as $\alpha \to 0$ and monotonically decreases to $4/\pi$ as $\alpha \to \infty$. Thus, in order for there to be a positive solution to (31), $m_2/m_1^2 > 4/\pi$. Unfortunately, there is a nonzero probability that this inequality is not met and therefore no solution exists. As might be expected, this happens more frequently when α is high and/or the number of samples used to estimate the moments is small. The problem is surmounted either by obtaining the numerically more intensive maximum likelihood estimate or by accepting either a large α (e.g., $\alpha = 100$) or the Rayleigh distribution as an approximate fit.

B. CRLB for K-Distribution Shape Parameter

The CRLB provides a means for establishing the best performance a parameter estimator may achieve [37]. Specifically, it provides a lower bound on the variance of an unbiased estimator. If the matched filter envelope data Y are *K*-distributed with PDF $f_Y(y;\, \alpha)$ as described in (7) but with the dependence on α made explicit, then the Fisher information of Y with respect to α, which is inversely proportional to the CRLB, is

$$J(\alpha) = E\left[\left\{\frac{\partial}{\partial \alpha} \log f_Y(Y|\alpha)\right\}^2\right] \tag{40}$$

and the CRLB is

$$\operatorname{Var}\{\hat{\alpha}\} \geq \frac{1}{nJ(\alpha)} = \text{CRLB} \tag{41}$$

where $\hat{\alpha}$ is an unbiased estimator of the shape parameter (i.e., $E[\hat{\alpha}] = \alpha$) and n is the number of independent samples of Y that are used to form $\hat{\alpha}$.

Noting that λ is a scale parameter, it is straightforward to see that $J(\alpha)$ is invariant to λ. Thus, the Fisher information need only be determined for $\lambda = 1$, which leads to the PDF

$$f_y(y|\alpha) = \frac{4}{\Gamma(\alpha)} y^{\alpha} K_{\alpha-1}(2y) \tag{42}$$

the log-likelihood function

$$\log f_y(y|\alpha) = \alpha \log y - \log \Gamma(\alpha) + \log K_{\alpha-1}(2y) + \log 4 \tag{43}$$

and its derivative with respect to α

$$\begin{aligned} \frac{\partial}{\partial \alpha} \log f_y(y|\alpha) &= \log y - \frac{\Gamma'(\alpha)}{\Gamma(\alpha)} + \frac{\frac{\partial}{\partial \alpha} K_{\alpha-1}(2y)}{K_{\alpha-1}(2y)} \\ &= \log y - \psi(\alpha) + \frac{\frac{\partial}{\partial \alpha} K_{\alpha-1}(2y)}{K_{\alpha-1}(2y)} \end{aligned} \tag{44}$$

where $\psi(\alpha)$ is the digamma function [17]. The third term in (44) may be obtained by approximating $K_{\alpha-1}(2y)$ when α is large and positive [17]

$$K_{\alpha-1}(2y) \approx \frac{\Gamma(\alpha-1)}{2y^{\alpha-1}}\left[1-\frac{y^2}{(\alpha-2)(\alpha-3)}\right]^{\alpha-3}. \qquad (45)$$

The partial derivative of (45) with respect to α, normalized by $K_{\alpha-1}(2y)$, is then

$$\begin{aligned}\frac{\frac{\partial}{\partial\alpha}K_{\alpha-1}(2y)}{K_{\alpha-1}(2y)} &\approx \psi(\alpha-1)-\log y+\log\left[1-\frac{y^2}{(\alpha-2)(\alpha-3)}\right] \\ &\quad + \frac{y^2(2\alpha-5)(\alpha-2)^{-2}}{(\alpha-3)\left[1-\frac{y^2}{(\alpha-2)(\alpha-3)}\right]} \\ &\approx \psi(\alpha-1)-\log y+\frac{y^2}{\alpha^2} \qquad (46)\end{aligned}$$

where the final result is obtained by assuming that $\alpha \gg 1$, $\alpha \gg y$, and $\log(1-\delta) \approx -\delta$ for small δ.

Inserting (46) into (44) and then (40) and noting that $\psi(\alpha) - \psi(\alpha-1) \approx 1/\alpha$ for large α, the Fisher information is seen to be approximated by

$$\begin{aligned}J(\alpha) &\approx \alpha^{-2}E\left[\left(\frac{Y^2}{\alpha}-1\right)^2\right] \\ &= \alpha^{-2}\frac{E\left[\left(Y^2-E[Y^2]\right)^2\right]}{E[Y^2]^2} = \alpha^{-2}\mathrm{SI}(\alpha) \qquad (47)\end{aligned}$$

where SI (α) is the scintillation index (i.e., the variance of the matched filter intensity divided by the square of the average intensity). For the *K*-distribution, the scintillation index is

$$\mathrm{SI}(\alpha) = 1 + \frac{2}{\alpha} \qquad (48)$$

which is approximately one for large α (i.e., when the *K*-distribution is near the Rayleigh distribution).

The CRLB is then approximately

$$\mathrm{CRLB} \approx \frac{\alpha^2}{n\left(1+\frac{2}{\alpha}\right)} \approx \frac{\alpha^2}{n} \qquad (49)$$

for large α which implies that it is harder to estimate α when the *K*-distribution is nearly Rayleigh (i.e., when the two parameter model is well described by a one-parameter model). Numerical evaluation of the CRLB through Monte-Carlo integration of (40) with a first order difference approximation to the derivative with respect to α confirmed the above approximation as accurate for large α.

ACKNOWLEDGMENT

The authors wish to thank K. Fisher and B. La Cour for pointing out the work of Lord [27], and C. Holland for many helpful discussions and his efforts in organizing and leading the SCARAB sea trial.

REFERENCES

[1] N. P. Chotiros *et al.*, "Acoustic backscattering at low grazing angles from the ocean bottom. Part II. Statistical characteristics of bottom backscatter at a shallow water site," *J. Acoust. Soc. Amer.*, vol. 77, no. 3, pp. 975–982, 1985.

[2] M. Gensane, "A statistical study of acoustic signals backscattered from the sea bottom," *IEEE J. Ocean. Eng.*, vol. 14, pp. 84–93, Jan. 1989.

[3] S. Stanic and E. G. Kennedy, "Fluctuations of high-frequency shallow-water sea-floor reverberation," *J. Acoust. Soc. Amer.*, vol. 91, no. 4, pp. 1967-1973, 1992.

[4] W. K. Stewart, D. Chu, S. Malik, S. Lerner, and H. Singh, "Quantitative sea-floor characterization using a bathymetric sidescan sonar," *IEEE J. Oceanic Eng.*, vol. 19, pp. 599–610, Oct. 1994.

[5] A. P. Lyons and D. A. Abraham, "Statistical characterization of high-frequency shallow-water sea-floor backscatter," *J. Acoust. Soc. Amer.*, vol. 106, no. 3, pp. 1307–1315, 1999.

[6] P. A. Crowther, *Fluctuation Statistics of Sea-Bed Acoustic Backscatter*. New York: Plenum, 1980, pp. 609–622.

[7] D. Middleton, "New physical-statistical methods and models for clutter and reverberation: The KA-distribution and related probability structures," *IEEE J. Oceanic Eng.*, vol. 24, pp. 261–284, July 1999.

[8] E. Jakeman and P. N. Pusey, "A model for non-Rayleigh sea echo," *IEEE Trans. Antennas Propagat.*, vol. AP-24, pp. 806–814, Nov. 1976.

[9] E. Jakeman and R. J. A. Tough, "Non-Gaussian models for the statistics of scattered waves," *Adv. Phys.*, vol. 37, no. 5, pp. 471–529, 1988.

[10] K. D. Ward, "Compound representation of high resolution sea clutter," *Electron. Lett.*, vol. 17, no. 16, pp. 561–563, 1981.

[11] P. Z. Peebles, Jr., *Radar Principles*. New York: Wiley, 1998.

[12] H. Griffiths, J. Dunlop, and R. Voles, "Texture analysis of sidescan sonar imagery using statistical scattering models," in *High Frequency Acoustics in Shallow Water*, N. G. Pace, E. Pouliquen, O. Bergem, and A. P. Lyons, Eds. La Spezia, Italy: NATO SACLANT Undersea Research Centre, pp. 187–194.

[13] S. Dugelay, N. G. Pace, G. J. Heald, and R. J. Brothers, "Statistical analysis of high frequency acoustic scatter: What makes a statistical distribution?," in *Proc. Fifth Eur. Conf. Underwater Acoustics, ECUA'00*, Lyon, France, July 2000, pp. 269–274.

[14] M. Gu and D. A. Abraham, "Using McDaniel's model to represent non-Rayleigh reverberation," *IEEE J. Oceanic Eng.*, vol. 26, pp. 348–357, July 2001.

[15] H. L. Van Trees, *Detection, Estimation, and Modulation Theory: Part III*. New York: Wiley, 1971.

[16] A. Papoulis, *Probability, Random Variables, and Stochastic Processes*, 3rd ed. New York: McGraw-Hill, 1991.

[17] J. Spanier and K. B. Oldham, *An Atlas of Functions*. Washington, DC: Hemisphere, 1987.

[18] C. G. Fox and D. E. Hayes, "Quantitave methods for analyzing the roughness of the sea floor," *Rev. Geophys.*, vol. 23, pp. 1–48, 1985.

[19] A. L. Anderson, F. Abegg, J. A. Hawkins, M. E. Duncan, and A. P. Lyons, "Bubble populations and acoustic interaction with the gassy floor of Eckernfoerde Bay," *Continental Shelf Res.*, vol. 18, no. 14–15, pp. 1807–1838, 1998.

[20] J. Escartin, P. A. Cowie, R. C. Searle, S. Allerton, N. C. Mitchell, C. J. MacLeod, and P. Sloogweg, "Quantifying tectonic and magmatic strain at a slow-spreading ridge segment (mid-Atlantic ridge, 29 N)," *J. Geophys. Res.*, vol. 105, no. B5, pp. 10 421–10 427, 1999.

[21] N. C. Mitchell, M. A. Tivey, and P. Gente, "Sea-floor slopes at mid-ocean ridges from submersible observations and implications for interpreting geology from sea-floor topography," *Earth Planetary Sci. Lett.*, vol. 183, pp. 543–545, 2000.

[22] S. W. Anderson, E. R. Stofan, J. J. Plaut, and D. A. Crown, "Block size distributions on silicic lava flow surfaces: Implications for emplacement conditions," *Geol. Soc. Amer. Bull.*, vol. 110, no. 10, pp. 1258–1267, 1998.

[23] M. Golombek and D. Rapp, "Size-frequency distributions of rocks on mars and earth analog sites: Implications for future landed missions," *J. Geophys. Res.*, vol. 102, pp. 4117–4129, 1997.

[24] H. Medwin and C. S. Clay, *Fundamentals of Acoustical Oceanography*. Boston, MA: Academic, 1998.

[25] I. S. Gradshteyn and I. M. Ryzhik, *Table of Integrals, Series, and Products*, fifth ed, A. Jeffrey, Ed. San Diego, CA: Academic, 1994.

[26] M. Evans, N. Hastings, and B. Peacock, *Statistical Distributions*, 3rd ed. New York: Wiley, 2000.

[27] R. D. Lord, "The use of the Hankel transform in statistics I. General theory and examples," *Biometrika*, vol. 41, no. 1/2, pp. 44–55, 1954.

[28] D. M. Drumheller, "Padé approximations to matched filter amplitude probability functions," *IEEE Trans. Aerosp. Electron. Syst.*, vol. 35, pp. 1033–1045, July 1999.

[29] R. J. Urick, *Principles of Underwater Sound*. New York: McGraw-Hill, 1983.

[30] W. S. Burdic, *Underwater Acoustic System Analysis*. Englewood Cliffs, NJ: Prentice-Hall, 1984.

[31] K. D. Ward, "Compound representation of high resolution sea clutter," in *Proc. IEE Conf. Publ. 216 (Radar-82)*, 1982, pp. 203–207.

[32] C. W. Holland and J. Osler, "High-resolution geoacoustic inversion in shallow water: A joint time- and frequency-domain technique," *J. Acoust. Soc. Amer.*, vol. 107, no. 3, pp. 1263–1279, 2000.

[33] D. A. Abraham and C. W. Holland, "Statistical analysis of low-frequency active sonar reverberation in shallow water," in *Proc. 4th Eur. Conf. Underwater Acoustics*, Rome, Italy, Sept. 1998.

[34] D. A. Abraham and P. K. Willett, "Active sonar detection in shallow water using the Page test," *IEEE J. Oceanic Eng.*, vol. 27, pp. 35–46, Jan. 2002.

[35] M. Fisz, *Probability Theory and Mathematical Statistics*, 3rd ed. New York: Wiley, 1963.

[36] E. B. Manoukian, *Modern Concepts and Theorems of Mathematical Statistics.* New York: Springer Verlag, 1985.

[37] R. V. Hogg and A. T. Craig, *Introduction to Mathematical Statistics*, 4th ed. New York: Macmillan, 1978.

[38] J. V. DiFranco and W. L. Rubin, *Radar Detection.* Dedham, MA: Artech House, 1980.

[39] R. S. Raghavan, "A method for estimating parameters of K-distributed clutter," *IEEE Trans. Aerosp. Electron. Syst.*, vol. 27, pp. 238–246, Mar. 1991.

[40] I. R. Joughin, D. B. Percival, and D. P. Winebrenner, "Maximum likelihood estimation of K distribution parameters for SAR data," *IEEE Trans. Geosci. Remote Sensing*, vol. 31, pp. 989–999, Sept. 1993.

[41] L. Råde and B. Westergren, *Beta β Mathematics Handbook*, 2nd ed. Boca Raton, FL: CRC, 1990.

Douglas A. Abraham received the B.S., M.S., and Ph.D. degrees in electrical engineering, and the M.S. degree in statistics, all from the University of Connecticut, Storrs, in 1988, 1990, 1993, and 1994, respectively.

He is currently a Senior Research Associate with the Applied Research Laboratory, Pennsylvania State University. During 1989–1995, he was with the Naval Undersea Warfare Center, New London, CT. During 1995–1998, he was a Senior Scientist at the NATO SACLANT Undersea Research Centre, La Spezia, Italy. During 1998–2000, he held a Visiting Faculty Position at the University of Connecticut. His work is primarily in the area of statistical signal processing applied to underwater acoustic applications. His current interests are in representing and accounting for non-Rayleigh active sonar reverberation in signal processing algorithms for detection, classification and localization.

Anthony P. Lyons received the B.S. degree in physics from Henderson State University, Arkadelphia, AR, in 1988 and the M.S. and Ph.D. degrees in oceanography from Texas A&M University, College Station, in 1991 and 1995, respectively.

He worked as a Scientist at the SACLANT Undersea Research Center, La Spezia, Italy, from 1995 to 2000. where he was involved in a variety of projects in the area of environmental acoustics. He is currently a Senior Research Associate at the Applied Research Laboratory, Pennsylvania State University, State College, where he is engaged in studies of high-frequency shallow-water propagation, acoustic interaction with the sea floor, and high-resolution characterization of sea-floor sediments.

Dr. Lyons is a member of the Acoustical Society of America.

Reverberation Envelope Statistics and Their Dependence on Sonar Bandwidth and Scattering Patch Size

Douglas A. Abraham, *Member, IEEE,* and Anthony P. Lyons, *Member, IEEE*

Abstract—**Increasing transmit waveform bandwidth in an active sonar-system results in an increase in the signal-to-reverberation power ratio in reverberation-limited environments, but also changes the probability density function of the reverberation envelope. A recent model that relates a description of the sonar system and environment to the parameters of the K-distribution [1] predicts that the shape parameter (α) is proportional to range, beamwidth, and the density of scattering patches on the sea floor and is inversely proportional to bandwidth. In this paper, the bandwidth relationship is examined with real data from a low-frequency active sonar system with a towed array receiver. The inverse proportionality is observed at low bandwidths as a trend away from a Rayleigh-distributed envelope (decreasing α) as bandwidth increases. However, a trend back toward Rayleigh reverberation (increasing α) is observed as bandwidth continues to increase. Hypothesizing that the increase in α arises from overresolving scattering patches in range and not in angle, the model of [1] is extended to account for patch size relative to that of the sonar-resolution cell. The shape parameter of a moment-matched K-distribution derived from the extended model is then seen to provide a good fit to that estimated from the data.**

Index Terms—**Bandwidth, clutter, K-distribution, non-Rayleigh, reverberation, sonar.**

I. INTRODUCTION

IN order to combat increased reverberation power levels in shallow-water operational areas, active sonar systems are being designed with higher bandwidth transmit waveforms and larger receiving arrays. Both of these improvements have the effect of limiting the contribution of reverberation in each range-bearing resolution cell of the sonar by decreasing the cell size and thereby increasing the signal-to-reverberation power ratio [2], [3]. Unfortunately, this can also have the effect of changing the statistical distribution of the reverberation-induced matched filter envelope from the traditionally assumed Rayleigh probability density function (pdf) to one with heavier tails and, therefore, a higher probability of false alarm [1], [4], [5]. In order to appropriately simulate or predict the performance of an active sonar system in the presence of such non-Rayleigh reverberation, physics-based models are necessary that accurately reflect the changes in the reverberation envelope pdf as a function of sonar system and environmental parameters.

Of the few physics-based models (e.g., Rayleigh distribution, K-distribution [6], [7], Crowther's model [8], Middleton's KA-distribution [9], or McDaniel's model [10]) only the K-distribution allows for the analysis of the reverberation envelope pdf as a function of sonar system or environmental parameters [1]. It was proposed in [1] that reverberation be described as arising from a finite number of scattering patches that dominate the background, with each having a Gaussian distributed response and an exponentially distributed size. The resulting matched filter envelope was shown to be K-distributed despite the Gaussian response of each individual patch. A "patch" may consist of a rough rock outcrop, a buried river channel, a shell bed, or any small area on the sea floor with acoustic scattering properties that are substantially different from its surroundings [11]–[13].

In [1], the shape and scale parameters of the K-distribution were related to the number of patches within the sonar's range-bearing resolution cell and their average size. The shape parameter of the K-distribution (α), which describes how Rayleigh-like the reverberation envelope pdf is, was found to be equal to the number of patches in the sonar's range-bearing resolution cell and, therefore, proportional to the beamwidth of the sonar and inversely proportional to its bandwidth. An analysis [1] of data taken during the NATO SACLANT Undersea Research Centre's SCARAB 1997 sea trial illustrated the beamwidth relationship. In this paper, the bandwidth relationship is examined. As seen in Section II, the shape parameter of the K-distribution, as estimated from the SCARAB 1997 data, initially decreases as bandwidth increases, but then begins to increase, contrary to the expectation of the model in [1]. In Section III, it is hypothesized that this may arise from overresolving some of the patches in range, although not in angle. The model of [1] is then extended to account for the size of the patch relative to the sonar range-bearing resolution cell and is seen to exhibit a trend toward larger values of the shape parameter when bandwidth is increased beyond the point of overresolving the patches in range. In Section IV, the model is seen to provide a good fit to estimates of the shape parameter obtained from the SCARAB 1997 data as bandwidth increases.

II. BACKGROUND

The model developed in [1] describes reverberation as arising from a finite number of patches within each range-bearing resolution cell of the sonar that dominate the local background. The response of an individual patch is assumed to be Gaussian

Manuscript received November 1, 2002; revised August 13, 2003. This work was sponsored by the Office of Naval Research under Grants N00014-02-1-0115 and N00014-01-1-0352.

The authors are with the Applied Research Laboratory, Pennsylvania State University, State College, PA 16804 USA (e-mail: abrahad@psu.edu).

Digital Object Identifier 10.1109/JOE.2004.824039

distributed as a result of either interface scattering or scattering from a multitude of point scatterers; however, owing to its exponentially distributed size, the overall response has heavier tails than the Gaussian pdf (or the Rayleigh pdf when considering the matched filter envelope). The complex matched filter output for a single range-bearing resolution cell is described as

$$\tilde{Z} = \sum_{i=1}^{n} \sqrt{B_i}\tilde{Z}_i \tag{1}$$

where n is the number of patches and B_i is the area of the ith patch. The term $\tilde{Z}_i$ represents the Gaussian response of the ith patch and is zero-mean complex Gaussian distributed with variance σ^2, which is the backscattered power per unit area. Note that σ^2 may depend on both frequency and grazing angle [14]–[16]. Assuming that the patches have exponentially distributed sizes with mean $E[B_i] = \mu$, the resulting matched filter envelope $Y = |\tilde{Z}|$ is K-distributed with pdf

$$f_Y(y) = \frac{4}{\sqrt{\lambda}\Gamma(\alpha)} \left(\frac{y}{\sqrt{\lambda}}\right)^{\alpha} K_{\alpha-1}\left(\frac{2y}{\sqrt{\lambda}}\right) \tag{2}$$

where $K_\nu(\cdot)$ is the Basset function (i.e., a modified Bessel function of the third kind) [17] with order ν, λ is a scale parameter, α is the shape parameter, and the power is $E[Y^2] = \alpha\lambda$. As the shape parameter of the K-distribution increases, the envelope pdf tends toward the Rayleigh pdf, while smaller values of α are representative of severely non-Rayleigh reverberation.

In [1], the shape parameter of the K-distribution was related to the number of patches in the sonar's range-bearing resolution cell (n) according to

$$\alpha = n \tag{3}$$

and the scale parameter related to the average patch size through

$$\lambda = \mu\sigma^2. \tag{4}$$

Thus, a large number of patches in the sonar-resolution cell results in a large value of α and Rayleigh-like reverberation and a small number produces heavier-tailed reverberation. Assuming that the patches are located in a uniformly random manner on the ocean floor, the number of patches in a resolution cell should be proportional to the beamwidth of the sonar's receiving array and inversely proportional to the bandwidth. This leads to the expectation that increasing bandwidth will result in a proportionately smaller shape parameter of the K-distribution and, therefore, heavier tails and a higher probability of false alarm.

As a motivating example, estimates of the K-distribution shape parameter from one full ping of data are shown as bandwidth is varied in the form of histograms in Fig. 1. The data are from the SCARAB 1997 sea trial [18], which was organized and led by Dr. C. Holland and sponsored by the NATO SACLANT Undersea Research Centre, La Spezia, Italy. The details of the experiment and data analysis are given in Section IV. For each bandwidth, a histogram is formed from all of the shape parameter estimates obtained from a single ping. A decreasing trend in the shape parameter estimates is clearly observed as bandwidth is increased from 0.5 Hz to approximately 8 Hz, beyond which the trend is toward higher values. Thus, as bandwidth increases, the data appear to become more non-Rayleigh at first but then tend back toward the Rayleigh distribution, contradicting the expectation that they continue to become more non-Rayleigh.

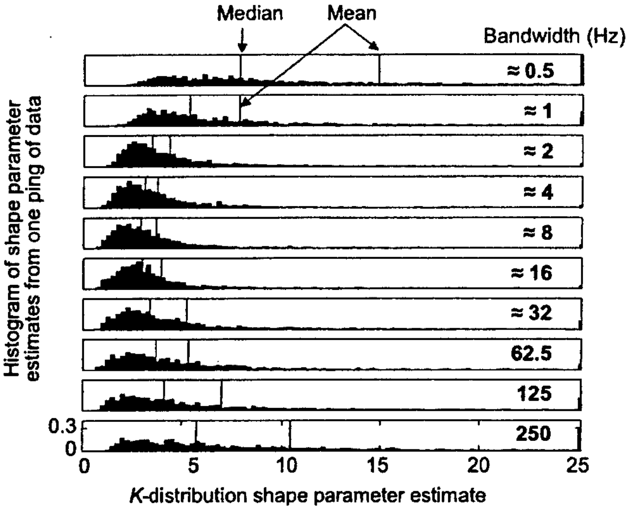

Fig. 1. Histograms of the estimates of the K-distribution shape parameter from a single ping for various bandwidths. The expected trend toward lower values of α as bandwidth increases is evident at the lower bandwidths, but does not persist as bandwidth continues to increase.

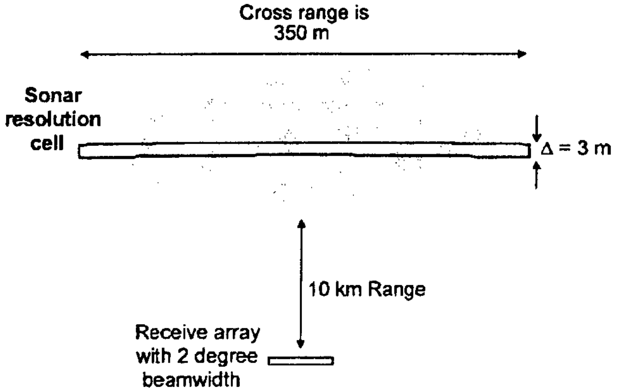

Fig. 2. Typical sonar-resolution cell illustrating asymmetry between down- and cross-range extents.

The relationships of (3) and (4), which lead to the expectation that reverberation continues to become more non-Rayleigh as the sonar-resolution cell size is reduced (e.g., by increasing bandwidth), were derived under the assumption that all of the patches are always fully within the sonar's range-bearing resolution cell. In this paper, these relationships will be referred to as the unresolved patch model. Sonar systems using high-bandwidth transmit waveforms or large aperture arrays (e.g., as obtained through synthetic aperture sonar processing) may violate this assumption, so the model of [1] could break down when the resolution cell is on the order of the average patch size. It is hypothesized that the "bandwidth effect" (illustrated in Fig. 1) of a trend away from Rayleigh reverberation followed by a reversal back toward Rayleigh reverberation with increasing bandwidth is the result of overresolving scattering patches. Owing to the asymmetry between the down- and cross-range extents of the sonar range-bearing resolution cell for a towed array receiver, as illustrated in Fig. 2, the patches are more likely to be overresolved in range than in angle. For example, a sonar system

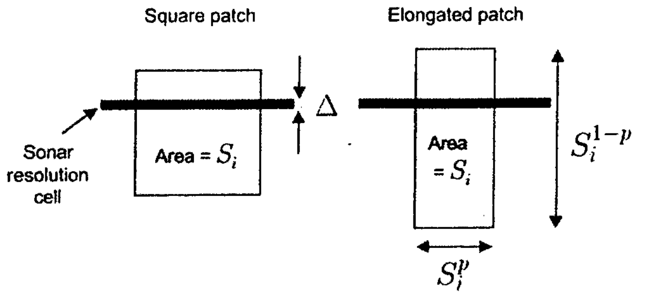

Fig. 3. Square and elongated patches and sonar-resolution cell small enough to overresolve the patches.

with an array receiver with a two-degree beamwidth (similar to the towed array used in the SCARAB sea trial at broadside) and a 250-Hz bandwidth transmit waveform will have a 3-m down-range extent and a 350-m cross range at 10 km. In the following sections, the model of [1] is first extended to account for patch size and is then compared to estimates of the shape parameter obtained as a function of bandwidth from the SCARAB 1997 data.

III. MODELING—ACCOUNTING FOR PATCH SIZE

Accounting for the size of the patch with respect to the sonar-resolution cell in (1) will affect the contribution B_i by limiting it when the patch is larger than the resolution cell. Additionally, the number of patches in the sonar's resolution cell depends on the average patch size, although only significantly so when the patches are not fully within the resolution cell. When the sonar-resolution cell begins to overresolve the patches, the number of patches may not decrease proportionately with the resolution cell size; that is, n and, therefore, α may no longer be inversely proportional to bandwidth W. In this section, both of these mechanisms are considered and seen to contribute to the "bandwidth" effect.

In order to evaluate the effect of patch size on the reverberation envelope statistics, we must assume a shape for the patches. First, consider a square patch, as depicted in Fig. 3, with size (area) S_i, which is exponentially distributed with mean μ and pdf

$$f_S(s) = \frac{1}{\mu} e^{-\frac{s}{\mu}} \quad \text{for} \quad s \geq 0. \tag{5}$$

Let the down-range extent of the range-bearing resolution cell be Δ, defined in meters. If c is the speed of sound in meters per second, then

$$\Delta \approx \frac{c}{2W} \tag{6}$$

where W is the bandwidth of the transmit waveform in Hertz.

When the down-range extent of the sonar-resolution cell is smaller than a patch, the effective area of the patch in the resolution cell is reduced. For the square patch, the effective area becomes $B_i = \Delta\sqrt{S_i}$ when it is overresolved and remains $B_i = S_i$ when it is not overresolved or, equivalently,

$$B_i = \sqrt{S_i} \min\{\Delta, \sqrt{S_i}\}. \tag{7}$$

The manner in which the patch area is limited can play a significant role in determining the statistics of the reverberation envelope. Suppose that the patch has shape and orientation with respect to the sonar-resolution cell such that it is elongated, as illustrated in Fig. 3, and therefore suffers significant reduction when overresolved. This may be approximated by generalizing (7) to

$$B_i = S_i^p \min\left\{\Delta, S_i^{1-p}\right\} \tag{8}$$

where $p = 0.5$ represents the square patch and $0 < p < 0.5$ represent patches that have been elongated in range. Elongation in range may arise as a result of the orientation of nonisotropic patches (e.g., megaripples, exposed ridges, or buried river channels) or by acoustic propagation through a shallow-water environment where the response of a patch is spread over several multipath arrivals making its down-range extent seem larger than the actual size. The generalized form of (8) affords control over the rapidity with which the effect of the random size of a patch is limited when it is overresolved in range with a smaller value of p, resulting in a very rapid limitation. Such a model may provide an adequate approximation to the response of different patch shapes and orientations.

In the following sections, the effect on the reverberation envelope statistics that arises from accounting for patch size in the number of patches and the contribution of each patch is evaluated using the generalized patch shape model, represented by (8), where the down-range extent of the patch is assumed to be S_i^{1-p} when the patch has area S_i.

A. Average Number of Patches

Suppose that m patches are placed in a large area in a uniformly random fashion. We wish to determine the average number of patches that contribute to a particular range-bearing resolution cell of length Δ under the assumption that it is not possible to overresolve the patches in bearing (i.e., the beamwidth of the sonar is such that the cross-range extent of the resolution cell is large compared with the average patch size). The problem then simplifies to one dimension (range) with the patches falling uniformly in the large interval, within which the sonar-resolution cell occupies a small part. Without a loss of generality, let the sonar-resolution cell (length Δ) and the large interval (length a) be centered at the origin. Thus, the resolution cell covers the interval $(-(\Delta/2), \Delta/2)$ and resides in the larger interval $(-(a/2), a/2)$.

Suppose that the ith patch is centered at X_i and has down-range extent S_i^{1-p}, as shown in Fig. 4. The actual number of patches that contribute to the range-bearing resolution cell is a binomial (m, ν) random variable where ν is the probability that there is an intersection between the patch and the sonar-resolution cell. As expected, this results in the Poisson distribution as $m \to \infty$ so long as the product $m\nu$ tends to a constant greater than zero as $m \to \infty$. The quantity in which we are interested is the average number of patches in any given cell, $m\nu$, as a function of the cell size Δ and the average patch size μ. The

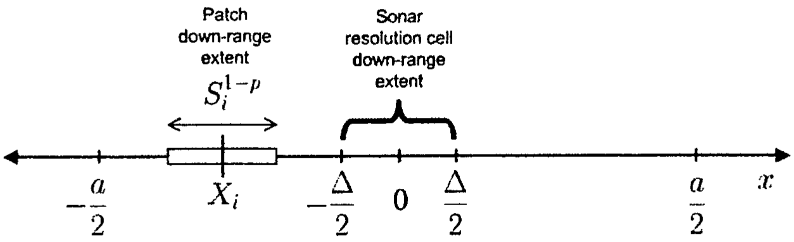

Fig. 4. Down-range extent of the ith patch relative to sonar-resolution cell $(-(\Delta/2), \Delta/2)$ and large interval containing all patches $(-(a/2), a/2)$.

probability of a patch contributing to the sonar-resolution cell may be described as

$$\begin{aligned}\nu = &\Pr\left\{ X_i - \frac{S_i^{1-p}}{2} < \frac{\Delta}{2} \middle| X_i > \frac{\Delta}{2} \right\} \\ &+ \Pr\left\{ X_i + \frac{S_i^{1-p}}{2} > -\frac{\Delta}{2} \middle| X_i < -\frac{\Delta}{2} \right\} \\ &+ \Pr\left\{ |X_i| < \frac{\Delta}{2} \right\}. \end{aligned} \tag{9}$$

With X_i being uniformly distributed on $(-(a/2), a/2)$, the third term is easily seen to be

$$\Pr\left\{ |X_i| < \frac{\Delta}{2} \right\} = \frac{\Delta}{a}. \tag{10}$$

Owing to symmetry, the first two terms of (9) are equal. Therefore, we focus on the first term and define the event A^+ as the occurrence of $\{X_i > (\Delta/2)\}$ and note that X_i given A^+ is uniformly distributed on $(\Delta/2, a/2)$. Recalling that S_i is exponentially distributed with mean μ and conditioning on both X_i and A^+

$$\begin{aligned}&\Pr\left\{ X_i - \frac{S_i^{1-p}}{2} < \frac{\Delta}{2} \middle| X_i, A^+ \right\} \\ &= \Pr\left\{ S_i > \left[2\left(X_i - \frac{\Delta}{2} \right) \right]^{\frac{1}{q}} \middle| X_i, A^+ \right\} \\ &= e^{-\frac{1}{\mu}\left[2\left(X_i - \frac{\Delta}{2}\right)\right]^{\frac{1}{q}}} \end{aligned} \tag{11}$$

where $q = 1 - p$.

The conditioning over X_i is removed by taking the expectation over $X_i | A^+$

$$\begin{aligned}&\Pr\left\{ X_i - \frac{S_i^{1-p}}{2} < \frac{\Delta}{2} \middle| A^+ \right\} \\ &= \frac{2}{(a-\Delta)} \int_{\frac{\Delta}{2}}^{\frac{a}{2}} e^{-\frac{1}{\mu}\left[2\left(x - \frac{\Delta}{2}\right)\right]^{\frac{1}{q}}} dx \\ &= \frac{q\mu^q}{(a-\Delta)} \int_0^{y_1} y^{q-1} e^{-y} dy \\ &= \frac{q\mu^q}{(a-\Delta)} \gamma(q, y_1) \end{aligned} \tag{12}$$

where $y_1 = ((a-\Delta)^{1/q})/\mu$, the pdf of $X_i | A^+$, is $2/(a-\Delta)$ for $x \in (\Delta/2, a/2)$ and $\gamma(q, y)$ is the incomplete gamma function [19] of order q and argument y.

Defining $\rho = \Delta/a$ and assuming that ρ is small (e.g., by letting $a \to \infty$ to remove the edge effects of the large field of patches), the probability of a patch contributing to the sonar-resolution cell is seen to be

$$\begin{aligned}\nu &= \frac{\Delta}{a} + 2\frac{q\mu^q}{(a-\Delta)}\gamma(q, y_1) \\ &= \rho + 2\frac{q\mu^q \rho}{\Delta(1-\rho)}\gamma(q, y_1) \\ &\approx \rho\left(1 + \frac{2q\Gamma(q)\mu^q}{\Delta}\right) \\ &= \rho\left(1 + \frac{2}{\delta}\right) \end{aligned} \tag{13}$$

where the limit $\gamma(q, y_1) \to \Gamma(q)$ as $a \to \infty$ has been used and

$$\delta = \frac{\Delta}{\mu^q \Gamma(q+1)} \tag{14}$$

is the ratio of the range-resolution cell size to the average patch down-range extent $(E[S_i^q] = \mu^q \Gamma(q+1))$.

The average number of patches may then be evaluated by inserting (13) into $n = m\nu$, yielding

$$\begin{aligned}n &= m\rho\left(1 + \frac{2}{\delta}\right) \\ &= \beta\Delta\left(1 + \frac{2}{\delta}\right) \end{aligned} \tag{15}$$

$$= \mu^q \Gamma(q+1)\beta\delta\left(1 + \frac{2}{\delta}\right) \tag{16}$$

where $\beta = m/a$ is the rate of occurrence of the patches (in this case, the number of patches per meter down range). Examining (15), it is seen that when δ is large, the average number of patches is directly proportional to the size of the range-bearing resolution cell and the size and density of the patches. However, as δ decreases, the dependence of n on the sonar-resolution cell size diminishes, which is seen in Fig. 5 where n normalized by $\beta\mu^q\Gamma(q+1)$ is plotted against δ^{-1} (which is proportional to bandwidth) for the elongated patch and also for the unresolved patch model. Under the latter model, the number of patches continues to decrease with δ.

Thus, accounting for the size of the patches in the average number of patches in a resolution cell cannot alone account for the observed increase in the shape parameter that is observed in the data as bandwidth increases. In the following section, it is seen that this occurs as a result of limiting the contribution of each individual patch when it becomes overresolved in range.

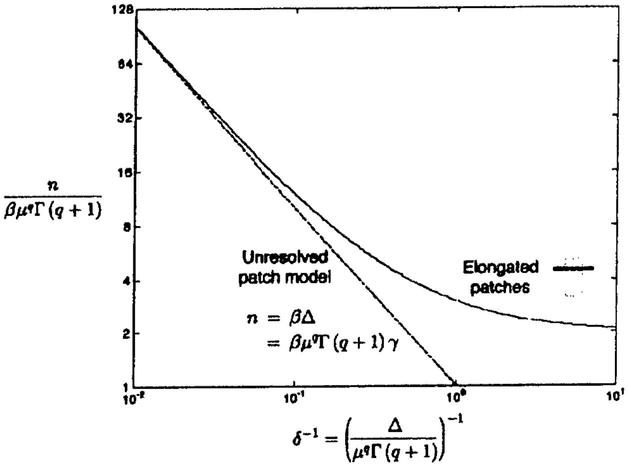

Fig. 5. Average number of patches in a resolution cell normalized by patch density (β) and average down-range extent ($\mu^q\Gamma(q+1)$) as a function of δ^{-1}, which is proportional to bandwidth.

B. Individual Patch Contribution

When a patch is larger than the sonar-resolution cell, its contribution will be spread across several resolution cells. This may be accounted for in the complex matched filter output of (1) by replacing B_i with the appropriately limited patch contribution, as in (8). If the resolution cell is very large as compared with the patches ($\Delta \gg \mu^q\Gamma(q+1) = E[S_i^q]$), then $B_i = S_i$, approximately, which leads to a K-distributed matched filter envelope following [1]. However, when Δ is on par with μ, the matched filter envelope is not necessarily K-distributed. The derivation of the envelope pdf for the case of (8) is not straightforward analytically, although it may be possible numerically by using Hankel transforms [20]. Thus, we are forced to consider alternative means of evaluating the shape and tail behavior of the envelope pdf. To facilitate a comparison with real data, where the shape parameter of the K-distribution is used to describe how far the reverberation envelope pdf is from the Rayleigh distribution, higher order moments are used to obtain the shape and scale parameters of a K-distribution with identical moments. This may be further justified by the fact that the envelope pdf tends to the K-distribution as Δ becomes large with respect to μ^q (e.g., $\delta = (\Delta/(\mu^q\Gamma(q+1))) \to \infty$).

The odd moments of the matched filter envelope (i.e., $E[|\tilde{Z}|^i]$ when $i = 1, 3, 5, \ldots$) are quite difficult to obtain in terms of the moments of the patch sizes. Fortunately, the even moments are tractable. Owing to the independence of the patch contributions, the second moment is easily seen to be

$$m_2 = E\left[|\tilde{Z}|^2\right] = n\sigma^2 E[B] \tag{17}$$

where B represents the contribution of an individual patch and has pdf $f_B(b)$. Obtaining the fourth moment requires more effort. Expanding $|\tilde{Z}|^4$ into the product $\tilde{Z}\tilde{Z}^*\tilde{Z}\tilde{Z}^*$ and then extracting the four summations results in

$$\begin{aligned} m_4 &= E\left[|\tilde{Z}|^4\right] \\ &= \sum_{i,k,l,m=1}^{n} E[\sqrt{B_i B_k B_l B_m}]E\left[\tilde{Z}_i\tilde{Z}_k^*\tilde{Z}_l\tilde{Z}_m^*\right] \end{aligned} \tag{18}$$

where the expectations involving the patch sizes and their complex Gaussian responses are separable because they are independent. Assuming that $\tilde{Z}_i$ and $\tilde{Z}_k$ are independent if $i \neq k$, that $E[\tilde{Z}_i] = 0$ and that $E[\tilde{Z}_i^2] = 0$ (which arises from the complex Gaussian nature of $\tilde{Z}_i$ and requires the real and imaginary parts of $\tilde{Z}_i$ to be independent, zero mean, and have equal variance [21]), then the latter expectation over the $\tilde{Z}_i$ terms will be zero except when

- $i = k = l = m$, which happens n times;
- $i = k$ and $l = m$ but $i \neq l$, which happens $n(n-1)$ times;
- $i = m$ and $l = k$ but $i \neq l$, which happens $n(n-1)$ times.

Noting that $E[|\tilde{Z}_i|^2] = \sigma^2$ and $E[|\tilde{Z}_i|^4] = 2\sigma^4$ and exploiting the fact that the aforementioned occurrences are mutually exclusive, (18) may be simplified to

$$\begin{aligned} m_4 &= nE[B^2]E\left[|\tilde{Z}|^4\right] \\ &\quad + 2n(n-1)E[B]^2E\left[|\tilde{Z}|^2\right]^2 \\ &= 2n\sigma^4E[B^2] + 2n(n-1)\sigma^4E[B]^2 \end{aligned} \tag{19}$$

which describes the fourth moment of the matched filter envelope in terms of the first and second moments of the contribution of an individual patch. To illustrate the use of (17) and (19), suppose that the patches have exponentially distributed sizes with mean μ (i.e., the patches are not overresolved)

$$f_B(b) = \frac{1}{\mu}e^{-\frac{b}{\mu}} \tag{20}$$

which is known to result in a K-distributed matched filter envelope. The first and second moments of B are simply μ and $2\mu^2$, respectively, which, when inserted into (17), results in

$$\begin{aligned} m_2 &= n\,\mu\sigma^2 \\ &= \alpha\lambda \end{aligned} \tag{21}$$

where $\alpha = n$ and $\lambda = \mu\sigma^2$ are the shape and scale parameters of the K-distribution as related to the number of patches and their average size from [1]. The fourth moment is seen to be

$$\begin{aligned} m_4 &= 4n\sigma^4\mu^2 + 2n(n-1)\sigma^4\mu^2 \\ &= 2\alpha(\alpha+1)\lambda^2 \end{aligned} \tag{22}$$

which is easily verified using the product formulation of the K-distribution.

The shape and scale parameters of the moment-matched K-distribution are the values of α and λ that satisfy (21) and (22). They are obtained by inverting (21) and (22) to obtain these equivalent parameters (call them $\tilde{\alpha}$ and $\tilde{\lambda}$) in terms of the second and fourth moments of the matched filter envelope

$$\tilde{\alpha} = \frac{2m_2^2}{m_4 - 2m_2^2} \tag{23}$$

and

$$\tilde{\lambda} = m_2 \left(\frac{m_4}{2m_2^2} - 1 \right). \tag{24}$$

Substituting (17) and (19) into the above two equations then provides $\tilde{\alpha}$ and $\tilde{\lambda}$ in terms of the moments of the contribution of an individual patch

$$\tilde{\alpha} = n \left(\frac{E[B]^2}{E[B^2] - E[B]^2} \right) \tag{25}$$

and

$$\tilde{\lambda} = \sigma^2 E[B] \left(\frac{E[B^2] - E[B]^2}{E[B]^2} \right). \tag{26}$$

The similarity of the matched filter envelope to a Rayleigh pdf may then be evaluated by inserting $E[B]$ and $E[B^2]$ along with n from (16) into (25). When $\tilde{\alpha}$ is large, the envelope pdf is near Rayleigh and when it is small, the pdf can have significantly heavier tails than the Rayleigh pdf.

Eq. (25) also illustrates that even if the individual patches do not have exponentially distributed sizes (as is assumed in [1]), the shape parameter of the moment-matched K-distribution is proportional to the number of patches in the sonar-resolution cell, which is in turn proportional to beamwidth and range and inversely proportional to bandwidth as long as the patches are not overresolved. This result is significant in that changes in the shape parameter may be predicted as a function of changes in the sonar-resolution cell size irrespective of the validity of the exponentially sized patch assumption, as long as the patches are not overresolved. When the patches become overresolved, the patch contribution B will change with bandwidth and affect $\tilde{\alpha}$, as described in the following paragraphs.

1) Elongated Patches: Using (8), $B = S^p \min\{\Delta, S^q\}$, it is necessary to obtain the first two moments of the limited patch contribution, where the patch area S is exponentially distributed with mean μ. Noting that $Y = S/\mu$ is exponentially distributed with unit mean, the average limited contribution is

$$\begin{aligned} E[B] &= E\left[S^p \min\{\Delta, S^q\}\right] \\ &= \mu E\left[Y^p \min\left\{\frac{\Delta}{\mu^q}, Y^q\right\}\right] \\ &= \mu \int_0^\infty y^p \min\{d_q, y\}^q e^{-y} dy \\ &= \mu \int_0^{d_q} y e^{-y} dy + \mu d_q^q \int_{d_q}^\infty y^p e^{-y} dy \\ &= \mu \{\gamma(2, d_q) + \delta \Gamma(q+1) \Gamma(p+1, d_q)\} \end{aligned} \tag{27}$$

where

$$d_q = \left(\frac{\Delta}{\mu^q} \right)^{\frac{1}{q}} = [\Gamma(q+1)\delta]^{\frac{1}{q}} \tag{28}$$

and $\Gamma(\nu, x) = \Gamma(\nu) - \gamma(\nu, x)$ is the complementary incomplete gamma function of order ν and argument x [19]. The second moment of B may be similarly found as a function of the incomplete gamma functions

$$\begin{aligned} E[B^2] &= E\left[S^{2p} \min\{\Delta, S^q\}^2\right] \\ &= \mu^2 E\left[Y^{2p} \min\left\{\frac{\Delta}{\mu^q}, Y^q\right\}^2\right] \\ &= \mu^2 \int_0^\infty y^{2p} \min\{d_q, y\}^{2q} e^{-y} dy \\ &= \mu^2 \int_0^{d_q} y^2 e^{-y} dy + \mu^2 d_q^{2q} \int_{d_q}^\infty y^{2p} e^{-y} dy \\ &= \mu^2 \left\{\gamma(3, d_q) + \delta^2 [\Gamma(q+1)]^2 \Gamma(2p+1, d_q)\right\}. \end{aligned} \tag{29}$$

Insertion of (27) and (29) into (25) and (26) then yields the equivalent shape and scale parameters in terms of δ, the ratio of the sonar down-range resolution to the average down-range extent of a patch

$$\tilde{\alpha} = n \left\{ \frac{\gamma(3, d_q) + \delta^2 [\Gamma(q+1)]^2 \Gamma(2p+1, d_q)}{[\gamma(2, d_q) + \delta \Gamma(q+1) \Gamma(p+1, d_q)]^2} - 1 \right\}^{-1} \tag{30}$$

and

$$\begin{aligned} \tilde{\lambda} &= \mu\sigma^2 \{\gamma(2, d_q) + \delta \Gamma(q+1) \Gamma(p+1, d_q)\} \\ &\times \left\{ \frac{\gamma(3, d_q) + \delta^2 [\Gamma(q+1)]^2 \Gamma(2p+1, d_q)}{[\gamma(2, d_q) + \delta \Gamma(q+1) \Gamma(p+1, d_q)]^2} - 1 \right\}. \end{aligned} \tag{31}$$

As $\delta \to \infty$, the terms within the braces of (30) and (31) go to one and, thus, $\tilde{\alpha} \to n = \alpha$ and $\tilde{\lambda} \to \mu\sigma^2 = \lambda$, the values expected for the K-distribution as derived in [1]. This corresponds to the case in which the range-resolution cell size becomes large as compared with the average patch size (i.e., the patches are fully within the sonar-resolution cell).

When the down-range extent of the sonar-resolution cell becomes extremely small (i.e., $\delta \to 0$), the shape parameter of the equivalent K-distribution (30), after normalization by n, tends to a finite (for $p > 0$) constant greater than one (for $p < 1$)

$$\lim_{\delta \to 0} \frac{\tilde{\alpha}}{n} \to \frac{\Gamma^2(p+1)}{\Gamma(2p+1) - \Gamma^2(p+1)} > 1 \tag{32}$$

indicating that the return toward the Rayleigh distribution is limited at some finite value of $\tilde{\alpha}$ (a Rayleigh distributed envelope would require $\tilde{\alpha} \to \infty$). This implies that increasing bandwidth eventually results in no change in the envelope pdf, a result that may affect the maximum bandwidth at which a sonar system should be operated in terms of its detection and false alarm performance.

The shape parameter of the moment-matched K-distribution of (30), after being normalized by n, is shown in Fig. 6 as a function of δ^{-1}, which is proportional to bandwidth. When δ is large (the left side of the figure where δ^{-1} is small), it is clear that $\tilde{\alpha} = n$, which is expected because all of the patches lie within the sonar-resolution cell. However, as δ decreases (i.e., bandwidth increases), the patches begin to be overresolved in range and it is seen that $\tilde{\alpha}$ becomes greater than n, implying

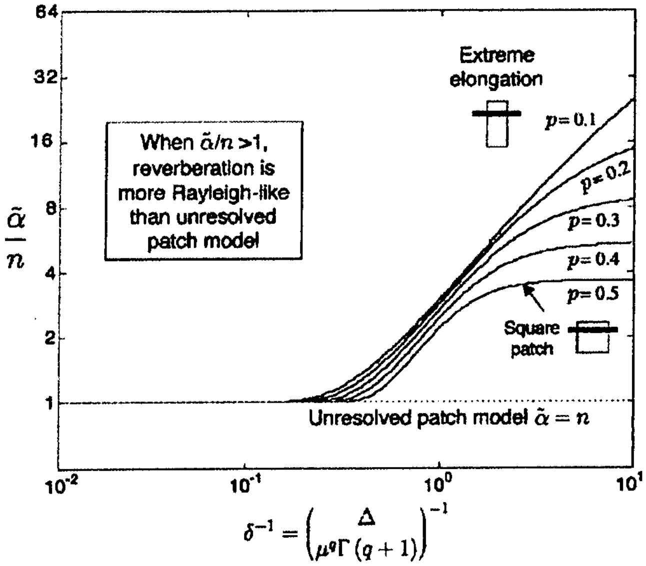

Fig. 6. Shape parameter of the equivalent K-distribution normalized by n as a function of δ^{-1}, which is proportional to bandwidth. When δ is small (large δ^{-1}), the shape parameter is greater than n, indicating that the envelope pdf has lighter tails than would be expected for unresolved patches.

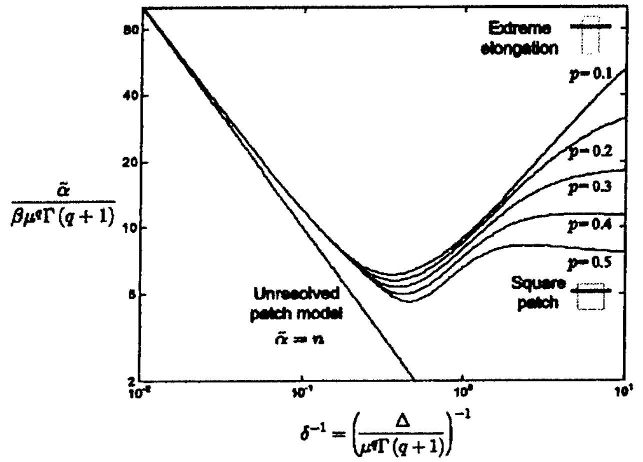

Fig. 7. Shape parameter of the equivalent K-distribution normalized by $\beta\mu^q\Gamma(q+1)$ as a function of δ^{-1}, which is proportional to bandwidth. The bandwidth effect observed in real data of a decrease and then an increase in the shape parameter as bandwidth increases is evident in the model.

that the tails of the envelope pdf are lighter than would be expected for unresolved patches. Thus, the bandwidth effect noted in Fig. 1 may arise from overresolution of patches in range. It is also interesting to note that, irrespective of p, once $\tilde{\alpha}/n$ begins to rise above one, it does so at a constant rate that is nearly proportional to δ^{-1}.

C. Combined Effect on the K-Distribution Shape Parameter

The results of (16) and (30) (i.e., Figs. 5 and 6) are combined and illustrated in Fig. 7, where it is seen that the shape parameter of the moment-matched K-distribution will first decrease inversely proportional to bandwidth while the patches are all within a resolution cell, then increase when they begin to be overresolved in range and finally (although not necessarily monotonically) level off at some finite value. In the large δ region (small δ^{-1}), the shape of the patches is clearly not very important, as they are all within the resolution cell. However, as δ becomes smaller (e.g., $\delta < 0.5$), the shape of the patches begins to play a more important role, as can be seen by the spread of the curves in the right side of Fig. 7. Thus, the exact shape and position of the curve when δ is small will be difficult to predict; however, a trend back toward Rayleigh reverberation is clearly identified for the elongated patch model once the patches begin to be overresolved. This trend, however, does not continue monotonically to Rayleigh reverberation, as described in the previous section. It is interesting to note that the point at which $\tilde{\alpha}$ stops increasing depends on the elongation of the patch with it occurring at higher bandwidths for more extreme elongation. This effect most likely arises from the increased proximity of the envelope pdf to the Rayleigh distribution that occurs when the patches are more elongated [as evidenced by (32), which increases to ∞ as p decreases to zero].

D. Generalization of the Current Model

The model developed in this section may be improved in several areas. First, the assumption that the patches dominate the background may be relaxed to include an additive Gaussian term reflecting a lower level background, as in [13]. The assumption that there is only one size scale of patches may be generalized to include multiple scales or a continuum of scales, although the latter case may present some difficulties in the derivation of the pdf or even moments of the matched filter envelope. The bandwidth limitations of typical sonar systems may make the continuum description unnecessary, although accounting for multiple scales is sensible and should be mathematically tractable.

A further limitation of the current modeling lies in the lack of a strict incorporation of the frequency-dependent effects of the sonar system and scattering. The source and receive arrays will induce frequency dependencies both spectrally (varying power level with frequency) and spatially (varying beamwidths with frequency). As previously mentioned, the backscattered strength per unit area (σ^2) will have frequency and grazing-angle dependence. A generalization of the summation in (1) through a decomposition into K frequencies results in

$$\tilde{Z} = \sum_{i=1}^{n}\sum_{k=1}^{K}\sqrt{B_{i,k}}\tilde{Z}_{i,k} \tag{33}$$

where the contribution of the ith patch is now $B_{i,k}$ with a Gaussian component $\tilde{Z}_{i,k}$ with power σ_k^2, making the spatial and spectral dependence explicit. Assuming that there is no spatial dependence (i.e., that the patches are equally within the beam at all frequencies) implies $B_{i,k} = B_i$, which results in

$$\tilde{Z} = \sum_{i=1}^{n}\sqrt{B_i}\sum_{k=1}^{K}\tilde{Z}_{i,k} = \sum_{i=1}^{n}\sqrt{B_i}\tilde{Z}_i \tag{34}$$

which is identical to (1) where the power of $\tilde{Z}_i$ is simply the combined power over the individual frequencies $\sigma^2 = \sum_{k=1}^{K}\sigma_k^2$.

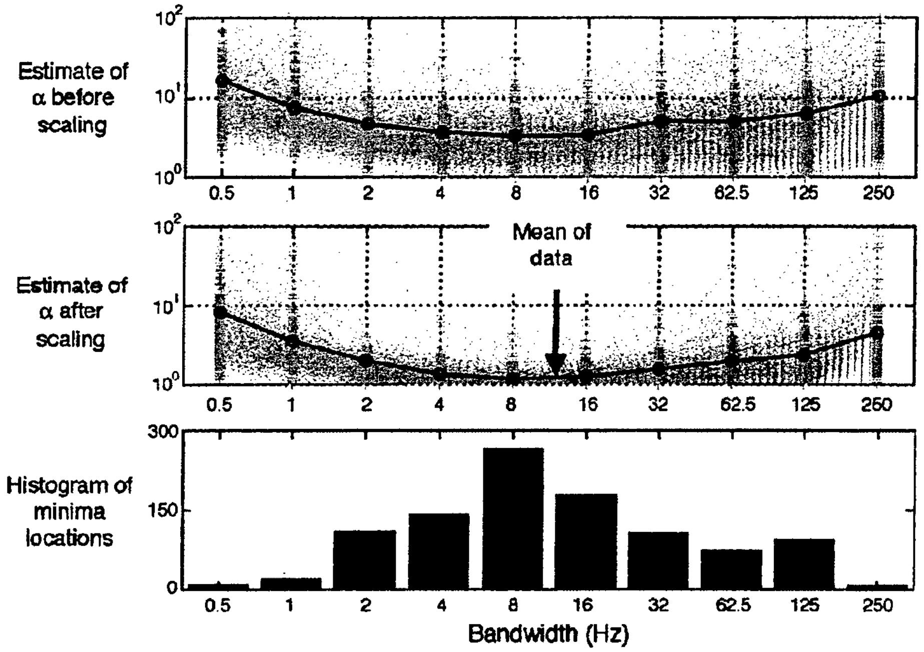

Fig. 8. (Top) Estimates of the shape parameter from one ping of data prior to scaling by the minimum value over bandwidth. (Middle) Estimates of the shape parameter from one ping of data after scaling by the minimum value (in each analysis window) over bandwidth. (Bottom) Histogram of the minima locations.

IV. REAL DATA ANALYSIS

The motivating example of Section II illustrated an unexpected trend of the K-distribution shape parameter increasing at higher bandwidths. The previous section hypothesizes that this may occur as a result of overresolving patches in range. In this section, more data from the SCARAB 1997 sea trial are examined and compared to the model developed in Section III in terms of the K-distribution shape parameter. The sea trial was performed by the NATO SACLANT Undersea Research Centre and led by Dr. C. Holland. The data to be analyzed are from 49 pings of a 2-s linear frequency modulated (LFM) waveform spanning 450–700 Hz, transmitted by the towed vertically directive source (TVDS) and received by the Centre's low-frequency towed hydrophone array comprising 128 elements spaced every half meter. The data are beamformed, matched filtered, and normalized prior to statistical analysis.

Further details related to the sea trial and data acquisition may be found in [1], [18]. Of particular relevance is the result that 97.4% of the data were considered well fit by the K-distribution based on a Kolmogorov–Smirnov test at a $p = 0.05$ confidence level [1]. This result implies that the shape parameter of the K-distribution is an accurate descriptor of the reverberation envelope pdf. Additionally, owing to the downward refracting sound velocity profiles measured during the cruise, the reverberation data are expected to be dominated by bottom scattering. Although some of the data are dominated by local shipping (certain beams at later times in the ping cycles) or may be dominated by volume scattering, these results are overwhelmed by the majority of beam-time processing windows that are dominated by bottom scattering.

A. Bandwidth Analysis

Evaluation of the pdf of the reverberation envelope as a function of bandwidth from real data requires careful processing of the data. The following describes the technique developed to estimate the shape parameter of the K-distribution from reverberation data arising from a broad-band transmission. Essentially, the data are band-pass filtered into subbands, which are then used to estimate the shape parameter. The steps of the process are described below, along with the results of processing the SCARAB data.

The input data are assumed to be beamformed but not basebanded or matched filtered. Only data acquired after the active sonar transmission and before the transition from a reverberation-limited to an ambient-noise-limited condition are processed. In the SCARAB data, this resulted in processing data from about 3.25 to 10 km in range.

1) **Baseband**—Form the complex envelope of the reverberation data by frequency shifting by the center frequency followed by low-pass filtering.
2) **Decimate**—The complex basebanded data should be decimated so that the sampling frequency is equal to the bandwidth. It is possible to use data that are oversampled; however, the procedure is not described herein.
3) **Match filter and normalize**—Match filter the data and apply a mean-power level normalizer [e.g., a cell-averaging constant false alarm rate (CA-CFAR) normalizer [22]] to the complex envelope. Choose the normalizer window size small enough to capture the variation in the power level. The result should be a complex sequence with nearly unit power. A split-window CA-CFAR normalizer was used with leading and lagging windows 0.4 s

(100 samples for a 250-Hz bandwidth) wide and a gap of 20 ms (5 samples) around the test sample.

4) **Filter data into bands**—Filter the normalized matched filter complex envelope data into m bands using an m-point discrete Fourier transform (DFT). This results in a filter-bank of m subbands, each with bandwidth W/m.
5) **Normalize sub-band data**—Apply a normalizer (e.g., CA-CFAR) to each subband. This is required because the reverberation may have a varying spectral level with frequency (e.g., as may be induced by the source transducer or propagation). When filtering into many subbands (large m), there may not be many samples in the beam data for the normalizer, which forces the use of a small window. A window 100 samples long was used except when there were not enough samples, in which case a window using 80% of the available samples was used. When there is not full overlap between the normalizer window and the data (i.e., at the beginning and end of the time sequence), the estimate of the power from the nearest full window is used. When extremely low bandwidths (or very short data sequences) lead to small normalizer windows, the resulting poor power estimate can increase the variability of the envelope data, which will seem like a departure toward heavier tailed data. This was observed when a short segment of ambient noise was processed and seen to be small compared with the trends observed in the reverberation-limited data.
6) **Estimate the shape parameter**—Take the absolute value of the normalized subband data and estimate the shape parameter using data from all of the frequency bands over short windows in range. This is easily accomplished by reordering the matrix of subband data into a single sequence and using overlapping windows of the same size for all bandwidths. The method of moments estimator, as described in [1], [23] and [24], was used with a window 2 s (500 samples) long. By sharing data across all bands, the shape parameter estimate always uses 500 samples and the same initial data (i.e., the same range window) to form the estimates for all bandwidths.
7) **Normalize by minimum shape parameter estimate**—The shape parameter estimate is expected to vary as a result of environmental variability (e.g., when the bottom-scattering properties change) and because the size of the sonar-resolution cell increases with range and beamwidth, both of which vary over the ping. This variability is illustrated in the topmost graph of Fig. 8, where all of the shape parameter estimates from one ping of data are shown as a function of bandwidth. In order to remove this variability, the estimates from each analysis window are normalized by the minimum value for the analysis window over all bandwidths, as seen in the middle graph of Fig. 8.
8) **Average over each ping**—The estimate of the shape parameter can be quite noisy, particularly when it is large, as evidenced by the Cramer–Rao lower bound on the variance of an unbiased estimate that is proportional to α^2 when α is large [1]. Thus, the normalized curves are averaged over each ping. Owing to both the variability of the shape parameter estimate and the potential environmental variability (e.g., patches with differing average size), the minimum in each analysis window may not occur at the same bandwidth. A histogram of the location of the minimum in each analysis window for one ping of data is shown in the bottom graph of Fig. 8, where it is seen that most of the minima occur at 4-, 8-, and 16-Hz bandwidths. The average is formed only over the analysis windows having a minimum at one of these bandwidths. The results are shown, respectively, in Figs. 9–11, where the expected inverse proportionality of the shape parameter relative to bandwidth is observed in each figure for the bandwidths below where the minimum occurs, followed by a trend upward that is well fit by that predicted by the elongated patch model with either $p = 0.2$ (Fig. 9) or $p = 0.1$ (Figs. 10 and 11). The fit is particularly good for Fig. 10 with the minima at 8 Hz. The equivalent shape parameter for the elongated patch model has been scaled by its minimum and then shifted on the abscissa so the minimum point aligns with the minimum bandwidth of the particular figure.

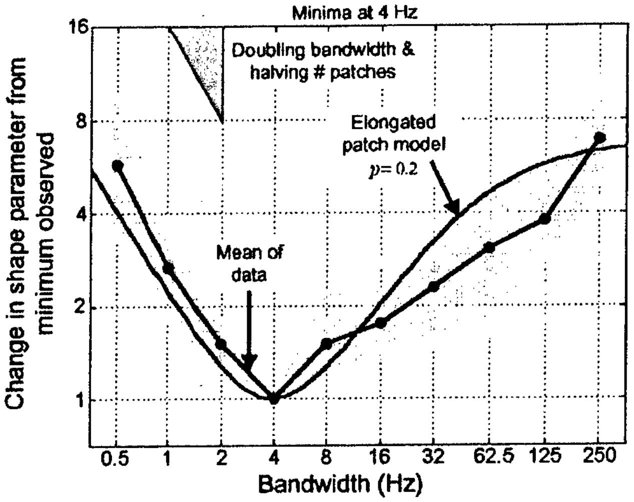

Fig. 9. Change in the estimated K-distribution shape parameter when the minima occur at 4-Hz bandwidth. The + marks are the average values from each ping, the "o" marks are the averages over all pings for data with minima at the given bandwidth. The change predicted by the elongated patch model with $p = 0.2$ is seen to represent the observed data well at low bandwidths and through the minimum but overestimates the shape parameter at higher bandwidths.

B. Discussion

1) Model Fit: At bandwidths below that achieving the minimum in the shape parameter curves, the real data fit the model quite well in Figs. 9 (4 Hz) and 10 (8 Hz), but not in Fig. 11 (16 Hz), where they seem to follow the data and model with a minimum at 8 Hz. This most likely arises from the high variance of the shape parameter estimate causing the minimum to erroneously occur at 16 Hz rather than 8 Hz. As such, the data may be shared over multiple bandwidth minima; however, this will result in a smearing of the data that appears as a lifting of the normalized minimum above unity. At bandwidths greater than the minimum point, a slope approximately proportional to

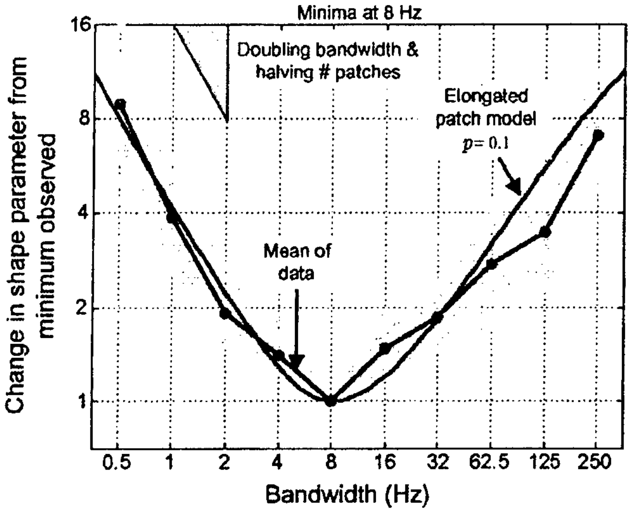

Fig. 10. Change in the estimated K-distribution shape parameter when the minima occur at 8-Hz bandwidth. The + marks are the average values from each ping and the "o" marks are the averages over all pings for data with minima at the given bandwidth. The change predicted by the elongated patch model with $p = 0.1$ is seen to represent the observed data extremely well except at the highest bandwidths.

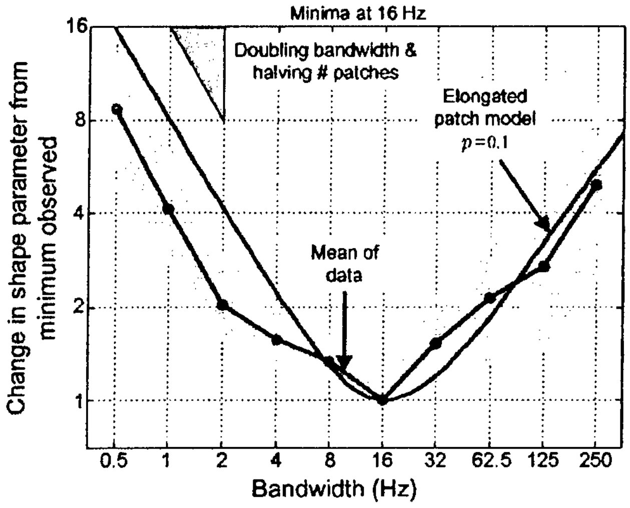

Fig. 11. Change in the estimated K-distribution shape parameter when the minima occur at 16-Hz bandwidth. The + marks are the average values from each ping and the "o" marks are the averages over all pings for data with minima at the given bandwidth. The change predicted by the elongated patch model with $p = 0.1$ is seen to overestimate the observed data at low bandwidths, but represent the data from the minimum through to higher bandwidths well.

bandwidth is observed in Figs. 10 and 11 and the larger spread expected from the increased dependence on patch shape is quite evident in Fig. 9.

2) *Corroboration of Results:* The model–data comparisons presented in Figs. 9–11 illustrate that the effective number of scattering patches ($\tilde{\alpha}$) predicted from a model assuming that elongated patches are overresolved provides a good approximation to the observed data, despite the obvious oversimplifications of the model development. To confirm that these results are not isolated, a small amount of data from the Office of Naval Research (ONR) Geo-clutter 2001 experiment[1] were analyzed. A similar trend in the shape parameter (i.e., a decrease followed by an increase) was observed as bandwidth increased over a 50-Hz band for a 2-s LFM transmit waveform spanning 390–440 Hz.

To insure that the effect is not an artifact arising from the signal processing, data were simulated to follow a K-distribution such that the data were independent from sample to sample at the highest bandwidth (i.e., all of the patches are fully within each resolution cell). As expected, the processing technique described in the previous section illustrated inverse proportionality between the estimated shape parameter and the bandwidth up to the highest bandwidth. That is, the shape parameter decreased monotonically as bandwidth was increased.

3) *Propagation Effects:* From (14), it seems that the average down-range extent of the patches may be determined from the bandwidth at which the minimum occurs in the shape parameter curve. Doing so with the SCARAB data results in patches on the order of hundreds of meters in down-range extent. However, the SCARAB sea trial occurred in a shallow-water environment subject to multipath propagation, which may have the effect of making the patches seem larger than they actually are. When none of the patches are overresolved, multipath propagation is expected to decrease the rate of decay of the shape parameter as bandwidth increases and may cause a leveling, but should not cause an increase. However, if propagation is combined with the overresolved patch model proffered in this paper, we expect that the primary effect will be a shift of the shape parameter curve of Fig. 7 to the left and perhaps a change in the slope where individual multipath are resolved. Until the propagation effect is clearly understood, curves like those shown in Figs. 9–11 cannot be used to estimate the size of the patches.

4) *Mathematical Explanation of the Bandwidth Effect:* Increased bandwidth is expected to result in heavier-tailed reverberation than Rayleigh, not more Rayleigh-like reverberation. Thus, the phenomenon of a return toward Rayleigh-like reverberation at high bandwidth, which is observed in both the data analysis and model, is in some sense counterintuitive. In order to explain this result, consider the central limit theorem (CLT), which states that the sum of independent and identically distributed random quantities tends toward a Gaussian random variable. Increasing bandwidth has two effects on the CLT argument. First, consider that it may not decrease the number of patches in a cell. This implies that increasing bandwidth may not make the reverberation more non-Rayleigh (i.e., a leveling of the shape parameter curve as observed in Fig. 5). The second effect is that the contribution of each patch is limited by reducing the non-Rayleigh-inducing effect of the patch size. This allows the Gaussianity of the interface scattering to become more dominant in each term of the sum (1), thereby increasing the convergence rate of the CLT and making the reverberation envelope more Rayleigh-like.

5) *Effect on Detection Performance:* When none of the patches are overresolved, increasing bandwidth has the dual effect of reducing the reverberation power level and increasing

---

[1] Data courtesy of Dr. J. Preston, Applied Research Laboratory, Pennsylvania State University, State College.

the tails of the envelope pdf. The former improves detection performance by increasing the signal-to-reverberation power ratio (SRR) [2] in a resolution cell, while the latter increases the probability of false alarm [1]. Overall, the increase in SRR is enough to provide a performance improvement both when the target is isolated to one resolution cell [20] or spread across several independent cells [25]. The bandwidth effect of a trend back toward Rayleigh-distributed reverberation at high bandwidths might initially lead one to suspect further improvement in detection performance. However, if overresolution of the patches is the underlying mechanism producing the phenomenon, then it may be expected to induce dependence of the data samples (though not necessarily correlation), which will reduce the effectiveness of detectors that rely on separating reverberation into independent cells to achieve a gain. Thus, a net gain in detection performance is not guaranteed.

Notwithstanding the above discussion on detection performance, false alarms arise from non-Rayleigh reverberation when it is treated as if it were Rayleigh distributed. At the highest bandwidth, the data exhibit shape parameter values 8–10 times larger than the minimum. This may still result in significantly non-Rayleigh reverberation, particularly when the minima are in the 1–3 range, as observed in Fig. 1. Some of the data, however, have minima greater than 5, which would result in shape parameters in the 40–50 range at the highest bandwidth, producing nearly Rayleigh distributed data. (The K-distribution with $\alpha = 50$ has a P_{fa} about 3.5 times that of the Rayleigh distribution when the Rayleigh $P_{\mathrm{fa}} = 10^{-6}$; with $\alpha = 5$, it is 126 times that of the Rayleigh distribution). If increasing the bandwidth enough produces nearly Rayleigh-like data, perhaps the normalizer can remove the majority of false alarms, enabling an improvement in overall system performance (e.g., after tracking and classification). The modeling of Section III predicts that this will not happen; however, the data shown in Figs. 9–11 do not illustrate the leveling of the shape parameter predicted by the model. As such, it is necessary to evaluate higher bandwidth data.

V. CONCLUSION

A recently developed non-Rayleigh reverberation model [1] predicts that active sonar reverberation is K-distributed with a shape parameter that is proportional to the size of the sonar-resolution cell and, therefore, inversely proportional to bandwidth. In this paper, an analysis technique was developed to estimate the shape parameter of the K-distribution as a function of bandwidth from reverberation data. The shape parameter estimates illustrate the expected inverse proportionality of the shape parameter with bandwidth for low bandwidths. However, at higher bandwidths, a trend back toward Rayleigh reverberation was observed at a rate approximately proportional to bandwidth. It was hypothesized that this occurs as a result of the sonar-system resolution cell overresolving patches in range and not in angle. The model of [1] was extended to account for overresolving individual patches, essentially extending the model to include a dependence of the reverberation envelope statistics on the size of the patches relative to the sonar-resolution cell and, consequently, a patch shape for which a generic representation of elongated patches was used. The shape parameter of the moment-matched K-distribution for the model was seen to follow the inverse proportionality expected at bandwidths that do not overresolve the patches and then increased when the patches began to be overresolved. A model–data comparison illustrated an accurate match at lower bandwidths and a reasonable match at higher bandwidths. (Note that, in this latter region, the shape of the patch plays a more important role than its size.)

The models and results of this paper may be used to improve the accuracy of sonar-system performance prediction and simulation and also open up several avenues of new research in terms of the effects of multipath propagation, geoacoustic parameter inversion, and sonar-system false alarm and detection performance. Clearly, the problem that is least understood is the effect of propagation on the reverberation envelope pdf. When combined with the overresolved patch model of this paper, such research may lead to techniques for the estimation of geoacoustic parameters such as patch size and density, as well as *in situ* optimization of sonar bandwidth for target detection.

REFERENCES

[1] D. A. Abraham and A. P. Lyons, "Novel physical interpretations of K-distributed reverberation," *IEEE J Oceanic Eng*, vol. 27, pp. 800–813, Oct. 2002.

[2] J. T. Kroenert, "Discussion of detection threshold with reverberation limited conditions," *J. Acoust. Soc. Amer.*, vol. 71, no. 2, pp. 507–508, 1982.

[3] W. S. Burdic, *Underwater Acoustic System Analysis*, 2nd ed. Upper Saddle River, NJ: Prentice-Hall, 1991.

[4] D. A. Abraham and C. W. Holland, "Statistical analysis of low-frequency active sonar reverberation in shallow water," in *Proc. 4th Eur. Conf. Underwater Acoustics*, Rome, Italy, Sept. 1998.

[5] D. A. Abraham and A. P. Lyons, "Reverberation envelope statistics and their dependence on sonar beamwidth and bandwidth," in *Impact of Littoral Environmental Variability on Acoustic Predictions and Sonar Performance*, N. G. Pace and F. B. Jensen, Eds. Norwell, MA: Kluwer, 2002, pp. 539–546.

[6] E. Jakeman and P. N. Pusey, "A model for non-Rayleigh sea echo," *IEEE Trans. Antennas Propagat*, vol. 24, pp. 806–814, Nov. 1976.

[7] E. Jakeman and R. J. A. Tough, "Non-Gaussian models for the statistics of scattered waves," *Adv. Phys.*, vol. 37, no. 5, pp. 471–529, 1988.

[8] P. A. Crowther, *Fluctuation Statistics of Sea-Bed Acoustic Backscatter*. New York: Plenum, 1980, pp. 609–622.

[9] D. Middleton, "New physical-statistical methods and models for clutter and reverberation: The KA-distribution and related probability structures," *IEEE J. Oceanic Eng.*, vol. 24, pp. 261–284, July 1999.

[10] S. T. McDaniel, "Seafloor reverberation fluctuations," *J. Acoust. Soc. Amer.*, vol. 88, no. 3, pp. 1530–1535, 1990.

[11] C. W. Holland, E. Michelozzi, P. Boni, F. Cernich, R. Rossi, and J. Osler, "Geoclutter Features on the Malta Plateau," SACLANT Undersea Research Centre, La Spezia, Italy, SR-368, 2002.

[12] A. P. Lyons and D. A. Abraham, "Statistical characterization of high-frequency shallow-water seafloor backscatter," *J. Acoust. Soc. Amer.*, vol. 106, no. 3, pp. 1307–1315, 1999.

[13] A. P. Lyons, D. A. Abraham, and E. Pouliquen, "Predicting scattered envelope statistics of patchy seafloors," in *Impact of Littoral Environmental Variability on Acoustic Predictions and Sonar Performance*, N. G. Pace and F. B. Jensen, Eds. Norwell, MA: Kluwer, 2002, pp. 211–218.

[14] D. R. Jackson, D. P. Winebrenner, and A. Ishimaru, "Application of the composite roughness model to high-frequency bottom backscattering," *J. Acoust. Soc. Amer.*, vol. 79, no. 5, pp. 1410–1422, 1986.

[15] P. D. Mourad and D. R. Jackson, "A model/data comparison for low-frequency bottom backscatter," *J. Acoust. Soc. Amer.*, vol. 94, no. 1, pp. 344–358, 1993.

[16] A. Ishimaru, *Wave Propagation and Scattering in Random Media*. New York: Academic, 1978.

[17] J. Spanier and K. B. Oldham, *An Atlas of Functions*. New York: Hemisphere, 1987.

[18] C. W. Holland and J. Osler, "High-resolution geoacoustic inversion in shallow water: A joint time- and frequency-domain technique," *J. Acoust. Soc. Amer.*, vol. 107, no. 3, pp. 1263–1279, 2000.
[19] I. S. Gradshteyn and I. M. Ryzhik, *Table of Integrals, Series, and Products*, 5th ed, A. Jeffrey, Ed. San Diego, CA: Academi, 1994.
[20] D. A. Abraham, "Signal excess in *K*-distributed reverberation," *IEEE J. Oceanic Eng.*, vol. 28, pp. 526–536, July 2003.
[21] N. R. Goodman, "Statistical analysis based on a certain multivariate complex Gaussian distribution (an introduction)," *Ann. Math. Stat.*, vol. 34, pp. 152–177, 1963.
[22] P. P. Gandhi and S. A. Kassam, "Analysis of CFAR processors in nonhomogenous background," *IEEE Trans. Aerosp. Electron. Syst.*, vol. 24, pp. 427–445, July 1988.
[23] D. A. Abraham, "Modeling Non-Rayleigh Reverberation," SACLANT Undersea Research Centre, La Spezia, Italy, SR-266, May 1997.
[24] I. R. Joughin, D. B. Percival, and D. P. Winebrenner, "Maximum likelihood estimation of K distribution parameters for SAR data," *IEEE Trans. Geosci. Remote Sensing*, vol. 31, pp. 989–999, Sept. 1993.
[25] D. A. Abraham, "Broadband detection in K-distributed reverberation," in *Proc. IEEE Sensor Array and Multichannel Signal Processing Workshop*, Aug. 2002, pp. 53–57.

Douglas A. Abraham (S'92–M'93) received the B.S., M.S., and Ph.D. degrees in electrical engineering in 1988, 1990, and 1993, respectively, and the M.S. degree in statistics in 1994, all from the University of Connecticut, Storrs.

He was with the Naval Undersea Warfare Center in New London, CT from 1989 to 1995, was a Senior Scientist at the NATO SACLANT Undersea Research Centre, La Spezia, Italy, from 1995 to 1998, and held a Visiting Faculty position at the University of Connecticut from 1998 to 2000. He is currently a Senior Research Associate with the Applied Research Laboratory, Pennsylvania State University, State College. His work is primarily in the area of statistical signal processing applied to underwater acoustic applications. His current research interests include representing and accounting for non-Rayleigh active sonar reverberation in signal-processing algorithms for detection, classification and localization.

Anthony P. Lyons (M'96) received the B.S. degree in physics from Henderson State University, Arkadelphia, AR, in 1988 and the M.S. and Ph.D. degrees in oceanography from Texas A&M University, College Station, in 1991 and 1995, respectively.

He was a Scientist at the SACLANT Undersea Research Centre, La Spezia, Italy, from 1995 to 2000, where he was involved in a variety of projects in the area of environmental acoustics. He is currently a Senior Research Associate at the Applied Research Laboratory, The Pennsylvania State University, State College, where he is engaged in studies of high-frequency shallow-water propagation, acoustic interaction with the sea floor, and high-resolution characterization of sea-floor sediments.

Dr. Lyons is a Member of the Acoustical Society of America.

IEEE JOURNAL OF OCEANIC ENGINEERING, VOL. 29, NO. 2, APRIL 2004

Simulation of Non-Rayleigh Reverberation and Clutter

Douglas A. Abraham, *Senior Member, IEEE,* and Anthony P. Lyons, *Member, IEEE*

***Abstract*—The simulation of active sonar reverberation time series has traditionally been done using either a computationally intensive point-scatterer model or a Rayleigh-distributed reverberation-envelope model with a time-varying power level. Although adequate in scenarios where reverberation arises from a multitude of scatterers, the Rayleigh model is not representative of the target-like non-Rayleigh reverberation or clutter commonly observed with modern high-resolution sonar systems operating in shallow-water environments. In this paper, techniques for simulating non-Rayleigh reverberation are developed within the context of the finite-number-of-scatterers representation of K-distributed reverberation, which allows control of the reverberation-envelope statistics as a function of system (beamwidth and bandwidth) and environmental (scatterer density and size) parameters. To avoid the high computational effort of the point-scatterer model, reverberation is simulated at the output of the matched filter and is generated using efficient approximate methods for forming K-distributed random variables. Finite impulse response filters are used to introduce the effects of multipath propagation and the shape of the reverberation power spectrum, the latter of which requires the development of a prewarping of the K distribution parameters to control the reverberation-envelope statistics. The simulation methods presented in this paper will be useful in the testing and evaluation of active sonar signal processing algorithms, as well as for simulation-based research on the effects of the sonar system and environment on the reverberation-envelope probability density function.**

***Index Terms*—Clutter, K distribution, multipath, non-Rayleigh, reverberation, simulation, sonar.**

I. INTRODUCTION AND BACKGROUND

TESTING and evaluation of active sonar signal-processing algorithms and active sonar system-performance models is often done with simulated reverberation time series and modeled target responses [1]. There are two principal models used in the simulation of sonar reverberation: the point-scatterer model and the Rayleigh reverberation-envelope model [2]. The former assumes that reverberation is the result of a coherent combination of the reflections from many point scatterers [3], [4], each of which are simulated. Simulators based on this method [5], [6] are inherently computationally intensive and led to the development of simulators with a reverberation-envelope that follows a Rayleigh probability density function (pdf). The Rayleigh pdf arises from a central limit theorem argument that a large number of point reflectors will result in Gaussian-distributed reverberation and, hence, a Rayleigh-distributed envelope. Such reverberation simulators [1], [7]–[10] obtain the time-varying reverberation power level from any of several models [2], [11] and account for various sonar system configurations (e.g., multibeam or bistatic sonar systems) and environmental conditions (e.g., complex propagation and reverberation from surface, volume, and bottom scattering). However, with the advent of high-resolution sonar systems and a greater emphasis on operation in shallow-water environments, sonar systems have increasingly been observed to produce target-like non-Rayleigh reverberation or clutter arising from inhomogeneities in the bottom or sub-bottom [12]–[16]. Accurate simulation of clutter is imperative in the evaluation of automated sonar signal-processing algorithms because clutter produces false alerts in detection and tracking systems that assume that reverberation follows a Rayleigh pdf. The point-scatterer simulation methods have direct control over the statistics of the scattering and, therefore, are capable of simulating clutter; however, they are too computationally intensive for practical use. In this paper, a simulation method is proffered, which affords control over the reverberation-envelope statistics that are necessary for simulating clutter without the computational effort that simulating individual scatterers requires.

At the matched filter envelope, clutter may be represented statistically by a pdf having a tail that is greater than the Rayleigh distribution [12], [16]–[19]. Many distributional models have been used in a phenomenological manner to describe this departure from the Rayleigh distribution, including the Weibull, log-normal, and Rayleigh-mixture distributions. However, these models do not provide the fundamental basis for understanding how the reverberation time series is affected by the environmental conditions (e.g., scattering or propagation) or the sonar system (e.g., beamwidth and bandwidth) that is necessary for the accurate simulation of reverberation and clutter, particularly with regard to the envelope statistics. The finite-number-of-scatterers representation of the K distribution developed in [20] represents an initial step toward such a model, which characterizes the system and environmental dependencies. This new interpretation of the K distribution is derived under the assumption that the reverberation in a given range-bearing resolution cell arises from a finite number of discrete scatterers or sea-floor patches with exponentially distributed scattering cross-sections. The complex envelope of the reverberation time series arising from direct-path propagation after beamforming and matched

---

Manuscript received July 27, 2003; revised March 6, 2004. This work was supported by the Office of Naval Research under Grants N00014-02-1-0115 and N00014-03-1-0245.

The authors are with the Applied Research Laboratory, The Pennsylvania State University, State College, PA 16804-0030 USA (e-mail: abrahad@psu.edu; apl2@psu.edu).

Digital Object Identifier 10.1109/JOE.2004.828202

filtering for the discrete-scatterer model may be represented by (cf., [20, eq. (4)])

$$\tilde{X}(t) = \sum_{i=1}^{m} B_i e^{j\phi_i} \tilde{R}_{ss}(t - \gamma_i) \qquad (1)$$

where B_i, ϕ_i, and γ_i are, respectively, the amplitude, phase, and delay of the reflection from the ith scatterer, m is the number of scatterers contributing to this beam, and $\tilde{R}_{ss}(t)$ is the autocorrelation function of the complex envelope of the transmit waveform. Owing to the finite width of $\tilde{R}_{ss}(t)$, approximately $n(t)$ of the m scatterers are active at (two-way) travel time t, a number proportional to slant-range r_s (meters) to the scatterer along the direct path, beamwidth θ_b (radians), density of scatterers on the sea floor β (number per square meter), and inversely proportional to sonar bandwidth W (Hertz) and cosine of grazing angle $\theta_g(t)$ (radians)

$$n(t) = \frac{c r_s \theta_b \beta}{2W \cos\theta_g(t)} = \frac{c^2 t \theta_b \beta}{4W \cos\theta_g(t)} \qquad (2)$$

where c is the speed of sound in meters per second. As shown in [20], when the scatterer cross-sections are exponentially distributed, the pdf of the reverberation envelope at time t is K-distributed with shape parameter $\alpha = n(t)/2$ and scale parameter $\lambda = 4\mu^2$, where $\mu = E[B_i]$ is the average cross-section of a scatterer.

The sea-floor patch model results in a complex envelope (cf. [20, eq. (18)])

$$\tilde{X}(t) = \sum_{i=1}^{n(t)} \sqrt{B_i(t)} \tilde{Z}_i(t) \qquad (3)$$

where $B_i(t)$ is the exponentially distributed area of the ith patch at travel time t and $\tilde{Z}_i(t)$ is its complex Gaussian-distributed response arising from interface scattering. The number of patches $n(t)$ is as described in (2), where β is taken as the number of patches per square meter. As derived in [20], the reverberation envelope at time t is K distributed with shape parameter $\alpha = n(t)$ and scale parameter $\lambda = \mu\sigma^2$, where $\mu = E[B_i]$ is the average area of a patch and σ^2 is the backscattered power per unit area in the patch.

These models allow direct control of the reverberation-envelope pdf in terms of system and environmental parameters. For example, localized regions containing inhomogeneities in the sea floor that produce clutter (e.g., patches of shellfish, gravel, or sea grass [16]; exposed ridges [19]; [21]; gas vents; mud volcanoes [22], [23]; or buried river beds [24], [25]) may be approximated by geographically varying scatterer or patch density β and average size μ, with β directly influencing the reverberation-envelope statistics. Currently, β and μ must be chosen either based on estimates obtained from a statistical analysis of reverberation or arbitrarily with smaller values of β, resulting in reverberation that is more distinctly non-Rayleigh. In the future, it may be possible to determine β and μ by direct measurement or from evolutionary modeling of geological processes.

There are additional limitations of the finite-number-of-scatterers K-distribution model; it was developed for reverberation arising from exponentially sized scatterers on or in the bottom that are all within the sonar resolution cell. Thus, it is not necessarily appropriate for simulating scatterers that are larger than a sonar resolution cell [26], [27] or those with other than exponentially distributed size. However, based on the goodness of fit that the K distribution enjoys in a wide variety of situations [14], [16], [20], [28], [29], it may be a good approximation to the latter. Ambient noise and reverberation arising from scattering off of the surface or inhomogeneities in the volume may of course be added using appropriate models [1], [7], [10], [30], [2], [11], [31] in situations where they contribute significantly.

In the following sections, techniques are developed for the simulation of K-distributed reverberation or clutter. The focus is on an efficient implementation that accurately represents the reverberation-envelope statistics and retains the appropriate temporal and spectral characterization in terms of multipath propagation, range effects, and oversampling of the data (i.e., a sampling frequency greater than the transmit waveform bandwidth). Efficient methods for generating K-distributed random numbers are presented in Section II. Such techniques are crucial as direct generation of K-distributed random numbers is computationally equivalent to simulating individual scatterers. How to efficiently modify the direct-path reverberation time series to account for the effects of propagation is presented in Section III and how to shape the reverberation spectrum while controlling the envelope statistics is described in Section IV. The methods presented in this paper generate reverberation at the complex envelope stage (i.e., after basebanding and low-pass filtering), after beamforming and matched filtering. The reverberation time series are also produced in a normalized state; that is, the power is constant and equal to one. The expected decay in reverberation power level, as obtained by an appropriate model [2], [11], may be applied after generation of the normalized time series, at which time target, ambient noise, and other reverberation components may be added.

The simulation methods proffered in this paper are intended for use in testing and evaluating signal-processing algorithms, such as statistical normalizers [32], detectors, or trackers, which operate on normalized matched filter data. As such, they may not precisely represent the statistics for a given scenario, but should provide the correct trends, as system or environmental parameters are varied. The simulation techniques should also prove to be useful in the evaluation of environmental effects on reverberation-envelope statistics arising from propagation or multiple component sea floors when theoretical analysis is not feasible.

II. GENERATING K-DISTRIBUTED RANDOM VARIATES

Random variates are variables generated from pseudorandom numbers that are uniformly or Gaussian distributed and are widely used to generate random observations from probability distributions for use in simulation models such as the ones presented in this paper. K-distributed reverberation, after matched filtering but prior to formation of the envelope, may be simulated by generating a complex Gaussian-random variate and a gamma-distributed random variate according to the compound representation of the K distribution [20], [33]. If $\tilde{Z}$ is complex Gaussian distributed with zero mean and a power λ

and V is independent of $\tilde{Z}$ and gamma distributed with a shape parameter α and unit scale, then

$$\tilde{X} = \sqrt{V}\tilde{Z} \tag{4}$$

will produce a K-distributed envelope ($= |\tilde{X}|$) with shape α and scale λ. The $\tilde{}$ denotes that the variable is complex. Generation of the complex Gaussian random variate is straightforward from standard Gaussian (zero-mean and unit-variance) random variates

$$\tilde{Z} = \sqrt{\frac{\lambda}{2}}(W_R + jW_I) \tag{5}$$

where W_R and W_I are independent, zero-mean, unit-variance, real Gaussian random variables. However, generation of the gamma-distributed variate is not as straightforward. There are several techniques for generating random variates, including the inverse transform, convolution, acceptance–rejection, and composition methods. As described in DeVroye [34], the most common method used for generating random variates from the gamma distribution is the acceptance–rejection method, which is based on the ability to easily generate random numbers from a distribution similar to the distribution required. The acceptance–rejection method is an iterative technique requiring the generation of a random number of variates from this surrogate distribution and is, thus, inherently slow as compared with direct methods and, therefore, is undesirable for simulating large amounts of K-distributed reverberation data.

When α is a natural number, V may be generated by summing α exponential random variables and is most easily implemented by

$$V = \sum_{i=1}^{\alpha} -\log U_i \tag{6}$$

where U_i are independent uniformly distributed random variates on $[0, 1]$. When 2α is a natural number, the distribution of V is the scale of a chi-squared distribution with 2α degrees of freedom. As such, V may be generated directly according to

$$V = \frac{1}{2}\sum_{i=1}^{2\alpha} W_i^2 \tag{7}$$

where W_i are standard Gaussian-random variates. A more efficient implementation that exploits (6) is

$$V = \sum_{i=1}^{\lfloor\alpha\rfloor} -\log U_i + (\alpha - \lfloor\alpha\rfloor)W_1^2 \tag{8}$$

where $\lfloor\alpha\rfloor$ is the floor function returning the integer closest to α toward $-\infty$. Clearly, this can be computationally intensive when α is large, as occurs when the reverberation envelope is nearly Rayleigh distributed and is akin to the simulation of every scatterer. To counter this extreme computational burden and to provide a means for efficiently simulating data when 2α is not a natural number, approximate methods are presented in the following sections for large, moderate, and small values of α.

A. Large α Approximation

When α is large, the gamma distribution may be approximated by a Gaussian density function, a result arising from the central limit theorem. Thus, V may be generated according to

$$V \approx \alpha + \sigma_0 W \tag{9}$$

where W is a standard Gaussian-random variable. The mean of the Gaussian approximation is chosen to be α, that of the gamma variate. The variance (σ_0^2) may be chosen to match either the second or fourth moments of the gamma distribution. To match the second moment, the variance of the Gaussian component is chosen as

$$\sigma_0^2 = \alpha \tag{10}$$

and, to match the fourth moment, it is

$$\sigma_0^2 = -\alpha^2 + \sqrt{\alpha^4 + 2\alpha^3 + \frac{11}{3}\alpha^2 + 2\alpha}. \tag{11}$$

Even for large α, V has a small but nonzero probability of being negative [when $\alpha = 20, \Pr\{V < 0\} = 3.9 \times 10^{-6}$ using (10) and 7.4×10^{-6} using (11)]. Therefore, it is prudent to take the absolute value of V prior to using it in (4).

The quality of the Gaussian-based approximation is evaluated by determining the change in threshold that is required to obtain the desired probability of false alarm (P_{fa}). A large change indicates a poor approximation in the tails of the pdf and a small change implies a greater accuracy of the approximation in the vicinity of the design P_{fa}. Owing to the approximate linearity of the logarithm of the probability of false alarm with respect to the intensity threshold at large values, a first-order Taylor series about the threshold yielding the desired P_{fa} in the exact K distribution may be used to determine how the threshold must change in the approximation to achieve the desired P_{fa}. Define the logarithm of the P_{fa} for the K distribution as $p(h) = \log[1 - F_K(h)]$, where h is the intensity threshold and $F_K(h)$ is the cumulative distribution function (cdf) of a K-distributed matched filter intensity

$$F_K(h) = 1 - \frac{2}{\Gamma(\alpha)}\left(\frac{h}{\lambda}\right)^{\alpha/2} K_\alpha\left(2\sqrt{\frac{h}{\lambda}}\right) \tag{12}$$

for $h \geq 0$ and similarly define $\hat{p}(h) = \log[1 - \hat{F}_K(h)]$ for the approximation $\hat{F}_K(h)$. The first-order Taylor series about h_0 for the latter is

$$\begin{aligned}\hat{p}(h) &\approx \hat{p}(h_0) + \hat{p}'(h_0)(h - h_0)\\ &\approx \hat{p}(h_0) + p'(h_0)(h - h_0)\end{aligned} \tag{13}$$

where the approximation $\hat{p}'(h_0) \approx p'(h_0)$ has also been made. The latter derivative is easily obtained from the pdf and cdf of the K distribution

$$p'(h) = \frac{-f_K(h)}{1 - F_K(h)} \tag{14}$$

where the pdf of the K-distributed matched filter intensity is

$$f_K(h) = \frac{2}{\lambda\Gamma(\alpha)}\left(\frac{h}{\lambda}\right)^{(\alpha-1)/2} K_{\alpha-1}\left(2\sqrt{\frac{h}{\lambda}}\right) \tag{15}$$

for $h > 0$. The intensity threshold h_0 is chosen according to the desired probability of false alarm $F_K(h_0) = 1 - P_{\text{fa}}$.

The probability of false alarm for the Gaussian-based approximation model is not straightforward to determine analytically, forcing a numerical evaluation. From the compound representation of (4), the intensity of the matched filter output has form

$$Y = |\tilde{X}|^2 = VW \tag{16}$$

where W is exponentially distributed with mean λ. An integral equation for the P_{fa} may be obtained by first conditioning on V, determining the exceedance probability, and then removing the conditioning

$$\begin{aligned}\hat{P}(h) &= e^{\hat{p}(h)} = 1 - \hat{F}_K(h)\\ &= \int_{-\infty}^{\infty} \frac{1}{\sqrt{2\pi}\sigma_0} \exp\left\{-\frac{h}{\lambda v} - \frac{(v-\alpha)^2}{2\sigma_0^2}\right\} dv. \end{aligned}\tag{17}$$

In this paper, (17) is evaluated numerically by using Romberg integration [35].

Equation (13) may now be used to determine the threshold at which $\hat{p}(h) = p(h_0) = \log P_{\mathrm{fa}}$; that is, where the approximate distribution produces the desired P_{fa}. Relative to the threshold for the exact K distribution (h_0), this is

$$\begin{aligned}\frac{h}{h_0} &\approx 1 + \frac{p(h_0) - \hat{p}(h_0)}{h_0\, p'(h_0)}\\ &= 1 - \frac{[1 - F_K(h_0)]}{h_0\, f_K(h_0)} \log\left\{\frac{1 - F_K(h_0)}{1 - \hat{F}_K(h_0)}\right\}\\ &= 1 - \frac{P_{\mathrm{fa}}}{h_0 f_K(h_0)} \log\left\{\frac{P_{\mathrm{fa}}}{1 - \hat{F}_K(h_0)}\right\}. \end{aligned}\tag{18}$$

Equation (18) is plotted in decibels in Fig. 1 for $P_{\mathrm{fa}} = 10^{-6}$ and $\lambda = 1/\alpha$; the latter is required to yield unit power. In this figure, it is seen that the Gaussian-based approximations underestimate the P_{fa} and also that choosing the variance of the Gaussian approximation by the fourth moment results in less error than the second moment. This likely occurs at the expense of a higher error at lower threshold values compared with the second moment approach; however, the error typically is greatest at the highest threshold. Based on the results shown in Fig. 1, the Gaussian-based approximation using (11) to obtain the variance is recommended when $\alpha \geq 20$, where the error in the P_{fa} threshold (in the vicinity of $P_{\mathrm{fa}} = 10^{-6}$) is always less than two tenths of a decibel. Two advantages of this approximation technique over other methods are as follows: 1) the computational effort required to generate K-distributed random variables is not proportional to α and 2) the Gaussian variate W in (9) and the complex Gaussian variate $\tilde{Z}$ in (4) need only be generated once for use with any $\alpha \geq 20$.

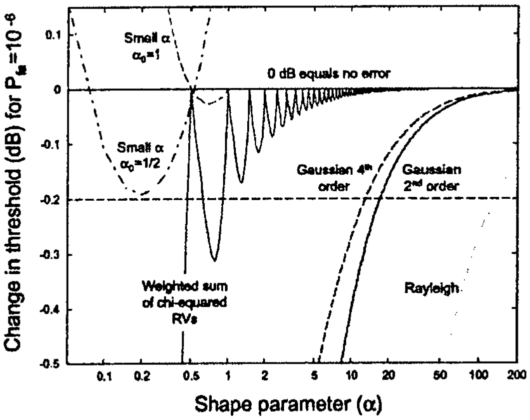

Fig. 1. Change in the threshold for $P_{\mathrm{fa}} = 10^{-6}$ between exact and approximate K distributions for the large α Gaussian-based, moderate α chi-squared-based, and small α power-law-based approximations.

B. Moderate α Approximation

As seen in Fig. 1, the Gaussian-based approximation to K-distributed random variables is less accurate when α drops below around 20, as is expected for central limit-theorem-based arguments. An alternative approximation may be found by decomposing the gamma-random variable into a weighted sum of chi-squared random variables and exploiting the aforementioned relationship between the gamma and chi-squared distributions. Exploiting the fact that the sum of two independent gamma random variates with the same scale parameter is gamma distributed with a shape parameter equal to the sum of the individual ones, V may be decomposed according to

$$V = V_{\alpha_0} + V_{\alpha_1} \tag{19}$$

where V_{α_0} and V_{α_1} are gamma-distributed random variables with unit scale and shape parameters

$$\alpha_0 = \frac{\lfloor 2\alpha \rfloor}{2} \tag{20}$$

and $\alpha_1 = \alpha - \alpha_0$. The function $\lfloor \cdot \rfloor$ is the floor function that returns the integer nearest to the argument toward $-\infty$. As previously mentioned, V_{α_0} is the scale of a chi-squared random variable and may be easily generated according to (8). However, α_1 is always less than 0.5 and, therefore, V_{α_1} is not a chi-squared random variable. An approximation to V_{α_1} may be found in an appropriately scaled chi-squared random variate with one degree of freedom (which also is a gamma variate with a shape parameter of 0.5) to yield

$$V \approx V_{\alpha_0} + \rho V_{0.5} \tag{21}$$

where $\rho = 2(\alpha - \alpha_0)$. When 2α is a natural number, $\rho = 0$ and the approximation becomes exact.

In order to evaluate the efficacy of the approximation of (21) via (18), the cdf of the matched filter intensity $Y = |\tilde{X}|^2$ is necessary. This may be found numerically by using Hankel transforms [36], [37] of the joint characteristic function (JCF) of the complex envelope $\tilde{X}$. Conditioning on V, $\tilde{X}$ is zero-mean complex Gaussian distributed with a variance λV. Thus, the JCF of $\tilde{X}$ is

$$\begin{aligned}\Phi(a) &= E[e^{j\omega X_R + j\gamma X_I}]\\ &= E_V\left[e^{-\frac{a\lambda}{4}V}\right]\end{aligned}\tag{22}$$

where $a = \omega^2 + \gamma^2$. Note that this is simply the moment-generating function (MGF) of V evaluated at $t = -a\lambda/4$. Since V from (21) is the scaled sum of independent gamma-random variables, the MGF is the product of the individual components accounting for the scale

$$M_V(t) = E[e^{tV}] = \frac{1}{(1-t)^{\alpha_0}(1-\rho t)^{1/2}}. \tag{23}$$

Thus, the JCF of $\tilde{X}$ is

$$\Phi(a) = \frac{1}{\left(1+\frac{a\lambda}{4}\right)^{\alpha_0}\left(1+\frac{\rho a\lambda}{4}\right)^{1/2}} \tag{24}$$

and is inverted numerically to obtain the cdf of the matched filter intensity using a numerical Hankel transform [38], as described in [36] and [37].

Inserting the cdf obtained by inverting (24) into (18) as $\hat{F}_K(h_0)$, the efficacy of the chi-squared-based approximation is evaluated and shown in Fig. 1. The error in the P_{fa} threshold in the vicinity of $P_{\mathrm{fa}} = 10^{-6}$ is smaller than -0.2 dB for $\alpha > 1$; thus, this approximation is recommended for use in the region $1 \leq \alpha \leq 20$ and may also be used in the vicinity of $\alpha = 0.5$, although care should be taken to ensure that it is accurate.

C. Small α Approximation

The moderate α approximation presented in the previous section yields adequate results for $\alpha > 1$, but fails when $\alpha < 1$. In this region, the gamma-random variable may be approximated through a power-law transformation of a gamma variate with shape parameter $\alpha_0 = 1$ (for $1/2 < \alpha < 1$) or $\alpha_0 = 1/2$ (for $0 < \alpha < 1/2$)

$$V \approx \lambda_0 V_{\alpha_0}^p \tag{25}$$

where the scale λ_0 is chosen to keep the mean of V at α. The power p may be chosen to match higher order moments with a gamma distribution with shape parameter α. However, this choice is not as effective as choosing

$$p = \frac{1}{\alpha^{0.375}} \tag{26}$$

when $1/2 < \alpha < 1$ or

$$p = \frac{1}{(0.01 + 2\alpha)^{0.34}} \tag{27}$$

when $0 < \alpha < 1/2$, which have been chosen to limit the departure of the detection threshold for $P_{\mathrm{fa}} = 10^{-6}$, as shown in Fig. 1. In both cases, λ_0 is chosen as a function of p

$$\lambda_0 = \frac{\Gamma(\alpha_0)}{\Gamma(\alpha_0 + p)}\alpha \tag{28}$$

so that $E[V] = \alpha$.

The probability of false alarm for this model is not easily obtained analytically and, therefore, must be evaluated numerically. Conditioning on V, as done in Section II-A, results in

$$\hat{P}(h) = e^{\hat{p}(h)} = \int_0^\infty \frac{u^{\alpha_0 - 1}}{\Gamma(\alpha_0)} \exp\left\{-u - \frac{h}{\lambda\lambda_0 u^p}\right\} du \tag{29}$$

which is evaluated numerically by using Romberg integration [35].

D. Computational Efficiency

The techniques of the previous sections, though approximations, are direct methods for generating random variables and, therefore, are inherently quicker than the acceptance–rejection methods described in [34]. Although the acceptance–rejection methods may accept a random variable as gamma distributed after only a handful of iterations, the setup and computational requirements can also reduce the efficiency. For example, Best's XG rejection algorithm ([34], p. 410) requires more than 20 times the number of floating point operations (as estimated using Matlab to generate 1000 variates) than the Gaussian-based approximation of Section II-A for $\alpha \in [20, 100]$, with the latter being easier to implement. The moderate α method of Section II.B requires only slightly fewer floating point operations than the XG algorithm when $\alpha = 20$ and up to approximately 15 times fewer when $\alpha = 1$. The methods in Section II.C require an average of 3 or 1.33 times fewer floating point operations than Johnk's gamma generator ([34, p. 418]), respectively, for $\alpha_0 = 1$ and $\alpha_0 = 0.5$ over the range $\alpha \in (0, 1]$. Thus, the most significant savings are found in the large α regime, followed by the lower range of the moderate α regime. It should also be noted that, compared with generating individual scatterers (as in [5] and [6]), there is a savings proportional to the shape parameter for large α and, compared with generating a Rayleigh-distributed envelope, there is an added burden of generating the gamma-distributed variate V and in forming $\sqrt{V}\tilde{Z}$ of (4).

III. ACCOUNTING FOR THE EFFECTS OF PROPAGATION

The propagation of acoustic waves in shallow-water environments is known to complicate the structure of sonar signals received at an array. It is common to think of propagation as resulting in the reception of a transmitted waveform along multiple paths where, for a given source–receiver pair, the waveform arrives at different travel times, owing to varying path lengths. In simulating reverberation data, it is more appropriate to think of multipath propagation as causing the energy scattered from different parts of the sea floor to arrive at the receiver at the same travel time.

For an isovelocity sound–speed profile, consider simulating only the reverberation arising from direct-path propagation from the source to a scattering patch on the sea floor and back to a receiver. The time series would represent the scattering from the sea floor, as seen through direct-path propagation, and would be K distributed, as described in Section I. In order to account for the effect of multipath propagation, the response from different parts of the sea floor must be added to the direct-path time series at the current time. This may be approximated by using the sea-floor response as seen through the direct-path; that is, by finding the part of the direct-path time series caused by the desired part of the sea floor, applying a scale to account for grazing angle and boundary interaction, and adding it back to the direct-path time series. The resulting structure is a time-varying finite impulse response (FIR) filter applied to the direct-path time series, a common way to model reverberation [2]. In this section, an isovelocity sound–speed profile is used to develop the time-varying FIR filter and a piece-wise stationary implementation in order to generate normalized non-Rayleigh reverberation time-series data.

A. Multipath Delays and Amplitudes

In an isovelocity sound–speed environment, the paths connecting a source or receiver and the bottom may be enumerated by the number of boundary interactions they incur. This is illustrated in Fig. 2 for a colocated source and receiver at a depth d_0 in a water column of depth d_b (all distances are assumed to be

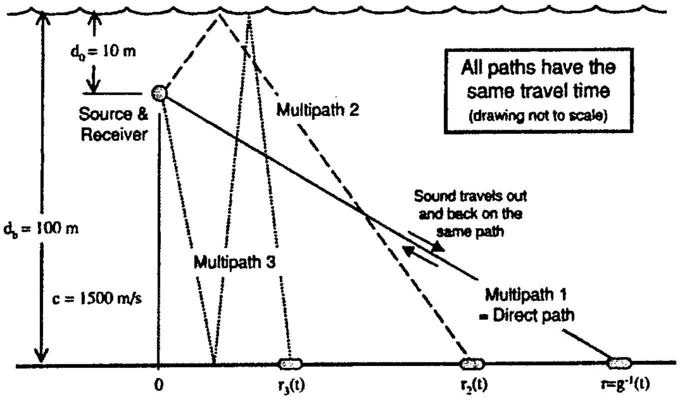

Fig. 2. Direct path and multipath that arrive at the same travel time and are defined by the number of boundary interactions in one-way travel.

in meters). In the following, reverberation is assumed to arise only from energy returning from the sea floor on the same path as it arrived. That is, hybrid paths [39] arising from energy scattered to angles other than the arriving angle do not contribute to reverberation. The two-way paths are, thus, enumerated according to the number of boundary interactions in the one-way propagation (e.g., the direct path has one boundary interaction, a surface–bottom path has two interactions, etc.)

The direct-path arrival from a scatterer at horizontal range r arrives at travel time

$$t = \frac{2}{c}\sqrt{r^2 + (d_b - d_0)^2} = g(r) \tag{30}$$

where c is the speed of sound in water in m/s. The function $g(r)$ defines the mapping of the direct-path propagation from the source to the scatterers at horizontal range r and back to the receiver and represents the *direct-path timeline.*

All paths with an odd number of boundary interactions will depart the source in a downward direction and, through the method of images [40], traverse a vertical distance equal to $id_b - d_0$, where i is the number of boundary interactions. Therefore, at time t, the path with i (odd) boundary interactions will interact with the sea floor at horizontal range

$$r_i(t) = \sqrt{\left(\frac{ct}{2}\right)^2 - (id_b - d_0)^2}. \tag{31}$$

The response of this part of the sea floor may be found in the direct-path timeline at time $g(r_i(t))$ that, when characterized as a delay from time t, becomes

$$\tau_i(t) = t - g\big(r_i(t)\big) \tag{32}$$

$$= t - \frac{2}{c}\sqrt{\left(\frac{ct}{2}\right)^2 - (i-1)d_b[(i+1)d_b - 2d_0]} \tag{33}$$

for i odd, which clearly indicates that the time delay for the direct path is zero $\big(\tau_1(t) = 0\big)$. Requiring the argument of the square root in (33) to be nonnegative provides an upper bound on i when it is odd

$$i_{\text{odd}} \le d_b^{-1}\left[d_0 + \sqrt{(d_b - d_0)^2 + \left(\frac{ct}{2}\right)^2}\right]. \tag{34}$$

The amplitudes of each path $a_i(t)$ must reflect their relative strengths and depend on how many times they interact with the boundaries and at what angle. In two-way propagation, these paths are subject to $i-1$ reflections off the surface, $i-1$ reflections off the bottom, and one instance of backscattering off the bottom. Thus, the path amplitude for the ith multipath may be described as

$$a_i(t) = R_s\big(\theta_{g,i}(t)\big)^{i-1} R_b\big(\theta_{g,i}(t)\big)^{i-1} \rho_b\big(\theta_{g,i}(t)\big) \tag{35}$$

for i odd, where $R_s(\theta_g)$ and $R_b(\theta_g)$ are, respectively, the reflection coefficients for the surface and bottom as a function of grazing angle, $\rho_b(\theta_g)$ is the backscattering coefficient for the bottom, and $\theta_{g,i}(t)$ is the grazing angle of the ith path at travel time t

$$\theta_{g,i}(t) = \arcsin\left(\frac{2(id_b - d_0)}{ct}\right) \tag{36}$$

for i odd. Owing to the dependence of (35) on the grazing angle, the multipath with the largest amplitude is not necessarily the direct path.

No spreading loss component is necessary because each path travels the same distance through the water and the time series will be normalized to unit power. The reflection and scattering coefficients may be formed from models representative of the local ocean environment (e.g., see [1], [40], and [41]). It also is possible and appropriate to include any system-dependent effects, such as transmit and receive beampatterns, in the path amplitudes.

A similar development follows for paths with an even number of boundary interactions. All paths with an even number of boundary interactions will depart the source in an upward direction and will traverse a vertical distance equal to $(i-1)d_b + d_0$. This yields a horizontal range of

$$r_i(t) = \sqrt{\left(\frac{ct}{2}\right)^2 - [(i-1)d_b + d_0]^2} \tag{37}$$

for i even and, following (32), a multipath delay of

$$\tau_i(t) = t - \frac{2}{c}\sqrt{\left(\frac{ct}{2}\right)^2 - id_b[(i-2)d_b + 2d_0]}. \tag{38}$$

Requiring the argument of the square root in (38) to be nonnegative provides an upper bound on i when it is even

$$i_{\text{even}} \le 1 + d_b^{-1}\left[-d_0 + \sqrt{(d_b - d_0)^2 + \left(\frac{ct}{2}\right)^2}\right]. \tag{39}$$

In two-way propagation, paths with an even number of boundary interactions are subject to i reflections off the surface, $i-2$ reflections off the bottom, and one instance of backscattering off the bottom. Thus, the path amplitude for the ith multipath may be described as

$$a_i(t) = R_s(\theta_{g,i}(t))^i R_b(\theta_{g,i}(t))^{i-2} \rho_b(\theta_{g,i}(t)) \tag{40}$$

for i even with grazing angle

$$\theta_{g,i}(t) = \arcsin\left(\frac{2((i-1)d_b + d_0)}{ct}\right). \tag{41}$$

B. Time-Varying FIR Filter Representation

With the amplitude and delay characterization of the multipath from the previous section, the reverberation time series may be described as the output of a time-varying FIR filter

$$\tilde{Y}(t) = \sum_{i=1}^{P} a_i(t) e^{-j2\pi f_c \tau_i(t)} \tilde{X}(t - \tau_i(t)) \tag{42}$$

where $\tilde{X}(t)$ is the complex envelope of the direct-path reverberation time series, f_c is the center frequency from which the data are basebanded, and the number of paths P is determined from (34) and (39). The complex term involving f_c and the delays $\tau_i(t)$ arises from characterizing the filter by using complex envelopes. As previously mentioned, $\tilde{X}(t)$ may be K distributed with a time-varying shape parameter as described in Section I and generated using the techniques of Section II. It may also be generated as described in Section IV to account for spectral shape and oversampling, formed to represent more complicated sea floors involving different types of scatterers or scattering mechanisms by sums of K-distributed components with or without an additive Gaussian component [42], or even by using kernels other than the exponentially distributed scatterer or patch size. It is important, however, that $\tilde{X}(t)$ be generated with a constant power level; that is, the higher order moments may vary, but the second moment must be constant with time. This may be thought of as simulating the statistics and not the power level of the sea floor, as seen through the direct path and, as shown in Section III-D, is required in order to exactly normalize the resulting time series to unit power. The overall reverberation power level may be applied to the normalized time series after accounting for the effect of the multipath propagation on the statistics. This allows for the immediate use of more realistic reverberation power-level codes in conjunction with an approximate statistical model.

Although the model of (42) properly accounts for the effects of the different grazing angle and boundary interaction of the multipath in terms of the power level, it is an approximation with respect to the desired shape parameter for the multipath contributions. The response of the ith multipath at travel time t is obtained from the direct-path time series at travel time $t-\tau_i(t)$, which has a shape parameter proportional to $t-\tau_i(t)$ and is inversely proportional to the cosine of the direct-path grazing angle at travel time $t-\tau_i(t)$ [cf., (2)]. The simulation may be made more accurate by generating the path with the most energy on it and by referencing the multipath delays to its timeline rather than using the direct-path timeline. This is straightforward to accomplish in a numerical implementation, as would be necessary for nonisovelocity sound speed profiles (see Section III-F), but is difficult analytically, so in this paper we simulate the direct path. Additional accuracy requires that the shape parameter for the multipath contribution be proportional to travel time t and inversely proportional to the cosine of the grazing angle of the ith multipath for travel time t. Fortunately, these differences will be relatively small at longer times, when the multipath arrive near to each other in the direct-path timeline and have similar grazing angles. Simulation of reverberation for earlier times, where the approximation is not necessarily adequate, is discussed in Section III-G where a two-dimensional (2-D) filtering approach is suggested as a more accurate alternative. Further limitations of the isovelocity example and discussion of how to extend these results to nonisovelocity sound–speed profiles using ray path models and full-wave models may be found in Section III-F.

C. Implementation

Development of the time-varying FIR filter representation of reverberation in the previous sections has been done by using continuous time-systems theory. However, sonar systems and, therefore, reverberation simulation, is typically performed in discrete time after sampling continuous time signals. This ultimately requires choosing a sampling frequency f_s for the complex envelope of the reverberation as a function of the bandwidth W of the transmit waveform. It is common to choose f_s to oversample the data by a factor of 3–5 (i.e., $3W \le f_s \le 5W$) to account for the Doppler of the target and for the Doppler spreading of the reverberation as induced by source, receiver, or scatterer motion. The formation of $\tilde{X}(nT)$, accounting for oversampling and Doppler, is described in Section IV.

It would be computationally intensive to directly implement the time-varying FIR filter of (42). A compromise is available if it can be assumed that the filter structure varies slowly enough with time to be well approximated by a piece-wise stationary filter. Within each block where the multipath structure is assumed to be constant, the now time-invariant FIR filter of (42) may be implemented in the frequency domain using fast Fourier transforms (FFTs). The frequency-domain implementation is desirable as it avoids having to quantize the delays to account for sampling. The impulse response of the filter is

$$h(t) = \sum_{i=1}^{P} a_i e^{-j2\pi f_c \tau_i} \delta(t-\tau_i) \tag{43}$$

where the time dependence on the amplitudes and delays has been dropped because they are assumed to be constant within a processing block. The transfer function then is

$$H(f) = \sum_{i=1}^{P} a_i e^{-j2\pi(f+f_c)\tau_i}. \tag{44}$$

If T_{st} is the time duration in seconds over which the multipath are considered stationary, then the number of time samples in a filter block is

$$L = \max\{1, \lfloor T_{\mathrm{st}} f_s \rfloor\}. \tag{45}$$

The impulse response of (43) has width

$$T_h = \max_{1<i\le P} \tau_i - \tau_0 \tag{46}$$

and will normally result in $T_h = \tau_P$ (when $\tau_0 = 0$ and $\tau_{i+1} > \tau_i$) and corresponds to

$$M = \lceil T_h f_s \rceil \tag{47}$$

time samples. For the direct-path-only case, $M = 1$ and $L = 1$. Note that not all of the paths need to be included in the impulse response. Limiting the paths to those within so many decibels of the peak path amplitude reduces the computational burden and allows a smaller FFT size, owing to a smaller value of M.

Direct use of an FFT in a filtering operation results in a circular convolution, not the linear convolution that is necessary to obtain the output of an FIR filter. However, by appropriately padding the input sequence and filter impulse response with zeros before taking the FFT, a linear convolution may be obtained. The "overlap-and-save" method, as described in [43], accomplishes this and may be applied to the piece-wise stationary FIR filter implementation, where each FFT block operates on a stationary segment. An $N = M + L - 1$ point discrete Fourier transform (DFT) is used to perform the convolution within each block, where the last $M - 1$ samples from the previous block of the input sequence are prepended to the length L data block and the first $M - 1$ samples of the output are discarded. Note that the value of M may be increased above the actual filter impulse-response duration so that N is a power of two to exploit the computational savings of the FFT over the DFT. In matrix-vector notation,[1] the filtering operation may be described as follows. Let the N-by-1 augmented input data vector containing the last $M - 1$ samples of the previous block and the L samples of the current block be $\mathbf{x}$. When processing the first block, the augmented vector can be formed by prepending $M - 1$ samples of $\tilde{X}(t)$ from earlier times or by prepending $M - 1$ zeros. Define $\mathbf{D}$ as the N-by-N DFT matrix (i.e., $\mathrm{DFT}\{\mathbf{x}\} = \mathbf{D}^H\mathbf{x}$) and $\mathbf{D}^H$ as the inverse DFT matrix (note that $\mathbf{D}^H\mathbf{D} = \mathbf{D}\mathbf{D}^H = \mathbf{I}$, where $\mathbf{I}$ is an identity matrix). The filtering operation may be described by a multiplication in the frequency domain by a diagonal matrix $\mathbf{H}$ with elements

$$\mathbf{H}_{(k,k)} = H\left(\frac{(k-1)}{N} f_s\right) \tag{48}$$

for $k = 1, \ldots, N$, where $H(\cdot)$ is the FIR filter transfer function from (44) and the frequency ordering $(f = ((k-1)/N)f_s)$ corresponds to that of the FFT algorithm in use. The augmented filter output data then is

$$\begin{aligned} \mathbf{y} &= \mathrm{IDFT}\{\mathbf{H}\,\mathrm{DFT}\{\mathbf{x}\}\} \\ &= \mathbf{D}\mathbf{H}\mathbf{D}^H\mathbf{x} \end{aligned} \tag{49}$$

from which the time series for this block is formed by discarding the first $M - 1$ elements.

Matlab code illustrating this technique may be found in Appendix II. In this code, both T_{st} and T_h are held constant throughout the entire ping. They may, however, be adapted as a function of travel time by exploiting the larger values of T_{st} and shorter values of T_h expected at later travel times to produce a more efficient implementation.

D. Normalization

Signal processing for active sonar systems requires a normalization algorithm to provide a constant false-alarm rate; that is, the time-varying reverberation power level must be removed before data can be compared to a threshold where exceedances result in an alarm. In this section, the power level of each data block described in the previous section is derived so that the time series may be normalized to have a constant power level.

If all the delays were integer multiples of the sampling time $(T = 1/f_s)$, then the power of the time series would be easily derived from (42). However, owing to the frequency-domain implementation of the filter, which does not place such a restriction on the delays, the power must be derived from (49). First, note that within a stationary time block the data $\tilde{Y}(t)$ have a constant power level owing to the wide-sense stationarity (i.e., constant mean and autocorrelation) of the input sequence $\tilde{X}(t)$ and the linearity and time-invariance of the FIR filter [44]. Thus, the power $E[|\tilde{Y}(t)|^2] = P_Y$ is constant within the block. The total power in all the samples of the augmented filter output vector $(\mathbf{y})$ may be obtained from (49) and P_Y is then obtained by scaling $E[\mathbf{y}^H\mathbf{y}]$ by N as

$$\begin{aligned} P_Y &= \frac{1}{N}E[\mathbf{y}^H\mathbf{y}] \\ &= \frac{1}{N}E[\mathbf{x}^H\mathbf{D}\mathbf{H}^H\mathbf{D}^H\mathbf{D}\mathbf{H}\mathbf{D}^H\mathbf{x}] \\ &= \frac{1}{N}E[\mathbf{x}^H\mathbf{D}\mathbf{H}^H\mathbf{H}\mathbf{D}^H\mathbf{x}] \\ &= \frac{1}{N}\mathrm{trace}\{\mathbf{H}\mathbf{D}^H E[\mathbf{x}\mathbf{x}^H]\mathbf{D}\mathbf{H}^H\} \\ &= \frac{1}{N}\mathrm{trace}\{\mathbf{H}\mathbf{D}^H\mathbf{R}_X\mathbf{D}\mathbf{H}^H\} \qquad (50) \\ &= \frac{P_X}{N}\mathrm{trace}\{\mathbf{H}\mathbf{H}^H\} \\ &= \frac{P_X}{N}\sum_{k=0}^{N-1}|H(f_s k/N)|^2 \qquad (51) \end{aligned}$$

where $\mathbf{R}_X = E[\mathbf{x}\mathbf{x}^H]$ in (50) is the covariance matrix of the vector $\mathbf{x}$ or the N-dimensional correlation matrix of the discrete time sequence $\tilde{X}(nT)$. If the sampled input data $\tilde{X}(nT)$ are uncorrelated, then $\mathbf{R}_X = P_X\mathbf{I}$ and P_Y simplifies to (51).

The simulation method discussed in Section IV produces discrete time data that are correlated and, therefore, (50) must be used where $\mathbf{R}_X$ is the correlation matrix of the discrete time sequence $\tilde{X}_n = \tilde{X}(nT)$. The direct-path time series $\tilde{X}_n$ is formed by applying an FIR filter with coefficients $b_1, \ldots, b_L$ to a white K-distributed random process $\{\tilde{W}_n\}$

$$\tilde{X}_n = \sum_{i=1}^{L} b_i \tilde{W}_{n-i+1}. \tag{52}$$

As such, the covariance matrix $\mathbf{R}_X$ is a Toeplitz matrix (i.e., constant values along the diagonals) with coefficients

$$\begin{aligned} r_k &= E[\tilde{X}_n \tilde{X}_{n+k}] \\ &= \sum_{i=1}^{L}\sum_{j=1}^{L} b_i b_j^* E[\tilde{W}_{n-i+1}\tilde{W}_{n+k-j+1}] \\ &= \alpha_0\lambda_0 \sum_{i=1}^{L}\sum_{j=1}^{L} b_i b_j^* \delta_{k-(j-i)} \\ &= \alpha_0\lambda_0 \sum_{i=-\infty}^{\infty} b_i b_{i+k}^* \end{aligned} \tag{53}$$

where the definition of the last line requires that $b_i = 0$ for $i < 1$ and $i > L$ and illustrates that the Toeplitz coefficients may be obtained by correlating (or convoluting if the b_i are symmetric) the FIR filter coefficients with themselves. Note that $r_{-k} = r_k^*$ and $r_k = 0$ when $|k| > L$.

---

[1] In this paper, bold lower-case letters are vectors, bold upper-case letters are matrices, and a superscript ^{H} represents the conjugate–transpose operator.

Examining (50), it is seen that the off-diagonal elements of the matrix $\mathbf{D}^H\mathbf{R}_X\mathbf{D}$ are not required. Defining the kth diagonal element as

$$S_k = \mathbf{d}_k^H\mathbf{R}_X\mathbf{d}_k \tag{54}$$

the power is simply

$$P_Y = \frac{1}{N}\sum_{k=1}^{N} S_k|H(f_s(k-1)/N)|^2. \tag{55}$$

Owing to the Toeplitz form of $\mathbf{R}_X$, S_k may be efficiently determined through the use of an FFT

$$\begin{aligned} S_k &= \sum_{i=0}^{N-1}\sum_{l=0}^{N-1} r_{i-l}\, e^{-j2\pi(i-l)\frac{k}{N}} \\ &= \sum_{m=-(N-1)}^{N-1} (N-|m|)r_m\, e^{-j2\pi m\frac{k}{N}} \\ &= \sum_{m=0}^{N-1}(N-m)\left[r_m\, e^{-j2\pi m\frac{k}{N}} + r_m^*\, e^{j2\pi m\frac{k}{N}}\right] - Nr_0 \\ &= U_k + U_k^* - Nr_0 \\ &= 2\mathcal{R}e(U_k) - Nr_0 \end{aligned} \tag{56}$$

where $r_0 = \sum_{i=1}^{L}|b_i|^2$ and U_k is the kth bin of the N-point DFT of the sequence

$$u_m = (N-m)r_m \tag{57}$$

for $m = 0,\ldots,N-1$.

The augmented data vector $\mathbf{y}$ from (49) is then normalized by dividing by the square root of P_Y, taken from (51) or (55), resulting in $\mathbf{z} = \mathbf{y}/\sqrt{P_Y}$. The time series data are formed by taking the last L vector elements to produce the normalized time series $\tilde{Z}(t) = \tilde{Y}(t)/\sqrt{P_Y}$ for $t = nT$ in the block.

E. Simulation Example

Consider the scenario of Fig. 2 where a colocated source and receiver are at a depth of 10 m in 100 m of water with an isovelocity profile with sound speed $c = 1500$ m/s. The techniques described in the previous sections are used to simulate the normalized complex matched-filter output for a 100-Hz bandwidth waveform centered at 2000 Hz from 2 to 12 s into the ping. The sea floor is assumed to produce a K-distributed response with a constant shape parameter $\alpha_0 = 1$. Although the shape parameter should change with travel time according to (2), it is left fixed in this example to emphasize and isolate the effects of multipath propagation on the matched filter envelope and, therefore, the probability of false alarm (P_{fa}). The amplitudes of each path are determined according to (35) and (40), where the reflection and scattering coefficients are obtained as described in Appendix I. Only those paths within 15 dB of the peak path amplitude are retained.

The normalized reverberation-intensity time series is shown in Fig. 3, both with and without multipath, the latter of which may be considered to be direct-path-only propagation. Without multipath (the upper plot), the data are simply K distributed with a shape parameter of 1, which results in a heavier tail in the envelope pdf than for Rayleigh reverberation, as evidenced by the number of threshold exceedances (20 in this particular realization). The threshold shown on the plot is for $P_{\text{fa}} = 10^{-3}$ for a Rayleigh-distributed reverberation envelope and, because there are 10^3 independent samples in the plot, only one threshold exceedance would be expected were the Rayleigh hypothesis true. When multipath are added, it is expected that the reverberation-envelope pdf becomes more Rayleigh-like, owing to the increase in the number of scatterers that contribute at any given travel time over the direct-path case. This is evidenced by the smaller number of threshold exceedances in the lower plot of Fig. 3 (five in this realization) and also by the P_{fa} curves found in Fig. 4. The P_{fa} for the K–distribution model and direct-path data are approximately two and a half orders of magnitude greater than the Rayleigh P_{fa} when the latter is at 10^{-5}, while the P_{fa} of the multipath affected data lies in between.

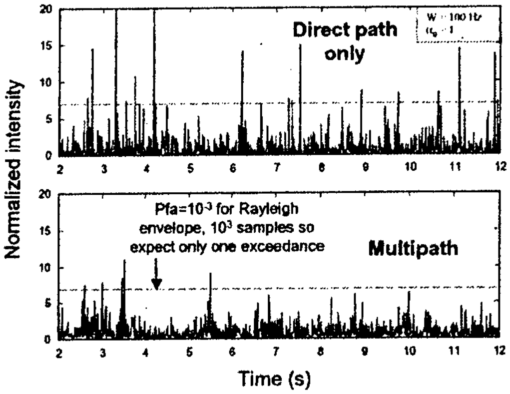

Fig. 3. Normalized reverberation intensity with and without multipath. The Rayleigh-reverberation threshold for $P_{\text{fa}} = 10^{-3}$ is shown on the figure, which contains 10^3 samples so, on average, one threshold crossing is expected in the upper plot for Rayleigh-distributed data and less than one in the lower plot, owing to the correlation introduced by the multipath.

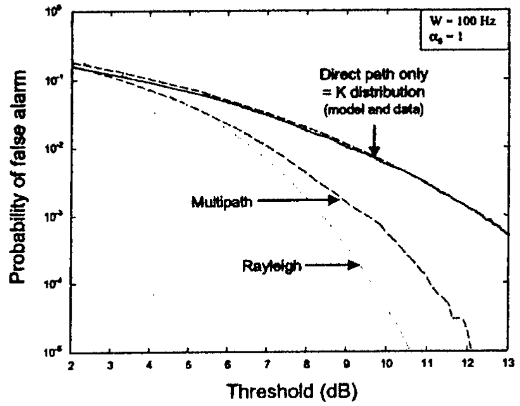

Fig. 4. Probability of false alarm with and without multipath, compared with that for Rayleigh reverberation. As expected, multipath shifts the P_{fa} curve toward Rayleigh.

In addition to making the reverberation data more Rayleigh-like, multipath propagation is also expected to increase the correlation of the data in time. The complex time-series data with and without multipath are used to estimate the autocorrelation function of the data. An increase in the correlation is evident in the curves shown in Fig. 5. As the data are from multiple ranges with varying multipath, the result is an average and, therefore, is smeared over many ranges. This illustrates the difficulty in using at-sea data to

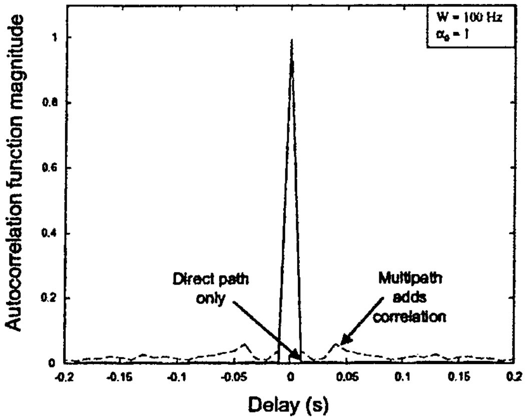

Fig. 5. Magnitude of the autocorrelation function estimates with and without multipath. Clearly, multipath increases the correlation of the reverberation in time.

determine the effects of environmental conditions such as multipath propagation, where the effect changes with range and even ping when the source or receiver are not stationary. The direct-path data for this example are independent from sample to sample, a situation that represents a flat reverberation spectrum and, therefore, an impulse such as an autocorrelation function. As discussed in Section IV, more realistic spectra may be simulated, including accounting for oversampling of the data. Note that the P_{fa} curves and the correlation functions of Figs. 4 and 5 are estimated from 100 independent realizations of the reverberation time series shown in Fig. 3, illustrating the utility of non-Rayleigh reverberation simulation that allows the generation of an ensemble of pings with identical statistical characterization.

F. More Complicated Propagation Conditions

The isovelocity sound–speed environment developed earlier in this section is useful for illustrating the proffered simulation technique, but is limited in that it does not account for many of the conditions more representative of shallow-water propagation. Inclusion of a generic sound–speed profile is the most straightforward and immediate extension. As is commonly done for ray-model-based reverberation codes [2], the multipath delays may be computed numerically for each range and tabulated according to their time of arrival. However, this increase in fidelity has an accompanying cost as compared with implementing the isovelocity sound–speed profile. For example, even though the different multipath arrive at the same time, they may have varying lengths, requiring an accounting for different spreading losses on each path. Additionally, the structure of the multipath may have abrupt rather than smooth changes with range. For example, many downward-refracting profiles in shallow-water environments will result in multipath structures with no direct path beyond a certain range. This may be handled by replacing the direct-path timeline of the isovelocity example of Section III-A by the path with minimum travel time or maximum amplitude. Such abrupt changes in the multipath structure cause equivalent nonstationarity in the FIR filter structure of (42), requiring careful setting of the duration over which the impulse response is assumed to be stationary.

Ray models are certainly appropriate at higher frequencies [40]; however, it should also be possible to simulate non-Rayleigh reverberation using full-wave propagation solutions such as normal mode, parabolic equation, or wavenumber integration. In a manner similar to Ellis' [45], development of a reverberation power-level model based on normal modes, reverberation may be simulated using a normal-mode solution to shallow-water propagation where ray-mode analogies and group velocities are used to obtain arrival times for the modes. The full wave codes may also be used through Fourier synthesis by forming the two-way channel-impulse response $h(t, r)$ as a function of horizontal range (r) and mapping this to a particular timeline; e.g., the one created by the time of maximum contribution of the sea floor $t = g(r) = \arg\max_\tau |h(\tau, r)|$. This mapping is then used to appropriately form the time-varying impulse response of the filter applied to $\tilde{X}(t)$.

G. Travel Time and Grazing-Angle Effects

As previously discussed, accounting for multipath propagation by applying an FIR filter to the direct-path reverberation time series is an approximation requiring that the multipath arrive relatively close to each other in travel time and have minimally different grazing angles, a situation that occurs for large travel times. If, however, the reverberation time series must be simulated for very short ranges, it is possible to account for this effect through the use of a 2-D FIR filter. At travel time t, let the shape parameter desired for the ith path be

$$\alpha_i(t) \propto \frac{t}{\cos\theta_{g,i}(t)} \tag{58}$$

and define the maximum shape parameter required to be drawn from the direct-path time series as $\alpha_{\max}(t)$. This may be approximated by the upper bound

$$\alpha_{\max}(t) \leq \max_i \alpha_i(t + \tau_{\max}) \tag{59}$$

over $i = 1, \ldots, P$, where $\tau_{\max}$ is the largest delay for any multipath at any travel time in the direct-path timeline. Now, generate a set of direct-path reverberation time series $\tilde{X}_k(t)$ for $k = 1, \ldots, K$ and set the shape parameter to

$$\alpha_0(t) = \frac{\alpha_{\max}(t)}{K}. \tag{60}$$

These time series may be thought of abstractly as the direct-path response to strips of the sea floor, where a varying number are combined to produce the response for each multipath at any given travel time. The reverberation response accounting for multipath is then representable as a time-varying 2-D FIR filter

$$\tilde{Y}(t) = \sum_{i=1}^{P} a_i(t) \sum_{k=1}^{L_i(t)} \tilde{X}_k(t - \tau_i(t)) \tag{61}$$

where

$$L_i(t) = \left\lceil \frac{\alpha_i(t)}{\alpha_0(t - \tau_i(t))} \right\rceil \tag{62}$$

of the K time series from travel time $t - \tau_i(t)$ are combined to form the response of the ith multipath for travel time t. Clearly, choosing a larger K improves the accuracy in simulating the travel time and grazing angle effects at the expense of an increase in computational effort. The approximation of (42) is obtained from (61) by making $L_i(t)$ constant.

IV. ACCOUNTING FOR REVERBERATION SPECTRUM AND OVERSAMPLING

The methods presented in Section II may be used to generate a sequence of independent K-distributed random variables. This produces a flat-frequency spectrum, which may be acceptable when the sampling rate and transmit waveform bandwidth are equal, but in general is not realistic and is certainly not appropriate when the data are oversampled. Oversampling by a factor of three to five is common in active sonar signal processing and introduces correlation between samples and a shaped spectrum that must be accounted for in simulating reverberation data.

The spectral shaping may be introduced by forming a discrete time series at the complex envelope stage with a white spectrum and applying a linear filter designed to match the spectrum of the reverberation after matched filtering. This has been done using theoretical spectra [3], [4], [7] and autoregressive models [1], [8]. Unfortunately, filtering changes the higher order moments of the input data; that is, if K-distributed input data are used, the filter output data are not necessarily K distributed. The following sections describe how to choose the coefficients of an FIR filter and the statistical character of the input sequence so as to control the spectrum and distribution of the filter output.

A. *Filter Coefficients*

Faure [3] and Ol'shevskii [4] describe the autocorrelation function and power spectrum of reverberation from a point-scatterer model, including the effects of random motion of the scatterers and motion of the source or receiver. For bottom reverberation, the scatterers are expected to be stationary so only Doppler effects arising from source and receiver motion need to be considered. Suppose that the Doppler scale induced by the motion of a colocated source and receiver is β_0 [i.e., if $s(t)$ is the transmit waveform, then $s(\beta_0 t)$ is the effective waveform in the water]. Then, according to Faure [3], the complex envelope of the reverberation prior to matched filtering will have a power spectrum

$$S_{rr}(\omega) = \frac{1}{\beta_0^2}\left|S\left(\frac{\omega}{\beta_0}\right)\right|^2 \tag{63}$$

where $S(\omega)$ is the Fourier transform of $\tilde{s}(t)$, the complex envelope of the transmit waveform. After matched filtering against the transmit signal with a Doppler scale β_1, the spectrum becomes

$$S_{xx}(\omega) = \frac{1}{\beta_0^2\beta_1^2}\left|S\left(\frac{\omega}{\beta_0}\right)S^*\left(\frac{\omega}{\beta_1}\right)\right|^2. \tag{64}$$

The spectrum of the simulated reverberation will be shaped by passing a white random process $\tilde{W}(t)$ with unit power through a linear time-invariant filter. If the transfer function of the filter is $B(\omega)$, then the power spectrum of the filter output will be

$$S_{xx}(\omega) = |B(\omega)|^2 \tag{65}$$

which, when equated to (64), yields

$$B(\omega) = \frac{1}{\beta_0\beta_1}S^*\left(\frac{\omega}{\beta_0}\right)S\left(\frac{\omega}{\beta_1}\right). \tag{66}$$

The impulse response of the filter is the inverse Fourier transform of $B(\omega)$ and is easily found to be

$$b(t) = \int_{-\infty}^{\infty} s^*(\beta_0 t)s(\beta_1(t+\tau))\,dt \tag{67}$$

using the convolution and time-reversal properties of the Fourier transform. This also is the ambiguity function of the transmit waveform when the Doppler scale β_0 arises from source motion and β_1 from the matched filtering operation. Note that when there is no Doppler effect (i.e., $\beta_0 = \beta_1 = 1$), the filter impulse response is simply the transmit waveform autocorrelation function $b(t) = \tilde{R}_{ss}(t)$.

In practice, the implementation will be in discrete time and the filter will have a finite-length impulse response with enough taps to accurately capture the decay in the ACF. For wide-band waveforms with high-range resolution, this will not require very many taps. Sampling the ACF every one-over-the-bandwidth approximately results in a filter impulse response that is a Dirac delta function. Oversampling results in an impulse response that decays more slowly, which will be illustrated with an example in Section IV-C.

B. *Equivalent Shape Parameter and Prewarping*

Passing Gaussian data through a linear filter will produce Gaussian output data; however, applying a linear filter to K-distributed data will not necessarily produce a K-distributed output. That the K distribution is closed under addition when the scale parameters are the same [20] implies that the output will be K distributed if the FIR filter coefficients are constant. When the filter coefficients are not constant, as would normally be the case, the output data may still be well represented by the K distribution and are likely to be sufficiently close for most simulation purposes. It is, however, still necessary to control the pdf at the output of the filter. This may be accomplished by choosing the shape parameter of the input K distribution so that the *equivalent* shape parameter of the output is as desired. As described in [26] and [27], the equivalent shape parameter is determined by matching the second and fourth moments of the matched filter envelope with those of the K distribution and inverting the resulting equations for the shape and scale parameters.

Suppose that the input sequence to the FIR filter is the independent and identically distributed (i.i.d.) discrete-time sequence $\tilde{W}_n$ having a K-distributed envelope with a shape parameter α_0 and a scale parameter λ_0. If the filter coefficients are $b_1, \ldots, b_L$, then the filter output at time step n is

$$\tilde{X}_n = \sum_{i=1}^{L} b_i\tilde{W}_{n-i+1}. \tag{68}$$

The average intensity then is

$$\begin{aligned} m_2 &= E[|\tilde{X}_n|^2] \\ &= \sum_{i=1}^{L}\sum_{j=1}^{L} b_i b_j^* E[\tilde{W}_{n-i+1}\tilde{W}_{n-j+1}^*] \\ &= \alpha_0\lambda_0\sum_{i=1}^{L}|b_i|^2 \end{aligned} \tag{69}$$

where

$$E[\tilde{W}_i\tilde{W}_j^*] = \alpha_0\lambda_0\delta_{i-j} \tag{70}$$

where δ_i is the Kronecker delta function.

The average squared intensity is found in a similar manner, i.e.,

$$\begin{aligned} m_4 &= E[|\tilde{X}_n|^4] \\ &= \sum_{i,j,k,l=1}^{L} b_i b_j^* b_k b_l^* E[\tilde{W}_{n-i+1}\tilde{W}_{n-j+1}^*\tilde{W}_{n-k+1}\tilde{W}_{n-l+1}^*] \\ &= \sum_{i=1}^{L} |b_i|^4 E[|\tilde{W}_{n-i+1}|^4] \\ &\quad + 2\sum_{i=1}^{L}\sum_{k=1,\neq i}^{L} |b_i|^2|b_k|^2 E[|\tilde{W}_{n-i+1}|^2]E[|\tilde{W}_{n-k+1}|^2] \\ &= 2\alpha_0\lambda_0^2\sum_{i=1}^{L}|b_i|^4 + 2\alpha_0^2\lambda_0^2\left[\sum_{i=1}^{L}|b_i|^2\right]^2 \\ &= 2m_2^2 + 2\alpha_0\lambda_0^2\sum_{i=1}^{L}|b_i|^4 \end{aligned} \tag{71}$$

where simplification of the second line is achieved by noting that the expectation is zero unless $i = j = k = l$ or $i = j$ and $k = l$ with $i \neq k$ or $i = l$ and $j = k$ with $i \neq j$, all of which are mutually exclusive. Further simplification requires (70) and

$$E[|\tilde{W}_i|^4] = 2\alpha_0(\alpha_0 + 1)\lambda_0^2 \tag{72}$$

which is easily derived from the product form of the K distribution. It should be noted that the filter output sequence $\tilde{X}_n$ will be wide-sense stationary as long as the input data are wide-sense stationary. This does not require all of the higher order moments of the input sequence to be constant, only the mean and the autocorrelation function. Since $\tilde{W}_n$ has a white spectrum, zero mean, and unit power, it is wide-sense stationary. Varying α_0, the shape parameter of the input sequence, while keeping $\lambda_0 = 1/\alpha_0$, does not affect this result, but will in fact alter the statistics of the resulting reverberation sequence $\tilde{X}_n$.

The equivalent shape and scale parameters that describe the higher order moments of the filtered output are now easily obtained from m_2 and m_4 [26], [27] as

$$\begin{aligned} \tilde{\alpha} &= \frac{2m_2^2}{m_4 - 2m_2^2} \\ &= \alpha_0\left[\frac{\left(\sum_{i=1}^{L}|b_i|^2\right)^2}{\sum_{i=1}^{L}|b_i|^4}\right] \end{aligned} \tag{73}$$

and

$$\begin{aligned} \tilde{\lambda} &= \frac{m_4 - 2m_2^2}{2m_2} \\ &= \lambda_0\left[\frac{\sum_{i=1}^{L}|b_i|^4}{\sum_{i=1}^{L}|b_i|^2}\right]. \end{aligned} \tag{74}$$

Note that if $b_i = 1$, the output is expected to be K- distributed with shape parameter $L\alpha_0$ and scale λ_0, because the K distribution is closed under addition when the scale parameters are the same. The equivalent shape and scale parameters of (73) and (74) produce exactly these results.

These relationships are used to determine what shape and scale parameter the K-distributed input sequence $\tilde{W}_i$ should have in order to produce the desired statistical character after spectral shape filtering takes place. In a manner similar to that found in the design of digital filters from continuous time models, this process prewarps the shape and scale parameters so that the output can be controlled. The prewarped values are easily obtained from (73) and (74) as

$$\alpha_0 = \alpha\left[\frac{\sum_{i=1}^{L}|b_i|^4}{\left(\sum_{i=1}^{L}|b_i|^2\right)^2}\right] \tag{75}$$

and

$$\lambda_0 = \lambda\left[\frac{\sum_{i=1}^{L}|b_i|^2}{\sum_{i=1}^{L}|b_i|^4}\right] \tag{76}$$

where α and λ are the desired shape and scale parameters. When it is not necessary to simulate an exact value of α, the random-number generation is more efficient when α_0 is set to the nearest half-integer (i.e., set $\alpha_0 = \text{round}(2\alpha_0)/2$ and appropriately adjust λ_0). Otherwise, the techniques developed in Section II may be used to efficiently generate K-distributed data when $2\alpha_0$ is not an integer. These methods should also be used when α_0 is large owing to their computational savings over other Gamma-random variate-generation methods.

C. Simulation Example

In order to illustrate the use of filtering for spectral shaping and prewarping for control of the reverberation pdf, consider simulating a linear frequency-modulated (LFM) waveform with bandwidth $W = 100$ Hz, duration $D = 1$ s, sampling frequency $f_s = 200$ Hz, shape parameter $\alpha = 3$, scale parameter $\lambda = 1/\alpha = 1/3$, and no source–receiver motion-induced Doppler effects.

The autocorrelation function of an LFM waveform [46], after accounting for basebanding by the center frequency, is approximately

$$\tilde{R}_{ss}(\tau) = \frac{\sin\left(\pi W\tau\left(1 - \frac{|\tau|}{D}\right)\right)}{\pi W\tau}. \tag{77}$$

The digital filter that shapes the spectrum is formed from $\tilde{R}_{ss}(\tau)$ by sampling about the origin every $1/f_s$ seconds. Choosing an odd number of filter taps $L = 2K+1$, the FIR filter coefficients are

$$b_i = \tilde{R}_{ss}((i - 1 - K)T) \tag{78}$$

for $i = 1, \ldots, L$ where $T = 1/f_s$ is the sampling period. For signals that do not have an analytic expression or approximation for their ACF, the filter coefficients may be easily obtained numerically by generating the complex envelope of the transmit waveform at the appropriate sampling rate and Doppler scale and performing a numerical correlation for the desired number of lags (K positive and negative).

Setting $K = 20$, which yields an $L = 41$ tap FIR filter, and applying (75) and (76) results in $\alpha_0 = 1.02$ and $\lambda_0 = 0.495$. The moderate α method described in Section II-B is used to generate 10 000 + L independent K-distributed random variables

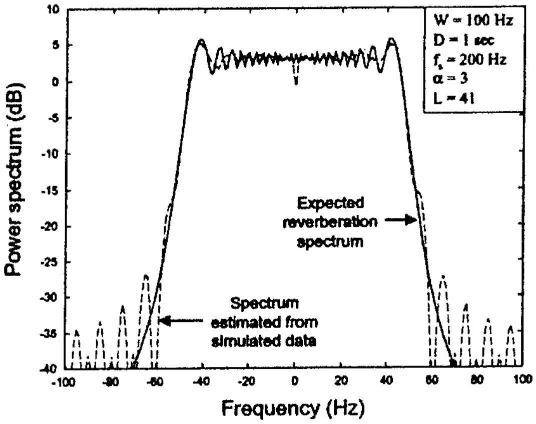

Fig. 6. Reverberation spectrum as estimated from simulated data and transmit waveform. A 41-tap FIR filter was used to shape the spectrum of the simulated data.

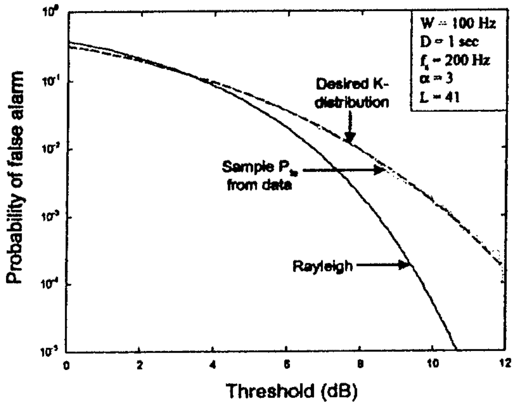

Fig. 7. Probability of false alarm estimated from intensity of simulated data compared with desired K distribution P_{f_k} and the Rayleigh envelope P_{f_r}.

(at the complex envelope stage) with shape parameter α_0 and scale λ_0. These are filtered using an FIR filter with coefficients described in (78) and the first L output samples are discarded to account for the transient response of the filter. The resulting sequence is used to evaluate the reverberation spectrum and envelope pdf.

The spectrum of the simulated reverberation time series is estimated using a Welch periodogram with a window size equal to the signal duration (1 s), 50% overlap, and a Hanning window. It is compared with the modulus of a DFT of the transmit waveform raised to the fourth power [from (64) with $\beta_0 = \beta_1 = 1$] in Fig. 6, where it is seen to well represent the desired spectrum in terms of width and falloff in the transition bands, although the mainlobe ripple is not precisely represented and there are slightly elevated sidelobes in the rejection band, although they are still more than 30 dB below the peak value. Increasing the number of taps improves the matching at the expense of an increase in computational effort, to the point where there is little noticeable difference within 40 dB of the peak value when $K = 100$.

The probability of false alarm is estimated from the 10 000 samples of data and compared with that of the desired K distribution in Fig. 7, where the accuracy of the simulation is evident. The data, however, are not exactly K distributed, owing to the approximation used in the random-number generation and to the filter used to shape the spectrum. That the prewarped shape parameter α_0 is close to an integer indicates that the former does not play a large roll in this example. Evidently, the filtering also does not largely change the reverberation distribution from the desired K distribution, although any such differences would be more likely to appear at higher thresholds where the moment-matching is less effective. However, for the purposes of simulating the performance of sonar systems in more realistic reverberation conditions, this small mismatch will almost certainly be less than that introduced by other modeling errors.

V. CONCLUSION

Simulating sonar reverberation has traditionally been done by using either a computationally intensive point-scatterer model or a Rayleigh-distributed reverberation-envelope model with a time-varying power level. Although adequate in scenarios where reverberation arises from a multitude of scatterers, the Rayleigh model is not representative of the target-like non-Rayleigh reverberation or clutter that is commonly observed with modern sonar systems in shallow-water environments. In this paper, techniques for simulating non-Rayleigh reverberation were developed within the context of the finite-number-of-scatterers representation of K-distributed reverberation. This model effectively bridges the gap between the point-scatterer and Rayleigh-envelope models. Approximate methods for generating K-distributed random variables were developed to allow an efficient numerical implementation and to avoid the computational effort associated with simulating the response of individual scatterers. The effects of acoustic propagation through a shallow-water environment were induced by a piece-wise stationary FIR filter and a frequency-domain implementation and normalization. This combination allows statistical control of the reverberation envelope and incorporation of multipath propagation at the sonar resolution cell level, as opposed to the scatterer level for point-scatterer simulators, significantly reducing the required computational effort. Shaping of the reverberation power spectrum was also accomplished by an FIR filter chosen according to the transmit waveform and the Doppler effect induced by source–receiver motion and wide-band Doppler-matched filtering. Because the spectral shaping filter alters the statistics of the reverberation, a prewarping of the K distribution parameters was developed to allow control of the statistics of the filter output.

The fundamental limitation and benefit of the proffered simulation method is that the reverberation is generated after beamforming and matched filtering. The disadvantages of this method lie in the restriction to simulating reverberation, arising from scatterers that are smaller than the resolution cell of the sonar, an inability to include beam-to-beam correlation, and more generally a lack of control over individual scatterers. The advantage lies in the ability to quickly generate non-Rayleigh reverberation following a statistical distribution parameterized by the sonar system (beamwidth and bandwidth) and the environment (scatterer size and density), while correctly accounting for multipath propagation and spectral shape.

APPENDIX I
REFLECTION AND SCATTERING COEFFICIENTS

As described in Jensen *et al.* [40], the bottom reflection coefficient is

$$R_b(\theta_g) = \frac{\rho_b c_b \sin\theta_g - \rho_w \sqrt{c_w^2 - c_b^2 \cos^2\theta_g}}{\rho_b c_b \sin\theta_g + \rho_w \sqrt{c_w^2 - c_b^2 \cos^2\theta_g}} \tag{79}$$

where $c_w = 1500$ m/s is the speed of sound in water, $c_b = 1600$ m/s is the speed of sound in the bottom, $\rho_w = 1000$ kg/m^3 is the density of water, and $\rho_b = 2000$ kg/m^3 is the density of the bottom.

The surface reflection coefficient is

$$R_s(\theta_g) = -\exp\left\{-2k^2\sigma_s^2 \sin^2\theta_g\right\} \tag{80}$$

where $k = 2\pi/\lambda = 2\pi f/c_w$ is the wavenumber (units are 1/m) and σ_s is the root mean square (rms) roughness of the surface in meters. In the simulation of Section III, the frequency is held fixed at 2000 Hz; however, the frequency-domain implementation of the multipath filter in (44) allows a frequency-dependent amplitude to be applied to each path for the surface-reflection term.

Lambert's law is used for the bottom backscatter coefficient

$$\rho_b(\theta_g) = \sin\theta_g. \tag{81}$$

APPENDIX II
MATLAB CODE

A. Control Program—test.m

Note that the function `xcorr` requires Matlab's Signal Processing Toolbox.

```
% Generate reverb w/ and w/out multipath,
% display data, & perform statistical analysis.
clc; clear all
% Initialization
bw = 100; % Bandwidth of transmit waveform (Hz)
c = 1500; % Speed of sound in water (m/s)
d0 = 10; % Source depth (m)
db = 100; % Bottom depth (m)
t0 = 2; % Start time (s)
pfa = 1e-3; % Pfa for threshold in figure(1)
delt = 1/(pfa*bw); % Do 1/pfa indep. samples
tst = 0.5; % Time of stationarity of channel
alp = 1; % Shape parameter of K-distributed data
iseed = 50; % Seed to reset random number generators
% Generate reverb data with & without multipath
rand(‘state’, iseed); randn(‘state’, iseed);
[y, z, t0] = reverb(bw, tst, t0, delt, alp, d0, db);
% Plot normalized matched filter intensity data
tz = t0 + (0:(length(z)-1))/bw;
ty = t0 + (0:(length(y)-1))/bw;
h0 = -log(pfa); % Rayleigh env. threshold
figure(1); subplot(211);
plot(tz, abs(z).^2, [min(tz) max(tz)], h0*[1 1], ‘r--’);
axis([t0 t0 + delt 0 20]); subplot(212);
plot(ty, abs(y).^2, [min(tz) max(tz)], h0*[1 1], ‘r--’);
axis([t0 t0 + delt 0 20]);
```

```
% Simulate several sets to estimate correlation and Pfa
nset = 1e5*pfa;
for i = 1:nset-1;
  [yy, zz] = reverb(bw, tst, t0, delt, alp, d0, db);
  y = [y;yy]; z = [z;zz]; fprintf(‘.’);
end;
% Estimate and plot correlation
maxlag = ceil(0.2*bw);
[Rz, lags] = xcorr(z, z, maxlag, ‘unbiased’);
[Ry, lags] = xcorr(y, y, maxlag, ‘unbiased’);
lags = lags/bw; figure(2);
plot(lags, abs(Rz), ‘b-’, lags, abs(Ry), ‘r--’);
axis([min(lags) max(lags) 0 1.1]);
% Estimate and plot Pfa
h = linspace(0.01, max(max(abs(y)), max(abs(z)))^2, 100);
Fy = 1-cumsum(hist(abs(y).^2, h))/length(y);
Fz = 1-cumsum(hist(abs(z).^2, h))/length(z);
Fr = exp(-h); % Rayleigh Pfa
% Compute Pfa of K distribution
a = 1/alp; b = alp; tmp = 2*sqrt(h)/sqrt(a);
Fk = exp(b*log(tmp)+log(besselk(b, tmp)) - ...
  gammaln(b) - (b-1)*log(2));
figure(3); hdb = 10*log10(h);
semilogy(hdb, Fy, ‘r--’, hdb, Fz, ‘b-’, hdb, Fr, ‘g--’, ...
    hdb, Fk, ‘b--’);
axis([2 13 1e-5 1]);
```

B. Reverberation-Generation Code—reverb.m

```
function [ye, y0, t0]  =  reverb(fs, tst, t0, delt, alp, d0,
db)
% [ye, y0] = reverb(fs, tst, P, t0, delt, alp, d0, db)
% Reverb time series with m-path based on iso
% sound speed in a range-independent env
%  ye  =  reverb time series w/ m-path
%  y0 = direct path reverberation time series
%  fs = sampling frequency & bandwidth (Hz)
%  tst = time m-path is assumed stationary (s)
%  t0 = received time to start simulation (s)
%  delt = duration of output signal (s)
%  alp = shape par of input K dist (integer > = 1)
%  d0 = source depth (m)
%  db = bottom depth (m)
%
c = 1500; % Speed of sound (m/s)
fc = 2000; % Center frequency for basebanding (Hz)
trimdb = 15; % Remove paths < Peak-trimdb
% Start and end times of simulation
t0 = max(t0, 2*(db-d0)/c);
t1 = t0+delt;
% Find maximum delay -> largest FIR filter size
maxdel = 0;
for t = t0:1:t1,
  [ti, ai] = mpath_iso(t, c, d0, db, trimdb);
  maxdel = max(maxdel, max(ti));
end;
m = max(1, ceil(maxdel*fs));
% Stationarity time -> data block size
```

```
L = max(1, ceil(tst*fs));
% Kick up FIR filter size to allow for an FFT
n = 2^nextpow2(m+L-1); m = n-L+1;
% Number of blocks to get to end time
nb = ceil(delt*fs/L);
% Generate channel filter
tb = t0+(L/fs)/2+(0:nb-1)*L/fs; % Time of block
fv = (0:n-1)'*fs/n; % Frequency order for FFT
% Channel txf fcn for time block
for i = 1:nb,
  [ti, ai] = mpath_iso(tb(i), c, d0, db, trimdb);
  H(:, i) = exp(-j*2*pi*(fc+fv)*ti)*ai';
end;
% Simulate direct path (K-dx RV's w/ shape = alp)
y0 = (randn(L*nb+m-1, 1)+···
  sqrt(-1)*randn(L*nb+m-1, 1))/sqrt(2);
y0 = sqrt(-sum(log(rand(L*nb+m-1, alp)), 2)/alp).*y0;
% Indices into data vector for block-wise fft
ind = (1:m+L-1)'*ones(1, nb)+ones(m+L-1, 1)*L*(0:nb-1);
% Form matrix of blocks, fft, filter, ifft
ye = ifft(fft(y0(ind)).*H);
% Discard first m-1 samples of each block
Py = ones(L, 1)*real(diag(H'*H))'/n;
ye = reshape(ye(m:end, :)./sqrt(Py), L*nb, 1);
%-----------------------------------------------
function [tau, a] = mpath_iso(t, c, d0, db, trimdb)
% Multipath delay times and amplitudes at time t
pw = 1000; % Density of water (kg/m^3)
pb = 2000; % Density of bottom (kg/m^3)
cb = 1600; % Speed of sound in bottom (m/s)
fc = 2000; % Frequency for surface loss (Hz)
rms_rough = 0.1; % Surface RMS roughness (m)
% Find maximum number of paths
imaxodd = 2*floor(((d0+sqrt((db-d0)^2+···
          (t*c/2)^2))/db-1)/2)+1;
imaxeven = 2*floor((1+(-d0+sqrt((db-d0)^2+···
          (t*c/2)^2))/db)/2);
P = max(imaxodd, imaxeven); i = (1:P)';
% For odd values of i
iodd = find(rem(i/2, 1) = = 0.5);
if any(iodd),
  tau(iodd) = t-(2/c)*sqrt((t*c/2)^2-(i(iodd)-1).*...
        db.*((i(iodd)+1)*db-2*d0));
  tgr = asin(2*(i(iodd)*db-d0)/(c*t));
  z1 = pw*sqrt(c^2-(cb*cos(tgr)).^2);
  z2 = pb*cb*sin(tgr);
  Rb = abs((z2-z1)./(z2+z1));
  Rs = -exp(-8*(pi*rms_rough*sin(tgr)*fc/c).^2);
  Sb = abs(sin(tgr));
  a(iodd) = (Rs.^(i(iodd)-1)).*(Rb.^(i(iodd)-1)).*Sb;
end;
% For even values of i
ieven = find(rem(i/2, 1) = = 0);
if any(ieven),
  tau(ieven) = t-(2/c)*sqrt((t*c/2)^2-i(ieven).*···
          db.*((i(ieven)-2)*db+2*d0));
  tgr = asin(2*((i(ieven)-1)*db+d0)/(c*t));
  z1 = pw*sqrt(c^2-(cb*cos(tgr)).^2);
  z2 = pb*cb*sin(tgr);
  Rb = abs((z2-z1)./(z2+z1));
  Rs = -exp(-8*(pi*rms_rough*sin(tgr)*fc/c).^2);
  Sb = abs(sin(tgr));
  a(ieven) = (Rs.^(i(ieven))).*(Rb.^(i(ieven)-2)).*Sb;
end;
% Remove paths within trimdb of peak
trim = 10^(trimdb/20);
ind = find(abs(a)>max(abs(a))/trim);
a = a(ind); tau = tau(ind);
```

REFERENCES

[1] S. G. Chamberlain and J. C. Galli, "A model for numerical simulation of nonstationary sonar reverberation using linear spectral prediction," *IEEE J. Oceanic Eng.*, vol. OE-8, pp. 21–36, Jan. 1983.

[2] P. C. Etter, *Underwater Acoustic Modeling*, 2nd ed. London, U.K.: E & FN SPON, 1996.

[3] P. Faure, "Theoretical model of reverberation noise," *J. Acoust. Soc. Amer.*, vol. 36, no. 2, pp. 259–266, 1964.

[4] V. V. Ol'shevskii, *Characteristics of Sea Reverberation.* New York: Consultants Bureau, 1967.

[5] D. W. Princehouse, "REVGEN, a real-time reverberation generator," in *Proc. IEEE Int. Conf. Acoustics, Speech, Signal Processing*, vol. 2, 1977, pp. 827–835.

[6] F. C. Marshall, "A conceptual model of reverberation in the ocean," in *Proc. IEEE Int. Conf. Acoustics, Speech, Signal Processing*, vol. 2, 1977, pp. 836–839.

[7] W. S. Hodgkiss Jr., "An oceanic reverberation model," *IEEE J. Oceanic Eng.*, vol. OE-9, pp. 63–72, Apr. 1984.

[8] J. C. Luby and D. W. Lytle, "Autoregressive modeling of nonstationary multibeam sonar reverberation," *IEEE J. Oceanic Eng.*, vol. OE-12, pp. 116–129, Jan. 1987.

[9] R. P. Goddard, "The sonar simulation toolset," in *Proc. OCEANS'89 Conf.*, vol. 4, 1989, pp. 1217–1222.

[10] R. L. Culver and S. T. McDaniel, "Bistatic ocean surface reverberation simulation," in *Proc. IEEE Int. Conf. Acoustics, Speech, Signal Processing*, vol. 2, 1991, pp. 1453–1456.

[11] P. C. Etter, "Recent advances in underwater acoustic modeling and simulation," *J. Sound Vibration*, vol. 240, no. 2, pp. 351–283, 2001.

[12] N. P. Chotiros *et al.*, "Acoustic backscattering at low grazing angles from the ocean bottom. Part II. Statistical characteristics of bottom backscatter at a shallow water site," *J. Acoust. Soc. Amer.*, vol. 77, no. 3, pp. 975–982, 1985.

[13] P. A. Crowther, "Fluctuation statistics of sea-bed acoustic backscatter," in *Fluctuation Statistics of Sea-Bed Acoustic Backscatter*, W. A. Kuperman and F. B. Jensen, Eds. New York: Plenum, 1980, pp. 609–622.

[14] H. Griffiths, J. Dunlop, and R. Voles, "Texture analysis of sidescan sonar imagery using statistical scattering models," in *High Frequency Acoustics in Shallow Water*, N. G. Pace, E. Pouliquen, O. Bergem, and A. P. Lyons, Eds, La Spezia, Italy, June/July 1997, pp. 187–194.

[15] D. A. Abraham and C. W. Holland, "Statistical analysis of low-frequency active sonar reverberation in shallow water," in *Proc. 4th Eur. Conf. Underwater Acoustics*, Rome, Italy, Sept. 1998, pp. 795–800.

[16] A. P. Lyons and D. A. Abraham, "Statistical characterization of high-frequency shallow-water seafloor backscatter," *J. Acoust. Soc. Amer.*, vol. 106, no. 3, pp. 1307–1315, 1999.

[17] M. Gensane, "A statistical study of acoustic signals backscattered from the sea bottom," *IEEE J. Oceanic Eng.*, vol. 14, pp. 84–93, Jan. 1989.

[18] S. Stanic and E. G. Kennedy, "Fluctuations of high-frequency shallow-water seafloor reverberation," *J. Acoust. Soc. Amer.*, vol. 91, no. 4, pp. 1967–1973, 1992.

[19] W. K. Stewart, D. Chu, S. Malik, S. Lerner, and H. Singh, "Quantitative seafloor characterization using a bathymetric sidescan sonar," *IEEE J. Oceanic Eng.*, vol. 19, pp. 599–610, Oct. 1994.

[20] D. A. Abraham and A. P. Lyons, "Novel physical interpretations of K-distributed reverberation," *IEEE J. Oceanic Eng.*, vol. 27, pp. 800–813, Oct. 2002.

[21] M. Max, N. Portunato, and G. Murdoch, *Sub-Seafloor Buried Reflectors Imaged by Low Frequency Active Sonar*, La Spezia, Italy: SACLANT Undersea Research Centre, 1996.

[22] C. W. Holland, E. Michelozzi, P. Boni, F. Cernich, R. Rossi, and J. Osler, *Geoclutter Features on the Malta Plateau*, La Spezia, Italy: SACLANT Undersea Research Centre, 2002.

[23] C. W. Holland, G. Etiope, A. V. Milkov, E. Michelozzi, and P. Favali, "Mud volcanos discovered offshore Sicily," *Marine Geology*, vol. 199, pp. 1–6, 2003.

[24] N. C. Makris *et al.*, "The geoclutter experiment 2001: Remote acoustic imaging of sub-bottom and seafloor geomorphology in continental shelf waters," *J. Acoust. Soc. Amer.*, vol. 112, no. 5, p. 2280, 2002.

[25] J. R. Preston and D. A. Abraham, "Statistical characterization of geologic clutter observed on the STRATAFORM," *J. Acoust. Soc. Amer.*, vol. 112, no. 5, p. 2282, 2002.

[26] D. A. Abraham and A. P. Lyons, "Reverberation envelope statistics and their dependence on sonar beamwidth and bandwidth," in *Impact of Littoral Environmental Variability on Acoustic Predictions and Sonar Performance*, N. G. Pace and F. B. Jensen, Eds. Norwell, MA: Kluwer, 2002, pp. 539–546.

[27] ——, "Reverberation envelope statistics and their dependence on sonar bandwidth and scatterer size," *IEEE J. Oceanic Eng.*, vol. 29, pp. 1–12, Jan. 2004.

[28] S. Dugelay, N. G. Pace, G. J. Heald, and R. J. Brothers, "Statistical analysis of high frequency acoustic scatter: What makes a statistical distribution?," in *Proc. 5th Eur. Conf. Underwater Acoustics (ECUA'00)*, Lyon, France, July 2000, pp. 269–274.

[29] M. Gu and D. A. Abraham, "Using McDaniel's model to represent non-Rayleigh reverberation," *IEEE J. Oceanic Eng.*, vol. 26, pp. 348–357, July 2001.

[30] S. T. McDaniel, "Sea surface reverberation: A review," *J. Acoust. Soc. Amer.*, vol. 94, no. 4, pp. 1905–1922, 1993.

[31] R. C. Gauss, R. F. Gragg, D. Wurmser, J. M. Fialkowski, and R. W. Nero, "Broadband models for predicting bistatic bottom, surface, and volume scattering strengths," Naval Research Lab., Washington, DC, Sept. 30, 2002. Report NRL/FR/7100-02-10, 042.

[32] D. A. Abraham, "Statistical normalization of non-Rayleigh reverberation," in *Proc. OCEANS'97 Conf.*, Halifax, NS, Canada, Oct. 1997, pp. 500–505.

[33] K. D. Ward, "Compound representation of high resolution sea clutter," *Electron. Lett.*, vol. 17, no. 16, pp. 561–563, 1981.

[34] L. DeVroye, *Non-Uniform Random Variate Generation*. New York: Springer-Verlag, 1986.

[35] J. H. Mathews and K. D. Fink, *Numerical Methods Using MATLAB*. Englewood Cliffs, NJ: Prentice-Hall, 1999.

[36] D. A. Abraham, "Signal excess in K-distributed reverberation," *IEEE J. Oceanic Eng.*, vol. 28, pp. 526–536, July 2003.

[37] D. M. Drumheller, "Padé approximations to matched filter amplitude probability functions," *IEEE Trans. Aerosp. Electron. Syst.*, vol. 35, pp. 1033–1045, July 1999.

[38] W. L. Anderson, "Computer program numerical integration of related Hankel transforms of orders 0 and 1 by adaptive digital filtering," *Geophys.*, vol. 44, no. 7, pp. 1287–1305, 1979.

[39] D. D. Ellis and J. B. Franklin, "The importance of hybrid ray paths, bottom loss, and facet reflection on ocean bottom reverberation," in *Progress in Underwater Acoustics*, H. M. Merklinger, Ed. New York: Plenum, 1987, pp. 75–84.

[40] F. B. Jensen, W. A. Kuperman, M. B. Porter, and H. Schmidt, *Computational Ocean Acoustics*. New York: Amer. Inst. Physics, 1994.

[41] R. J. Urick, *Principles of Underwater Sound*. New York: McGraw-Hill, 1983.

[42] A. P. Lyons, D. A. Abraham, and E. Pouliquen, "Predicting scattered envelope statistics of patchy seafloors," in *Impact of Littoral Environmental Variability on Acoustic Predictions and Sonar Performance*, N. G. Pace and F. B. Jensen, Eds. New York: Kluwer, 2002, pp. 211–218.

[43] J. G. Proakis and D. G. Manolakis, *Digital Signal Processing*, 2nd ed. New York: Macmillan, 1992.

[44] R. D. Yates and D. J. Goodman, *Probability and Stochastic Processes*. New York: Wiley, 1999.

[45] D. D. Ellis, "A shallow-water normal-mode reverberation model," *J. Acoust. Soc. Amer.*, vol. 97, no. 5, pp. 2804–2814, 1995.

[46] J. V. DiFranco and W. L. Rubin, *Radar Detection*. Norwood, MA: Artech House, 1980.

Douglas A. Abraham (S'92–M'93–SM'04) received the B.S., M.S., and Ph.D. degrees in electrical engineering in 1988, 1990, and 1993, respectively, and the M.S. degree in statistics in 1994, all from the University of Connecticut, Storrs.

He was with the Naval Undersea Warfare Center, New London, CT, from 1989 to 1995, was a Senior Scientist with the NATO SACLANT Undersea Research Centre, La Spezia, Italy, from 1995 to 1998, held a Visiting Faculty position with the University of Connecticut from 1998 to 2000, and currently is a Senior Research Associate with the Applied Research Laboratory, Pennsylvania State University, State College. His work is primarily in the area of statistical signal processing applied to underwater acoustic applications. His current research interests are in representing and accounting for non-Rayleigh active sonar reverberation in signal-processing algorithms for detection, classification, and localization.

Anthony P. Lyons (M'96) received the B.S. degree in physics from Henderson State University, Arkadelphia, AR, in 1988 and the M.S. and Ph.D. degrees in oceanography from Texas A&M University, College Station, in 1991 and 1995, respectively.

He was a Scientist with the SACLANT Undersea Research Centre, La Spezia, Italy, from 1995 to 2000, where he was involved in a variety of projects in the area of environmental acoustics. He currently is a Senior Research Associate with the Applied Research Laboratory, The Pennsylvania State University, State College, where he is engaged in studies of high-frequency shallow-water propagation, acoustic interaction with the sea floor, and high-resolution characterization of sea-floor sediments.

Dr. Lyons is a Member of the Acoustical Society of America.

Non-Rayleigh Reverberation Characteristics Near 400 Hz Observed on the New Jersey Shelf

John R. Preston, *Member, IEEE,* and Douglas A. Abraham, *Senior Member, IEEE*

Abstract*—A descriptive analysis of reverberation statistics is presented for data taken during the 2001 Acoustic Clutter Reconnaissance Experiment, which was conducted on the Office of Naval Research (ONR) STRATAFORM area off the coast of New Jersey. Large area plots of reverberation versus topography are presented as a lead-in to describe the statistics of the reverberation and clutter that were observed during this experiment. A comparison of polar plot appearance of spikiness with a measure of non-Rayleigh behavior seems to correlate reasonably well and suggests that the polar plots may be useful as such an indicator of non-Rayleighness. Statistical analysis of the reverberation showed that a moderate-to-large portion of the data examined were nearly Rayleigh and that most of the data (Rayleigh-like and non-Rayleigh) were well fit by the K distribution. The bistatic data were seen to be uniformly and significantly more non-Rayleigh than the monostatic data. This disparity is believed to be mostly accounted for by the lower reverberation-to-ambient noise power levels in the monostatic data and the smaller vertical beamwidth of the bistatic source, rather than having arisen from the bistatic geometry. Analysis of the shape parameter of the K distribution as a function of bandwidth illustrated the "bandwidth" effect where the shape parameter first decreases inversely proportional to bandwidth, but then increases in a trend back toward the Rayleigh distribution at higher bandwidths. The shape-parameter estimates are seen to be well fit by the elongated patch model of Abraham and Lyons. The monostatic data were observed to have a minimum occurring at a smaller bandwidth than for the bistatic data, a result explained by the larger time spread of the multipath expected for the monostatic source owing to its larger vertical beamwidth. Analysis of a small amount of data from the 2003 Acoustic Clutter Experiment, recently conducted on the New Jersey Shelf, predicts a smaller bandwidth for the minimum of the shape-parameter curve compared to the 2001 data. It is believed that the sound-speed profiles in 2003 lead to more bottom interaction than in 2001 and, therefore, produced a larger time spread in the multipath, leading to a minimum occurring at a lower bandwidth. The results of this paper indicate that many of the phenomena observed in the analysis of reverberation-envelope statistics may be explained by appropriately considering the effects of propagation in conjunction with the sonar system with which the environment is probed.

***Index Terms*—Clutter, K distribution, non-Rayleight, reverberation, sonar.**

I. INTRODUCTION

SHALLOW-WATER low-frequency (<5 kHz) active sonar reverberation often can contain display clutter (i.e., target-like returns), usually from the ocean bottom [1], [2]. To further explore the origins of active sonar clutter, medium-range reverberation measurements and analyzes were recently conducted in the 2001 Acoustic Clutter Reconnaissance Experiment (ACRE) and the 2003 Acoustic Clutter Experiment, sponsored by the Office of Naval Research (ONR), Arlington, VA. The STRATAFORM area (short for strata formation on margins) off New Jersey was selected as the experiment area because of the high-resolution geologic and geoacoustic data that have already been collected there, because the area is known to contain buried river channels and other sub-seafloor features that may give rise to clutter, and because it is representative of continental-shelf shallow-water areas (see, for example, [3]–[8]). The 2001 experiment was a joint research effort led by the Massachusetts Institute of Technology (MIT), Cambridge, and included the Nato Undersea Research Centre (NATO URC, formerly SACLANTCEN), La Spezia, Italy, and its Research Vessel (R/V) *Alliance*, the Applied Research Laboratory at The Pennsylvania State University (ARL-PSU) State College, and the Naval Undersea Warfare Center, Newport, RI. In addition, the Space and Naval Warfare Systems Center San Diego and Naval Facilities Engineering Service Center provided a moored bistatic source courtesy of the Multi-static ASW Capabilities Enhancement Program Office at ONR, the Woods Hole Oceanographic Institute, Woods Hole, MA, set the moorings, and the University of Rhode Island, Kingston, ran the *R/V Endeavor* (a University–National Oceanographic System vessel). Many additional preliminary results and a full discussion of the 2001 ACRE sea-trial details can be found in the main overview of the results [9] and in the Geological Clutter Acoustics Experiment Report [10]. The 2003 experiment involved all the same participants except NATO URC and in 2003 the Naval Research Laboratory joined the research group.

These experiments were designed to: 1) improve our understanding of the physical mechanisms that scatter incident energy from on or below the sea floor into a receiver and can possess target-like characteristics (clutter); 2) improve the understanding of the effects of sediment composition on clutter and reverberation; 3) improve the understanding of the effects of surface morphology and composition on scattering and clutter; 4) assess the suitability of current high-fidelity reverberation and scattering models for model/data comparison and prediction; and 5) ultimately find ways to minimize the impact of clutter in shallow water via a better understanding of its relation to the underlying physics.

The principal objective of this work is to statistically characterize the non-Rayleigh behavior of reverberation seen during the 2001 ACRE sea trial over three geologically distinct subareas and to explore any dependencies of the reverberation sta-

Manuscript received August 3, 2003; revised March 10, 2004. This work was supported by the Office of Naval Research under Dr. J. Simmen (more recently Dr. N. Chotiros) and Dr. J. Kravitz, both in Code 321, under Grant N00014-03-0113 and Grant N00014-02-1-0115.

The authors are with the Applied Research Laboratory, The Pennsylvania State University, State College, PA 16804 USA (e-mail: preston@ciao.arl.psu.edu; abrahad@psu.edu).

Digital Object Identifier 10.1109/JOE.2004.830730

tistics on the sonar system or environmental characterization [goals 2), 3), and 5), above]. Section II presents an overview of the two experiments along with representative reverberation power-level and transmission-loss plots. In Section III, the main results are presented, summarizing the non-Rayleigh behavior of monostatic and bistatic pings along tracks in each of the three geologically distinct subareas. Some initial statistical observations from the 2003 Acoustic Clutter Experiment are included to evaluate changes in statistical behavior between the two sea trials. Finally, some of the data are compared with a model that predicts the effects of non-Rayleigh behavior as a function of bandwidth [11].

II. REPRESENTATIVE REVERBERATION OBSERVATIONS

This section contains an overview of the 2001 Acoustic Clutter Reconnaissance Experiment and introduces the three sites from which data are taken for the statistical analysis of Section III. Three tracks from the 2001 experiment were selected for detailed statistical characterization both for monostatic and bistatic reverberation. A discussion of large-area reverberation results (polar plots) for the three 2001 tracks is presented after the overview as a lead-in to the presentation of the non-Rayleigh statistical behavior of reverberation on the New Jersey STRATAFORM area. The clutter seen in the polar plots will be shown to often be indicative of what a sonar might sense, as well as giving insight into how the beam time series relates to the terrain. In conjunction with the transmission loss analysis of Section II-B4, these results help explain many of the phenomena observed in the statistical analysis of Section III.

A. *Overview of the 2001 Acoustic Clutter Reconnaissance Experiment*

The 2001 Acoustic Clutter Reconnaissance Experiment was conducted from April 25 to May 8, 2001. Coherent pulse-reverberation measurements were taken over the nine days from April 27 to May 5, 2001, during which time over 3000 pings were transmitted and recorded. Local reflection-loss experiments were conducted by Holland from May 5 to May 7 (see [12] for a description of his techniques). Extensive oceanographic and transmission-loss measurements were made as part of the sea trial. Reverberation measurements were carried out using a towed horizontal line array (HLA) in conjunction with a towed source for monostatic measurements and a moored source for bistatic measurements. Objectives included validation of physics-based models of scattering from bottom and subbottom features [13], [14].

The *R/V Endeavor* deployed and operated the bistatic source consisting of a moored vertical array of seven omnidirectional XF-4 flextensional sources vertically spaced at 1.625 m with a total on-axis source level of (usually) 222 dB re 1 μPa at 1 m at 420 Hz. The primary equipment for the monostatic reverberation measurements deployed by NATO URC's *R/V Alliance* were two omnidirectional Mod 40 flextensional sources vertically spaced at 1.9 m with a total on-axis source level of 212 dB re 1 μPa at 1 m at 400 Hz. The horizontal line array was a 254-m three-aperture Prakla low-frequency array with design frequencies of 375, 750, and 1500 Hz. For all the 2001 results, the 127-m aperture (750-Hz design frequency) was used, corresponding to a beam width of 2.2° at 400 Hz. Although the Prakla array had a dynamic range limitation of 12 bits at the hydrophones' analog-to-digital converters, the 48 dB of variable gain was used to minimize clipping over all but approximately the first second after the direct arrivals. Signals used for both monostatic and bistatic measurements were linear frequency-modulated (LFM) or time-gated sinusoids contained in the 370–450-Hz band. In what is presented below, only an LFM sweep from 390–440 Hz is used, but there are three variants since pulse lengths of 0.5, 1, or 2 s were used. Multiple tow directions are necessary to resolve the left–right ambiguity of the line array, so tracks were often paired with offset headings typically between 15° and 30°. The array was towed at a speed of 4–5 kn. After a turn, the arrays were allowed to stabilize (about 10 min), after which interleaved monostatic and bistatic coherent pulses were transmitted to make reverberation measurements. Track legs were often 10 km in length, so the time required for each leg of the experiment was typically about 75 min, plus at least 15-min time required on the turns (the typical turning angle was ~210°).

Fig. 1 shows all the ship tracks (in green), along with the STRATAFORM area bathymetry [3], the buried river-channel centers (in black), subbottom horizons called R–reflectors (in red, where a higher impedance layer comes closest to the sea floor), and small surficial features such as iceberg scours (in blue); all provided by Goff [6]. Centers of the three primary Sites 1–3 are indicated on the map as S1, S2, and S3. These sites are generic subareas in Fig. 1 and are very roughly 25 × 25 km in size. This STRATAFORM area is considered to be representative of many continental shelf areas but, as will be explained later, each of the three sites has some unique geologic properties. The bathymetry structure was mapped to resolutions of about 30 m over the study area. Further details of the receiving arrays, and of the ARL-PSU data acquisition, processing, and display descriptions, are in [15] and [16]. Time domain beamforming and signal basebanding was done in software using algorithms developed by NATO URC's R. Hollett.

B. *Selected Reverberation Results From ACRE*

1) Site 1: Site 1 was selected because it had the highest concentration of known buried river channels [3], [17]. It is covered by sandy sediment with relatively high compressional speeds [18]. Typical river channels are 10–1000 m across and meander over kilometer scales in length and are buried 1–15 m deep in this area. The first example of this section describes reverberation from a ping on track 87 near N 39° 18′ and E 72° 50′ at Site 1. This ping is from May 4. Water depths ranged from ~65–85 m. The sound speed there on that day was near 1492 m/s at the surface, with a moderate sound-channel axis around 50 m and sound–speed minimums of 1472–1475 m/s. The Prakla array was deployed to a nominal depth of ~35 m and the *R/V Endeavor* source center was at 41 m and the *R/V Alliance* source was centered at 30 m. Winds were moderate with a Beaufort wind force ~4–5. Directional background noise was often present and ship traffic seemed to be light to moderate.

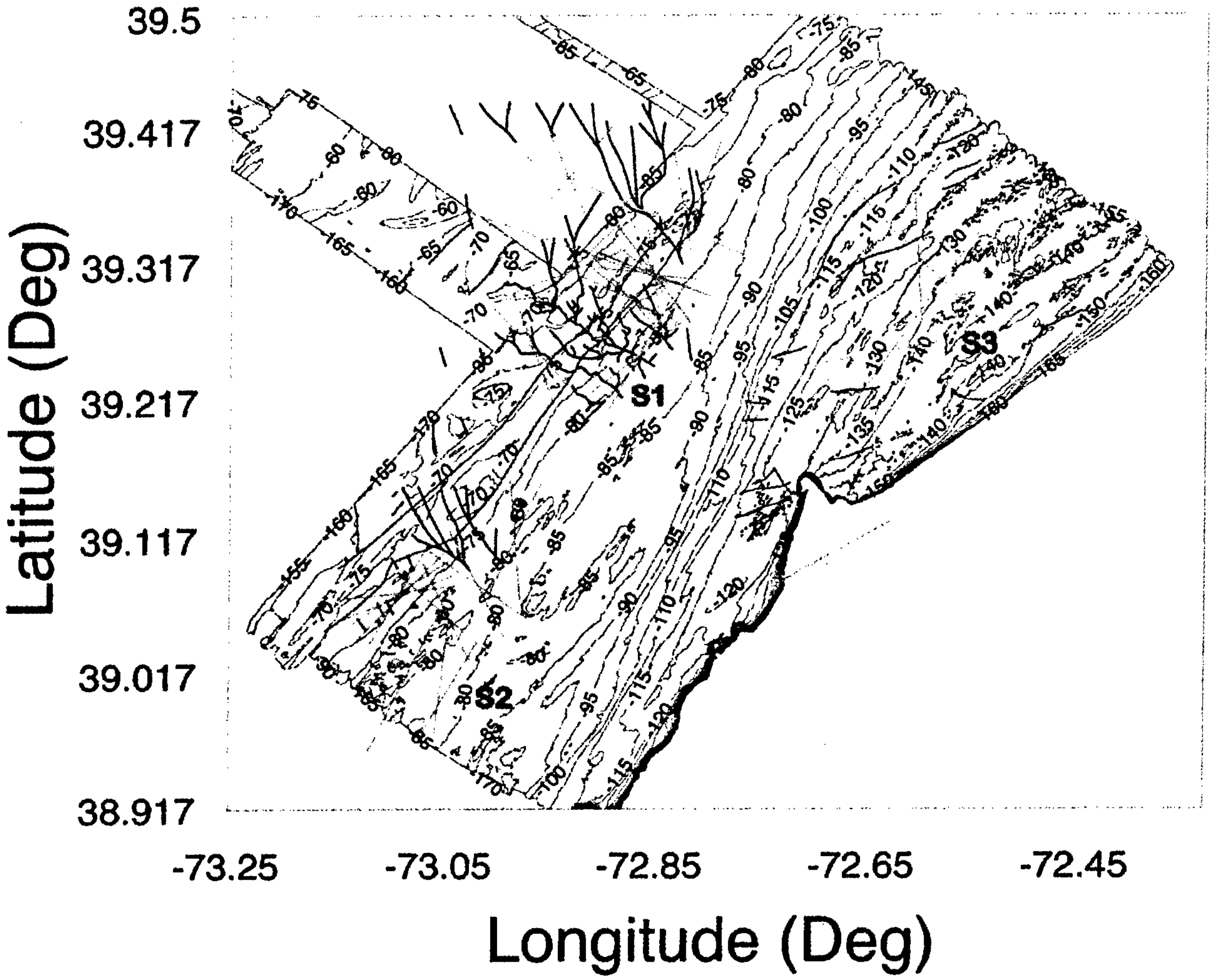

Fig. 1. Map of STRATAFORM area bathymetry and 2001 ACRE ship tracks (green lines), buried river channels (black dendritic lines), subbottom horizons (red), and small topographic features (blue), courtesy of Goff *et al.* [3], [17]. Primary sites (regions) S1, S2, and S3 are indicated in red.

Fig. 2 shows the polar display of this matched filtered bistatic reverberation event from track 87, Site 1, on the towed array in a 50-Hz band centered at 415 Hz from a 1-s LFM ping. This figure, and all subsequent polar plots of reverberation, employs a compression algorithm in range [19] prior to plotting. However, only the uncompressed matched filtered time series are used in Section III to perform the statistical analysis of the clutter. Fig. 2 also contains an overlay of the geologic features including both old (thin dendritic lines) and new river-channel interpretations (thick dendritic lines) by Nordfjord *et al.* [20] and Goff *et al.* [21]. Higher ambient noise (shipping) was present near both endfire directions. Reverberation is color-coded versus intensity and time is mapped bistatically into location using actual source and receiver locations. Directional ambient noise (usually shipping) above the average background noise is seen as radials from the array in the plots. This is a single ping, so the data contain the array ambiguity, i.e., there is a mirror image about array heading that is distorted in the bistatic displays. In these plots, clutter is defined as localized returns that are well above the background. After reviewing many plots similiar to Fig. 2, one can say that there is some correlation between some of the clutter and the buried river channels SW of the source/receiver ellipse (the lineated returns that follow the channels, but in this figure those partial correlations are obscured by the river channel overlay). Clearly, there are other clutter returns that are not well mapped to any currently known features.

2) Site 2: Site 2 was selected because of the erosional blowout pits shown in blue in Fig. 1 [17] and because of its proximity to previous transmission-loss measurements by other researchers [22]. The blowout pits are roughly 1–10-m deep and often less than 1 km in extent. It also is covered with a high-speed sandy sediment [18]. The second example of this section describes reverberation from a ping on May 1, track 17, near N 39° 05′ and E 73° 05′ at Site 2. Water depth was approximately 70–85 m. Fig. 3 shows the sound-speed profiles for five times, taken from *R/V Alliance* during the seven tracks run on this day. Most of the profiles showed speeds of 1485–1487 m/s at the surface and typically had a very weak sound-channel axis and a sound speed minimum of ~1473–1478 m/s at a depth of ~32–50 m. However, as first noted by Gauss and Ellis [23], the sound-speed structure at this site was highly variable

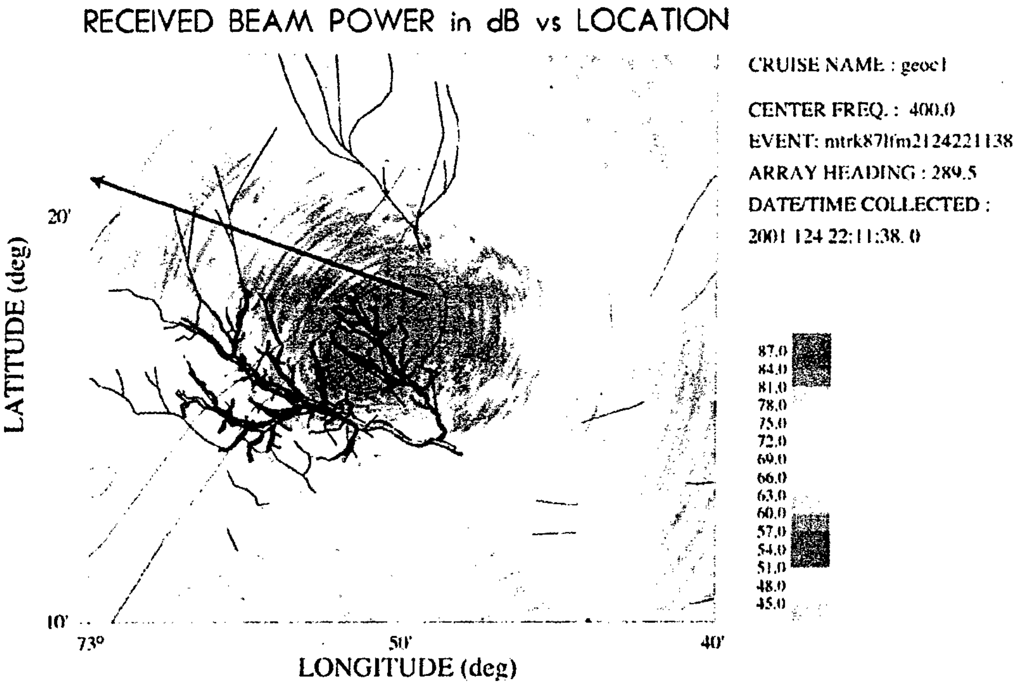

Fig. 2. Polar plot of the bistatic matched-filtered reverberation near Site 1 on the New Jersey Shelf using a 1-s LFM from 390 to 440 Hz, track 87. The black arrow indicates the array heading (the base of the arrow indicates the array position and the tip of the triangle symbol Λ) in the ellipse shows the location of the bistatic source. River-channel interpretations (from 2002 and 2003) are courtesy of Nordfjord *et al.* [20] and Goff *et al.* [21].

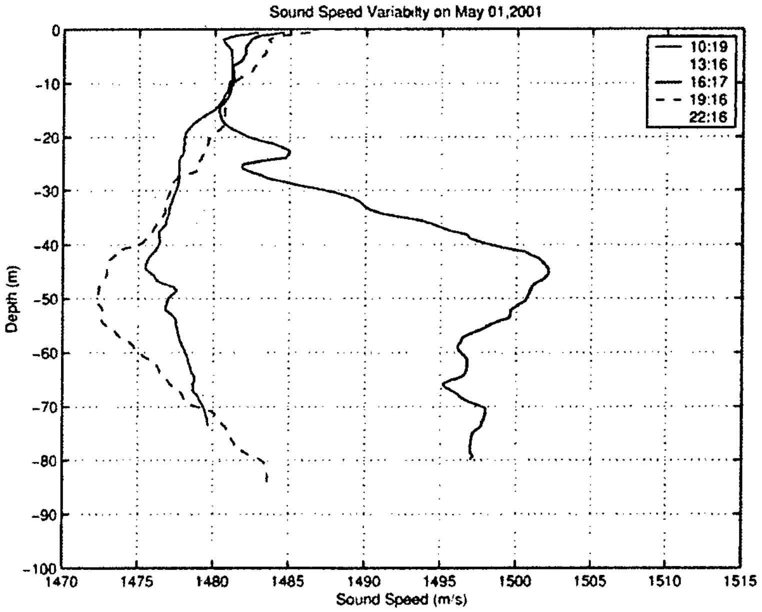

Fig. 3. Variability in sound speed during reverberation measurements near Site 2 on May 1, 2001.

in space and probably at least somewhat variable in time. The profile taken at 16:17 was mostly taken to the south of Site 2 nearer the shelf break and in the deeper water in the Site 2 area. The other four (well-behaved) profiles were taken in the shallower section of Site 2 to the north–northwest. These four profiles are more typical of shallow-water areas. The reason for the difference is that there are warm-water eddies from the Gulf Stream that can bring warm water nearer the shelf break and can result in higher speed areas in the middle of the water column. Winds were moderate with a Beaufort wind force ∼3–4.

Fig. 4 shows the polar display of matched filtered bistatic reverberation from track 17 at Site 2, on a towed array in the same 50-Hz band centered at 415 Hz from a 1-s LFM ping. The Prakla array was deployed to a nominal depth of ∼42 m and the *Endeavor* source was at 55 m and the *R/V Alliance* source was centered at 36 m. In this case, most higher level noise is coming from the near forward endfire direction, with noise also

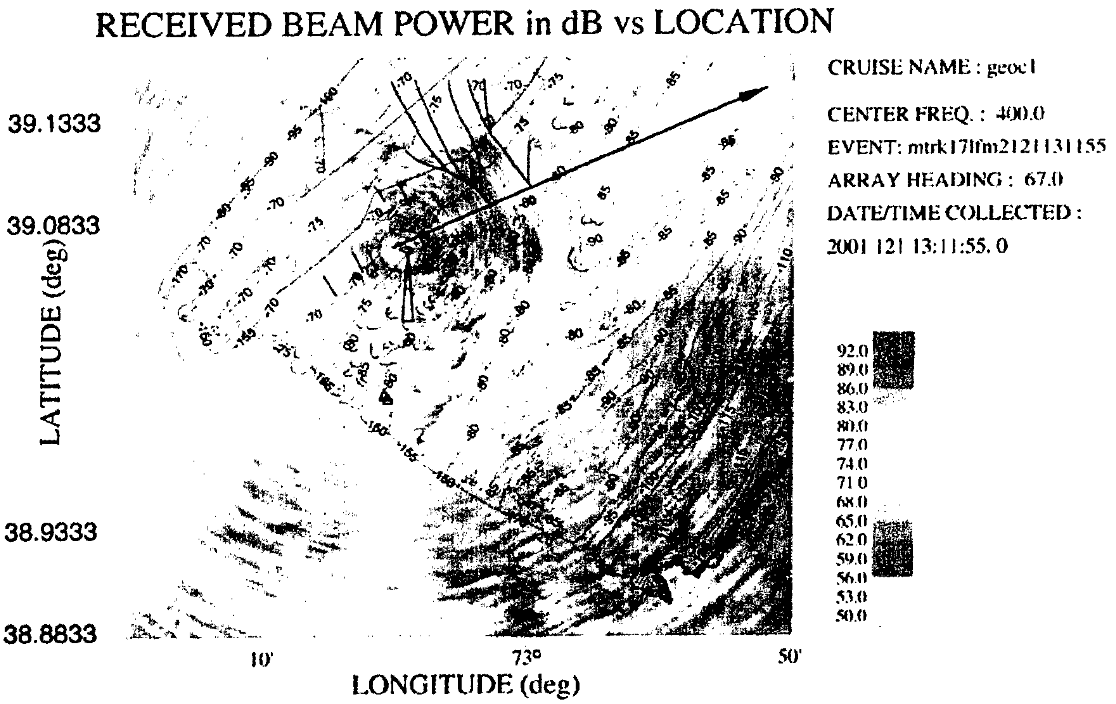

Fig. 4. Polar plot of the bistatic matched filtered reverberation near Site 2 on the New Jersey Shelf using a 1-s LFM from 390–440 Hz, track 17. The black arrow direction indicates the array heading, the base of the arrow the array position, and the tip of the long thin triangle in the ellipse shows the location of the bistatic source.

from near-aft endfire. Strong azimuthally anisotropic scattering is usually associated with bathymetric features (here, anisotropy refers to azimuthally dependent scattering as seen by the receiver array). Strong scattering can clearly be seen from the large orange-colored splotches running from SW to NE between the 80-m contours and almost due south of the source-receiver ellipse. (Note that the contour line is referred to here only to help locate clutter features; it is not implied that it produces a strong return by itself.) A look at other pings shows that the area just described and not its mirror image is the source of the high backscatter. These features were persistent from ping to ping, but change apparent shape over the track, as seen by the array. There is no obvious bottom or subbottom feature indicated near these splotches. Hypotheses among the Acoustic Clutter team researchers for the source of these returns include: 1) unmapped river-channel branches [7], [8]; 2) possible gas pockets; or 3) biologic activity [24]. Also, there are the two closely spaced acoustic reflectors deployed ~ 8 km due south of the source, which give a nice reflection in this event (shown as two triangles (△△) near an 80-m contour label).

3) Site 3: Site 3 was selected because it is an area covered by stiff clay and, as a result, contains low-relief iceberg scours [17] (shown in blue in Fig. 1). It has a somewhat lower sediment compressional sound speed than Sites 1 and 2 [18]. Typical iceberg scours have approximately 1–2-m relief and are order 10 m across and usually are less than a few kilometers in extent. This final example from the 2001 experiment shows reverberation from a ping on track 64 near N 39° 15′ and *E* 72° 37′ at Site 3. This ping is from May 2. Water depths ranged from ~95–140 m. The sound speed was spatially quite variable, near 1490–1495 m/s at the surface, with a moderate sound-channel axis in the shallower parts near Site 3, but becoming stronger as the water depth increased (see [16]). Critical depths (the depth where sound speed at the surface is exceeded causing nonbottom interacting paths to become important) ranged from 50–100 m in the deeper profiles. Sound-speed minimums of 1473–1475 m/s at depths of ~31–52 m were observed at this site on this day. The same trend of seeing warmer water masses as the ship moved to the southwest is true at this site also. The Prakla array was deployed to a nominal depth of ~65 m and the *R/V Endeavor* source center was at 84 m and the *R/V Alliance* source was centered at 65 m. Winds were very light: the logs show a Beaufort wind force of ~2–3.

Fig. 5 shows the polar display of a matched filtered bistatic reverberation event from track 64 on the towed array in a 50-Hz band centered at 415 Hz from a 1-s LFM ping. Ambient noise (shipping) seemed high only close to forward endfire directions. After looking at many polar plots (not shown here), there is some good correlation between some clutter returns and the area between the two *R* reflectors (in red) near the 120-m contours northwest of *R/V Alliance* in Fig. 5. This also was a source of very high backscatter in the SUS experiments of the 2001 Boundary Characterization Experiment conducted between Sites 1 and 3 two weeks later (see [16]). There also is some correlation between some of the clutter and highly corrugated bathymetry from over the shelf break to the south of *R/V Alliance.* (In this plot, the above two clutter areas are on ambiguous bearings from each other.)

4) Some Observations Regarding Transmission Loss and Bottom Insonification: In order to better understand some of the statistical results of Section III, it is instructive to model how the sound is insonifying the bottom (and water column). It is not

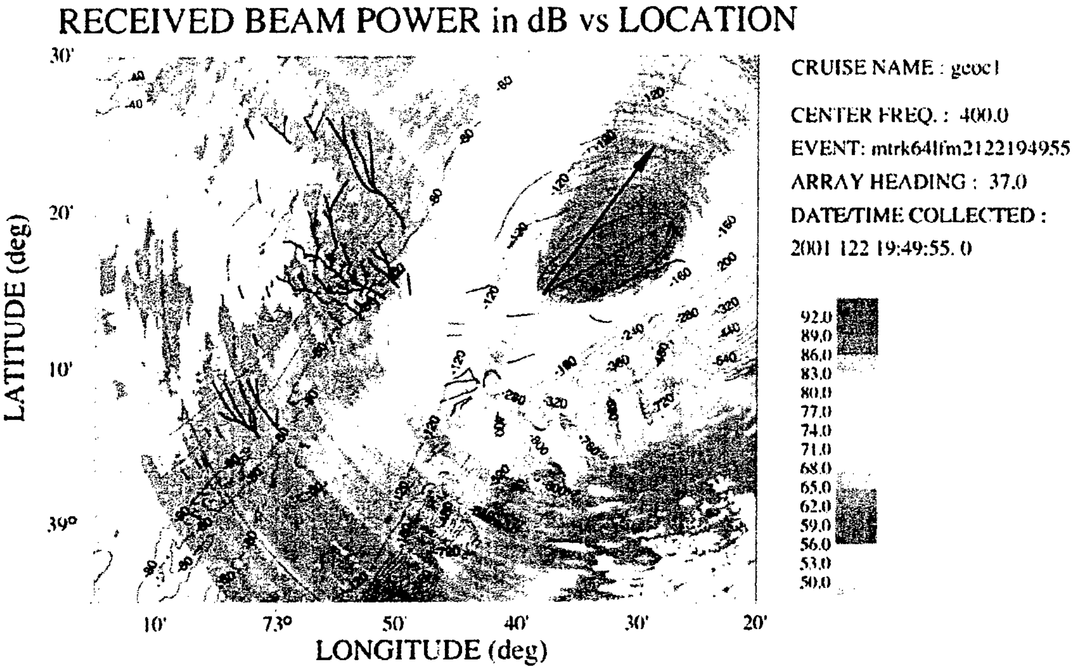

Fig. 5. Polar plot of the bistatic matched filtered reverberation near Site 3 on the New Jersey Shelf using a 1-s LFM from 390–440 Hz, track 64. The black arrow indicates the array heading, the base of the arrow the array position, and the tip the triangle symbol ∧ in the ellipse shows the location of the bistatic source.

possible to show all the results; therefore, an example from track 87 at Site 1 is selected, where the modeled transmission loss is computed using the range-dependent acoustic model (RAM), a high-angle parabolic equation code by Collins [25]. Close to Site 1, during the 2001 Boundary Characterization Experiment, an SUS inversion technique was used to estimate a geoacoustic model for the sediment [16]. The southward-looking broadside beam (200°T) from near the center of track 87, where *R/V Alliance* was almost due north of the source (see Fig. 2) has been selected. Fig. 6 shows the estimated transmission loss at 400 Hz from the monostatic two-element source on *R/V Alliance* for a source depth of 30 m. The inset on the right shows the sound–speed profile used in the computation; a weak duct was present at that time and location. Note the modest range dependence along the track with a depth range of ±3 m. One can see that, for the monostatic transmission, the sound field is fairly diffuse up to about the 18-km range.

By contrast, a similar computation was made for the seven-element bistatic source on *R/V Endeavor*. This time, a line of bearing from the source that crossed the monostatic line at about midpoint was chosen. In this case, the bearing direction was 223°T. The result is shown in Fig. 7. Here, one can see that the larger vertical aperture of this source produces considerably more focusing of the sound field near the center of the water column. More importantly, along the bottom there are many more gaps in the bottom insonification than were observed in the monostatic case. The transmission loss from a point source scatterer at an average bottom depth back to the array produced a diffuse field with no focusing.

When similar modeling was done for Site 2 (not shown here), however, the radial selected was more variable in depth (±14 m) and the sound–speed profile changed fairly substantially (three profiles from Fig. 3 were used). The geoacoustic model used at Site 2 was from Evans and Carey [22]. The result was that both the monostatic and bistatic fields were diffuse near the sea floor, but the bistatic field remained more focused in the water column than the monostatic field. The point of this is that, for much of the Site 1 data, the transmission-loss results shown in Figs. 6 and 7 are probably representative. At Site 2 in directions away from the southeast quadrant and away from the shelf break, the profiles are similar to Site 1 and the focusing differences shown in Figs. 6 and 7 should be present. Otherwise, the conditions need to be modeled on a case-by-case basis to check these effects.

One final point is that the initial sediment compressional speeds at Site 1 were estimated at 1660 m/s and at Site 2 to be 1560 m/s, but jumping to 1610 m/s after 5 m. Ram modeling shows the field in the sediment decays rapidly away from the water-bottom interface at both sites. As one reviewer pointed out, the 15 or more dB attenuation visible in the one-way modeling in the first 3 m of the sediment implies buried feature returns will suffer double this from scattering, so favors biologic scatterers in the water column if present, as the probable cause for the observed clutter, even with much lower target strengths from biologics. Coupling that with bottom scattering strengths, which decrease with lower grazing angles versus the flat grazing-angle dependence from water-column volume scattering makes the argument for biologics as a source of the clutter even stronger. Similar arguments were previously noted by other reserchers as well [26].

5) Some Remarks on Data From the 2003 Experiment: Bistatic data were also collected during the recent 2003 Acoustic Clutter Experiment on the New Jersey Shelf. For this experiment, the receiver was the new ONR Five Octave Research Array (FORA) [27], using a 64-element subaperture cut for 500

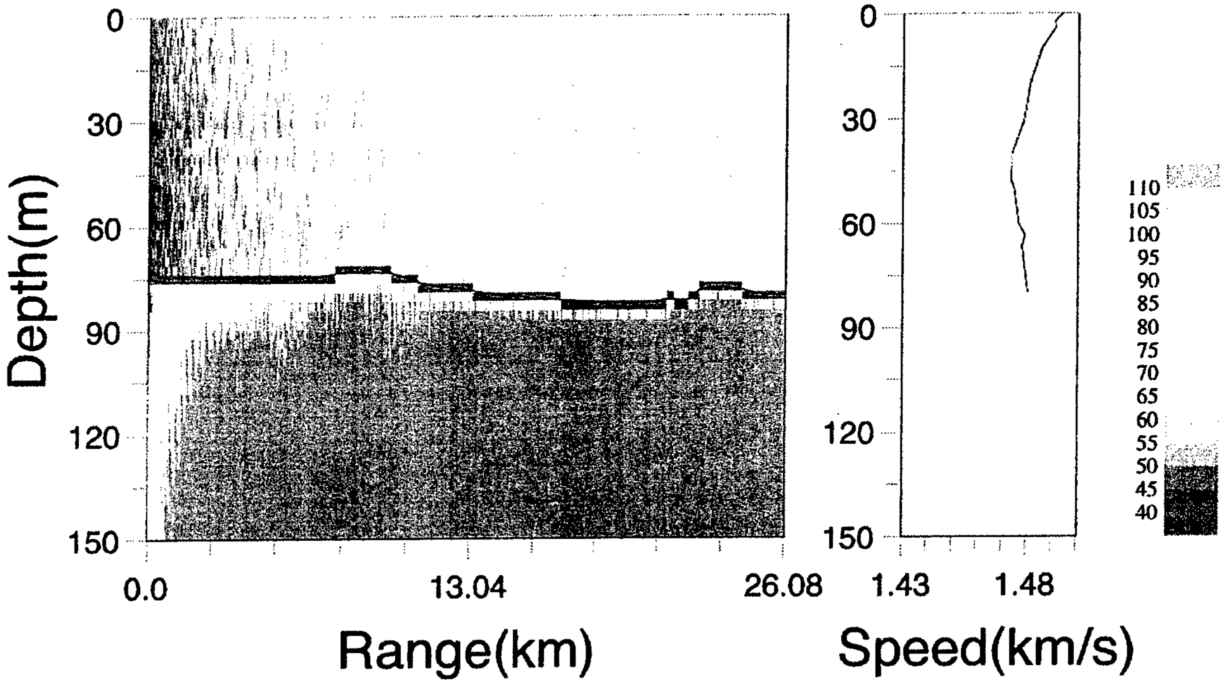

Fig. 6. Computed transmission loss (decibels) at 400 Hz at Site 1 for the monostatic source along a line of bearing from track 87 heading 200° T. The sound–speed profile is shown on the right.

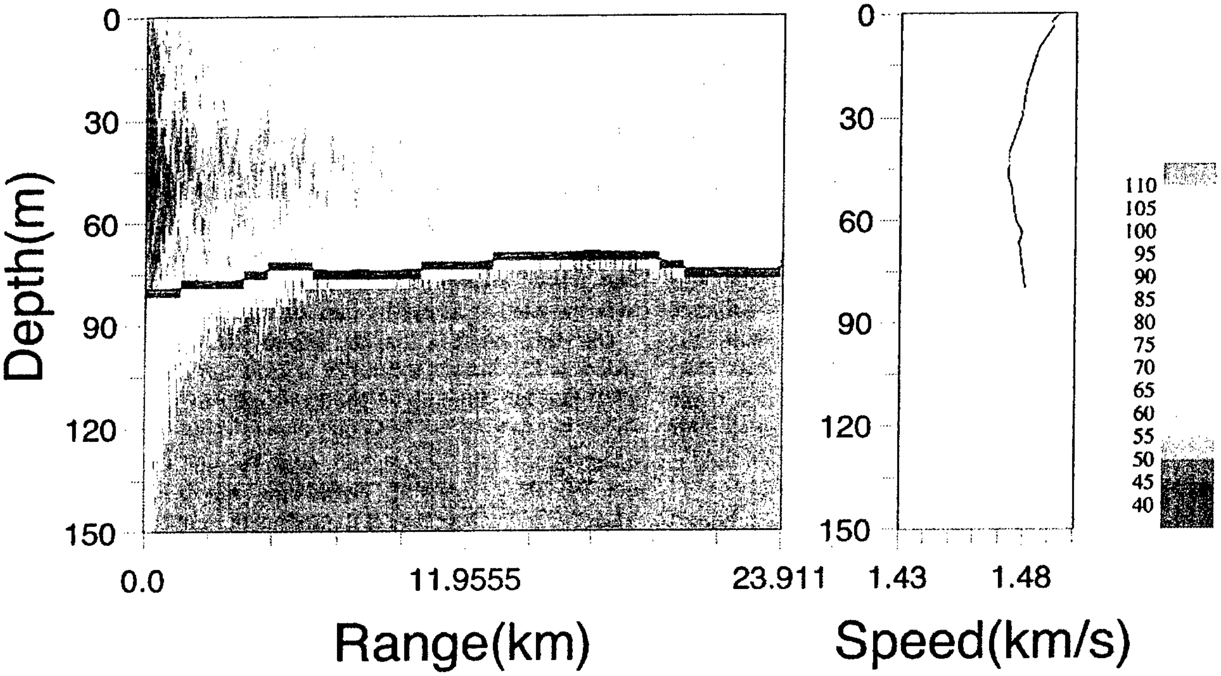

Fig. 7. Computed transmission loss (decibels) at 400 Hz at Site 1 for the bistatic source along a crossing line of bearing from the bistatic source at Site 1 heading 223° T. The sound–speed profile is shown on the right.

Hz. The source was identical to that used in 2001 for bistatic data collection. The FORA has 19 bits of dynamic range at the hydrophones, about 42 dB more than the Prakla array. The main difference from 2001 is the theoretical (Hann-shaded) broadside beamwidth for FORA at 400 Hz is 3.0°, not 2.2°. The statistical analysis in Section III will include a few results from the FORA receiver. The sound speeds were generally measured as simpler downward-refracting profiles implying a lot of bottom interacting paths and should mean that the bistatic source will not show the focusing effects shown in Section II-B4 for the 2001 data. Also, the sound–speed structure was not nearly as variable spatially as in 2001.

III. STATISTICAL CHARACTERIZATION OF THE CLUTTER

In the case where reverberation after beamforming and matched filtering is caused by diffuse and/or numerous sources, the envelope statistics can usually be described by a Rayleigh probability distribution. When that is not the case, more complex statistical characterizations are needed. Several probability density functions (pdfs) have been considered for this, including the Weibull, log-normal, Rayleigh-mixture, and K distributions [28]–[34].

Recently, a novel physics-based derivation of the K distribution [35] based on a finite number of scattering elements within the sonar range-bearing resolution cell has allowed the analysis of the reverberation-envelope pdf as a function of system parameters such as beamwidth and bandwidth [11], [35], [36]. In this section, the fit of the K and Rayleigh distributions to the data observed on the New Jersey Shelf during the two Acoustic Clutter Experiments is examined and then the shape parameter of the K distribution is evaluated from the data as a function of bandwidth and is compared with the change predicted by an elongated patch model [11].

The pdf of the K distribution for the matched filter envelope Y is

$$f_Y(y) = \frac{4}{\sqrt{\lambda}\Gamma\alpha}\left(\frac{y}{\sqrt{\lambda}}\right)^{\alpha} K_{\alpha-1}\left(\frac{2y}{\sqrt{\lambda}}\right) \tag{1}$$

where $K_\nu(x)$ is the modified Bessel function of the second kind with order ν and argument x, α is the shape parameter, and λ is a scale parameter controlling the power that is $\alpha\lambda$. The cumulative distribution function (cdf) of the K distribution is

$$F_Y(y) = 1 - \frac{2}{\Gamma(\alpha)}\left(\frac{y}{\sqrt{\lambda}}\right)^{\alpha} K_{\alpha}\left(\frac{2y}{\sqrt{\lambda}}\right). \tag{2}$$

When the shape parameter is large, the K distribution approaches the Rayleigh pdf and when it is small, it can have tails significantly heavier than the Rayleigh pdf. In the model described in [35], it was also shown that α is proportional to the number of scattering elements (discrete scatterers or scattering patches) in the sonar's range-bearing resolution cell and, therefore, is proportional to beamwidth and is inversely proportional to bandwidth. However, as examined in [11] and [36], when bandwidth is increased to the point where some of the scattering elements are overresolved in range, the shape parameter actually begins to increase in a trend back toward the Rayleigh distribution. This non-monotonic bandwidth dependence has only previously been observed on data from the NATO Undersea Research Centre's SCARAB 1997 sea trial [36].

In this paper, the bandwidth analysis is performed on the ACRE sea-trial data where the elongated patch model of [11] is seen to provide a good fit to the K distribution shape parameter as estimated from the data. As derived in [35], suppose that K-distributed reverberation arises from the contributions of many patches having random sizes (B_i) and Gaussian responses ($\tilde{Z}_i$) that arise from interface scattering. The complex envelope of the reverberation (cf. [11, eq. (1)]) is

$$\tilde{Z} = \sum_{i=1}^{n} \sqrt{B_i}\tilde{Z}_i \tag{3}$$

where n is the number of patches contributing to the sonar resolution cell. The elongated patch model of [11] assumes that the contribution (area) of each patch is

$$B_i = \min\{S_i^p\Delta, S_i\} \tag{4}$$

where S_i is the exponentially distributed scatterer size in m^2, $\Delta = c/(2W)$ is the downrange extent of the sonar range resolution cell in m, c is the speed of sound in m/s, W is the bandwidth in Hertz, and $p \in (0,1)$ controls how elongated the patch is. Elongation in range is obtained with $p \in (0, 0.5)$, while elongation in cross-range is obtained from $p \in (0.5, 1)$. Extreme elongation occurs in range as $p \rightarrow 0$.

A. Data Normalization

Prior to statistical evaluation of the reverberation envelope, the time-varying mean power level of the reverberation time series must be removed. Such a detrending of the data is identical to the processing found in active sonar systems prior to implementation of a detection algorithm and, in the context of false alarms arising from clutter, helps to focus our analysis of reverberation on the areas of degraded sonar system performance. Normalization differs from fixed time-varying gain (TVG) systems where a deterministic scale is applied to the data to remove a known time dependence (e.g., to remove the effects of cylindrical spreading or sonar resolution cell area). Such TVG systems can in fact induce apparent non-Rayleighness, as the resulting data still have some residual time-varying power level.

Normalization requires the estimation of the reverberation power level as a function of time. This is most efficiently accomplished using a cell-averaging normalizer [37], [38], which may be implemented by using a finite impulse response (FIR) filter to estimate the average power level in leading and lagging windows [39] about the cell being normalized. There are other normalizers that can provide more robust estimates of the reverberation power level (e.g., order statistic-based normalizers [37]), but these usually require significantly more computational effort. The large quantity of data processed in this analysis precluded the use of other normalizers.

Because the normalized data are formed by scaling the received data by an estimate of the reverberation power, the tails of the normalized data are heavier than that of the unnormalized data (after a perfect equating of the power). This adverse effect is minimized by keeping the windows of the reverberation power estimate large. However, they must be chosen to be small enough to capture the nonstationarity of the reverberation time series, which clearly depends on the complete acoustical characterization of each environment (sound velocity profiles, bathymetry, bottom characterization, etc.). Thus, each data set must be evaluated to determine the appropriate window size by viewing the normalized data. A properly tuned normalizer produces a time series with a constant background power level over a longer duration than the window size. A second more elusive indicator is that reasonable reverberation pdf models fit the normalized data; that is, if the data are not fit well by either a Rayleigh, K, Weibull, or log-normal distribution, then the normalizer is not working correctly. A Rayleigh mixture is not included in this list because it is flexible enough to provide a good fit to data that have not been properly normalized [40]. Admit-

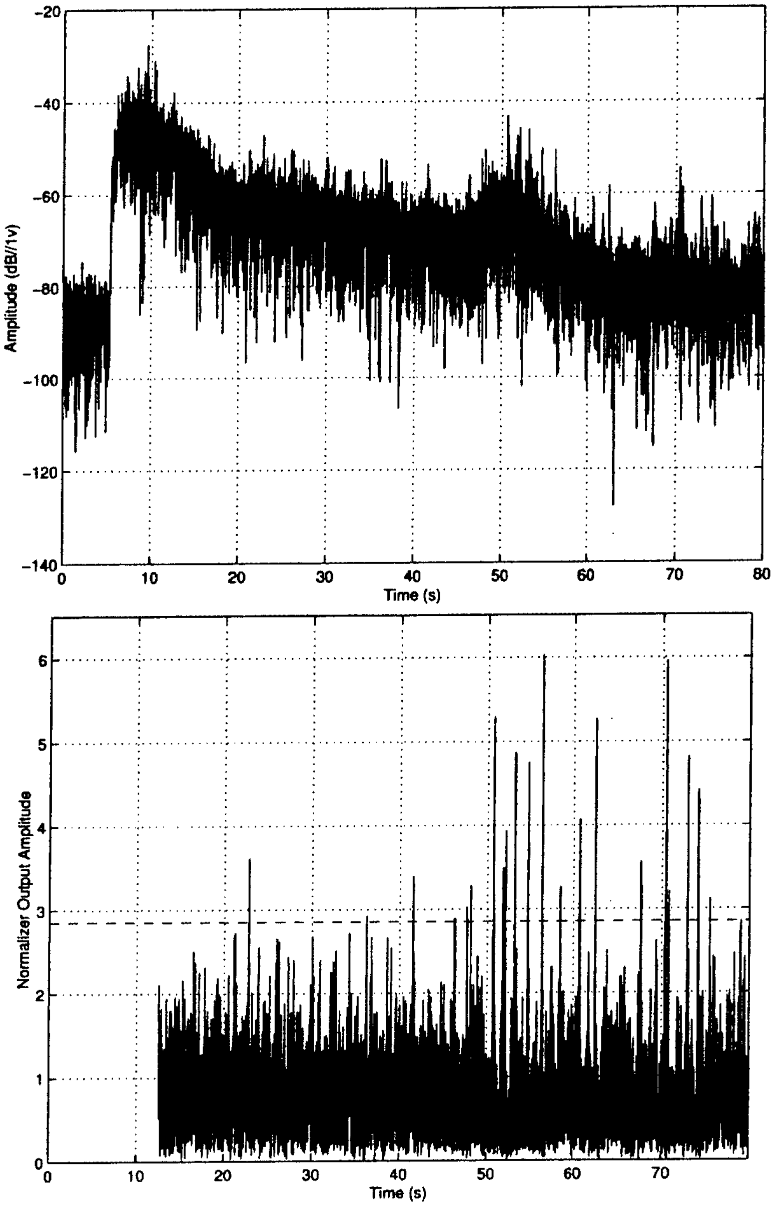

Fig. 8. Upper plot: Sample of matched-filtered beam time series for track 1 × at Site 1 (from a beam 15° forward of broadside). Lower plot: Sample of the cell-averaged normalizer output on the data shown in upper plot. The dashed line on the lower plot is the threshold chosen so that only one threshold crossing, on average, would occur when the data are Rayleigh distributed.

tedly, these are not well-defined quantitative measures of how well a normalizer is working and indicate that setting up a normalizer can be more of an art than a science.

For the majority of the Acoustic Clutter Experiment data, a split window approximately 1.6 s long (40 independent samples on each side of the cell being normalized) captured the nonstationarity of the reverberation. With the present case of a decimated sampling rate of 150 Hz and a 50-Hz bandwidth, 40 independent samples require windows 120 samples long on each side of the datum being normalized. The gap in the split window normalizer was three independent samples wide. Analysis is typically limited to times when reverberation exceeds the noise by 6 dB.

As an example of this process, consider the beam data shown in the upper portion of Fig. 8, which are taken from a beam 15° forward of broadside from track 1 × at Site 1. Application of the cell-averaging normalizer produces the time series shown in the lower portion of Fig. 8. The dashed line on the plot is the threshold chosen so that only one threshold crossing, on average, would occur when the data are Rayleigh distributed (i.e., the probability of false alarm is $1/n$ where n is the number of independent samples in the time series and the threshold is $\sqrt{\log n}$, where n is $\sim$ 3400 in this case). The time-varying nature of the time-series is evident in that the data seem to be slightly spikier for this particular beam at later times than at earlier times. The assessment that the later times for this beam are spikier is also borne out by the larger number of threshold exceedances as compared with earlier times and will be examined in further detail in Section III-B. These threshold exceedances would result in false alarms in an

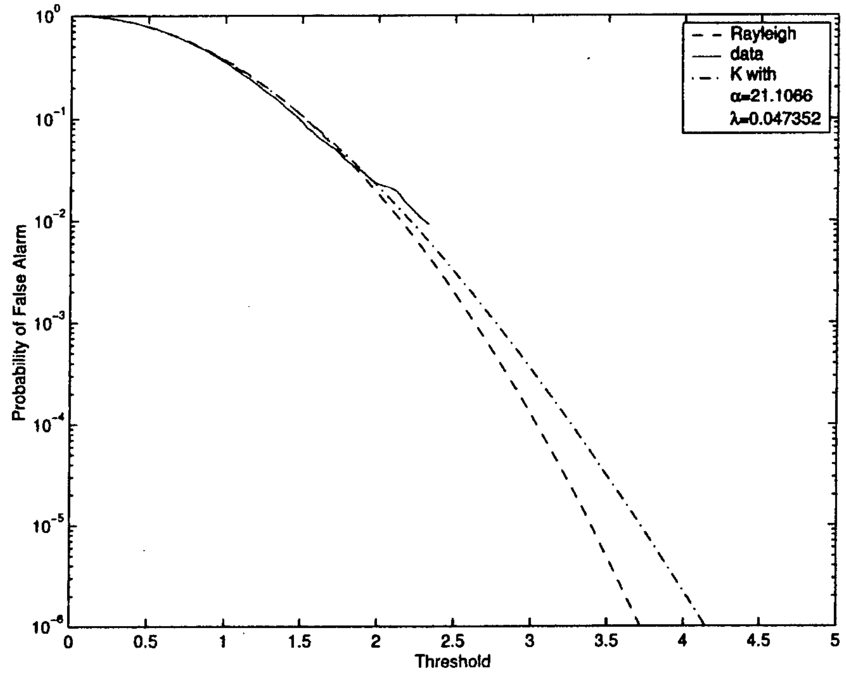

Fig. 9. PFA estimated from the first half of track 1 × (shown in Fig. 8) compared with that for the Rayleigh and K distributions. The data are only slightly non-Rayleigh and are well fit by the K distribution.

active sonar system and, therefore, are of significant interest. It should be noted that most beams that were examined did not display such diversity in the reverberation-envelope statistics; this beam was chosen to illustrate the potential nonstationary that can be induced by the environment. All of the beamformed data considered for statistical analysis are processed by the cell-averaging normalizer.

B. *Descriptive Analysis of the Reverberation Statistics*

Once the beamformed and matched-filtered data have been normalized to have unit power, the higher order moments may be evaluated for departure from the Rayleigh distribution and for fitting with the K distribution. In order to compare these statistical distributions to those estimated from the data, the parameters of each distribution must be estimated. For the Rayleigh distribution, the sample power is used. The K distribution, however, requires more effort to obtain estimates of its shape and scale parameters. The method of moments technique described by Joughin *et al.* [41] is used. In this technique, the analytical moments of the probability distribution are equated to those estimated from data and the resulting (possibly nonlinear) equations are inverted to obtain the parameter estimates. The specific algorithm employed for this data analysis (which requires an iterative solution to the moment equation) may be found in [35], where it is noted that there is a nonzero probability that the moment equations are not invertible. Any block of data where this occurs is not considered for further analysis.

Prior to this analysis of the higher order statistics, the data are thresholded at approximately the 15-dB level to remove outliers. That is, any values greater than 15 dB in the normalized data are removed before the statistical analysis is performed. These data are essentially discrete clutter that may be surface ships, ship wrecks, spatially isolated and well-defined clutter, or even electronic glitches from data acquisition and represent a small portion of the data analyzed. This threshold level corresponds to a $P_{fa} = 10^{-14}$ for Rayleigh-distributed data. Were the data K distributed, the P_{fa} would be $5 \cdot 10^{-5}$ when $\alpha = 1$, $4.8 \cdot 10^{-6}$ when $\alpha = 2$, and $4 \cdot 10^{-9}$ when $\alpha = 10$. Thus, even for data that are significantly non-Rayleigh ($\alpha = 1$), it is unlikely that reverberation would be incorrectly removed.

1) Fit of the K Distribution: The quality of the estimation of the K-distribution shape parameter improves as the number of independent samples used in the estimation increases. Thus, it is desirable to have as large a data block as possible, yet necessary that the pdf of the data remain stationary within the block. Fortunately, as can be seen by comparing the two plots in Fig. 8, the statistics of the normalized data vary more slowly than that of the prenormalized data, where the change in the average power dominates. As previously mentioned, the first half of the data in that particular beam seems less spiky than the latter half. This result runs counter to the expectation that to first order, the data should be more Rayleigh-like when the sonar resolution cell size increases, as it will for increasing range. (Resolution cells at the latest times in Fig. 8 are approximately seven times larger than those at the earliest times.) This then represents a nonstationarity with range in the dominant scattering mechanism. The nonstationarity is also evident in estimates of the probability of false alarm (P_{fa}), as seen in Figs. 9 and 10. In Fig. 9, the P_{fa} is estimated from the first half of the data in Fig. 8 and is seen to be only slightly non-Rayleigh, as emphasized by the moderate shape parameter estimated ($\hat{\alpha} = 21.1$), and well fit by the K distribution. In Fig. 10, the data are estimated from the latter half of the ping and are seen to be distinctly more non-Rayleigh ($\hat{\alpha} = 1.36$), although the K distri-

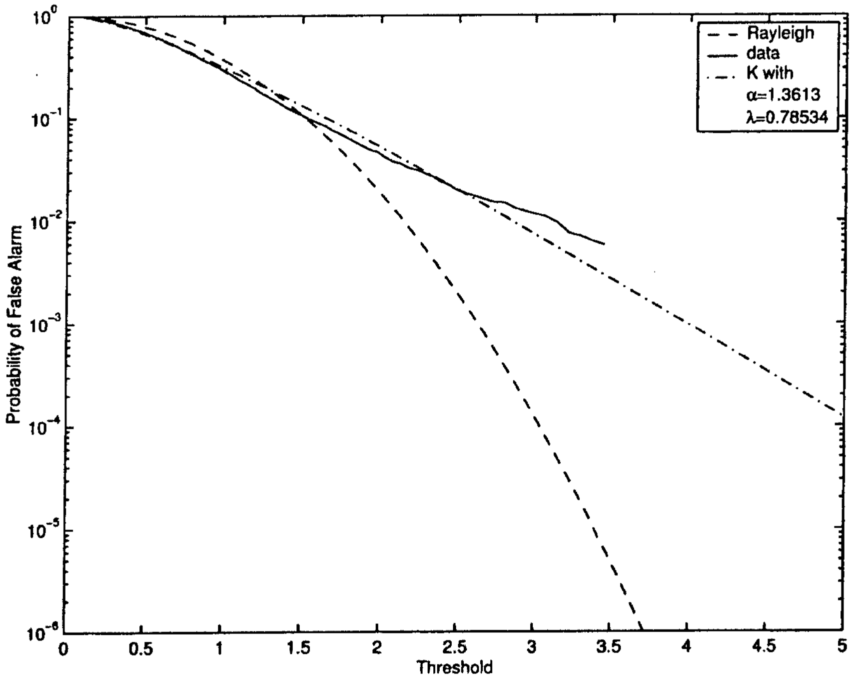

Fig. 10. PFA estimated from the second half of track 1 × (shown in Fig. 8) compared with that for the Rayleigh and K distributions. The data are significantly non-Rayleigh and are reasonably well fit by the K distribution.

bution still provides a reasonable fit. Further examination of the beam geometry indicates that the left-looking bearing (32°T) follows the 75-m bathymetry contour toward the head of the Hudson Canyon and the right-looking bearing (242°T) points gently upslope toward the New Jersey shoreline. At approximately 50 s, both beams depart the study area into regions where detailed bathymetry is not available, so a precise accounting for this clutter is not possible. It is, however, important to note that such clutter can occur at, or perhaps is accentuated by, relatively low reverberation-to-noise power ratios (RNRs). As can be seen in the upper plot of Fig. 8, the RNR dips as low as 6 dB between 50 and 80 s. Such situations may allow other scattering mechanisms or ambient noise to dominate the diffuse reverberation, although the latter is not a likely culprit in this case, based on the uncluttered 5 s of ambient noise visible at the beginning of the time record in the upper plot of Fig. 8.

These comparisons of the P_{fa} curves help to evaluate the fit of the pdf models; however, they are unwieldy and require visual interpretation. An alternative, more quantitative method lies in the use of the Kolmogorov–Smirnoff (K–S) test [42], which uses as a test statistic the maximum absolute difference between a model cdf and the sample cdf estimated from a block of data. The asymptotic p value is used to determine a threshold for accepting the model as either a good or bad fit to the data where the model uses parameters estimated from the data. The p value may be interpreted as the probability of observing a value of the test statistic more extreme when the pdf model being tested truly represents the data. Therefore, small p values lead to rejecting the hypothesis that the data follow the model being tested while larger ones lead to acceptance. The p value of the K–S test statistic for track 1 × is shown in Fig. 11, where it is estimated from blocks of data containing 500 independent samples (10 s of data). From the p value it can be seen that the first half of the ping is well modeled by both the Rayleigh and K distributions, while only the K distribution provides a good fit in the latter half. This may also be intuited from the estimate of the K-distribution shape parameter, which is large in the first half of the ping and small in the latter half.

In using the shape parameter of the K distribution for the statistical analysis of large quantities of reverberation data, it is first necessary to determine that the K distribution provides a good fit. For the broadside beam (or a nearby one if the broadside beam is dominated by ambient noise) from each ping on the three tracks described in Section II, the asymptotic p value [42] of the K–S test statistic is computed for both the Rayleigh and K distributions from blocks of 500 independent samples that overlap by 80%. The median p value over the beam for each of the distributions and the median estimated shape parameter is shown in Tables I–VI for each ping, with the odd-numbered tables representing the monostatic data and the even-numbered tables the bistatic data. Table VII contains the results from a small amount of bistatic data from the 2003 experiment (the monostatic source was not used in 2003). Of the 50 pings represented in these tables, only three have median p values such that the Rayleigh distribution provides a better fit than the K distribution. This does not necessarily imply that such a small percentage of the data are Rayleigh distributed, as evidenced by the summary statistics presented in Table VIII. There, it is seen that 59%–86% of the monostatic data blocks in each track passed the K–S test for a Rayleigh distribution at level 0.05 (i.e., the p value for the block was greater than 0.05), yet all of these data passed the test for the K distribution. Similarly for the bistatic data, 21%–56% of the data blocks in each track passed the test for a Rayleigh distribution and 86%–100% passed the test for

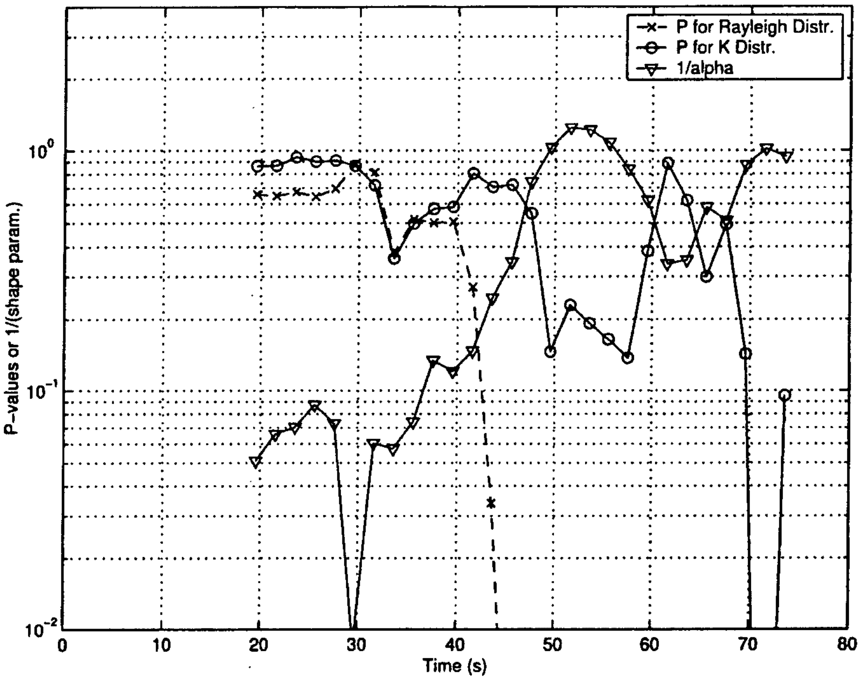

Fig. 11. K–S test statistic p values for the Rayleigh and K distributions for track 1 × and the inverse of the corresponding estimates of the K-distribution shape parameter α. The p values illustrate that the data are well fit by both the Rayleigh and K distributions in the first half, but are only well fit by the K distribution in the latter half. The K-distribution shape parameter correspondingly has high values (inverse small in the figure) in the first half and low values (inverse large in the figure) in the latter half.

TABLE I
STATISTICAL ANALYSIS OF MONOSTATIC DATA ALONG TRACK 87 AT SITE 1 FROM THE ACRE 2001 DATA SET. OF THE 13 PINGS ANALYZED, 58.8% OF THE DATA BLOCKS PASSED THE K–S TEST AT THE 0.05 LEVEL FOR THE RAYLEIGH DISTRIBUTION AND 100% PASSED FOR THE K DISTRIBUTION

Site	Pulse length (s)	Julian day/time	Track no.	Display clutter	Median α	Median p_K	Median p_R
1	1	124 234908	87	some	14.6	0.56	**0.87**
1	1	124 234458	87	some	3.72	**0.90**	0.01
1	1	124 233228	87	some	4.06	**0.45**	0.008
1	1	124 232818	87	some	20.2	**0.74**	0.35
1	1	124 231548	87	no	20.0	**0.83**	0.76
1	1	124 231138	87	no	9.11	**0.61**	0.13
1	1	124 225908	87	some	7.08	**0.74**	0.08
1	1	124 225458	87	some	2.16	**0.53**	6.0×10^{-7}
1	1	124 224228	87	yes	3.56	**0.48**	0.002
1	1	124 223818	87	no	13.7	**0.78**	0.39
1	1	124 222548	87	some	7.92	**0.86**	0.53
1	1	124 220908	87	some	4.18	**0.64**	0.11
1	1	124 220458	87	some	5.55	**0.91**	0.07

TABLE II
STATISTICAL ANALYSIS OF BISTATIC DATA ALONG TRACK 87 AT SITE 1 FROM THE ACRE 2001 DATA SET. OF THE EIGHT PINGS ANALYZED, 23.4% OF THE DATA BLOCKS PASSED THE K–S TEST AT THE 0.05 LEVEL FOR THE RAYLEIGH DISTRIBUTION AND 85.7% PASSED FOR THE K DISTRIBUTION

Site	Pulse length (s)	Julian day/time	Track no.	Display clutter	Median α	Median p_K	Median p_R
1	1	124 234048	87	yes	1.17	**0.24**	1.4×10^{-12}
1	1	124 233458	87	yes	1.65	**0.19**	3.3×10^{-7}
1	1	124 231818	87	yes	0.90	**0.054**	1.2×10^{-16}
1	1	124 230138	87	yes	3.43	**0.79**	0.0006
1	1	124 224458	87	yes	1.83	**0.10**	5.2×10^{-16}
1	1	124 222818	87	yes	18.1	**0.95**	0.64
1	1	124 221138	87	yes	2.41	**0.55**	0.0003
1	1	124 220048	87	yes	7.32	**0.84**	0.12

the K distribution. A random sampling of other pings that were analyzed exhibited similar trends; therefore, these results are expected to hold for the majority of the data from the 2001 experiment. Thus, the K distribution is accepted as a good model

TABLE III
Statistical Analysis of Monostatic Data Along Track 17 at Site 2 From the ACRE 2001 Data Set. Of the 6 Pings Analyzed, 66.7% of the Data Blocks Passed the KS Test at the 0.05 Level for the Rayleigh Distribution and 100% Passed for the K Distribution

Site	Pulse length (s)	Julian day/time	Track no.	Display clutter	Median α	Median p_K	Median p_R
2	0.5	121 124515	17	some	4.66	**0.95**	0.22
2	1	121 124835	17	some	20.7	**0.75**	0.49
2	0.5	121 132655	17	some	17.9	0.35	**0.36**
2	1	121 133015	17	some	2.67	**0.91**	0.0001
2	0.5	121 134335	17	some	3.26	**0.75**	0.01
2	1	121 134655	17	some	8.02	0.54	**0.80**

TABLE IV
Statistical Analysis of Bistatic Data Along Track 17 at Site 2 From the ACRE 2001 Data Set. Of the Nine Pings Analyzed, 20.8% of the Data Blocks Passed the K–S Test at the 0.05 Level for the Rayleigh Distribution and 88.1% Passed for the K Distribution

Site	Pulse length (s)	Julian day/time	Track no.	Display clutter	Median α	Median p_K	Median p_R
2	0.5	121 123655	17	yes	2.70	**0.60**	0.0002
2	1	121 124015	17	yes	2.28	**0.57**	0.0002
2	1	121 125335	17	yes	1.52	**0.54**	7.0×10^{-7}
2	1	121 130335	17	yes	1.48	**0.31**	7.0×10^{-6}
2	1	121 131155	17	yes	2.63	**0.87**	0.0009
2	1	121 132335	17	yes	2.30	**0.71**	0.001
2	1	121 133835	17	yes	1.82	**0.55**	6.8×10^{-7}
2	0.5	121 135155	17	yes	2.19	**0.63**	0.0001
2	1	121 135515	17	yes	4.19	**0.76**	0.048

TABLE V
Statistical Analysis of Monostatic Data Along Track 64 at Site 3 From the ACRE 2001 Data Set. Of the Five Pings Analyzed, 86.4% of the Data Blocks Passed the K–S Test at the 0.05 Level for the Rayleigh Distribution and 100% Passed for the K Distribution

Site	Pulse length (s)	Julian day/time	Track no.	Display clutter	Median α	Median p_K	Median p_R
3	1	122 194135	64	some	15.0	**0.82**	0.49
3	1	122 195815	64	some	3.30	**0.54**	7.1×10^{-5}
3	1	122 201455	64	some	16.6	**0.63**	0.30
3	1	122 203135	64	some	14.8	**0.70**	0.44
3	1	122 204815	64	some	35.7	**0.94**	0.937

TABLE VI
Statistical Analysis of Bistatic Data Along Track 64 at Site 3 From the ACRE 2001 Data Set. Of the Five Pings Analyzed, 34.7% of the Data Blocks Passed the K–S Test at the 0.05 Level for the Rayleigh Distribution and 100% Passed for the K Distribution

Site	Pulse length (s)	Julian day/time	Track no.	Display clutter	Median α	Median p_K	Median p_R
3	1	122 193315	64	some	9.72	**0.79**	0.14
3	1	122 194955	64	some	3.22	**0.63**	0.007
3	1	122 202315	64	some	5.25	**0.53**	0.19
3	1	122 205635	64	some	4.55	**0.83**	0.02
3	1	122 212955	64	some	4.75	**0.66**	0.008

TABLE VII
Statistical Analysis of Bistatic Data From the ACE 2003 Data Set. Of the Four Pings Analyzed, 56% of the Data Blocks Passed the K–S Test at the 0.05 Level for the Rayleigh Distribution and 100% Passed for the K Distribution

Site	Pulse length (s)	Julian day/time	Track no.	Display clutter	Median α	Median p_K	Median p_R
1	1	121 191225	85c	some	5.4	**0.74**	0.06
1	1	124 124405	lp_2	yes	2.6	**0.84**	0.0007
2	1	127 121405	141a_1	some	12.5	**0.91**	0.47
2	1	128 174405	201_2	yes	5.6	**0.84**	0.16

for further statistical analysis where the shape parameter represents the degree of Rayleighness of the data with high values being Rayleigh-like and low values having potentially significantly heavier tails.

The fifth column in Tables I–VII contains a qualitative assessment of the degree of clutter observed in the corresponding polar plot of each ping (three of these are found in Section II). In general, the pings that exhibit clutter in the polar plot are asso-

TABLE VIII
PERCENTAGE OF BLOCKS ON EACH TRACK PASSING THE K–S TEST AT LEVEL 0.05 AND MEDIAN α FOR THE SEVEN TABLES PRESENTED PREVIOUSLY

	Monostatic			Bistatic		
Event	Rayleigh	K	Median α	Rayleigh	K	Median α
Site 1/Track 87	58.8	100	5.45	23.4	85.7	1.99
Site 2/Track 17	66.7	100	6.17	20.8	88.1	2.30
Site 3/Track 64	86.4	100	15.7	34.7	100	4.75
2003 Misc.	n/a	n/a	n/a	56.0	100	5.34

ciated with lower α values than pings that do not. This indicates that it is possible to infer the presence of non-Rayleighness in the data by examining the polar plots.

2) Monostatic Versus Bistatic Comparison: There is a very clear difference in the reverberation-envelope statistics between the monostatic and bistatic data presented in Tables I–VI, where the latter are observed to be more non-Rayleigh than the former. The summary statistics shown in Table VIII indicate that the median shape parameter for the monostatic data was 2.68, 2.74, or 3.31 times larger than that for the bistatic data, respectively, for tracks 87, 17, and 64. There are many possible sources for this disparity, including diversity in the scatterer response, dominant scattering mechanism, sonar system transmitter, RNRs, or oceanographic conditions. However, owing to the consistency across the three sites over which the disparity is observed, the most likely contributors are systematic ones such as the RNR or differences in the sonar system transmitter.

The bistatic source had more transducers and a more vertically focused transmit beampattern, resulting in a source-power level approximately 10 dB greater than the monostatic source. Therefore, the bistatic source accentuates the lower order modes of the waveguide, keeping more energy in the middle of the water column and enabling propagation to greater ranges as compared with the monostatic source. This has led to a greater reverberation-limited regime in the bistatic data, which allowed the analysis of bistatic data from ranges approximately two or more times greater than that for the monostatic data. Despite the expectation that the larger ranges result in a proportionately larger K-distribution shape parameter, the dominant scattering mechanism may be different at these greater ranges, as for the data in Fig. 8, and bias the bistatic estimates toward lower shape-parameter values. However, the data shown in Fig. 8 were observed to be quite atypical, so this is not expected to produce the disparity observed in the reverberation statistics over all three tracks analyzed.

A more likely cause arises from the disparity in the reverberation power level with respect to the ambient noise power. The majority of the monostatic data analyzed were only about 6–10 dB above the noise level, whereas the RNR exceeded 20 dB for most of the bistatic data. Thus, the monostatic data may be contaminated by ambient noise, which is typically Gaussian distributed. (If the monostatic thresholds were set higher, there would not be enough data left on a beam to make any statistically significant conclusions.) The results of [43] illustrate how an additive Gaussian component can change the effective shape parameter of reverberation data.[1] Let the complex envelope of the received signal be $\tilde{X} = \tilde{U} + \tilde{Z}$, where the ambient noise is represented by $\tilde{Z}$, which is a zero-mean complex Gaussian distributed with power σ^2 and the reverberation is represented by $\tilde{U}$, which has a K-distributed envelope with shape parameter α_U and scale parameter λ_U. If r is the ratio of the reverberation to ambient noise power

$$r = \frac{\alpha_U \lambda_U}{\sigma^2} \tag{5}$$

then the equivalent shape parameter [11] of the envelope of $\tilde{X}$ is

$$\alpha_X = (1 + 1/r)^2 \, \alpha_U. \tag{6}$$

Thus, α_X is always greater than α_U; that is, $\tilde{X}$ is always more Rayleigh-like than $\tilde{U}$ and the two shape parameters are related by a multiplicative factor $(1 + 1/r)^2$. For an RNR of 6 dB, this results in a factor of 1.56 and for 10 dB a factor of 1.21. Thus, part—although not all—of the disparity between the monostatic and bistatic reverberation statistics may be accounted for by the lower RNR of the monostatic data.

The greater vertical directivity of the bistatic source (a 16.8° vertical beamwidth at 400 Hz) compared with that of the monostatic source (58.9° at 400 Hz) has another effect on the reverberation-envelope statistics. Owing to multipath propagation, reverberation at any given time is the coherent sum of the signals scattered from several different parts of the sea floor. The smaller vertical beamwidth of the bistatic source limits the number of paths (an equivalent argument can be made with modes), contributing to the reverberation. Thus, the effective number of scatterers contributing to reverberation at any given time is smaller and, therefore, the reverberation should appear to be more non-Rayleigh for the bistatic source because of its greater vertical directivity. This effect is confirmed in the transmission loss analysis of Section II-B4, where the bistatic source results in energy being more tightly focused along particular propagation paths than does the monostatic source. This increased focusing implies that there are more gaps in bottom insonification, which leads to fewer significant multipaths in the two-way channel-impulse response from source to bottom scatterer to receiver. In a modal interpretation, this results in fewer insonified modes. Based on a preliminary analysis of the effect of multipath propagation on the equivalent shape parameter (which is a topic of current research), a multiplicative factor of 2–7 is realistic for the difference between sources with the aforementioned vertical beamwidths in this type of environment. Note that if the dominant scattering mechanism were biologics in the water column, as has been hypothesized in [9] and [24], a similar effect to that described for the bottom scatterers would be expected.

---

[1] The effective shape parameter is that found by equating the moments of the K distribution with those of another distribution [11].

Thus, the disparity between the reverberation-envelope statistics of the monostatic and bistatic data from the 2001 experiment is believed to arise from a lower RNR in the monostatic data and from the greater vertical directionality of the bistatic source, which leads to the excitation of fewer modes and, therefore, fewer effective scatterers in the received reverberation at any given time. It is possible that there are differences between monostatic and bistatic scattering that may contribute to differences in the reverberation-envelope statistics; however, the two aforementioned sources are believed to dominate the statistics in this particular case. Although the reverberation-envelope statistics are more non-Rayleigh for the bistatic source, the increase in the signal-to-reverberation power ratio achieved by the vertical focusing will likely outweigh the increase in the probability of false alarm that arises from a lower shape parameter, as occurs when increasing bandwidth or the receive array aperture [44]. This highlights the importance of considering reverberation-envelope statistics in sonar system design.

3) Geographic Variability: After reviewing many polar plots of reverberation, like those in Section II, strong concentrated spiky clutter returns were seen generally from Sites 1 and 2, but less so at Site 3, where the clutter often came from larger connected scattering patches usually associated with bottom features. These observations are confirmed by the data in Tables I–VI and are obvious from Table VIII, where the median shape parameter estimate for the data at Site 3 is more than twice that for Sites 1 and 2.

As noted in Section II, the high clutter at Sites 1 and 2 sometimes correlates well with parts of buried features, like sections of the river channels and parts of the R reflectors (see also [9] and [16]). Other high clutter returns seem uncorrelated with any known features, be it surficial or sub-sea floor. However, much of the subbottom is still not mapped in the detail that is needed. The semirandom nature of these correlations makes it very difficult to conclude that these geologic features are the dominant scattering mechanism [9]. There usually does not seem to be a good correlation of the clutter returns with the iceberg scours ($\sim$ 1-m relief) or blowout pits ($\sim$ 5-m relief). Those features are both on the order of (or less than) one wavelength in height for the 400-Hz coherent pulse data presented here. The lower values of α at Site 3 are probably influenced by the fact that it was not possible to get the source and receiver below the much deeper and more pronounced sound channel in that area [9], [16], so ray paths to the bottom were more shielded. A very interesting observation from the 2001 experiments (including the 2001 Boundary Characterization Experiment) was that the sound–speed structure was much more variable in space than in time for the *R/V Alliance* expandable bathythermograph (XBT) data. The incursion of warm gulf stream water from eddies was much more likely as one moved toward deeper water on the New Jersey Shelf, with a resulting double-duct feature. In the shallower parts of the STRATAFORM area, the sound–speed profiles seemed more typical of shallow waters and usually were simpler downward-refracting or weakly ducted environments.

Results from SUS-based analysis in the same area during the 2001 Boundary Characterization Experiment indicated that the New Jersey Shelf was not a particularly high-clutter area compared to other rapid environmental assessment (REA) areas, like the Malta Plateau, the Scotian Shelf, or Kiparissia Bay, when using REA SUS processing techniques [15], [45], [46]. This might imply that many other REA areas could be even worse than the STRATAFORM area with respect to clutter when coherent pulses are used. However, the SUS results showed anisotropy in the diffuse reverberation as observed by a horizontal array.

One last observation is that comparison of polar plot appearance of spikiness with a measure of non-Rayleigh behavior seems to correlate reasonably well and suggests that the polar plots are valuable as such an indicator. However, they are much coarser than the actual data and, therefore, do not provide the precise characterization obtained from estimating the K-distribution shape parameter.

C. Bandwidth Analysis of the Shape Parameter

In this section, the dependence of the K-distribution shape parameter and, therefore, the reverberation-envelope statistics, on bandwidth is investigated. The transmit bandwidth of 50 Hz is not particularly large; however, the "bandwidth" effect first noted in [11] and [36] is observable. The bandwidth effect entails a decrease in the shape parameter of the K distribution inversely proportional to bandwidth when the sonar's resolution cell is larger than the scattering elements (patches or discrete scatterers) and is followed by a reversal back toward the Rayleigh distribution (i.e., larger values of the shape parameter) when the scattering elements are overresolved in range. The initial decrease in the shape parameter corresponds to a reduction in the number of scattering elements in each range-bearing resolution cell while the increase arises from a limitation of the randomness introduced by the downrange size of the scattering element. The minimum of the shape-parameter curve occurs when the downrange extent of the range-bearing resolution cell is near the *effective* size of the scattering elements. The effective size of the scattering elements is essentially their actual size convolved with the impulse response of the environment. Therefore, it is not possible (at this time) to obtain estimates of the size of the scatterers from the minima of these curves.

The processing described in [11] is implemented for bandwidths varying from approximately 0.8–50 Hz for 44 of the 50 pings analyzed in Section III-B. Similar to the analysis of Section III-B1, the shape-parameter estimates are formed from blocks of data in each beam consisting of 500 independent samples with 80% overlap; however, in this analysis, all beams are processed. The 2001 data consisted of 129 beams pointing from forward to aft endfire, the 2003 data only had 65 beams. The shape parameters for each data block are normalized by the minimum over all bandwidths in each block, averaged over each ping and over all pings, and shown as a function of bandwidth in Figs. 12–17 for the 2001 monostatic (even-numbered figures) and bistatic (odd-numbered figures) data from the three sites. The results for the 2003 bistatic data are found in Fig. 18. Normalization by the minimum

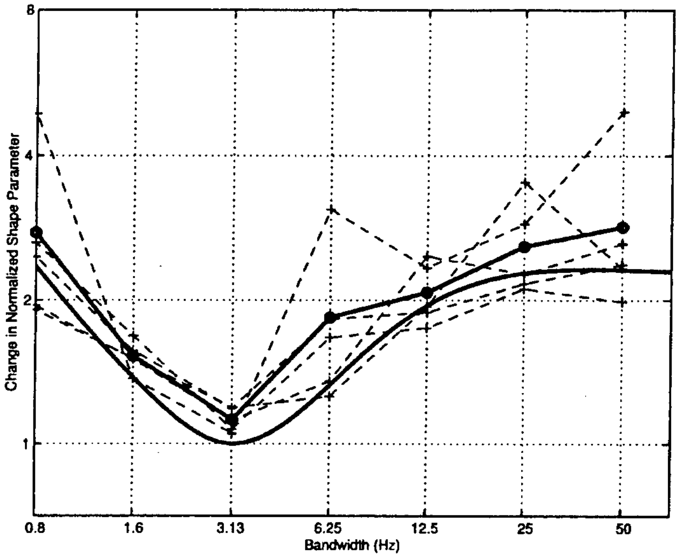

Fig. 12. Change in shape parameter of the K distribution from the minimum observed over various bandwidths where "+" marks are averages for each ping and "o" marks are averages over nine monostatic (lower power) pings from track 87 at Site 1 of the 2001 data. The solid line is that predicted from an elongated patch model (power = 0.4).

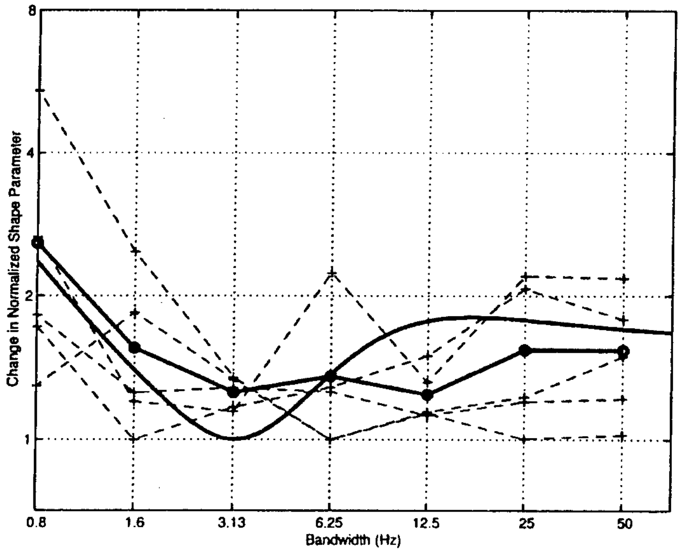

Fig. 13. Change in shape parameter versus bandwidth over seven bistatic (higher power) pings from track 87 at Site 1 of the 2001 data. The solid line is that predicted from an elongated patch model (power = 0.5).

shape parameter estimated in each data block allows comparison with the elongated patch model of [11] and removes the dependence of the shape parameter on the sonar resolution cell area, which clearly changes over the whole range of data analyzed. The elongated patch model of [11] with the power p, as indicated in the figure captions, is shown with each of the aforementioned plots and is seen to represent the data well.

Comparing the shape-parameter curves for the monostatic data to those for the bistatic data, it is seen that the minimum generally occurs at a lower bandwidth for the monostatic data. The difference is more clearly visible in the curves from Sites 2 and 3 than from Site 1. If the average size of the scatterers is small as compared with the time spreading induced by propagation, then the minimum of the shape parameter curve should be inversely proportional to the time extent of the two-way channel-impulse response (i.e., the time spread of the channel). Thus, the lower bandwidth of the minimum in the shape-parameter curve for the monostatic data corresponds to a commensurately larger time spread of the propagation, which arises from the larger vertical beamwidth of the monostatic source as compared with that of the bistatic source.

Although there are only four pings of data in the curves for the 2003 bistatic data, it is clear that the minimum occurs at a bandwidth nearly four times smaller than for the 2001 bistatic data from Site 2 and approximately two times smaller than for

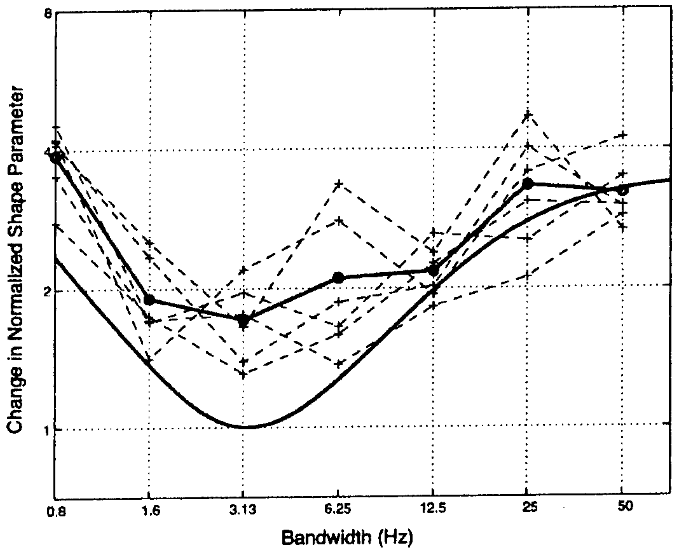

Fig. 14. Change in shape parameter versus bandwidth over six monostatic (lower power) pings from track 17 at Site 2 of the 2001 data. The solid line is what was predicted from an elongated patch model (power = 0.3).

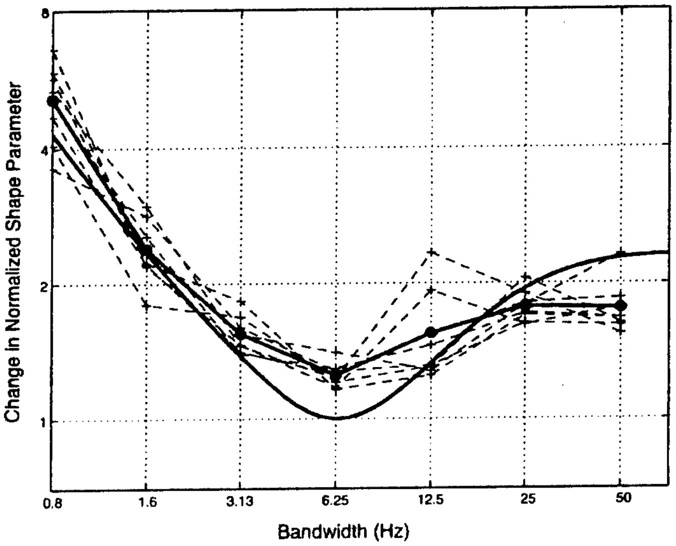

Fig. 15. Change in shape parameter versus bandwidth over eight bistatic (higher power) pings from track 17 at Site 2 of the 2001 data. The solid line is what was predicted from an elongated patch model (power = 0.4).

the 2001 bistatic data from Site 1, indicating that the effective size of the scattering elements is larger in the 2003 data.[2] Examination of polar plots of the reverberation during the 2003 experiment indicated that the clutter regions were more connected in both range and bearing, which may or may not translate into a larger effective size of the scattering elements. The sea states during the 2003 experiment were similar to those in 2001; however, as noted in Section II-B5, the sound–speed profiles measured in 2003 were generally more simply downward refracting, implying more bottom interaction. This may in fact result in a larger time spreading in the multipath, which would lead to a lower bandwidth for the minimum in the shape-parameter curves. This hypothesis is also supported by the fact that the median shape-parameter values seen in Table VIII are more than twice as large as those corresponding to the 2001 data, indicating that the 2003 data have more multipath contributing to the reverberation at any given time. This result should be qualified by the fact that only four pings of 2003 data have been analyzed thus far and, therefore, may not be representative of all of the data from this trial.

These results have several significant implications. Foremost is that the "bandwidth" effect is observable in these data and is not isolated to the data analyzed in [11] and [36], which were from the Capraia Basin north of Elba, Italy. Second is that the effect is observable for both monostatic and bistatic data, a hereto-

---

[2] The larger beamwidth of the array used in 2003 compared with that used in 2002 (3.0° versus 2.2° at 400 Hz for a broadside beam) is not expected to be a significant factor.

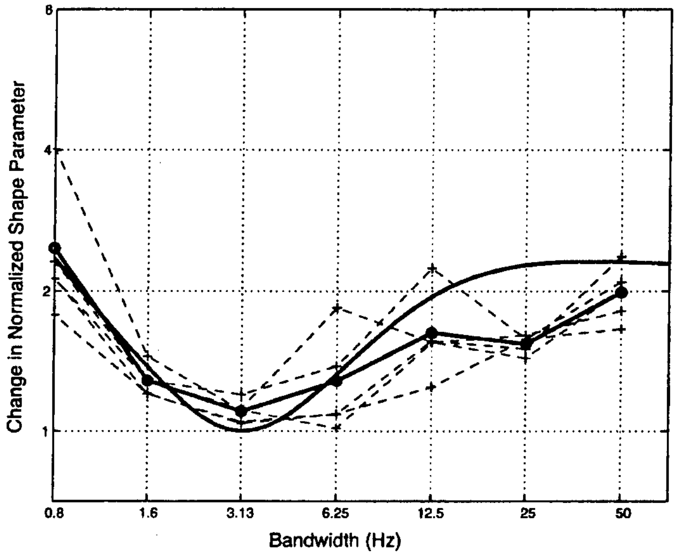

Fig. 16. Change in shape parameter vs. bandwidth over 5 monostatic (lower power) pings from track 64 at site 3 of the 2001 data. The solid line is that predicted from an elongated patch model (power $= 0.4$).

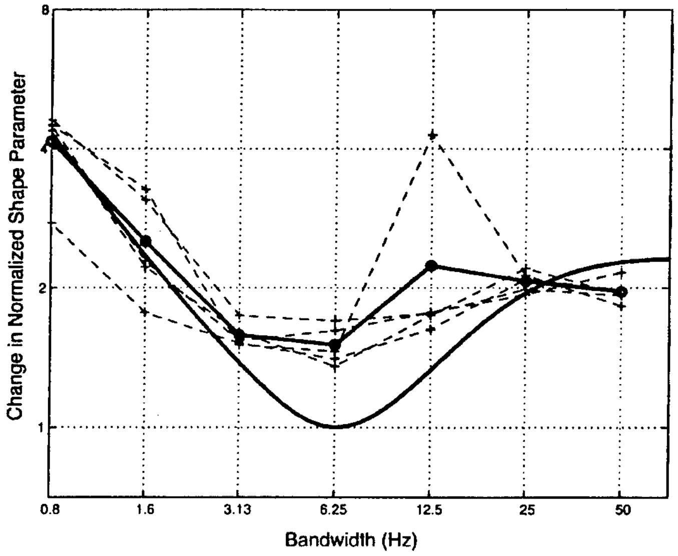

Fig. 17. Change in shape parameter versus bandwidth over five bistatic (higher power) pings from track 64 at Site 3 of the 2001 data. The solid line is what is predicted from an elongated patch model (power $= 0.4$).

fore unknown result. One also sees that the minima have shifted up from 3 to 6 Hz at Sites 2 and 3 when going from monostatic to bistatic data and that the minimum has shifted down, going from 2001 to 2003 bistatic data. This implies that any adaptation of a sonar system to optimize the bandwidth with respect to this effect will likely require *in situ* data analysis and indicates that further research is necessary to determine what effects dominate the location of the minimum of the shape-parameter curve; these observations indicate a high correlation with the time spread of the channel. Coupled with this last effect is a concern that the minimum of the shape-parameter curve occurs at such low bandwidths. It is traditionally assumed that broad-band sonar systems are desirable because performance improves as bandwidth increases. Kroenert [47] illustrates this as a reduction in detection threshold for Rayleigh-distributed reverberation. For K-distributed reverberation, this same result was shown [44] when the target echo and scattering elements are all within the sonar's resolution cell. It is not clear what will happen to sonar system performance when the inverse proportionality between the shape parameter and bandwidth assumed in [44] does not hold. One might expect that the larger shape parameter implies less clutter; however, it is expected that this will be countered by an increase in the correlation or dependence of the reverberation in time when the scatterers are overresolved. That the minimum can occur at such low bandwidths implies that the effect of overresolution of scattering elements on the sonar's performance will affect all but sonar systems using sinusoidal transmit waveforms and, therefore, requires investigation.

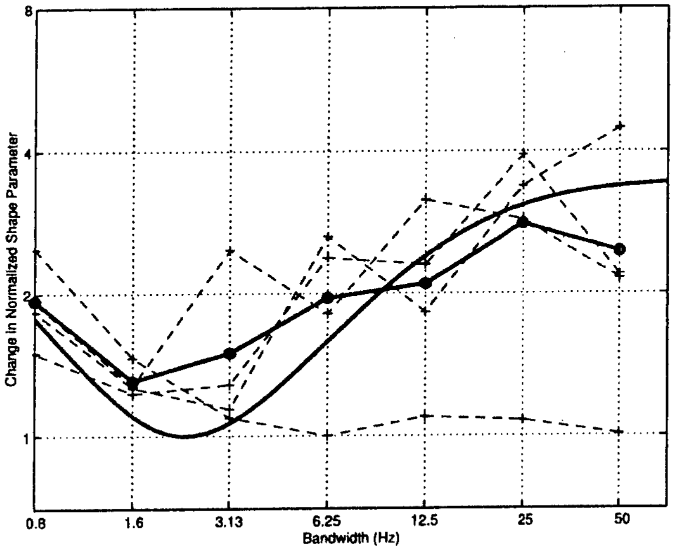

Fig. 18. Change in shape parameter versus bandwidth over four bistatic (higher power) pings from the 2003 data. The solid line is what is predicted from an elongated patch model (power = 0.3).

IV. CONCLUSION

This paper presents an analysis of the reverberation and clutter (clutter being defined as reverberation data producing false alarms in sonar systems) observed on the New Jersey Shelf during the 2001 Acoustic Clutter Reconnaissance Experiment. Polar plots were used to evaluate the power of the long-range diffuse reverberation and to make the initial identification of regions of high clutter. This was followed by a descriptive analysis of the reverberation-envelope statistics from the ACRE sea trial and a limited analysis of data from the 2003 Acoustic Clutter Experiment. Statistical analysis of the reverberation indicated that a majority of the data is well represented by the K distribution while a significant amount (21%–86% of the data on each track) are nearly Rayleigh distributed.

The bistatic data were observed to be uniformly and significantly more non-Rayleigh than the monostatic data. It was shown that this difference most likely arises from the disparity in the sonar sources, although bistatic scattering has not yet been ruled out as a potential contributor. The bistatic source had a higher source-power level, leading to higher reverberation power levels as compared with the ambient noise. The resulting shape-parameter estimate for the monostatic data was seen to be biased high by a multiplicative factor that increases as the RNR decreases when the ambient noise is Gaussian. The bistatic source also had more vertical directionality than the monostatic source, leading to more focusing of acoustic energy along distinct paths. This results in less multipath in the two-way channel-impulse response, which leads to a smaller shape parameter (i.e., more distinctly non-Rayleigh) for data from the source with a smaller vertical beamwidth.

Analysis of the K-distribution shape parameter as a function of bandwidth illustrated the "bandwidth" effect where the data become more non-Rayleigh as bandwidth increases, followed by a reversal back toward the Rayleigh distribution. These data were seen to be well represented by the elongated patch model of [11], which predicts this effect as arising from overresolution of scattering elements in range. It was observed that the minimum of the shape-parameter curve occurred at lower bandwidths for the monostatic data than for the bistatic data, which is accounted for by the larger channel time spread expected for data from a source with a larger vertical beamwidth. A difference in the shape-parameter curve minimum was also observed between the 2001 and 2003 bistatic data, with the latter occurring at a lower bandwidth. This most likely arose from the more simply downward-refracting sound–speed profiles measured in 2003, which resulted in more bottom interaction and, therefore, a larger channel time spread. One might expect that the larger shape parameter implies less clutter; however, it is expected that this will be countered by an increase in the correlation or dependence of the reverberation in time when the scatterers are overresolved. That the minimum can occur at such low bandwidths implies that the effect of overresolution of scattering elements on the sonar's performance will affect all but sonar systems using sinusoidal transmit waveforms and, therefore, requires investigation.

The results of this paper illustrate that the ocean environment in conjunction with the sonar system plays an important role in determining and interpreting the reverberation-envelope statistics, which directly impact the false-alarm performance of a sonar system. More realistic sonar system performance modeling, improved sonar system design, and *in situ* environmental adaptation may be achieved by appropriately accounting for these dependencies of the reverberation-envelope statistics.

ACKNOWLEDGMENT

The authors would like to thank N. Makris of the Massachusetts Institute of Technology (MIT), Cambridge, for leading the two acoustic clutter experiments and providing resources for some of the FORA software upgrades. They would also like to thank the technicians and crew on NATO URC's *R/V Alliance* and C. Holland, the Scientist-in-Charge for NATO URC on the *R/V Alliance* for the 2001 experiment, and Digital Systems Research for the initial (and substantial) acquisition software for FORA. They would also like to thank R. Hollett, NATO URC, for the beamforming and matched-filter software, L. Rulhmann, Consultant for MIT, for important upgrades to the new FORA acquisition system and for her help in interfacing with our reverberation-processing software, and E. Scheer of the Woods Hole Oceanographic Institute, Woods Hole, MA, for beamformer upgrades for the FORA processing. Finally, they would like to thank the reviewers for their excellent comments and suggestions.

REFERENCES

[1] D. A. Abraham and C. W. Holland, "Statistical analysis of low-frequency active sonar reverberation in shallow water," in *Proc. 4th Eur. Conf. Underwater Acoustics*, Rome, Italy, Sept. 1998, pp. 795–800.

[2] Y. Y. Dorfman and I. Dyer, "Monostatic and bistatic reverberation statistics west of the Mid-Atlantic ridge," *J. Acoust. Soc. Amer.*, vol. 106, no. 4, pp. 1755–1764, 1999.

[3] J. A. Goff, D. J. P. Swift, C. S. Duncan, L. A. Mayer, and J. Hughes-Clarke, "High resolution swath sonar investigation of sand ridge, dune and ribbon morphology in the offshore environment of the New Jersey margin," *Marine Geol.*, vol. 161, pp. 309–339, 1999.

[4] C. S. Fulthorpe, J. A. Austin, and G. S. Mountain, "Morphology and distribution of miocene slope incisions off New Jersey: Are they diagnostic of sequence boundaries?," *Geolog. Soc. Amer. Bull.*, vol. 112, pp. 817–828, 2000.

[5] J. A. Goff, H. C. Olsen, and C. S. Duncan, "Correlation of side-scan backscatter intensity with grain size distribution of sediments, New Jersey margin," *Geo-Marine Lett.*, vol. 20, pp. 43–49, 2000.

[6] C. S. Duncan, J. A. Goff, J. A. Austin, and C. S. Fulthorpe, "Tracking the last sea-level cycle: Seafloor morphology and shallow stratigraphy of the latest quaternary New Jersey middle continental shelf," *Marine Geol.*, vol. 170, no. 3/4, pp. 395–421, 2000.

[7] J. A. Austin, J. A. Goff, S. Gulick, C. S. Fulthorpe, S. Nordfjord, M. Weiderspahn, S. Saustrup, S. Schock, J. Wulf, K. Gjerding, L. Mayer, and C. Sommerfield, "Assessing the "GEO" in GEO-CLUTTER: New chirp sonar, sampling, and compressional wave veocity results from the New Jersey Shelf," *EOS Trans. Amer. Geophys. Union*, vol. 82, no. 47, paper OS42A-0456, 2001.

[8] C. S. Fulthorpe, J. A. Goff, J. A. Austin, S. Gulick, and S. Nordfjord, "Late quaterniary incisions and related shallow subsurface stratigraphy on the New Jersey mid-outer shelf: Preliminary results from ultra-high resolution chirp sonar images—Part II," *EOS Trans. Amer. Geophys. Union*, vol. 83, 2001.

[9] P. Ratilal, D. T. Symonds, Y. Lai, L. A. Ruhlmann, J. Goff, C. W. Holland, J. R. Preston, E. K. Scheer, M. T. Sundvik, and N. C. Makris, "Long range acoustic imaging of the continental shelf environment: The acoustic clutter reconnaisance experiment 2001," *J. Acoust. Soc. Amer.*, 2004, submitted for publication.

[10] "Geological Clutter Acoustics Experiment Initial Report," Office of Naval Research, Washington, DC, 2002.

[11] D. A. Abraham and A. P. Lyons, "Reverberation envelope statistics and their dependence on sonar bandwidth and scatterer size," *IEEE J. Oceanic Eng.*, vol. 29, pp. 1–12, Jan. 2004.

[12] C. W. Holland, R. Hollett, and L. Troiano, "Measurement technique for bottom scattering in shallow water," *J. Acoust. Soc. Amer.*, vol. 108, pp. 997–1011, 2000.

[13] N. C. Makris and P. Ratilal, "A unified model for reverberation and submerged object scattering in a stratified ocean waveguide," *J. Acoust. Soc. Amer.*, vol. 109, pp. 909–941, 2001.

[14] P. Ratilal and N. C. Makris, "Extinction theorem for object scattering in a stratified medium," *J. Acoust. Soc. Amer.*, vol. 110, pp. 2924–2945, 2001.

[15] D. D. Ellis, J. R. Preston, R. Hollett, and J. Sellschopp, "Analysis of towed array reverberation data from 160 to 4000 Hz during rapid response 97," presented at the SR 280, SACLANTCEN, July 2000.

[16] J. R. Preston, "Shallow water ocean reverberation data analysis and extraction of seafloor geo-acoustic parameters below 4 kHz," Ph.D. dissertation, The Pennsylvania State Univ., State College, 2002.

[17] J. A. Goff, personal communication, 2002.

[18] C. H. Holland, "Geoacoustic measurements on the New Jersey Shelf," in *Proc. Abstracts 144rd Meeting Acoustical Society of America*, vol. 112, Dec. 2002, Paper 2pUW9.

[19] J. R. Preston and W. Kinney, "Monostatic and bistatic reverberation using low-frequency linear FM pulses," *J. Acoust. Soc. Amer.*, vol. 93, pp. 2549–2565, 1993.

[20] S. Nordfjord, S. P. S. Gulick, J. A. Austin, J. A. Goff, and C. S. Fulthorpe, "Late quaternary incisions and related shallow subsurface stratigraphy on the New Jersey mid-outer shelf: Preliminary results from ultra-high resolution chirp sonar images—Part I," *EOS Trans. Amer. Geophys. Union*, vol. 83, no. 47, paper OS71P-0299, 2002.

[21] J. A. Goff and S. Nordfjord, "Interpolation of fluvial morphology using channel-oriented coordinate transformation: A case study from the New Jersey Shelf," Math. Geol., 2003, submitted for publication.

[22] R. B. Evans and W. M. Carey, "Frequency dependence of sediment attenuation in two low-frequency shallow-water acoustic experimental data sets," *IEEE J. Oceanic Eng.*, vol. 23, pp. 439–447, Oct. 1998.

[23] R. C. Gauss and D. D. Ellis, personal communication, 2001.

[24] R. W. Nero, C. H. Thompson, and R. H. Love, "Fish schools as potential clutter and false targets: Observations on the New Jersey Shelf," in *Proc. Abstracts 144th Meeting Acoustical Society of America*, vol. 112, Dec. 2002, Paper 2pUW3.

[25] M. D. Collins, "A split-step pade solution for parabolic equation method," *J. Acoust. Soc. Amer.*, vol. 93, pp. 1736–1742, 1993.

[26] P. Ratilal, S. Lee, and N. C. Makris, "Range-dependent reverberation modeling with the parabolic equation," in *Proc. Abstracts 146rd Meeting Acoustical Society of America*, vol. 114, Oct. 2003, Paper 1aUW4.

[27] K. M. Becker and J. R. Preston, "The ONR five octave research array (FORA) at Penn state," in *Proc. OCEANS'03*, San Diego, CA, Sept. 2003.

[28] N. P. Chotiros *et al.*, "Acoustic backscattering at low grazing angles from the ocean bottom. Part II. Statistical characteristics of bottom backscatter at a shallow water site," *J. Acoust. Soc. Amer.*, vol. 77, no. 3, pp. 975–982, 1985.

[29] M. Gensane, "A statistical study of acoustic signals backscattered from the sea bottom," *IEEE J. Oceanic Eng.*, vol. 14, pp. 84–93, Jan. 1989.

[30] S. Stanic and E. G. Kennedy, "Fluctuations of high-frequency shallow-water seafloor reverberation," *J. Acoust. Soc. Amer.*, vol. 91, no. 4, pp. 1967–1973, 1992.

[31] W. K. Stewart, D. Chu, S. Malik, S. Lerner, and H. Singh, "Quantitative seafloor characterization using a bathymetric sidescan sonar," *IEEE J. Oceanic Eng.*, vol. 19, pp. 599–610, Oct. 1994.

[32] H. Griffiths, J. Dunlop, and R. Voles, "Texture analysis of sidescan sonar imagery using statistical scattering models," in *High Frequency Acoustics in Shallow Water*, N. G. Pace, E. Pouliquen, O. Bergem, and A. P. Lyons, Eds. La Spezia, Italy: NATO SACLANT Undersea Research Centre, 1997, pp. 187–194.

[33] A. P. Lyons and D. A. Abraham, "Statistical characterization of high-frequency shallow-water seafloor backscatter," *J. Acoust. Soc. Amer.*, vol. 106, no. 3, pp. 1307–1315, 1999.

[34] S. Dugelay, N. G. Pace, G. J. Heald, and R. J. Brothers, "Statistical analysis of high frequency acoustic scatter: What makes a statistical distribution?," in *Proc. 5th Eur. Conf. Underwater Acoustics (ECUA'00)*, Lyon, France, July 2000, pp. 269–274.

[35] D. A. Abraham and A. P. Lyons, "Novel physical interpretations of K-distributed reverberation," *IEEE J. Oceanic Eng.*, vol. 27, pp. 800–813, Oct. 2002.

[36] ——, "Reverberation envelope statistics and their dependence on sonar beamwidth and bandwidth," in *Impact of Littoral Environmental Variability on Acoustic Predictions and Sonar Performance*, N. G. Pace and F. B. Jensen, Eds. Norwell, MA: Kluwer, 2002, pp. 539–546.

[37] P. P. Gandhi and S. A. Kassam, "Analysis of CFAR processors in nonhomogenous background," *IEEE Trans. Aerosp. Electron. Syst.*, vol. 24, pp. 427–445, July 1988.

[38] P. Z. Peebles Jr, *Radar Principles*. New York: Wiley, 1998.

[39] D. A. Abraham and P. K. Willett, "Active sonar detection in shallow water using the page test," *IEEE J. Oceanic Eng.*, vol. 27, pp. 35–46, Jan. 2002.

[40] M. Gu and D. A. Abraham, "Using McDaniel's model to represent non-Rayleigh reverberation," *IEEE J. Oceanic Eng.*, vol. 26, pp. 348–357, July 2001.

[41] I. R. Joughin, D. B. Percival, and D. P. Winebrenner, "Maximum likelihood estimation of K distribution parameters for SAR data," *IEEE Trans. Geosci. Remote Sensing*, vol. 31, pp. 989–999, Sept. 1993.

[42] M. Fisz, *Probability Theory and Mathematical Statistics*, 3rd ed. Melbourne, FL: Krieger, 1963.

[43] S. Watts, "Radar detection prediction in K-distributed sea clutter and thermal noise," *IEEE Trans. Audio Eng. Soc.*, vol. AE-23, pp. 40–45, Jan. 1987.

[44] D. A. Abraham, "Signal excess in K-distributed reverberation," *IEEE J. Oceanic Eng.*, vol. 28, pp. 526–536, July 2003.

[45] J. R. Preston, "Bottom parameter extraction from long range reverberation measurements," in *Proc. OCEANS'01*, Honolulu, HI, Nov. 2001.

[46] ——, "Some shallow water reverberation highlights and bottom parameter extractions in the 325–825 Hz region from the boundary characterization experiment," in *Proc. Geoclutter and Boundary Characterization'01*, Halifax, NS, Canada, Oct. 2001, pp. 43–48.

[47] J. T. Kroenert, "Discussion of detection threshold with reverberation limited conditions," *J. Acoust. Soc. Amer.*, vol. 71, no. 2, pp. 507–508, 1982.

John R. Preston (M'75) received the B. S. degree in physics from the University of Massachusetts, Amherst, the M.S. degree in physics from the University of Maryland, College Park, the M.S.E.E. degree from George Washington University, Washington, DC, and the Ph.D. degree in acoustics from The Pennsylvania State University, State College.

He was a Vice President with the Amron Corporation, Washington, DC, and held an appointment as a Principal Scientist with the NATO SACLANT Undersea Research Centre (SACLANTCEN), La Spezia Italy, from 1989 to 1994, where he planned, executed, and analyzed various reverberation experiments using acoustic arrays. He has also worked on problems associated with underwater propagation and signal processing. He has been a Senior Research Associate with the Applied Research Laboratory, The Pennsylvania State University, since 1995, where he is working on the Office of Naval Research's (ONR's) geoclutter program, inversion algorithms with Naval Air Warfare Center (NAWC) and ONR and with SACLANTCEN on rapid environmental assessment (REA) technology; these efforts are focused on sea-bottom reverberation. He has recently also worked on broad-band underwater propagation issues and has participated in or led numerous at-sea experiments.

Douglas A. Abraham (S'92–M'93–SM'04) received the B.S., M.S., and Ph.D. degrees in electrical engineering in 1988, 1990, and 1993, respectively, and the M.S. degree in statistics in 1994, all from the University of Connecticut, Storrs.

He was with the Naval Undersea Warfare Center, New London, CT, from 1989 to 1995, was a Senior Scientist with the NATO SACLANT Undersea Research Centre, La Spezia, Italy, from 1995 to 1998, held a Visiting Faculty position with the University of Connecticut from 1998 to 2000, and currently is a Senior Research Associate with the Applied Research Laboratory, Pennsylvania State University, State College. His work is primarily in the area of statistical signal processing applied to underwater acoustic applications. His current research interests are in representing and accounting for non-Rayleigh active sonar reverberation in signal-processing algorithms for detection, classification, and localization.

Proceedings of the Seventh European Conference on Underwater Acoustics, ECUA 2004
Delft, The Netherlands
5–8 July, 2004

THE EFFECT OF MULTIPATH ON REVERBERATION ENVELOPE STATISTICS

Douglas A. Abraham, Anthony P. Lyons, and Kyle M. Becker

Applied Research Laboratory, The Pennsylvania State University
P.O. Box 30, State College, PA 16804, USA
email: abrahad@psu.edu, apl2@psu.edu, kmbecker@psu.edu

Active sonar reverberation is often observed to have a non-Rayleigh envelope owing to a finite number of scattering elements in each sonar resolution cell. For direct-path-only propagation, the statistics of the reverberation follow that of the seafloor response. However, when including multipath propagation, the reverberation statistics are expected to be closer to the Rayleigh distribution than the seafloor response owing to the larger number of scattering elements that contribute at any given time. In this paper, the effect of multipath on the reverberation envelope statistics is quantified by deriving the equivalent K *distribution shape parameter (*$\tilde{\alpha}$*) as a function of transmit waveform bandwidth. Large values of* $\tilde{\alpha}$ *indicate Rayleigh-like statistics while smaller ones represent heavier-tailed reverberation. For bandwidths high enough to resolve all the multipath, it was determined that* $\tilde{\alpha}$ *is the shape parameter of the seafloor response multiplied by a number that depends on the multipath amplitudes and is between one and the number of paths. An isovelocity sound speed environment is used to illustrate that increasing the vertical aperture of a sonar's source makes reverberation envelope statistics more non-Rayleigh by reducing the number of multipath that contribute to reverberation.*

1. INTRODUCTION

Reverberation in active sonar systems is traditionally assumed to have an envelope following a Rayleigh probability density function (PDF) owing to a central limit theorem argument based on an infinite number of individual scatterers in each range-bearing resolution cell. However, recent models have shown that a finite number of randomly sized scattering elements (e.g., patches or discrete scatterers) can produce non-Rayleigh reverberation following the K distribution with a shape parameter (α) that is proportional to the average number of scattering elements in the sonar's resolution cell [1].

This paper examines the effects of multipath propagation on the reverberation envelope PDF as a function of sonar bandwidth for a finite number of scattering elements. The metric of comparison is the shape parameter of a moment-matched K distribution ($\tilde{\alpha}$) which is an indicator of how Rayleigh-like the PDF is; small values of $\tilde{\alpha}$ represent severely non-Rayleigh reverberation with heavy tails and large values of $\tilde{\alpha}$ are indicative of nearly Rayleigh reverberation.

In the following section, $\tilde{\alpha}$ is derived for seafloor environments including multipath leading to a K-distributed reverberation envelope with scattering elements that are fully within the sonar resolution cell. The resulting $\tilde{\alpha}$ is evaluated as a function of bandwidth for various ranges in an isovelocity shallow water environment illustrating the effect of source vertical aperture on reverberation statistics.

2. EFFECT OF MULTIPATH ON STATISTICS

Suppose that reverberation arises from scattering from a finite number of patches in each sonar resolution cell as derived in [1]. When each patch has an exponentially distributed area, the reverberation envelope becomes K-distributed. The complex envelope of the reverberation time series after beamforming and matched filtering may be characterized as

$$\tilde{X}(t) = b(t) * h(t) * \tilde{R}_{ss}(t) \tag{1}$$

where $\tilde{R}_{ss}(t)$ is the autocorrelation function of the basebanded transmit waveform, $h(t)$ is the impulse response of the propagation channel as described in [3], and $b(t)$ is the response of the seafloor to direct path propagation. For reverberation arriving at the sonar receiver at travel time t, it is assumed that the channel impulse response may be modeled as a sum of scaled (a_i) and delayed (τ_i) Dirac delta functions

$$h(t) = \sum_{i=1}^{L} a_i \, \delta\left(t - \tau_i\right). \tag{2}$$

The transmit waveform autocorrelation function is often approximated by a rectangular function with width equal to one over the transmit waveform bandwidth (W), $\tilde{R}_{ss}(t) \approx \sqcap(Wt)$ where $\sqcap(t)$ is the rectangle function which equals one when $|t| < 1/2$ and is zero otherwise. The convolution between the channel impulse response and the transmit waveform autocorrelation function may then be approximated by

$$\begin{aligned} h_W(t) = h(t) * \tilde{R}_{ss}(t) = \sum_{i=1}^{L} a_i \tilde{R}_{ss}\left(t - \tau_i\right) \;&\approx\; \sum_{i=1}^{L} a_i \sqcap\left(W(t - \tau_i)\right) && (3) \\ &=\; \sum_{j=1}^{P} \nu_j \sqcap\left(\frac{t - \phi_j}{\Delta_j}\right). && (4) \end{aligned}$$

Equation (3) is the sum of L potentially overlapping rectangle functions centered at times τ_i with width $1/W$ and complex heights a_i. Equation (4) simply recharacterizes this sum into a set of P non-overlapping rectangle functions centered at times ϕ_j with widths Δ_j and heights ν_j. The delays ϕ_j and widths Δ_j are easily found by first sorting all of the change-points of (3) $\{\tau_i \pm 1/(2W)\}$ into the ordered sequence $\{\gamma_j\}$ for $j = 1, \ldots, 2L$ and then letting each of the $2L - 1$ regions between adjacent change-points be a rectangle with width $\Delta_j = \gamma_{j+1} - \gamma_j$. The heights are formed according to $\nu_j = \sum_{i \in C_j} a_i$ where C_j is the set of indices i such that $\tau_i - 1/(2W) \leq \gamma_j$ and $\gamma_{j+1} \leq \tau_i + 1/(2W)$; that is, summing all of the input rectangle function amplitudes that contribute to the jth output rectangle function.

Finally, any of the rectangle functions having either zero amplitude ($\nu_j = 0$) or zero width ($\Delta_j = 0$) may be removed, leaving P non-overlapping rectangle functions. This technique may produce adjacent rectangle functions having equal amplitudes; however, this does not affect the following statistical analysis.

According to the finite-number-of-patches model of [1], $b(t)$ is a K-distributed random process

$$b(t) = \sum_{i=1}^{m} \sqrt{B_i}\tilde{Z}_i \delta\left(t - c_i\right) \tag{5}$$

where B_i, $\tilde{Z}_i$, and c_i are, respectively, the area, complex-Gaussian response, and delay associated with the ith patch. The distribution of the delays c_i depends on the frequency with which a patch occurs in $b(t)$. This may be characterized by

$$\beta_0(t) = \frac{t\theta_b \beta c^2}{4\cos\theta_g(t)} \tag{6}$$

which is the number of patches per second where θ_b is the beamwidth in radians, β is the density of patches per square meter on the seafloor, c is the speed of sound, and $\theta_g(t)$ is the grazing angle. The grazing angle should be chosen as that for the path arriving at time t with the largest amplitude [3].

Assuming that the average patch size $\mu = E[B_i]$ is much smaller than the sonar resolution cell at the highest bandwidth of interest implies that $b(t)$ has a flat spectrum over this frequency band and is therefore effectively white. If the scale parameter of $b(t)$ is a constant λ_0 over the interval (t_0, t_1), then $b(t)$ will have the property that $\tilde{X} = \int_{t_0}^{t_1} b(t)dt$ will have a K-distributed envelope with shape parameter $\int_{t_0}^{t_1} \beta_0(t)dt$ and scale parameter λ_0. Additionally, based on the independence of each scattering patch, if $\tilde{Y} = \int_{t_2}^{t_3} b(t)dt$ and the intersection between (t_0, t_1) and (t_2, t_3) is the null set, then $\tilde{X}$ and $\tilde{Y}$ are independent.

Using these properties, it can be seen that when $b(t)$ is convolved with $h_W(t)$ the reverberation time series may be represented as the sum of P independent K-distributed random variables $\tilde{X}_j$

$$\tilde{X}(t) = h_W(t) * b(t) \approx \sum_{j=1}^{P} \nu_j \int_{t-\phi_j-\Delta_j/2}^{t-\phi_j+\Delta_j/2} b(\tau)d\tau = \sum_{j=1}^{P} \tilde{X}_j. \tag{7}$$

Here the scale and shape parameters of $\tilde{X}_j$ are

$$\lambda_j = |\nu_j|^2 \lambda_0 \quad \text{and} \quad \alpha_j = \int_{t-\phi_j-\Delta_j/2}^{t-\phi_j+\Delta_j/2} \beta_0(\tau)d\tau \approx \beta_0(t-\phi_j)\Delta_j \tag{8}$$

where $\lambda_0 = \mu\sigma^2$ and σ^2 is the backscattered power per unit area of a patch. The approximation in Eq. (8) arises from assuming that $\theta_g(t)$ is constant over the time of integration.

It is convenient to approximate the sum in (7) by a single K-distributed random variable. Therefore, we wish to determine the equivalent shape and scale parameters [2] of the sum of independent K-distributed random variables with varying shape $\{\alpha_j\}$ and scale parameters $\{\lambda_j\}$. The equivalent shape and scale parameters are formed from the second and fourth moments of the matched filter envelope. The second moment is easily seen to be

$$m_2 = E\left[|\tilde{X}(t)|^2\right] = \sum_{j=1}^{P} E\left[|\tilde{X}_j|^2\right] = \sum_{j=1}^{P} \alpha_j \lambda_j \tag{9}$$

while the fourth moment requires slightly more effort

$$\begin{aligned} m_4 &= E\left[|\tilde{X}(t)|^4\right] = \sum_{i,j,k,l=1}^{P} E\left[\tilde{X}_i \tilde{X}_j^* \tilde{X}_k \tilde{X}_l^*\right] \\ &= 2\sum_{j=1}^{P} \alpha_j \lambda_j^2 + 2\left[\sum_{j=1}^{P} \alpha_j \lambda_j\right]^2 = 2\sum_{j=1}^{P} \alpha_j \lambda_j^2 + 2m_2^2. \end{aligned} \tag{10}$$

The equivalent scale and shape parameters are then

$$\tilde{\lambda} = \frac{m_4 - 2m_2^2}{m_2} = \frac{\sum_{j=1}^{P} \alpha_j \lambda_j^2}{\sum_{j=1}^{P} \alpha_j \lambda_j} \quad \text{and} \quad \tilde{\alpha} = \frac{2m_2^2}{m_4 - 2m_2^2} = \frac{\left[\sum_{j=1}^{P} \alpha_j \lambda_j\right]^2}{\sum_{j=1}^{P} \alpha_j \lambda_j^2}. \tag{11}$$

At longer travel times it is reasonable to approximate the patch density parameter by a constant over the duration of the multipath arrivals $\beta_0(t-\phi_j) \approx \beta_0(t-\phi_{\max}) = \beta_0$ where $\phi_{\max}$ is the delay pointing to the rectangle function with highest amplitude. This leads to a slight simplification of (11) which will be exploited in the following analysis.

When none of the multipath are resolved by the transmit waveform (i.e., $1/W > \max \tau_i - \min \tau_i$), $h_W(t) \approx \tilde{R}_{ss}(t) \sum_{i=1}^{L} a_i$ which leads to no change in the shape parameter $\tilde{\alpha} = \beta_0/W$ and a scale parameter $\tilde{\lambda} = |\sum_{i=1}^{L} a_i|^2 \lambda_0$. It should be noted that the matched filter envelope remains K-distributed under this condition. Conversely, when all of the multipath are resolved by the transmit waveform (i.e., $1/W < \min_{i \neq j} |\tau_i - \tau_j|$), then $\Delta_i = 1/W$, $\nu_i = a_i$, and $P = L$. Thus, $\lambda_j = |a_j|^2 \lambda_0$ and $\alpha_j = \beta_0/W$ which lead to equivalent scale and shape parameters

$$\tilde{\lambda} = \frac{\sum_{i=1}^{L} |a_i|^4}{\sum_{i=1}^{L} |a_i|^2} \lambda_0 \quad \text{and} \quad \tilde{\alpha} = \frac{\beta_0}{W} \frac{\left[\sum_{i=1}^{L} |a_i|^2\right]^2}{\sum_{i=1}^{L} |a_i|^4}. \tag{12}$$

By applying the Cauchy Schwartz inequality, it can be seen that $\tilde{\alpha}$ is bounded above by $L\beta_0/W$. By phrasing $\tilde{\alpha}$ as a Rayleigh quotient, it can be shown to be bounded below by β_0/W. Thus, when all multipath are resolved, the shape parameter of the matched filter envelope is simply the shape parameter with no multipath multiplied by a constant, which is dependent on the bandwidth and is between one and L, the number of paths. It is interesting to note the implication that, once the multipath are resolved, the shape parameter will resume decreasing in a manner inversely proportional to bandwidth.

It can be shown that for a random process $b(t)$ which is not K-distributed that the equivalent shape and scale parameters still follow (12) where β_0/W is replaced by the equivalent shape parameter of the input process $b(t)$.

3. ISOVELOCITY PROFILE EXAMPLE

An isovelocity sound speed scenario with a co-located source and receiver is used to illustrate the effect of multipath on reverberation statistics. The specifics of the environment are detailed in the upper right corner of Fig. 2. In Fig. 1, $\tilde{\alpha}$ for an omni-directional source and receiver (or for the broadside beam of a towed array receiver) is seen to increase with travel time and have breakpoints related to the frequencies associated with the cycle and doublet distances near the strongest multipath (the triangle and plus marks). The frequencies obtained from the water and source depths provide approximate breakpoints. In this example, the density of patches ($\beta_0(t)$) was held constant with time. Thus, the increase in $\tilde{\alpha}$ with travel time

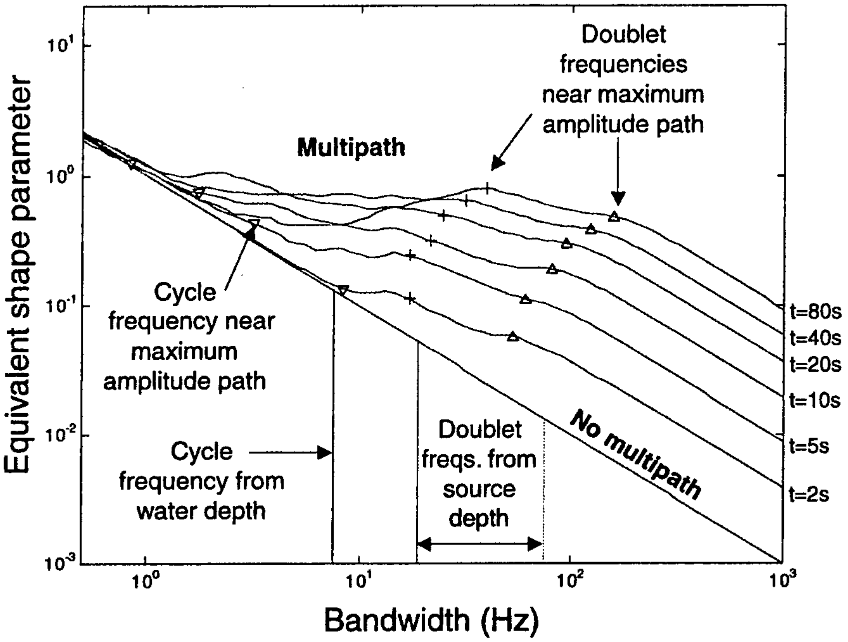

Fig. 1: Equivalent shape parameter ($\tilde{\alpha}$) vs. bandwidth for various two-way travel times.

observed in Fig. 1 arises from the multipath and not from an increasing size of the resolution cell.

The effect of having a source with vertical directionality is examined in Fig. 2 where $\tilde{\alpha}$ is shown for travel time $t = 20$ s for a source with center frequency $f_c = 1$ kHz and with $N = 1$, 9, or 17 transducers that are spaced vertically with design frequency $f_d = 2$ kHz. A smaller vertical beamwidth decreases the number of paths contributing to reverberation, which leads to a smaller $\tilde{\alpha}$ and more non-Rayleigh reverberation. The decrease in $\tilde{\alpha}$ can be significant: a factor of 1.8 for the $2\lambda_c$ array ($N = 9$) and a factor of 4 for the $4\lambda_c$ array ($N = 17$) after the multipath are resolved. Similar results have been observed recently in a data analysis of reverberation from sources with disparate vertical aperture. Note that these results are obtained for frequency independent beamforming; that is, a constant beamwidth for all frequencies.

4. CONCLUSIONS

Compared with direct-path-only propagation, it is seen that multipath propagation has no effect on $\tilde{\alpha}$ when the sonar bandwidth is small enough that all of the multipath lie within one resolution cell. However, when the bandwidth is large enough to resolve all of the multipath, it was found that $\tilde{\alpha}$ increases compared with that for direct-path-only propagation. That is, the reverberation becomes more Rayleigh-like, as would be expected when more scattering elements are added to each resolution cell. The increase in $\tilde{\alpha}$ manifests itself as a constant (with respect to bandwidth once the multipath are resolved) scale applied to the shape parameter for direct-path-only propagation that is bounded between one and L where L is the number of paths. When sonar bandwidth is such that some, though not all, of the multipath are resolved, a numerical model was developed to approximate $\tilde{\alpha}$.

An isovelocity sound speed example illustrated how the reverberation envelope statistics depend on the structure of the multipath, which in turn depends on the environmental characterization and the sonar system transmit and receive beampatterns. It was seen that having a source with vertical directivity makes the reverberation more non-Rayleigh than for an omni-

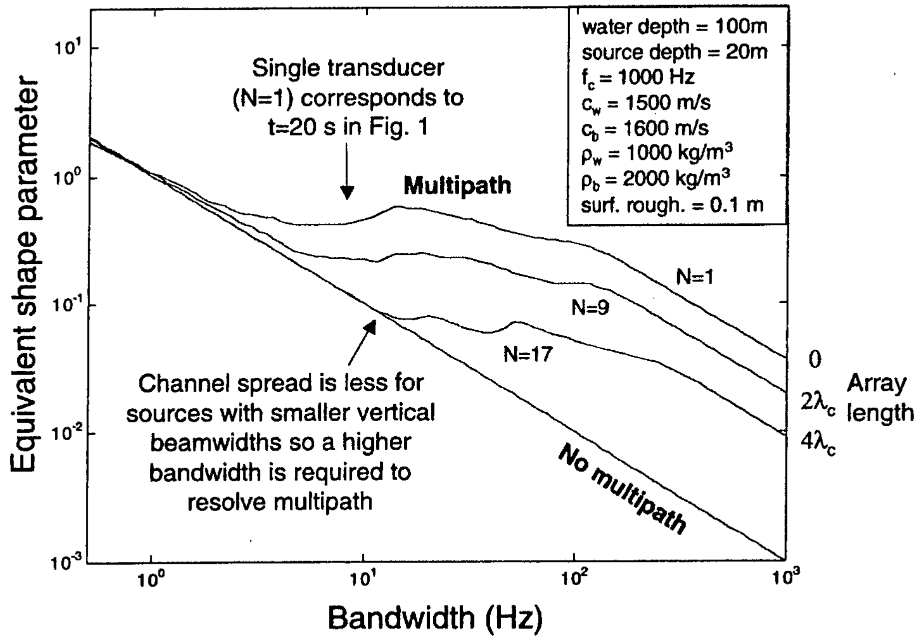

Fig. 2: Equivalent shape parameter $\tilde{\alpha}$ vs. bandwidth for sources with various vertical apertures.

directional source owing to a smaller number of multipath contributing to reverberation at any given time. The resulting increase in false alarms is most likely countered by the commensurate reduction in reverberation power level as is illustrated in [4] for increases in bandwidth or receive array aperture.

In addition to improving our understanding of how multipath affects reverberation envelope statistics, these results are also useful for improving the accuracy of sonar performance modeling through a better characterization of the probability of false alarm and how it varies with bandwidth under more realistic acoustic propagation conditions than has been previously considered.

5. ACKNOWLEDGEMENTS

This work was sponsored by the Office of Naval Research under grant numbers N00014-02-1-0115 and N00014-03-1-0245.

REFERENCES

[1] D. A. Abraham and A. P. Lyons, "Novel physical interpretations of K-distributed reverberation," *IEEE Jnl. of Oceanic Eng.*, 27(4), pp. 800–813, Oct. 2002.

[2] D. A. Abraham and A. P. Lyons, "Reverberation envelope statistics and their dependence on sonar bandwidth and scatterer size," *IEEE Jnl. of Oceanic Eng.*, 29(1), pp. 1–12, Jan. 2004.

[3] D. A. Abraham and A. P. Lyons, "Simulating non-Rayleigh reverberation and clutter," *IEEE Jnl. of Oceanic Eng.*, 2003, Submitted in July 2003.

[4] D. A. Abraham, "Signal excess in K-distributed reverberation," *IEEE Jnl. of Oceanic Eng.*, 28(3), pp. 526–536, July 2003.

ARRAY MODELING OF NON-RAYLEIGH REVERBERATION

Douglas A. Abraham and Anthony P. Lyons

Applied Research Laboratory, The Pennsylvania State University
P.O. Box 30, State College, PA 16804, USA
email: abrahad@psu.edu, apl2@psu.edu

Abstract

After matched filtering and beamforming, active sonar reverberation is often observed to have a non-Rayleigh distributed envelope, particularly for broadband transmit waveforms and large aperture arrays. Statistical analysis and modeling of the reverberation envelope has predominantly occurred after beamforming where the number of scattering elements contributing to reverberation is taken to be proportional to the array beamwidth. In this paper, a non-Rayleigh reverberation model is developed for an array of hydrophones in the farfield of the seafloor scattering. The effective number of scattering elements ($\tilde{\alpha}$), which is the shape parameter of the moment-matched K distribution, is derived for the conventional beamformer output. A narrowband approximation is developed for cases where the steering vector of the array does not change significantly over the band of the transmit waveform. An analysis of the conventional beamformer output for a towed array example illustrates that $\tilde{\alpha}$ from the array model is greater than that obtained from the 3-dB beamwidth, well approximated when the 6-dB beamwidth is used, and depends on the multipath structure and seafloor scattering statistics. High elevation-angle arrivals near the array endfire that contribute to beams at azimuths closer to broadside are seen to increase $\tilde{\alpha}$ in these beams with a commensurate reduction in $\tilde{\alpha}$ in the beams nearer to endfire. A technique for simulating non-Rayleigh array reverberation data is developed accounting for both multipath propagation and anisotropic seafloor scattering statistics.

1. INTRODUCTION

Active sonar reverberation is often assumed to follow a Rayleigh probability distribution owing to a large number of scatterers and a central limit theorem argument. However, when broadband transmit waveforms and large arrays reduce the size of the sonar resolution cell and therefore the number of independent scattering elements that contribute to reverberation, the envelope statistics can become non-Rayleigh. The K distribution may be used to represent such reverberation with the shape parameter related to the number of scattering elements in the resolution cell, a quantity assumed to be proportional to array beamwidth and inversely proportional to transmit waveform bandwidth [1].

In this paper, a model is developed to represent non-Rayleigh reverberation at the hydrophone level rather than after beamforming. The array response to scattering from the seafloor is formulated as the superposition of the response to angular sectors originating at the phase center of the array and spaced so that they are several times denser than the minimum azimuthal beamwidth of the array. This allows straightforward simulation of non-Rayleigh array data and more accurate evaluation of the statistics of the conventional beamformer output in conjunction with ray-based propagation in a shallow water environment. A towed-array example is used to illustrate the differences between array modeling and assuming a K-distribution shape parameter proportional to beamwidth.

2. ARRAY MODELING

For ease of exposition, an array model for non-Rayleigh reverberation will be developed and analyzed for a shallow water environment with a constant sound speed, range-independent bathymetry, and a ray based solution to the wave equation. Extension to more complicated environments follows readily [2]. It is further assumed that the array is in the far-field of the seafloor scattering and that the source and receiver are co-located.

Owing to multipath propagation, reverberation observed at two-way travel time t impinges on an array from a number of regions on the seafloor. As shown in [2, 3], this may be approximated by modeling the response of the seafloor to direct-path-only propagation and subsequently applying a time-varying finite impulse response (FIR) filter to account for the multipath arrivals. Define $x(t,\theta)$ as the complex envelope of the impulse response of the seafloor to insonification of an angular sector at azimuth θ with width $d\theta$ where only direct-path propagation is considered from the source to the scattering patch to the phase center of the receiving array. If a_p for $p = 1,\ldots,P$ are the amplitudes of the P multipath and τ_p are the corresponding delays that represent the reverberation at time t as defined in [2, 3], then

$$y(t,\theta) = R_0(t) * \sum_{p=1}^{P} a_p x(t-\tau_p,\theta) \tag{1}$$

approximates the reverberation measured at the phase center of the array from the azimuthal sector at θ after matched filtering where $R_0(t)$ is the autocorrelation function of the transmit waveform. In order to account for spatial non-stationarity in the statistical response of the seafloor, the statistics of $x(t,\theta)$ can vary with t and θ. Azimuthally dependent bathymetry and oceanography can be incorporated by forcing the multipath characterization to depend on θ in addition to time.

Let $\mathbf{d}(\theta,\phi,f)$ be the plane-wave steering vector at frequency f for an array comprising N hydrophones pointing to azimuth θ and elevation angle ϕ. In this paper, bold is used to denote vector or matrix variables, a superscript ^{T} the transpose operator and a superscript ^{H} the conjugate transpose operator. The reverberation received by the array may then be characterized in the frequency domain as

$$\mathbf{Y}(f) = S_0(f)\int_0^{2\pi} X(f,\theta)\sum_{p=1}^{P} a_p e^{-j2\pi f\tau_p}\mathbf{d}(\theta,\phi_p,f)d\theta \tag{2}$$

where $S_0(f)$ is the Fourier transform of $R_0(t)$, $X(f,\theta)$ is the Fourier transform of $x(t,\theta)$ and ϕ_p is the elevation angle of the pth multipath arrival from azimuthal angle θ. From this representation, it will be possible to perform a statistical analysis of the output of a conventional beamformer and to simulate non-Rayleigh reverberation at the hydrophone level.

Under direct-path-only propagation, the shape parameter α of the K distribution has been shown to be proportional to the number of scattering elements in a sonar resolution cell [1] and is a useful indicator of whether the reverberation envelope statistics are Rayleigh-like or more heavy-tailed. In this context, large values of α represent Rayleigh-like statistics while small values are indicative of heavier tailed reverberation. Although not explicitly necessary, it will be assumed in this paper that $x(t,\theta)$ is K-distributed with a shape parameter that varies with time as described in [1]–[3].

3. CONVENTIONAL BEAMFORMER STATISTICAL ANALYSIS

Application of a conventional beamformer (CBF) pointing to azimuth ψ_a and elevation ψ_e (i.e., direction $\psi = (\psi_a, \psi_e)$) with weight vector $\mathbf{w}(\psi, f)$ to the array data described in (2) results in the beam output

$$Y(f,\psi) = S_0(f)\int_0^{2\pi} X(f,\theta)\sum_{p=1}^{P} a_p e^{-j2\pi f\tau_p}\mathbf{w}^H(\psi,f)\mathbf{d}(\theta,\phi_p,f)d\theta = \int_0^{2\pi} X(f,\theta)C(f,\theta,\psi)d\theta \tag{3}$$

and the corresponding time domain signal

$$y(t,\psi) = \int_0^{2\pi}\int_{-\infty}^{\infty} x(t-s,\theta)c(s,\theta,\psi)\,ds\,d\theta \tag{4}$$

where $c(t,\theta,\psi)$ is the inverse Fourier transform of

$$C(f,\theta,\psi) \quad = \quad S_0(f)\sum_{p=1}^{P} a_p e^{-j2\pi f\tau_p}\mathbf{w}^H(\psi,f)\mathbf{d}(\theta,\phi_p,f). \tag{5}$$

Extending the results of [3], which derive the equivalent shape parameter [4] of a sum of independent but differently distributed K-distributed random variates, the equivalent shape parameter of the beam output $y(t,\psi)$ in (4) for a general $c(t,\theta,\psi)$ may be shown to be

$$\tilde{\alpha}(t,\psi) = \frac{\left[\int_0^{2\pi}\int_{-\infty}^{\infty}\alpha_0(t-s,\theta)|c(s,\theta,\psi)|^2\,ds\,d\theta\right]^2}{\int_0^{2\pi}\int_{-\infty}^{\infty}\alpha_0(t-s,\theta)|c(s,\theta,\psi)|^4\,ds\,d\theta} \approx \frac{\left[\int_0^{2\pi}\alpha_0(t,\theta)\int_{-\infty}^{\infty}|c(s,\theta,\psi)|^2\,ds\,d\theta\right]^2}{\int_0^{2\pi}\alpha_0(t,\theta)\int_{-\infty}^{\infty}|c(s,\theta,\psi)|^4\,ds\,d\theta} \tag{6}$$

where $\alpha_0(t,\theta)$ is the shape parameter of $x(t,\theta)$ and the approximation is obtained by assuming that $\alpha_0(t-s,\theta)$ varies slowly over the extent of $c(s,\theta,\psi)$ which is approximately the multipath extent $\max_p \tau_p - \min_p \tau_p$. The units of $\alpha_0(t,\theta)$ may be taken as the number of scattering elements per second per radian. Although these results are most easily derived assuming that $x(t,\theta)$ is a white random process in both t and θ, it is sufficient that the scattering elements be smaller than the smallest resolution cell in consideration, defined by the smallest beamwidth of the array and largest bandwidth of the transmit waveform.

If the transmit waveform has a narrow enough bandwidth for the array steering vector to not change over its frequency band, then a narrowband approximation to $C(f,\theta,\psi)$ of (5) may be written as

$$C(f,\theta,\psi) = S_0(f)\sum_{p=1}^{P} a_p b_p(\psi,\theta)e^{-j2\pi f\tau_p} \tag{7}$$

where $b_p(\psi,\theta) = \mathbf{w}^H(\psi,f_c)\mathbf{d}(\theta,\phi_p,f_c)$ is the response of the beamformer pointing to ψ at center frequency f_c to a signal arriving from the direction of the pth multipath from angle θ. The inverse Fourier transform of $C(f,\theta,\psi)$ is then the sum of scaled and delayed waveform autocorrelation functions, which simplifies (6) to

$$\tilde{\alpha}(t,\psi) = \frac{1}{W}\cdot\frac{\left[\int_0^{2\pi}\sum_{p=1}^{P}\alpha_0(t-\tau_p,\theta)|a_p b_p(\psi,\theta)|^2\,d\theta\right]^2}{\int_0^{2\pi}\sum_{p=1}^{P}\alpha_0(t-\tau_p,\theta)|a_p b_p(\psi,\theta)|^4\,d\theta} \tag{8}$$

where it is assumed that $\alpha_0(t,\theta)$ varies slowly over the length of $R_0(t)$ ($\approx$ one over the waveform bandwidth W), that the waveform autocorrelation function is well approximated by a rectangular pulse of width

$1/W$, and that the multipath do not interfere with each other. The last assumption implies that the bandwidth is large enough to isolate each multipath. Lower bandwidths may be considered by recharacterizing the multipath filter into a sum of orthogonal components as described in [3] resulting in a different set of amplitudes and delays and a slight modification to (8) to account for the width of each orthogonal component.

Evaluation of (6) and (8) for direct-path-only propagation in an isotropic scattering environment for an horizontal line array comprising N hydrophones spaced every d meters shows that the narrowband approximation for the equivalent shape parameter is accurate for bandwidths

$$W \leq \left[\frac{d}{c} \frac{\left(\sum_{i=1}^{N} w_i\right)^2}{\sum_{i=1}^{N} w_i^2} \right]^{-1} \quad \text{or, equivalently,} \quad \frac{W}{f_d} \leq 2 \frac{\sum_{i=1}^{N} w_i^2}{\left(\sum_{i=1}^{N} w_i\right)^2} \tag{9}$$

where w_i are the beamformer shading coefficients, c is the speed of sound, and $f_d = c/(2d)$ is the design frequency of the array. The term in the brackets in the first equation of (9) may be loosely described as the time it takes a wavefront arriving from endfire to cross the array, which is one characterization of when a waveform is narrowband with respect to array signal processing [5]. Equation (9) also accounts for non-uniform shading of the array, which effectively reduces the array aperture. Above these bandwidths, the narrowband approximation first underestimates $\tilde{\alpha}(t, \psi)$ by up to ten percent at broadside (less than one percent at endfire) and then overestimates $\tilde{\alpha}(t, \psi)$ with greater disparity as N increases.

The result of (8), though it is for the limited case of a narrowband waveform with enough bandwidth to resolve all multipath, is still representative of the change in $\tilde{\alpha}(t, \psi)$ arising from multipath propagation and will be used in the following section to illustrate the effect of array modeling of non-Rayleigh reverberation as opposed to beamformer output modeling in a towed-array example.

4. TOWED-ARRAY EXAMPLE

To illustrate the statistical analysis of the previous section, consider an omnidirectional source with a co-located line array receiver with $N = 16$ equally spaced hydrophones with a design frequency $f_d = 1200$ Hz and a transmit waveform center frequency $f_c = 1000$ Hz placed at 40 m depth in a water column 100 m deep. The parameters characterizing the isovelocity soundspeed and range-independent bathymetry environment are found in Fig. 1. Let the array be beamformed using a Hanning weighted conventional beamformer $\mathbf{w}(\psi, f) = \mathbf{W}\,\mathbf{d}(\psi, 0, f)$ where $\mathbf{W} = \operatorname{diag}\{w_i\}$ is a diagonal matrix containing the Hanning weights and the elevation angle is assumed to be zero. The seafloor is assumed to produce reverberation with a constant shape parameter $\alpha_0 = 0.1W180/\pi$ scattering elements per second per radian at travel time $t = 10$ s. The narrowband constraint of (9) dictates that $W \leq 247$ Hz, which in turn requires all multipath to be separated by at least 4 ms for (8) to hold. For the aforementioned waveguide, the closest multipath within 20 dB of the strongest path are separated by 4.3 ms, so the narrowband assumption is valid and these results are valid for $234 < W < 247$ Hz.

The equivalent shape parameter of (8) for direct-path-only propagation from long range scattering (i.e., the elevation angle is zero) is shown in Fig. 1 and compared with that estimated from the 3-dB and 6-dB beamwidths of the beamformer which are herein defined as the total angle in degrees where the beampattern is within the specified range of its peak value. Note that this may come from the mainlobe, sidelobes, or grating lobes of the beampattern. The shape parameter is then estimated by the beamwidth times $2\alpha_0/W$ which assumes that the seafloor only contributes at this time from the left and right azimuths. For example, using the 3-dB beamwidth at broadside of 13.6 degrees results in a shape parameter estimate $= 13.6 \cdot 2 \cdot 0.1 = 2.72$ scattering elements. Each of these methods illustrates that the shape parameter increases away from broadside to the array owing to the larger number of scattering elements contributing to the wider beams found toward endfire until the two sides of the conical beampattern begin to meet and reduce the total beamwidth near endfire. The ratio between the results of the array modeling and α-proportional-to-beamwidth techniques is presented in Fig. 2 where it is seen that the 3-dB beamwidth method underestimates the array-based model by 30% on average in this example. The 6-dB beamwidth approach, which is within 4% of the array modeling result on average, provides a more accurate approximation.

The model incorporating multipath for travel time $t = 10$ s is also shown in Fig. 1 along with an example of non-isotropic scattering where $\alpha_0(t, \theta)$ is varied with θ with more Rayleigh-like scattering near $\sin(\theta) = -0.3$ and less Rayleigh-like scattering near $\sin(\theta) = 0.6$. As is expected, multipath propagation results in reverberation that is more Rayleigh-like than the direct-path response with a shape parameter nearly twenty times larger. The effect of incorporating multipath at the array level is seen in Fig. 2 where high angle paths near endfire are seen to contribute to beams closer to broadside to the array resulting in a smaller shape parameter (relative to direct-path-only propagation) near endfire and a larger shape parameter slightly closer to broadside. Near broadside, the net change is essentially constant as the higher angle paths enter in the same beam as the lower angle paths. This effect is more pronounced at shorter travel times and less pronounced at later travel times owing to the decreasing influence of high angle paths on reverberation as travel time increases.

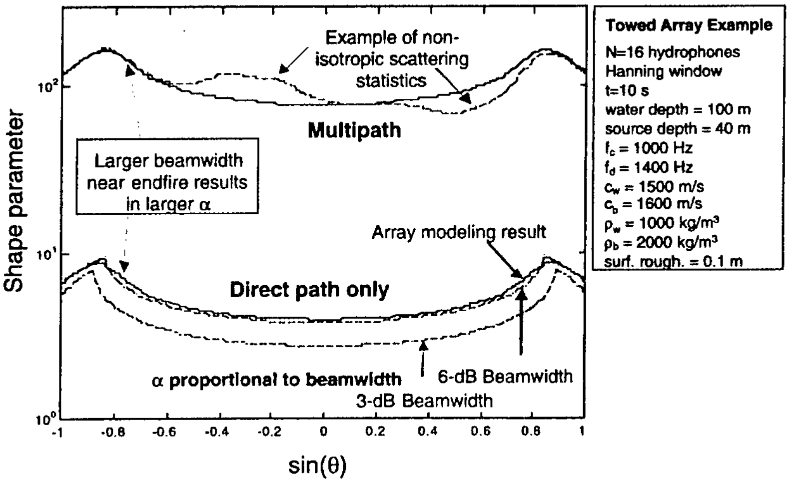

Fig. 1: Equivalent shape parameter of CBF beam output for direct path propagation from model and proportional to beamwidth and for multipath propagation with isotropic and non-isotropic scattering statistics.

5. SIMULATING ARRAY DATA

The array reverberation model described by (2) provides a means for simulating reverberation at the hydrophone level rather than the beam output. As in [2], it is assumed that the aforementioned character-

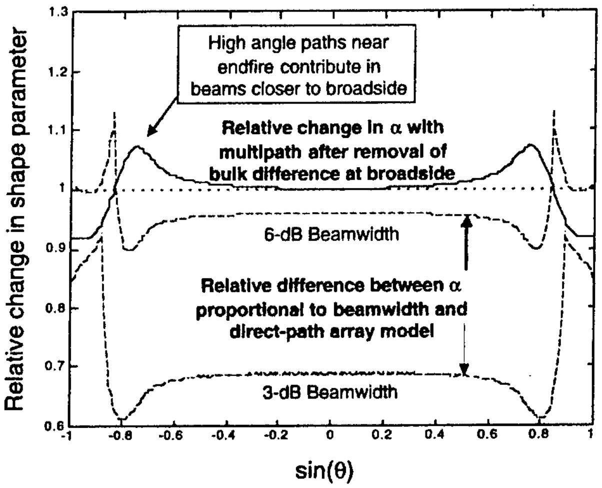

Fig. 2: Relative difference in equivalent shape parameter of CBF beam output between model and shape parameter proportional to beamwidth for direct path propagation and between direct path and multipath propagation after removal of the bulk difference at broadside.

ization of multipath is stationary over some small time span allowing a frequency domain implementation of the filter described in (1). The array data may be formed by first simulating the seafloor response arising from direct-path propagation to the phase center of the receiving array from angular sector θ,

$$\mathbf{x}_\theta = [x(t,\theta) \;\; x(t+T_s,\theta) \;\; \cdots \;\; x(t+(M-1)T_s,\theta)]^T, \tag{10}$$

where T_s is the sampling rate of the basebanded signal and there are M time samples in the processing block. Let the M-by-M matrix $\mathbf{U}$ represent the discrete Fourier transform (DFT); that is, the DFT of $\mathbf{x}_\theta$ is $\mathbf{X}_\theta = \mathbf{U}^H \mathbf{x}_\theta$ with inverse $\mathbf{x}_\theta = \mathbf{U}\mathbf{X}_\theta$. By defining

$$\mathbf{e}_\theta(f) = \sum_{p=1}^{P} a_p e^{-j2\pi f \tau_p} \mathbf{d}(\theta, \phi_p, f) \tag{11}$$

and $\mathbf{E}_\theta = [\mathbf{e}_\theta(f_1) \cdots \mathbf{e}_\theta(f_M)]$ with $f_k = f_c + (k-1-M/2)/(M T_s)$, the array data from angular sector θ may be characterized as

$$\mathbf{y}_\theta = \mathbf{E}_\theta \, \mathrm{diag}\{\mathbf{X}_\theta\} \, \mathbf{U}^T \tag{12}$$

which has row dimension N representing each hydrophone output and column dimension M representing the data in the processing block. Approximating the integral over θ as a finite summation yields

$$\mathbf{y} = d\theta \left[\sum_{i=1}^{L} \mathbf{E}_{\theta_i} \, \mathrm{diag}\{\mathbf{X}_{\theta_i}\} \right] \mathbf{U}^T \tag{13}$$

where $\theta_i = (i-1)2\pi/L$ and $d\theta = 2\pi/L$. It is recommended that L be chosen large enough to allow at least three and preferably five or more angular sectors within the narrowest beam of the array (e.g., that found at broadside).

If the transmit waveform has a narrow enough bandwidth for the steering vector to remain constant over its frequency band, then (12) simplifies to

$$\mathbf{y}_\theta = \mathbf{e}_\theta(f_c)\mathbf{X}_\theta^T\mathbf{U}^T = \mathbf{e}_\theta(f_c)\mathbf{x}_\theta^T \tag{14}$$

and the integration over θ may be efficiently described as

$$\mathbf{y} = d\theta\left[\mathbf{e}_{\theta_1}(f_c) \quad \cdots \quad \mathbf{e}_{\theta_L}(f_c)\right]\left[\mathbf{x}_{\theta_1} \quad \cdots \quad \mathbf{x}_{\theta_L}\right]^T. \tag{15}$$

6. CONCLUSION

An array model for non-Rayleigh reverberation has been developed that accounts for ray-based propagation in a shallow water environment, provides straightforward simulation of array data, and provides more accurate statistical analysis of the conventional beamformer output. The statistical analysis indicated that the K-distribution shape parameter for reverberation observed on an equi-spaced line array is well approximated by that estimated from the 6-dB array beamwidth and illustrated that propagation effects such as high-angle multipath arrivals can increase or decrease the shape parameter compared with direct-path only propagation. A simplification to the modeling, analysis, and simulation was developed for narrowband transmit waveforms along with a characterization of what bandwidths satisfy the narrowband constraint in terms of the statistics of a conventional beamformer output from an equi-spaced line array.

The modeling and analysis presented in this paper provide the means for assessing the effect of array beamforming on the statistics of reverberation in a shallow water environment and may lead to novel array design methodologies or new beamforming algorithms that account for non-Rayleigh reverberation.

7. ACKNOWLEDGEMENTS

This work was sponsored by the Office of Naval Research under grant numbers N00014-02-1-0115 and N00014-03-1-0245.

REFERENCES

[1] Abraham DA and Lyons AP. Novel physical interpretations of K-distributed reverberation. IEEE Jnl. of Oceanic Engineering 2002; 27(4): 800–813.

[2] Abraham DA and Lyons AP. Simulating non-Rayleigh reverberation and clutter. IEEE Jnl. of Oceanic Engineering 2004; 29(2) in press.

[3] Abraham DA, Lyons AP, and Becker KM. D. A. Abraham, A. P. Lyons, and K. M. Becker. The effect of multipath on reverberation envelope statistics, in *Proceedings of 7th European Conference on Underwater Acoustics*, Delft, The Netherlands, July 2004, in press.

[4] Abraham DA and Lyons AP. Reverberation envelope statistics and their dependence on sonar bandwidth and scatterer size. IEEE Jnl. of Oceanic Engineering 2004; 29(1):126–137.

[5] Van Trees HL. Optimum Array Processing. John Wiley & Sons, Inc., New York, 2002.